UNIVERSITY OF SOUTHAMPTON

PREPARATION AND CHARACTERISATION OF HIGH OXIDATION STATE COMPOUNDS OF TRANSITION METALS

A Thesis submitted for the

Degree of Doctor of Philosophy

by

Sandra Elizabeth Dann

Department of Chemistry

Southampton

February 1994

Acknowledgements

CONTENTS

CHAPTER 4: Structure and Oxygen Stoichiometry in the System

$Sr_3Fe_2O_{7-y}$ $(0 \leq y \leq 1)$ 88

CHAPTER 5: Structure and Oxygen Stoichiometry in the System

$Sr_3Co_2O_{7-z}$ $(0.94 \leq z \leq 1.22)$ 114

CHAPTER 6: Preparation of $Sr_3M_{2-x}N_xO_{7-g}$ Phases

M, N, = Fe, Co and Ni   144

UNIVERSITY OF SOUTHAMPTON

Abstract

FACULTY OF SCIENCE
CHEMISTRY

Doctor of Philosophy

Preparation and Characterisation of High Oxidation
State Compounds of the Transition Metals
by Sandra Elizabeth Dann.

The synthesis of a range of complex oxides containing iron(IV), cobalt(IV) and nickel(III) is reported. These materials have been characterised by powder x-ray and neutron diffraction, thermogravimetric analysis, Mössbauer spectroscopy and magnetic and electrical measurements.

A new, pure iron(IV) phase, Sr_2FeO_4 has been synthesised and studied. This material crystallises with the K_2NiF_4 structure with an unusually regular octahedral coordination around the high spin d^4 iron. No evidence for structural distortion has been found on cooling to 4.2K. The Néel temperature has been determined as 64K. Mössbauer measurements have shown the magnetic structure to be based on a spin helix; although the 4.2K neutron diffraction pattern only showed evidence of ordering in two-dimensions.

The system $Sr_3Fe_2O_{7-y}$ $(0 \leq y \leq 1)$, which adopts the Ruddlesden-Popper phase intergrowth of $SrFeO_3$ (perovskite) and Sr_2FeO_4 (K_2NiF_4), has been studied. The Néel temperature has been determined as 110K and the electronic d^n configuration high spin d^4. A charge disproportionation reaction is evidenced by Mössbauer spectroscopy in the pure Fe(IV) material such that $Fe^{4+} \rightleftharpoons Fe^{3+} + Fe^{5+}$. Magnetic ordering has been shown to occur in two-dimensions only with a doubled a lattice parameter. For oxygen stoichiometries below seven, one oxygen site in the perovskite block becomes partially occupied and is completely empty at $y = 1$, producing an unusual square pyramidal iron(III) coordination.

A new strontium cobaltate, $Sr_3Co_2O_{7-z}$ has been prepared. This material possesses a structure similar to the Ruddlesden-Popper phase $Sr_3Ti_2O_7$, but triples in the b lattice direction as z increases above 1.0. Tripling is a result of oxygen ordering where one oxygen site is completely and two others partially occupied.

Mixed transition-metal oxide phases have been studied in the system $Sr_3M_{2-x}N_xO_{7-g}$ M,N = Fe, Co and Ni. The cobalt/nickel system adopts the tripled orthorhombic phase at low nickel content, resuming the tetragonal $Sr_3Ti_2O_7$ structure at higher nickel levels. Refinement of neutron diffraction data indicates partial oxygen occupancy on two oxygen sites.

Phase behaviour as a function of preparative conditions and oxygen stoichiometry has been studied in the system $La_{1-x}Sr_xFeO_{3-\delta}$ $(0 \leq x \leq 1, 0 \leq \delta \leq 0.5)$. Mössbauer measurements have shown when $\delta \approx 0$, that charge disproportionation of Fe^{4+} into Fe^{3+} and Fe^{5+} occurs in the orthorhombic and rhombohedral regions $(0 \leq x \leq 0.7)$, whereas the Fe^{4+} oxidation state remains distinct in the cubic region $(0.7 \leq x \leq 1.0)$.

The solid solution of the form $LaFe_{1-x}Cu_xO_3$ $(0 \leq x \leq 0.3)$ has been prepared. Investigation of the iron oxidation state by Mössbauer spectroscopy shows that both transition metals are predominantly in the trivalent state.

Nomenclature

i) Description of Metal-Oxide Polyhedra.

Discrete metal-oxide polyhedra are encountered frequently in this thesis and are described as MO_x. For example, an iron-oxygen tetrahedron would be assigned the terminology FeO_4, tetrahedral.

ii) Oxidation States

A number of different terms have been used for designation of oxidation state in this work. Experimentally derived oxidation states are represented as Arabic Numerals, for example Fe^{4+}. Roman numerals in parenthesis are also used to denote the oxidation state e.g. Fe(III). Oxygen is always assumed to be divalent i.e. O^{2-} and so the superscript is not used. Intermediate oxidation states, calculated by Bond Valence calculations or from derived oxidation states such as $Fe^{3.5+}$, are not intended to reflect the real charge on the atoms concerned, but an average of all the ions over all sites within the structure.

CHAPTER 1

Introduction

1.1 Complex Oxide Materials

Complex metal oxides have many industrial applications which utilise the unique chemical and physical properties of the materials(1). A variety of characteristics such as electrical and magnetic behaviour or changeable oxygen stoichiometry are exploited: examples of these applications include solid state devices such as capacitors or magnets, waste disposal agents, heating elements and rechargeable batteries. The properties of these materials are influenced not only by their stoichiometry, but also by preparative conditions which can alter crystallite morphology.

A number of solid state devices use the electrical properties of complex metal oxides, which can vary from insulating through semiconducting and metallic to superconducting, in their operations. For example, two very different types of electrical behaviour are employed in thermistors and switching elements. Thermistors are semiconductors which exhibit a linear change in resistivity with temperature, in a particular temperature range, whereas switching elements display a large and sudden change in conductivity at a particular temperature.

Another major use of complex oxide materials is in waste disposal agents. Nuclear waste for reprocessing can be inserted in a solid matrix such as β - Al_2O_3 allowing easy transportation, regeneration and storage. In a similar way, the cage structure of zeolites can be used to remove harmful ions from solution. Powerful oxidising agents such as K_2FeO_4 (2) can be used to break down organic materials in solution.

Complex oxide materials which can support oxygen non-stoichiometry and contain elements with more than one possible oxidation state can be used in oxide electrodes. For example, the oxygen reduction/generation capacity of Mo_xO_y type materials are used in fuel cells and metal/air batteries. The rechargeable battery works on a different principle using a solid electrolyte which acts as an ion conductor and separator; the Na/S battery uses liquid sodium and sulphur together with a carbon felt as the two electrodes and β - Al_2O_3 as the ceramic solid electrolyte. β - Al_2O_3 acts as an ion separator and an electrolyte since it is a sodium ion, but not an electronic, conductor.

Good thermal stability and shock resistance are important characteristics of heating elements and materials such as calcium-doped zirconia or $LaCrO_3$ are used for this purpose. These materials are also required to exhibit high corrosion resistance within the

desired temperature range.

Since oxide materials have numerous applications, research into materials using ambient conditions has been both extensive and exhaustive. One possibility to produce new materials which have practical applications is to find new preparative methods which allow new oxidation states of the elements to be accessed. The interest in the higher oxidation states has increased recently due to the discovery of high temperature superconductivity in cuprates (3-5). These materials contain the rare trivalent copper ion which had previously been very poorly characterised. New methods of producing highly oxidised materials have been developed using both high pressure annealing techniques (6) and electrochemical oxidation (7). These new techniques can now be used to produce novel materials containing unusual oxidation states, with the aim of producing industrially valuable materials.

1.2 Oxidation States Across the Transition Series

The transition elements can be classified as metals with partly filled d shells. Characteristically they have high melting points, alloy forming capability and, with very few exceptions, variable valence. The maximum attainable oxidation state is, however, dependant on the position of the element in the transition series. The highest oxidation state of the elements in the first transition series first rises and then falls as the series is transversed. (Figure 1.1)

This pattern is the result of the changing screening power of the extra nuclear electrons. Although in hydrogen the subshells of each principal shell are equienergetic, in the more complex atoms the s, p, d, f, and g subshells split apart and drop to lower energies. This descent in energy occurs because the degree to which an electron in a particular orbital is shielded from the nuclear charge by other electrons decreases with atomic number. The effective nuclear charge therefore rises with atomic number for a particular oxidation state within a subshell.

The rise in the third ionisation potential after iron in the first transition series reflects the fall off in the screening power of the extra nuclear electrons, and results in a greater number of compounds containing trivalent iron than trivalent nickel. The rapid fall off in the oxidation state after manganese is another indication of the drop in screening

3

	Ti	V	Cr	Mn	Fe	Co	Ni	Cu
d^0	iv	v	vi	vii				
d^1	iii	vi	v	vi				
d^2	ii	iii	vi	v	vi			
d^3		ii	iii	vi	v			
d^4			ii	iii	vi	v		
d^5				ii	iii	vi		
d^6					ii	iii	vi	
d^7						ii	iii	
d^8						i	ii	iii
d^9							i	ii
d^{10}								i

▩ rare oxidation state   ☐ normal oxidation state

Figure 1.1 Oxidation States of the First Transition Series

power of the electrons realising a maximum oxidation state of six for iron. The highest level of oxidation continues to drop until for copper the only common oxidation states are Cu(I) and Cu(II)

1.3 Oxidation States of Iron

Iron is the first element, on traversing the 3d transition series, where removal of all d electrons to form M^{d+} is not yet possible. The maximum attainable oxidation state is in fact 6^+ but this is very rare and has been observed only in some oxo-species synthesised in hypochlorite solution (2). No compound of iron(VI) has been prepared by solid state methods.

The other oxidation states of iron include (II), (III), (IV) and (V) which can all be

prepared by solid state reaction. However, ambient conditions usually afford materials consisting mainly of tripositive iron. Mildly reducing conditions are required to generate pure iron(II) materials and highly oxidising for materials containing iron(IV) or iron(V).

1.3.1 Chemistry of Iron(II)

The divalent state is the second most common oxidation state for iron. Iron(II) forms salts with nearly all common anions (NO_2^- is an exception; iron(II) is oxidised to iron(III) and nitrous oxide is produced). These are normally prepared in solution and are typically green in coloration e.g. $[Fe(H_2O)_6]^{2+}$. Iron(II) salts can be easily oxidised to their iron(III) counterparts and compounds such as $FeCO_3$, which is formed in carbon dioxide rich waters (8), is oxidised to Fe_2O_3 in air. The stability of iron(II) salts to oxidation is significantly increased in acid solutions and is also affected by the nature of the ligands. Fe(II) compounds which are most stable tend to be nitrogen containing; $Fe(NH_3)_6^{2+}$ is known where the Fe(III) analogue is not. Divalent iron compounds with oxygen donor ligands such as oxalate are rare with the Fe(III) analogue being much more stable. The coordination number of Fe(II) compounds is typically six with a few other stereochemistries known. For example, FeX_4^{2-}, X = Cl^-, Br^- and I^- are tetrahedral and a number of unusual geometries such as square pyramidal occur in biochemical systems e.g. haemoglobin (9). Both high spin and low spin complexes are known, though the former is more common. Low spin complexes occur with ligands towards the high end of the spectrochemical series such as CN^- and are stabilised by the low spin d^6 arrangement.

Stoichiometric iron(II) oxide is very difficult to synthesise: iron oxalate is heated to produce the iron deficient phase $Fe_{1-x}O$, $0.05 \leq x \leq 0.16$ (10), whereupon further heat treatment in the presence of extra iron at 1050K and 50Kbar of nitrogen pressure produces the stoichiometric phase (11).

Very few solid state reactions of iron(II) oxide are documented. These are strictly limited to the alkali metal ferrates which are prepared using highly reducing conditions (12).

$$2Na_2O + FeO \rightarrow Na_4FeO_3 \qquad [1]$$

5
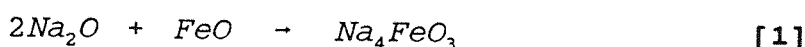
1.3.2 Chemistry of Iron(III)

Iron(III) is the most stable oxidation state of iron under atmospheric conditions. Fe(III) compounds exhibit a wide range of ligand stereochemistries and coordination geometries although most common are four-, five- and six-fold, the last being most typical. Complexes of iron(III) can be both low and high spin, but only ligands very high in the spectrochemical series, such as bipyridal, are capable of inducing spin pairing.

The most commonly used iron(III) oxide in solid state reactions is α-Fe_2O_3 which can be produced from heating FeO(OH) (13) at 200°C. This is a well known mineral, haematite, and has the corundum structure, the oxide ions forming a hexagonally close packed array, with the Fe(III) ions occupying octahedral interstices. By careful oxidation of Fe_3O_4 or heat treatment of FeO(OH), lepidocrocite, γ-Fe_2O_3 (14) is formed which may be regarded as a close packed array of oxide ions with Fe(III) ions randomly distributed over octahedral and tetrahedral interstices. A third, rare form of iron (III) oxide is ß-Fe_2O_3 which has a cubic structure of cell parameter 9.40Å and is similar to the mineral bixybite and ß-Mn_2O_3. It was first synthesised by the hydrolysis of $FeCl_3.H_2O$ (15); the structure consists of a body centred cubic lattice with two different iron sites which are both in a distorted octahedral environment.

α-Fe_2O_3 is the form used most frequently in solid state reactions. Pure iron(III) compounds in the solid state are normally generated by heat treatment of the constituent oxides e.g. LaFeO$_3$ is produced by heating haematite and lanthanum oxide at 1350°C for several days (16). Alternatively, some iron(III) oxides are produced by reduction of the mixed valence iron(III) and iron(IV) phase in hydrogen or *in vacuo* e.g. $Sr_2Fe_2O_5$ is produced by reducing the compound $SrFeO_{2.74}$ *in vacuo* (17). Characteristic of all preparations of iron(III) materials in the solid state are very high temperatures and long sintering times. They are generally high spin d^5 materials which exhibit antiferromagnetic ordering behaviour e.g LaFeO$_3$ is antiferromagnetically ordered at room temperature.

A wide range of iron(III) containing metal ferrites exist which can be synthesised by solid state methods. Associated with iron(III) chemistry in the solid state are many complex structures which have iron(III) in four, five and six coordination. A structure which occurs frequently is the brownmillerite structure (18). Brownmillerite, Ca_2FeAlO_5, has a structure consisting of alternating layers of corner-sharing octahedra and tetrahedra.

All the alkali earth metal ferrates such as $Sr_2Fe_2O_5$ (19), $Ba_2Fe_2O_5$ (20) and $Ca_2Fe_2O_5$ (21) (Figure 1.2) form this structure which features very distorted iron tetrahedra and octahedra. For example, in $Sr_2Fe_2O_5$ the tetrahedral bond distances of 1.92Å, 1.98Å and 1.82Å and octahedral bonding distances of 1.87Å, 2.09Å and 2.18Å are exhibited.
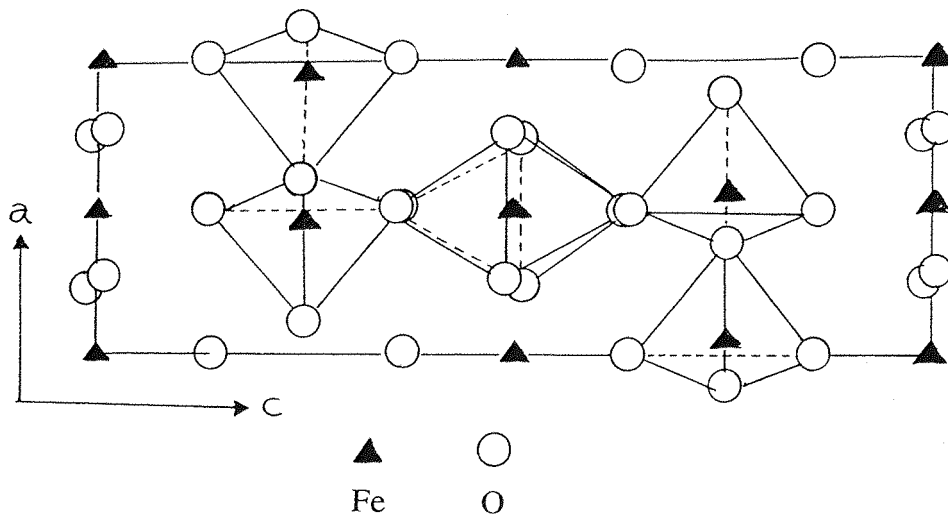
Figure 1.2 Projection Along the 110 Plane in $Ca_2Fe_2O_5$.

Lanthanide ferrites (Ln = Sm, Gd, La, etc) all have an orthorhombically distorted perovskite structure (Figure 1.3) which is now accepted as a structural type after the first recognised, the " $GdFeO_3$" structure (22).
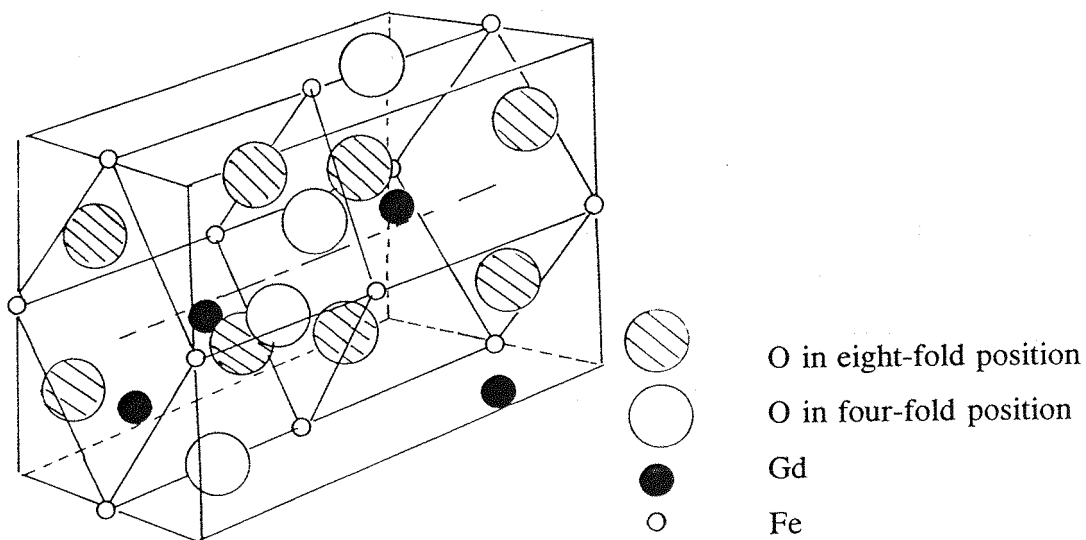
Figure 1.3 The $GdFeO_3$ Structure.

7

In the $GdFeO_3$ structure the Gd atom is twelve coordinate with eight different bonding distances. The transition metal ion has three different bond distances producing a distorted octahedral environment.

Another common structure in the solid state chemistry of Fe(III) is the K_2NiF_4 structure in which NaCl like layers of NiF are interleaved with perovskite, $KNiF_3$, blocks e.g. $LaSrFeO_4$ (23). There are a few other simple structures in solid state iron(III) chemistry such as the iron(III) spinels e.g. $ZnFe_2O_4$ (24). More complex and unusual structures also exist such as barium hexaferrate $BaFe_{12}O_{19}$ (25) and cubic $Ba_3Fe_2O_6$ (26) which has an 18Å unit cell.

1.3.3 Chemistry of Iron(IV)

The incidence of pure iron(IV) materials in both solid state and aqueous chemistry is rare although there is a significant number of mixed valence compounds containing trivalent and tetravalent iron.

In solution, chemical and electrochemical oxidation have been used to generate iron(IV) materials from the iron(III) analogues e.g. $[Fe(bipy)_3]^{4+}$ (27). Fe(IV) is generally six coordinate in these materials; four coordination is also known e.g. $[Fe(S_2CNR_2)]^{3+}$. These materials have been shown to be invariably low spin.

Pure iron(IV) materials in the solid state are limited to the ternary alkali and alkali earth metal oxides and are usually produced using high oxygen pressure. The coordination of the iron is normally six, the spin state, however, is a matter of dispute. $SrFeO_3$ was first prepared in 1965 using several hundred atmospheres of oxygen pressure (28) and is, perhaps, the most-studied iron(IV) material. Recently, an ambient method of synthesising $SrFeO_3$ has been reported using electrochemical means (29). $SrFeO_3$ is a metallic conductor with an antiferromagnetic ordering temperature of 134K. It forms a perfect perovskite cube with a cell parameter of 3.850Å even though the magnetic moment is indicative of a high spin d^4 material which would be expected to be Jahn-Teller (30) distorted. The high electrical conductivity indicates the e_g^* orbital is broadened into an itinerant electronic conduction band. Mössbauer measurements further support this hypothesis since the room temperature spectrum consists of a single resonance which separates into a single hyperfine sextet at low temperature (Figure 1.4). An insulator

which had high spin d^4 configuration should produce a quadrupole split doublet at room temperature due to the asymmetry of the electronic configuration leading to an electric field gradient.

Low temperature neutron diffraction measurements on $SrFeO_3$ have shown the magnetic reflections to belong to an unusual type of magnetic ordering behaviour based on an α-spin helix (31,32). No evidence to suggest a Jahn-Teller distorted ion was found in high resolution neutron diffraction measurements even at 4.2K.
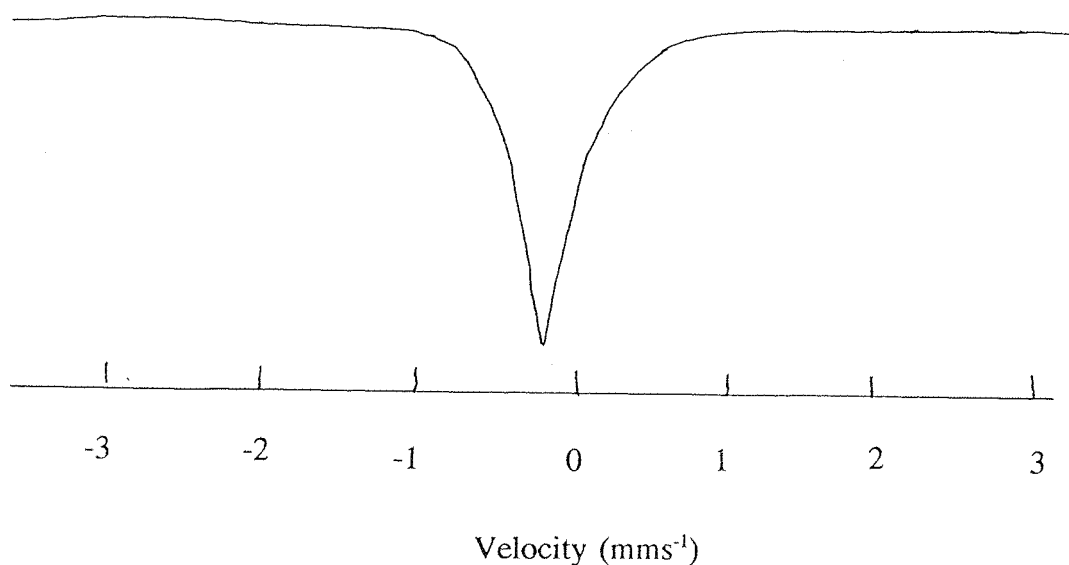
Figure 1.4 Mössbauer Spectrum of $SrFeO_3$ at 298K

$CaFeO_3$ is another well characterised iron(IV) material (33). The conditions required to produce pure $CaFeO_3$ are more oxidising than for the strontium material, typically 20Kbar and 1273K. $CaFeO_3$ has a tetragonally distorted perovskite structure with a = 5.325Å and c = 7.579Å. Semiconducting behaviour is exhibited and magnetic measurements suggest the presence of four unpaired electrons. However, the major difference between this material and $SrFeO_3$ is the low temperature Mössbauer behaviour. At temperatures exceeding 300K the spectrum consists of a singlet. On cooling the signal separates initially into two singlets of equal intensity and then, below the antiferromagnetic ordering temperature of 115K, into two hyperfine split sextets of equal intensity. The two

signals are not characteristic of iron(IV), but of iron(III) and iron(V) (Figure 1.5).

Velocity (mms^{-1})
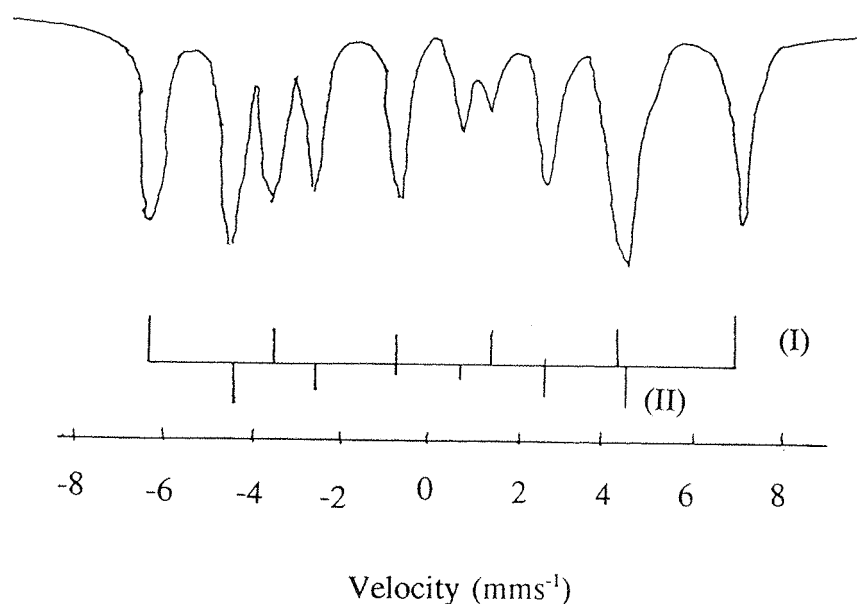
Figure 1.5 Mössbauer Spectrum of CaFeO$_3$ at 4.2K

1.3.3.1 Charge Disproportionation in Compounds of Iron(IV)

The low temperature behaviour of CaFeO$_3$ is a result of a charge disproportionation reaction. The effect observed in the Mössbauer spectrum as the temperature was lowered was first separation into two paramagnetic signals of equal intensity followed by separation into two magnetically ordered sextets. The chemical shift of the room temperature spectrum was also unusually low for an iron(IV) material at 0.07mms^{-1}. The two signals were identified by Takano (33) as belonging to iron(III) and iron(V) and a charge disproportionation reaction was proposed:

$$2Fe^{4+} \rightleftharpoons Fe^{3+} + Fe^{5+} \qquad [2]$$

10
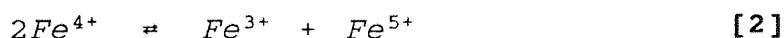
Evidence to support this mechanism has also been highlighted by Mössbauer spectroscopy of other iron(IV) systems, both by Takeda et al in the $La_{1-x}Sr_xFeO_3$ and $Ca_{1-x}Sr_xFeO_3$ systems (33) and by Battle et al in the $Sr_2LaFe_3O_{9-y}$ system (34), which is equivalent to x = 0.66 using the Takano formulation.

Takeda proposed that the disproportionation effect was a short range ordering effect, since there was no evidence by neutron, x-ray or electron diffraction to suggest a structural consequence of this reaction. Attempts by Battle, using low temperature neutron diffraction with moderate resolution (35), also showed no distortion in $Sr_2LaFe_3O_{8+y}$ from which he concluded that there was cationic disordering in the system.

1.3.4 Chemistry of Iron(V)

Iron(V) chemistry is very poorly documented in both solution and solid state chemistry. Solution chemistry is limited to reactions using the highly oxidising K_2FeO_4 (36) to produce alkali metal ferrates such as K_3FeO_4 (37). These materials have not been isolated as pure materials although there are some vibrational spectra reported for the anions (38). In both cases the iron(V) atom is thought to be four or six coordinate.

In 1990 the first iron(V) material was produced by solid state methods by heating potassium peroxide and $KFeO_2$ at 470°C in a gold tube for 18 days (39). These conditions produced the material K_3FeO_4 as black, needle-like crystals. (Figure 1.6) A molten salt method of producing Na_3FeO_4 (40) was reported in 1973.

1.3.5 Chemistry of Iron(VI)

Iron(VI) chemistry is much better documented than that of iron(IV) and iron(V). K_2FeO_4 was discovered in 1932 and can be used as an oxidant to remove organic materials from solution (2,33). This material has been used to generate a wide range of alkali and alkali earth metal iron(IV) compounds including $BaFeO_4$ (41) and Na_2FeO_4 (42). Synthesis has only been achieved in solution by oxidation of iron(III) nitrate in a super-saturated alkaline solution using hypochlorite (43). This compound can be isolated as purple/red crystals although purification is difficult due to the oxidising capability of the ion.

O   O

● K

. Fe
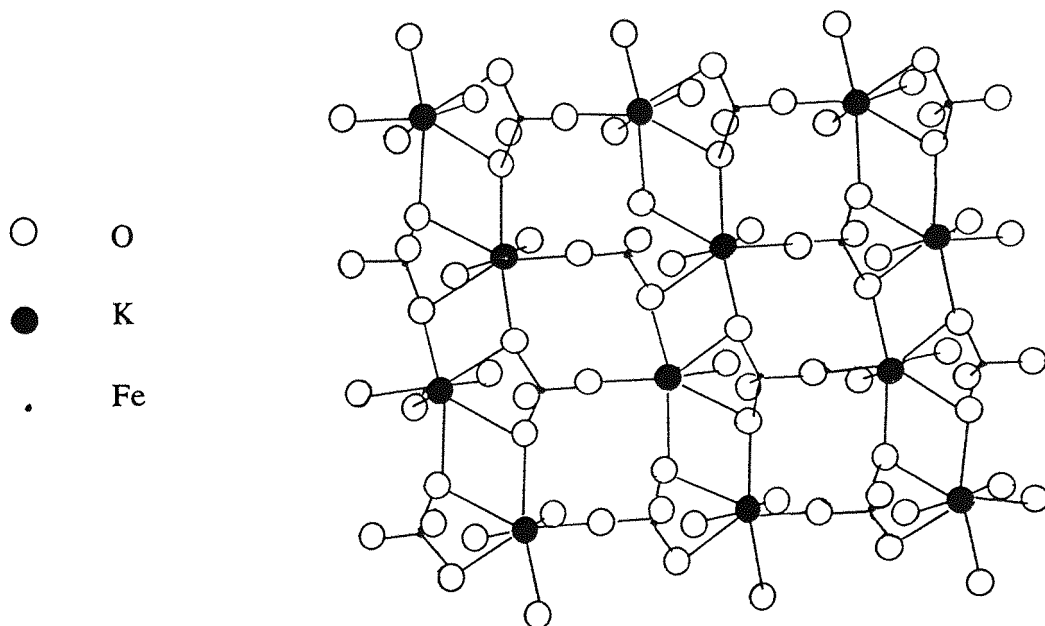
Figure 1.6 The Orthorhombic Structure of K_3FeO_4

1.3.6 Mixed Valence Compounds of Iron

There are many compounds of iron which contain more than one oxidation state. Most commonly are mixed valence iron(II) and iron(III) compounds such as Fe_3O_4 or Prussian Blue (44) although there are also numerous mixed valence iron(III) and iron(IV) compounds. Prussian Blue which can be used as a pigment has the formula $Fe_4^{III}[Fe^{II}(CN)_6]_3.xH_2O$. The structure is based on a three dimensional cubic framework with metal atoms at the corners of a cube with M^A - C - N - M^B links. There can be empty metal and CN sites depending on the stoichiometry (on the valence of M^A and M^B). Water molecules can also be bound to Fe^{III} in Prussian Blue.

Iron sulphur complexes have been extensively studied because of their relationship to nonheme iron sulphur proteins. They contain iron in both dipositive and tripositive and mixed valence states and have formulae $[Fe(SR)_4]^{1-,2-}$ (45) (Figure 1.7).

A prime feature of many of these systems and others with both iron and molybdenum are reversible electron transfer reactions and these give a clue to the importance of such polynuclear species in nature.

Mixed valence iron(III) and iron(IV) systems occur frequently in the ferrate
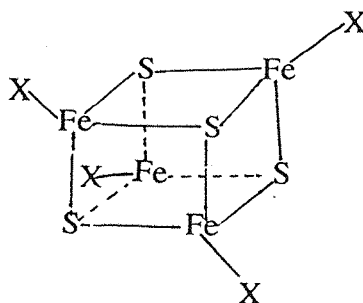
Figure 1.7 Cubane Structure of $[Fe(SR)_4]^{1-,2-}$

materials. Iron(IV) systems, such as $Sr_3Fe_2O_7$, can support a wide range of oxygen non-stoichiometry leading to interesting coordination geometries (46). For example, systematic removal of oxygen from the 110 plane in $SrFeO_{3-\delta}$ gives a compound $Sr_4Fe_4O_{11}$ which was first recognised by Greaves *et al* (47). Removal of all oxygen from this plane gives the pure iron(III) material $Sr_2Fe_2O_5$ (19). Other mixed valence ferrates include $CaFeO_{3-y}$ (48), $BaFeO_{3-y}$ (49) and Sr_2FeO_{4-y} (50) which can all be produced using ambient conditions of temperature and pressure.

1.4 Oxidation States of Cobalt

The reduction in stability of the very high oxidation states which was apparent with iron, continues with, and is accentuated in, cobalt. In solution, the relative stability of the divalent to trivalent state is further increased and the incidence of oxidation state (IV) or greater is very rare. The tripositive state is unstable in simple compounds, but the low spin complexes are exceedingly numerous and stable, especially where the donor atoms produce a significant ligand field. In contrast to iron, there are some important monovalent complexes of cobalt, an oxidation state which is almost unknown for any other first row transition element except copper (51).

Solid state compounds are abundant for the tripositive state although cobalt(II), (IV) and (V) are also known. The higher oxidation states require severe oxidative conditions and the compounds produced are very sensitive to atmospheric moisture.

13

1.4.1 Chemistry of Cobalt(II)

In contrast to iron(II), divalent cobalt is not easily oxidised to Co(III) in aqueous solutions containing no complexing agents. However, in basic conditions or in the presence of complexing agents high in the spectrochemical series, the stability of Co(III) is greatly improved.

The complexes formed by cobalt(II) are mostly either tetrahedral or octahedral, but five coordinate and square planar species are also known. There are more tetrahedral complexes of cobalt(II) than for any other transition metal. This is a result of the d^7 configuration which has the least disfavour for the tetrahedral configuration over the octahedral one, for any d^n. This small stability difference between these configurations can result in their simultaneous presence in solution e.g. thiocyanates in methanol (52). A wide range of both low and high spin complexes are known. The low spin octahedral complexes, however, are rare with a tendency to become four or five coordinate with the loss of ligands. Tetrahedral complexes are generally formed with monodentate anionic ligands such as Cl^-, Br^- or SCN^- although some bidentate cases are known with very bulky ligands e.g. N - alkylsalicylaldiminato, ß - diketonate anions. Both forms of five coordinate species, trigonal bipyramidal and square pyramidal, occur in both low and high spin configurations. A distinguishing characteristic between the most common coordination geometries is colour. Octahedral complexes tend to be pink or red, and tetrahedral blue, due to the two different transitions in the electronic spectrum.

Solid state chemistry of cobalt(II) is very rare since the cobalt(II) materials can be easily oxidised to cobalt(III) in air. This is exemplified by considering the oxide materials. Cobalt(II) oxide is produced by heating cobalt(II) nitrate or carbonate (53). This material is not stable to atmosphere oxidation and tends to oxidise to the other higher oxides, Co_3O_4, Co_2O_3. Despite these materials being susceptible to moisture, they are all widely used as a starting materials for the synthesis of cobalt materials in the solid state. A rare example of a pure divalent cobalt material in the solid state is La_2CoO_4 (54) which is prepared by reaction of CoO and La_2O_3 at 2000°C under carbon dioxide or argon. This material has an orthorhombic structure based on distortion of the K_2NiF_4 tetragonal system and is isostructural with La_2CuO_4.

1.4.2 Chemistry of Cobalt(III)

The instability of the tripositive state is evidenced by the rarity of simple salts and binary compounds whereas cobalt(II) forms them in abundance. e.g. uncomplexed cobalt (III) can be rapidly reduced by water (55). Cobalt (III) salts are generated from cobalt(II) in solution using oxygen or hydrogen peroxide and a surface active catalyst in the presence of ligands (56).

$$4 CoX_2 \; + \; 4NH_4X \; + \; 20NH_3 \; + \; O_2 \; \rightarrow \; 4 \, [Co(NH_3)_6] X_3 \; + \; 2H_2O \quad [3]$$
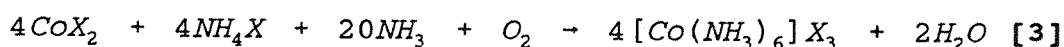
Compounds containing trivalent cobalt in the solid state are quite numerous. Both the pure cobalt(III) materials such as $Sr_2Co_2O_5$ (57) and mixed valence materials such as $SrCoO_{3-x}$ (58) exist. It is important to note however, that there are considerably fewer cobalt(III) materials than iron(III) compounds and the former tend to be more susceptible to atmospheric conditions.

Although the incidence of mixed valence cobalt compounds in the solid state is frequent, pure cobalt(III) materials are quite rare. Cobalt(III) materials generally require more oxidising conditions and more careful handling than their Fe(III) counterparts. For example, $LaFeO_3$ can be synthesised in air at 1350°C, whereas $LaCoO_3$ requires 1200°C and a pure oxygen atmosphere for reaction (59). However, cobalt(III) materials do form similar structures to the iron(III) systems e.g. $Sr_2Co_2O_5$ and $Sr_2Fe_2O_5$ exhibit the brownmillerite structure.

1.4.3 Chemistry of Cobalt(IV)

There are very few examples of cobalt(IV) in solution. An authentic example is alkyltetra (1-norbornyl) cobalt (60) which is low spin d^5 and paramagnetic. This compound is reasonably stable to both heat and air and can be electrochemically oxidised to the Co(V) ion, $[Co(nor)_4]^+$.

Pure cobalt(IV) compounds are more prevalent in the solid state than in solution. A selection of cobalt(IV) materials has been synthesised using autoclaves since the early

1970s. These materials generally contain alkali metal or alkali-earth metal ions such as sodium or strontium. A variety of complex structures are present, cobalt generally being present in six coordination e.g. $K_6Co_2O_7$ (61) or Li_8CoO_6 (62). The difficulty in preparing the pure cobalt(IV) materials is extreme in comparison to iron(IV). For example, $SrFeO_{3.00}$ (25) is synthesised at 450°C using 800bar of pressure, in contrast $SrCoO_{3.00}$ (63) can only be made using a diamond anvil device at 1000°C and a pressure of 65Kbar in the presence of $KClO_3$.

1.4.4 Chemistry of Cobalt (V)

The known chemistry of cobalt(V) is very limited. The only widely accepted example in solution being $Co[nor]_4^+$ (nor = 1-norbornyl) (60). Similarly, solid state syntheses to produce cobalt(V) materials are also uncommon; K_3CoO_4 is a proven example (64) and was produced by reaction in a oxygen at 460°C for several days.

1.4.5 Mixed Valence Compounds of Cobalt.

Mixed valence compounds of cobalt are significantly less common than the corresponding iron analogues. In fact, cobalt (II)/(III) compounds are exceptional; very few have been produced by electrochemical oxidation (65).

Mixed valence cobaltates containing both cobalt(III) and cobalt(IV) are more numerous e.g. $SrCoO_{3-\delta}$ (66), $La_{1-x}Sr_xCoO_3$ (67). These materials exhibit a wide range of oxygen non-stoichiometry and a variety of structures analogous to the $SrFeO_{3-\delta}$ system. A material with a doubled 'cubic' unit cell in which a = 7.70Å (68) is thought to be related to $Sr_4Fe_4O_{11}$. One phase which is not present in the iron system is $SrCoO_{2.70}$ which has a hexagonal structure (69).

1.5 Oxidation States of Nickel

Highest oxidation state stability decreases further with nickel such that only divalent nickel occurs in the ordinary chemistry of the element. The low oxidation states have considerable importance in catalysis (70). There is also a wealth of low oxidation state

chemistry applicable in organometallic chemistry. In solution, the occurrence of nickel(III) and nickel(IV) species is rare and in many of these it is not clear whether it is actually the metal atom rather than the ligand that is oxidised.

1.5.1 Chemistry of Nickel(II)

Nickel(II) compounds exhibit a wide range of ligand stereochemistries and coordination geometries. Three, four, five and six coordination is known with a variety of geometries; trigonal planar, tetrahedral, square planar, square pyramidal, trigonal bipyrimidal, octahedral and trigonal prismatic.

There are numerous binary compounds of nickel(II) which can be made in solution or in the solid state. Precipitation from solution can be used to produce a variety of salts including the hydroxide $Ni(OH)_2$ and the nickel halides (except the fluoride) are made directly from reaction of the elements. Other nickel compounds can also be obtained by direct reaction of nickel with non-metals such as P, As, Sb, C and B although not all are stoichiometric. Magnetically, nickel(II) materials have relatively simple behaviour and octahedral complexes invariably show two unpaired electrons.

Octahedral complexes are common e.g. $[Ni(H_2O)_6]^{2+}$ and five coordinate species with both square pyramidal and trigonal bipyrimidal exist in both high and low spin states. As a natural consequence of the d^8 configuration the planar geometry is preferred in the four coordinate species. The planar set of d orbitals give $d_{x^2-y^2}$ a uniquely high energy and the eight electrons occupy the other four d orbitals. The occupation of the antibonding level is unavoidable in the tetrahedral coordination. For Pd^{II} and Pt^{II} this factor is so important that no tetrahedral complexes are formed. The planar complexes are frequently red/brown or yellow in coloration e.g. yellow $Ni(CN)_4^{2-}$. Tetrahedral complexes are generally only formed where bulky ligands make planarity sterically impossible.

1.5.2 Chemistry of Nickel(III)

The evidence for trivalent nickel compounds in solution is limited. Ni(III) fluoride has been prepared as an impure, black, non-crystalline solid, marginally stable at 25°C (71) There are several well proven crystalline forms of NiO(OH). The more common form

ß - NiO(OH) (72), can be formed by oxidation of nickel(II) nitrate with bromine in aqueous potassium hydroxide below 25°C.

Macrocyclic nitrogen compounds containing nickel(II) can be electrochemically oxidised to the nickel(III) and, more rarely, nickel(IV) analogues (68). Tertiary phosphine complexes of this type were the first Ni(III) species to be made by halogen oxidation of $NiX_2(PR_3)_2$ (73). A similar organometallic derivative is shown below (Figure 1.8)
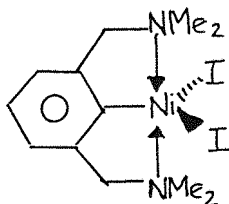
Figure 1.8 Macrocyclic Compound Containing Ni(III)

$NaNiO_2$ has been formed using molten salt chemistry (74). Oxygen gas is bubbled through molten alkali hydroxides contained in nickel vessels at 800°C.

Solid state preparations have been used to produce many compounds of nickel(III), mainly of the alkali metal or alkali earth metals such as $Sr_2Ni_2O_5$ (75). Preparation of Ni(III) oxides in the solid state usually requires long sintering times e.g. Na_5NiO_4 (76) is prepared by reaction for 7 days in a gold tube at 650°C.

1.5.3 Chemistry of Nickel(IV)

The chemistry of Ni(IV) is poorly documented in solution and in the solid state. In solution a few Ni(IV) compounds have been generated using electrochemical oxidation. Examples of this are some well established octahedral complexes with phosphine or arsine ligands which are produced by oxidation of Ni(II) e.g. $[diphos_2NiCl_2]^{2+}$ (77). Alkali metal salts such as the red purple, M_2NiF_6, (78) can be made by fluorination.

18

Tetravalent nickelates in the solid state are extremely rare with $BaNiO_3$ (79) and $SrNiO_3$ (75) the only well characterised examples although there is still some doubt about the oxygen stoichiometry of the compounds.

1.5.4 Mixed Valence Compounds of Nickel

Unlike cobalt and iron, nickel has another well known type of mixed valence material containing divalent and tetravalent nickel. These materials are based structurally on the partially oxidised tetracyanoplatinates which have alternating square planar and octahedral platinum atoms linked by halogens. However, the nickel compounds are more difficult to prepare due to the incidence of Ni(III). This unusual system is due to the stability of Ni(II) square planar and low spin d^6 Ni(IV) ions. The stability of this arrangement increases significantly in the Pt/Pd analogues where the high spin configurations are energetically disfavoured.

Mixed valence Ni(II)/Ni(III) compounds are also rare but an authentic example is $Ni_3O_2(OH)_4$ (80) which is formed by aging hot solutions of β - NiO(OH).

1.6 Mixed Transition Metal Oxides

There is (81-83) an enormous number of compounds which contain more than one transition metal ion. In some cases the individual oxidation states are difficult to ascertain, especially when there is a very small proportion of one ion. This is a problem encountered in doping studies of the high temperature superconductors (84) due to the very low levels of dopant. Generally, however, the relative ionisation potentials of the ions give a good indication to the probable oxidation state of the ion. For example, in $Sr_2FeTiO_{5.5}$ the titanium ion is in the tetravalent state and the iron in the trivalent state which could be predicted by the ionisation potentials of Fe = 56.8eV and Ti = 43.2eV (85) ($M^{3+} -> M^{4+}$). Mixed valence compounds containing iron can be characterised using Mössbauer spectroscopy by correlation with standard Mössbauer parameters.

1.7 Oxide Materials - Simple Building Blocks

There are many different complex structures in transition metal oxide chemistry generated by a variety of combinations of some basic building blocks. These structures consist of aggregates of O^{2-} ions with positive ions of various kinds and the number of oxygen ions surrounding a given ion being determined in a general way by the ratio of the radii of the ions and the O^{2-} ion. There are very few first row transition metal ions which can have coordination numbers greater than six. Larger ions, typically with relatively low oxidation states and with an ionic radius around 1Å, have coordination numbers as high as 12 e.g. Sr (1.13Å), Y (0.89Å) or K (1.33Å). Few have ionic radii which are similar in size to the oxide ion (1.40Å).

Generally many complex oxides are assemblies of O^{2-} ions in close packing (in which each has 12 nearest neighbours) with the smaller positive ions occupying the interstices between them. When the oxide ion and the A cation are of comparable sizes they form a close packed arrangement, with smaller positive ions occupying spaces between four or six oxide ions (giving tetrahedral or octahedral geometry). The oxide ions form a close packed rigid lattice and the structure will not collapse even if the small ions are absent (provided the structure is electrically neutral). Changes in valency maintain electrical neutrality and allow variation in the stoichiometry. When there are fewer small ions in the structure than available sites the atoms are often distributed statistically e.g. $\gamma\text{-Fe}_2O_3$. In addition to cationic vacancies, this type of structure can support varying degrees of oxide ion vacancy, leading to many non-stoichiometric and mixed valence materials.

The simplest type of complex oxide structure is the solid solution of one oxide in another i.e. ions of more than one kind randomly occupy the cation positions in a simple oxide structure M_xO_y. e.g. CeO_2 (fluorite structure) with UO_2 to give uranium cerium blue $Ce_{1-x}U_xO_2$. An element with two possible oxidation states can exist in a structure characteristic of more complex oxides e.g. Ti_3O_5 forms the pseudobrookite structure (86) Fe_2TiO_5 i.e. $[Ti^{3+}_2Ti^{4+}O_5]$. If elements in a solid solution replace ions in an orderly way a superstructure of the simple structure is formed e.g. $LiNiO_2$, NaCl superstructure.

The structures basically exist as two main types

i)   close packed oxide layers

all tetrahedral holes occupied	Be_2SiO_4
all octahedral holes occupied	XYO_2 e.g. $LiNiO_2$
⅔ " " "	XYO_3 e.g. $FeTiO_3$
½ " " "	XYO_4 e.g. $MgWO_4$
	XY_2O_6 e.g. Niobite

ii)   close packed X + 3O layers

all octahedral holes occupied	ABO_3 perovskite
	$A_2B'B''O_6$ cryolite

During the course of this work the latter type of oxide structure is encountered most frequently. These structures include ABO_3, K_2NiF_4 and general intergrowths of the two which are discussed further below.

1.7.1 The Perovskite Structure

Since the discovery of ferroelectric properties in $BaTiO_3$ (87) in 1945, ABO_3 compounds with the perovskite structure have been comprehensively studied. These studies resulted in a wealth of materials with ferroelectric and piezoelectric properties. By 1955 numerous combinations of A and B had been tested and Galasso (88) had produced a variety of perovskite materials with more than one element in the B position. Today there are an enormous number of perovskite based compounds with more than one element in both A and B positions.

Most compounds with the general formula ABO_3 have the perovskite structure. The atomic arrangement of atoms in this structure was first determined for the mineral perovskite $CaTiO_3$. At this time the structure of $CaTiO_3$ was thought to be represented by Ca ions at the corners of a cube with Ti at the body centre and oxide ions on the centre

of the faces. (Figure 1.9) The space group of this material being Pm3m. Although $CaTiO_3$ was later found to be orthorhombic (89) the name perovskite was continued to be used to describe this cubic array of ions. In fact, few compounds have the perfect perovskite structure at room temperature, but do assume it at high temperatures. In the structure the A cation is coordinated with twelve oxide ions and the B cation by six.
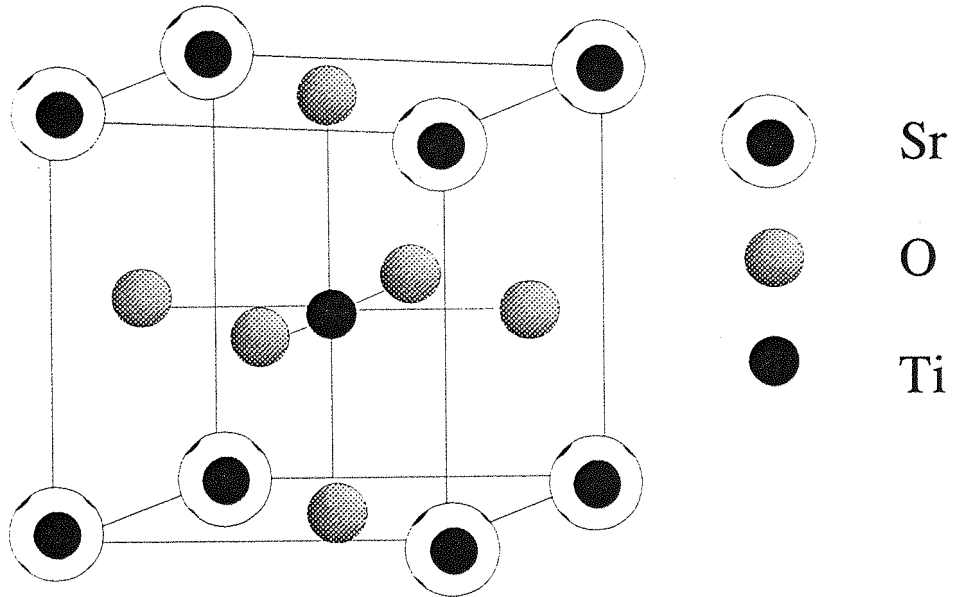
Figure 1.9 The Perovskite Structure.

Consequently, A is normally somewhat larger than B. Ideally, for contact between the A,B, and O ions, the radii R should satisfy the equation [4].

$$R_A \ + \ R_O \ = \ \sqrt{2} \ (\ R_B \ + \ R_O \ ) \qquad\qquad [4]$$

Goldschmit (90) has shown that the cubic perovskite structure is only stable when a tolerance factor, t, defined by the equation [5].

$$R_A \ + \ R_O \ = \ t\sqrt{2} \ (\ R_B \ + \ R_O \ ) \qquad\qquad [5]$$

lies between 0.8 and 0.9. This factor can have a larger range when the perovskite

structure is distorted.

For electrical neutrality in this perovskite structure the sum of the positive charges should be six. This can clearly be made up in a number of ways e.g. A can be $1+$, $2+$, and $3+$, whilst B is $5+$, $4+$ and $3+$. Oxygen vacancy results in one ion having dual valence. Therefore, compounds which can exist in a variety of oxidation states, such as the transition metals, have been extensively studied in oxygen deficient perovskites.

The most common perovskites are formed with trivalent and tetravalent B cations. However, these two systems ($A^{2+}B^{4+}O_3$, $A^{3+}B^{3+}O_3$) have very different structural formations as a function of the ionic radii or tolerance factors. For $A^{2+}B^{4+}O_3$ the vast majority of compounds are cubic or pseudo-cubic with very small structural distortions (Fig 1.10). However, for $A^{3+}B^{3+}O_3$ (Fig 1.11) the largest number of compounds are found with the orthorhombic structure first determined for $GdFeO_3$ by Geller and Wood (22). A common structure observed in both of these systems is the rhombohedral cell formed by $LaCuO_3$ (91) and $BaTiO_3$ (92) below 90°C.

Ternary oxides can be both A-cation or anion deficient. The tungsten bronzes provide a good example of cation deficiency e.g. Na_xWO_3 ($0.3 < x < 0.95$) (93). Oxygen deficiency in the perovskite structure and its effect depend on the elements involved; $SrBO_{3-x}$ B = Ti, V have a wide range of oxygen stoichiometry e.g. $0 < x < 0.5$. The titanium system retains the perfect perovskite cube over this range. $SrFeO_{3-x}$ (94), $CaMnO_{3-x}$ (95) and $SrCoO_{3-x}$ (96) are all capable of supporting a wide range of oxygen non-stoichiometry. However, the cubic perovskite structure is not retained and many new structures are formed e.g. $Sr_2Co_2O_5$ (56) brownmillerite, $Ca_3Mn_3O_8$ (97) orthorhombic and $SrFeO_{2.84}$ (98) tetragonal.

1.7.2 The K_2NiF_4 Structure

The K_2NiF_4 structure (99) is a tetragonal structure closely related to the perovskite structure, ABX_3. In the simplest case the perovskite blocks are now interspaced with AX layers giving a new formula $AXABX_3$ i.e. A_2BX_4 generating a tetragonal structure. The B atoms have the same six fold coordination, but the A atoms become nine coordinate.

This structure is similar to the perovskite and can also be discussed in terms of tolerance factors. Tolerance factors for typical K_2NiF_4 materials lie between 0.85 and

0.985 as suggested by Ruddlesden and Popper (100). When tolerance factors are low the K_2NiF_4 structure does not form suggesting that, contrary to the perovskite structure, the radius of the A cation cannot be reduced much below the geometrical conditions for touching spheres i.e. $t = 1$.

1.7.3 Ruddlesden-Popper Phases.

These materials were first characterised in 1957 (101,102). The K_2NiF_4 structure forms part of this group where n perovskite layers are interleaved with AX layers. This terminology generates the K_2NiF_4 when $n = 1$. The structure was first determined for the strontium titanates and is known in this system up to $n = 3$. The difficulty in producing these materials increases as the periodic table is transversed and the value of n increases. For example, there is no nickel analogue of the strontium titanate Sr_2TiO_4. The structure of the three well known titanate phases is shown in Figure 1.12.

1.8 Bond Valence Theory

The method of assignment of single, double or triple bonds which is applicable to organic chemistry cannot be used in crystalline, non-molecular inorganic chemistry. In the past, due to this unsuitability of the classical valence bond model to inorganic structures, materials have been described mostly by purely geometric means. The most widely used descriptive techniques in structural inorganic chemistry are close packing of spheres and the linking of coordination polyhedra. However, these methods are purely descriptive and do not give any direct information regarding bond strengths and respective site valences.

The determination of the exact valence of elements in a structure is often impossible since these geometric techniques do not allow the strength of bonds to be quantified. Since the discovery of high temperature superconducting oxides containing mixed valence copper (3-5) the ability to assign different oxidation states to crystallographically distinct sites has become important. To overcome the limitations of the geometric methods, an empirical approach has been designed to describe bonds in non-molecular inorganic solids. A number of workers have developed this technique but two authors, Zachariasen and Brown, are primarily responsible for the theory.

24
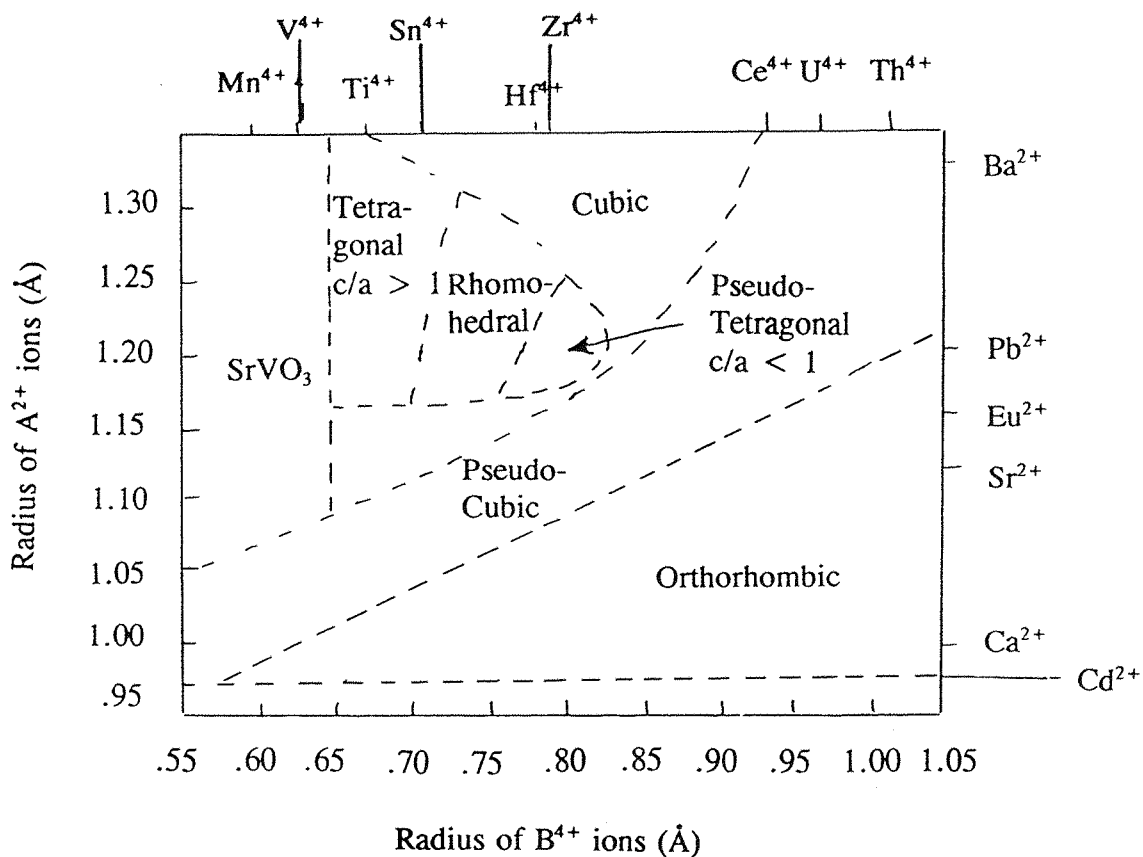
Figure 1.10 Change in Structure with Ionic Radii in $A^{2+}B^{4+}O_3$
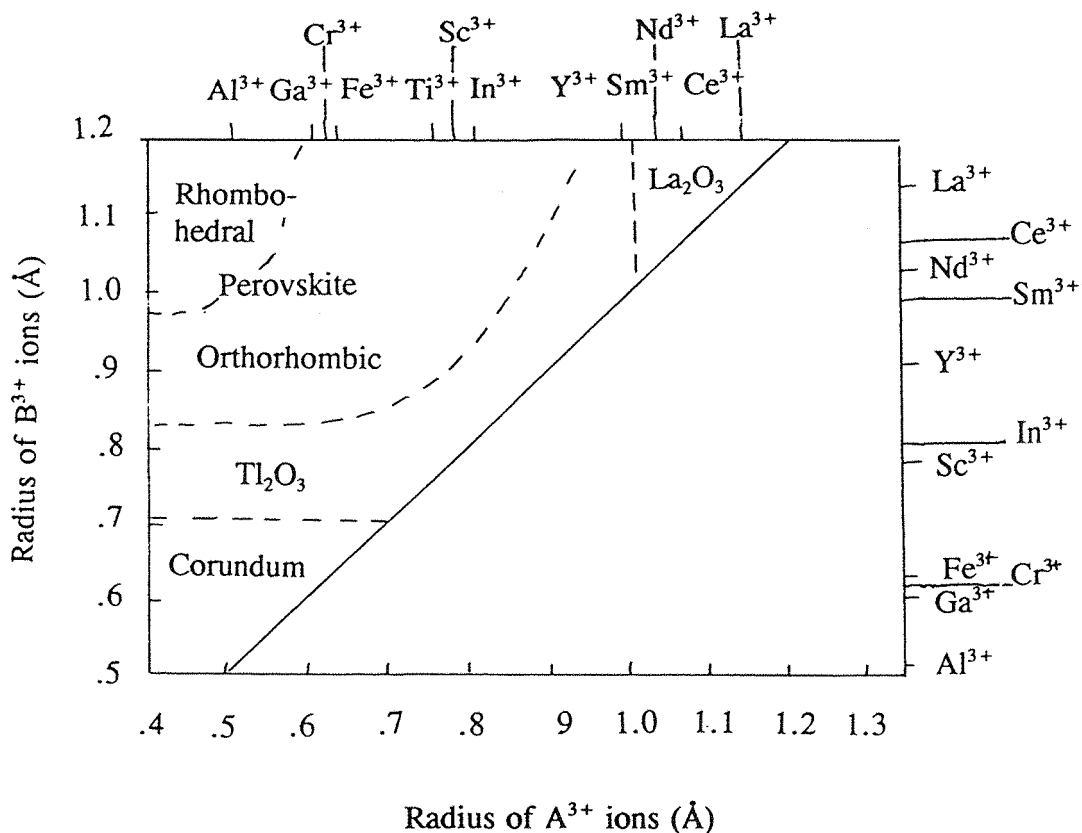
Figure 1.11 Change in Structure with Ionic Radii for $A^{3+}B^{3+}O_3$

25
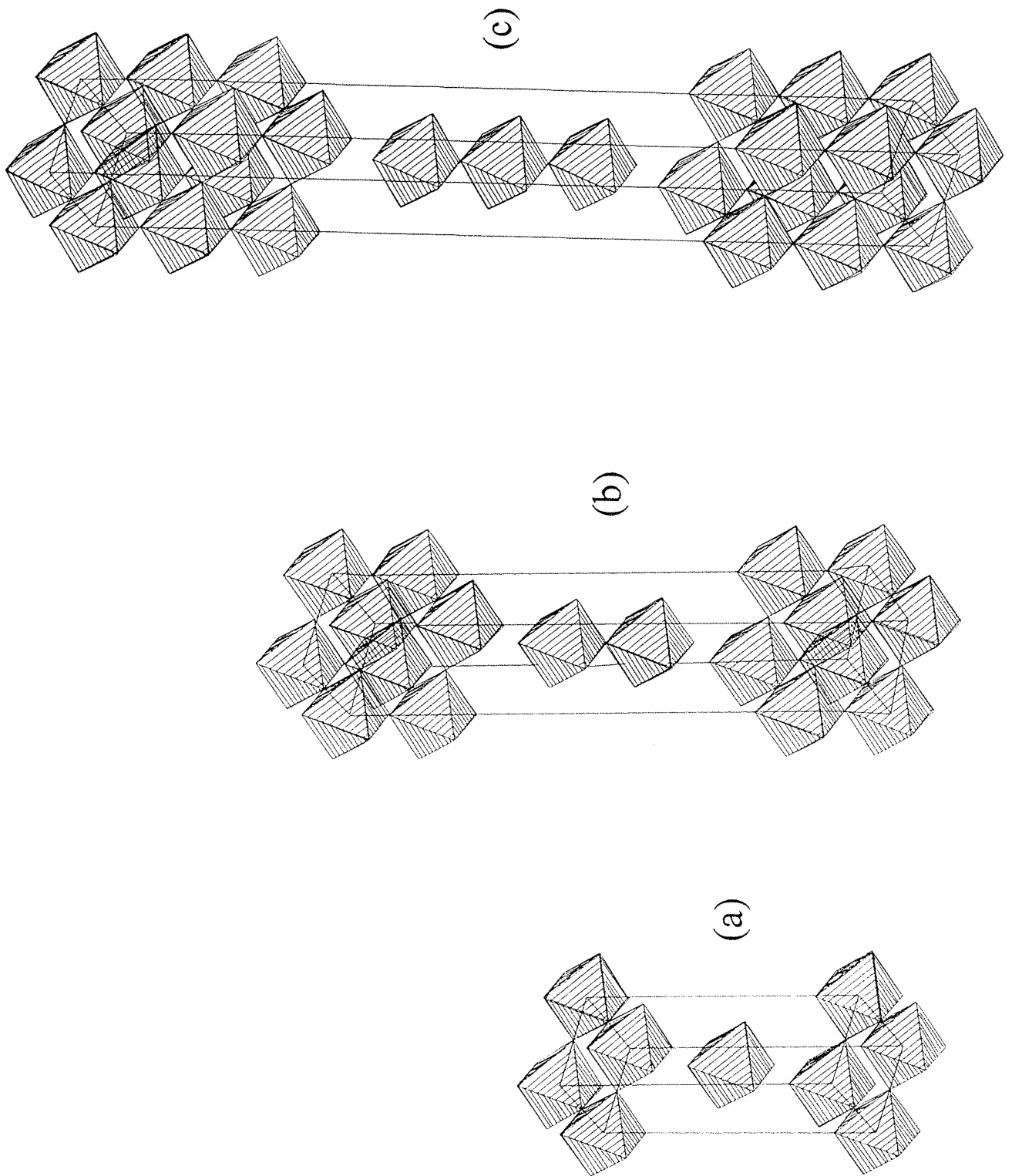
Figure 1.12 Ruddlesden-Popper Phases $A_{n+1}B_nO_{3n+1}$, n = 1, 2 and 3.

Detailed accounts of the theory have been published and a review of the work including many references to earlier publications has been published by Brown (103).

In a similar way to valence bond theory this empirical model attempts to assign valences or strengths to individual bonds. The major difference between the two approaches is that unlike the classical method this model allows non-integral values for the bond valence of a site. Individual bond values are summed in the empirical model around a particular atom to evaluate an atom site valence which is analogous to that performed in classical theory. The new model is designed, not to replace the descriptive techniques, but to be used in addition to it and allow a more complete structural and chemical characterisation of inorganic solids to be achieved.

The terminology for the empirical method is somewhat confusing and is known under a variety of different titles. These various names for the technique have precisely the same meaning and are consequently interchangeable. In this work the theory will be termed "Bond Valence Theory" although other terminologies may be encountered elsewhere.

In Bond Valence Theory, bonds are assigned with individual bond valences which represent the strength of the particular bond. These bond valences (or bond strengths) are related to the actual bond lengths and are derived from them. Notionally the longer a bond length is, the weaker the interaction between the two ions. The actual theory is then constructed by the development of a mathematical expression that can relate the observed bond lengths to the associated bond valences which are summed to give the site valence. The valence of an atom V_j, is defined as a sum of the individual bond valences [6]:-

$$V_j = \sum_i s_{ij} \qquad [6]$$

The individual bond valences s_{ij} are similarly related to the actual bond lengths R_{ij}.

The relationship between the observed bond length and the associated bond strength can be described by a number of mathematical expressions. However, only two of these are regularly used and recently one of these appears to have gained in popularity to the detriment of the other. These expressions are both described using constants which are element specific. The constants are determined by the examination of the bond lengths of

as many well characterised compounds as possible of a particular element in a known oxidation state. These parameters are completely empirical and are not derived from theory. Tables of parameters for a large number of cation to oxygen and cation to fluoride interactions (104) has been collated by Brown.

The expression that has recently proven to be more widely used is derived from Pauling's studies into describing electrostatic bond strength (1947). Rearrangement of Pauling's expression gives the actual equation used [7].

$$S_{ij} \quad = \quad \exp\left[\frac{R_0 \ - \ R_{ij}}{B}\right] \qquad\qquad [7]$$

The other, less commonly used expression is [8]:-

$$S_{ij} \quad = \quad \left(\frac{R_0}{R_{ij}}\right)^N \qquad\qquad [8]$$

R_{ij} is the observed bond length and R_0 is the bond length derived for unit bond valence (i.e. the length of a bond classically described as a single bond). The constants B and N, which are specific to each element, describe the slope of the curve that describes the bond length - bond strength relation.

Once constants required for the expressions have been obtained from accurately characterised compounds of known cation valence, the expressions are complete and can be used predictively in more complex systems i.e. observed bond lengths from complicated materials can be utilised by application of equations [7] and [8] and the resultant valences around a cation site summed to give an effective valence for that site. Brown has performed many such calculations and has ascertained that the calculated effective valence should be within 0.1 of the actual valence which although, within an acceptable degree of reliability, does suggest effective valence calculations cannot be applied definitively.

One limitation of these calculations is they assume the system is in a relaxed state (105). This is not always the case. Systems under compression will demonstrate shortened bond lengths which lead to increased bond valences and effective site valences. This particular effect has been named "overbonding" and can lead to misleadingly high effective site valences. Similarly, a structure which has been expanded and is overstretched can contain sites which are "underbonded" giving deceptively low valences.

The errors in these calculations which were observed by Brown are therefore likely to be a result of the effects of strain.

There are an enormous number of complex structures and coordination geometries reported for the first row transition metal elements. Changes in structure as a result of changing oxygen stoichiometry is sometimes difficult to appreciate without knowledge of local environment of the atoms. Bond valence theory allows the local changes in bond length around an atom to be converted into a site valence. The magnitude of the site valence can then be utilised in understanding structural changes and the validity of a particular structural model to another when undertaking structural refinements.

1.9 The Scope of This Work

The aim of this work is to investigate the solid state chemistry of novel, and previously poorly-characterised, compounds containing late transition metals in high oxidation states. Particular attention is paid to the detailed structural chemistry of these materials including the local geometry and coordination of the highly oxidised ions.

The largest part of this work is involved with the study of iron(IV) materials many of which had been poorly studied and in which compounds with similar structures have vastly contrasting physical properties. Mixed valence systems are also studied in detail to investigate the effect of oxygen stoichiometry on structure and local ion coordination. Doping studies using different transition metal ions are performed to examine the effect on charge disproportionation.

A new strontium cobaltate is studied which has a tripled Ruddlesden-Popper structure and doping experiments are carried out on this system to investigate the effect on both structure and ion coordination.

1.10 References

1   M.A. Subramanian, G. Aravamudan, G.V. Subba Rao. J. Sol. Stat. Chem. **31**, 329-35. (1980).

2   J.M. Schreyer, G.W. Thompson, L.T. Ockerman. Inorg. Syn. **13**, 489-91. (1968)

3   J.G. Bednorz, K.A. Muller. Z. Phys. **B64**, 189. (1986)

4   C.W. Chu, P.H. Hor, R.L. Meng, L. Gao, Z.L. Huang. Science. **235**, 567. (1988)

5   J.M. Tarascon, Y. Le Page, L.H. Greene, B.G. Bagley, P. Barboux, D.M. Huang, G.W. Hull, W.R. McKinnan, M. Giroud. Phys. Rev. B. **38**, 2504, (1989)

6   D.B. Currie, B. Cleaver. High P. High T. **263-9**, (1990)

7   A. Wattiaux, J.C. Park, J.C. Grenier, M. Pouchard. C. R. Acad. Sci. Serr. 2. **310**, 1047-52. (1990)

8   N.N. Greenwood, A. Earnshaw. *Chemistry of the Elements.* Pergamon Press Ltd. 1269. (1986)

9   M. Dekker. Iron in Model and Natural Compounds. **7**, 417. (1978)

10   D.J.C. Yates, J.A. McHenry. Inorg. Chem. **26**, 3193. (1986)

11   F.A. Cotton, G. Wilkinson. *Advanced Inorganic Chemistry*. 5th Edn. John Wiley and Sons Ltd. 711. (1988)

12   R. Hoppe, Z. Rieck. Z. Anorg. Allgem. Chem. **437**, 95. (1977)

13   F.A. Cotton, G. Wilkinson. *Advanced Inorganic Chemistry*. 5th Edn. John Wiley and Sons. 712. (1988)

14   F.A. Cotton, G. Wilkinson. *Advanced Inorganic Chemistry*. 5th Edn. John Wiley and Sons Ltd. 712. (1988)

15   H. Bonnevie, M.D. Svendson. Naturwissenschaften. **45**, 542. (1958)

16   M. Marezio, P.D. Dernier. Mat. Res. Bull. **6**, 23-30. (1971)

17   Y. Takeda, K. Kanno, T. Takada, O. Yamamoto. J. Sol. Stat. Chem. **63**, 237-49. (1986)

18   A.A. Colville, S. Geller. Acta. Cryst. **B27**, 2311-5. (1971)

19   M. Harder, H.K. Muller-Buschbaum. Z. Anorg. Allgem. Chem. **464**, 169-75. (1980)

20   M. Parras, M. Vallet-Regi, J.M. Gonzalez-Calbet, M.A. Alario-Franco, J.C.

Grenier, P. Hagenmuller. Mat. Res. Bull. **22**, 1413. (1987)

21　J. Berggren. Acta. Chem. Scand. **25**, 3616-24. (1971)

22　S. Geller, E.A. Wood. Acta. Cryst. **9**, 563. (1956)

23　J.L. Soubeyroux, P. Courbin, L. Fournes, D. Fruchart, G. Le Flem. J. Sol. Stat. Chem. **31**, 313-20. (1980)

24　National Bureau Standards. Monogr. **25**, 60. (1971)

25　R. Routil, R. Barham. Can. J. Ceram. **52**, 3235. (1974)

26　C. Brisi, L. Montorsi. Ann. Chim. **62**, 641. (1972)

27　W. Levason, S.K. Harbron, S.T. Higgins. J. Am. Shem. Soc. **108**, 526. (1986).

28　J.B. MacChesney, R.C. Sherwood, J.F. Potter. J. Chem. Phys. **43**, 1908-13 (1965)

29　A. Wattiaux, L. Fournes, A. Demourges, N. Bernaben, J.C. Grenier, M. Pouchard. Sol. Stat. Comm. **77**, 489-93. (1991)

30　M. Breza. Acta. Cryst. **B46**, 573-5. (1990)

31　T. Takeda, Y. Yamagughi, H. Watanabe. J. Phys. Soc. Jap. **33**, 967-9. (1972)

32　H. Oda, Y. Yamagughi, H. Takei, H. Watanabe. J. Sol. Stat. Chem. **42**, 101. (1977)

33　Y. Takeda, S. Naka, M. Takano, T. Shinjo, T. Takada, M. Shimada. Bull. Inst. Chem. Soc. Jap. **13**, 61. (1978)

34　P.D. Battle, T.C. Gibb, S. Nixon. J. Sol. Stat. Chem. **79**, 75-85. (1989)

35　P.D. Battle, T.C. Gibb, P. Lightfoot. J. Sol. Stat. Chem. **84**, 271-9. (1990)

36　B. Helferich, K. Lang. Z. Anorg. Allgem. Chem. **263**, 913-5. (1950)

37　K. Wahl, W. Klemm, G. Wehrmeyer. Z. Anorg. Allgem. Chem. **285**, 322-7. (1956)

38　G. Vilchez, W.P. Griffith. J. Chem. Soc. Dalt. Trans. 1416-21. (1972)

39　R. Hoppe, K. Mader. Z. Anorg. Allgem. Chem. **586**, 115-24. (1990)

40　T.B. Temple, G.W. Thickett. Aust. J. Chem. **26**, 1137-41. (1973)

41　R. Scholder, W. Zeiss, F. Knidervater, W. Klemm. Z. Anorg. Allgem. Chem. **283**, 338-45. (1956)

42　L.T. Ockerman, J.M. Schreyer. J. Am. Chem. Soc. **73**, 547-8. (1951)

43　M.L. Hoppe. E.O. Schlemper, R.K. Murmann. Acta. Cryst. **B38**, 2237-9. (1982)

44   K. Ogura, K. Takamagari. J. Chem. Soc. Dalt. Trans. 1519. (1986)

45   D. Coucouvanis, A. Salifoglou, M.G. Kanatzidis. Inorg. Chem. **25**, 2460. (1986)

46   S.E. Dann, D.B. Currie, M.T. Weller. J. Sol. Stat. Chem. **97**, 179. (1992)

47   B.C. Tofield, C. Greaves, B.E.F. Fender. Mat. Res. Bull. **10**, 737-46. (1975)

48   K. Vidyasagar. Inorg. Chem. **23**, 1206-8. (1984)

49   S. Mori. J. Phys. Soc. Jap. **28**, 44-9. (1970)

50   R. Scholder, H. Bunsen, W. Zeiss. Z. Anorg. Allgem. Chem. **283**, 330-7. (1956)

51   P. Jaitnet, W. Huber, A. Gieren, H. Betz. J. Organomet. Chem. **311**, 379. (1986)

52   H.B. Silver, M.A. Murguia. Inorg. Chem. **24**, 3794. (1985)

53   F.A. Cotton, G. Wilkinson. *Advanced Inorganic Chemistry.* 5th Edn. John Wiley and Sons Ltd. 725. (1988)

54   H. Lehmann, H.K. Muller-Buschbaum. Z. Anorg. Allgem. Chem. **470**, 59-63. (1980)

55   F.A. Cotton, G. Wilkinson. *Advanced Inorganic Chemistry.* 5th Edn. John Wiley and Sons Ltd. 727. (1988)

56   F.A. Cotton, G. Wilkinson. *Advanced Inorganic Chemistry.* 5th Edn. John Wiley and Sons Ltd. 732. (1988)

57   J.C Grenier, S. Ghodbane, G. Demazeau, M. Pouchard, P, Hagenmuller. Mat Res. Bull. **14**, 831. (1979)

58   T. Takeda, Y. Yamaguchi, H. Watanabe. J. Phys. Soc. Jap. **33**, 967-9. (1972)

59   A.N. Petrov, V.A. Cherepanov, O.F. Kononchuk, L. Ya Gavrilova, J. Sol Stat. Chem. **87**, 69-76. (1990)

60   E.K. Bryne, K.H. Theopald. J. Am. Chem. Soc. **109**, 1282. (1987)

61   M. Jansen, R. Hoppe. Z. Anorg. Allgem. Chem. **409**, 152-62. (1974)

62   M. Jansen, R. Hoppe. Z. Anorg. Allgem. Chem. **398**, 54-62. (1973)

63   I. S. Shoplygin, V.B. Lazarov. J. Russ. Inorg. Chem. **30**, 3214-6. (1985)

64   C. Brendal, W. Klemm U. Hofmann. Z. Anorg. Allgem. Chem. **320**, 59-63. (1963)

65   C.E. Summer, G.R. Steinmetz. J. Am. Chem. Soc. **107**, 6124. (1985)

66   Y. Takeda, R. Kanno, T. Takada, O. Yamamoto. Z. Anorg. Allgem. Chem. **540**, 259. (1986)

67   N. Yamazoe, S. Furukawa, Y. Teraoka, T. Seiyama. Chem. Lett. 2019-22. (1982)

68   H. Takei, H. Oda, H. Watanabe, I. Ahindo. J. Mat. Sci. **13**, 519-22. (1978)

69   T. Takeda, Y. Yamaguchi, H. Watanabe. J. Phys. Soc. Jap. **33**, 970. (1972)

70   P.W. Jolly, G. Wilke. *The Organic Chemistry of Nickel.* Vol **II**. Academic Press Inc. (1975).

71   F.A. Cotton, G. Wilkinson. *Advanced Inorganic Chemistry.* 5th Edn. John Wiley and Sons Ltd. 752. (1988)

72   O. Glemser. J. Einerhand. Z. Anorg. Allgem. Chem. **261**, 48. (1950)

73   G. Van-Koten. J. Am. Chem. Soc. **105**, 1379. (1983)

74   L. Dyer, B. Borie, P. Smith. J. Am. Chem. Soc. **76**, 1499-503. (1954)

75   Y. Takeda, T. Hashino, H. Miyamoto, F. Kanamaru, S. Kume, M. Koizumi. J. Inorg. Nucl. Chem. **34**, 1599-601. (1972)

76   H. Zentgraf, R. Hoppe. Z. Anorg. Allgem. Chem. **462**, 61-70. (1980)

77   W. Levason, S. Higgins, M.C. Feiters, A.T. Steel. J. Chem. Soc. Dalton. Trans. 317, (1986)

78   W.W. Wilson, K.O. Christie. Inorg. Chem. **23**, 326. (1984)

79   Y. Takeda, F. Kanamura, M. Shimada, M. Koizumi. Acta. Cryst. **B32**, 2464-6 (1976)

80   F.A. Cotton, G. Wilkinson. Adv. Inorg. Chem. **V**, 752. (1988)

81   K. Asai. H. Seikizawa. J. de. Phys. **40**, 18-20. (1979)

82   Y. Miyamoto, T. Yamamoto. M. Koizumi. M. Shimada. Phys. Stat. Sol. A. **95**, K187-91. (1986)

83   J. Rodriguez, J.M. Gonzalez-Calbet. Mat. Res. Bull. **21**, 429. (1986)

84   I. Felner, B. Brosh. Phys. Rev. B. **43**, 365-7. (1991)

85   R.C. Weast. *Handbook of Chemistry and Physics.* 56th Edn. Chemical Rubber Company Ltd. (1975)

86   W. Syvinski, D. Schulz, G. McCarthy. JCPDS Grant In Aid Report (1988)

87   S. Naka, F. Nakakita. Y. Suwa. M. Inogaki. Bull. Chem. Soc. Jap. **47**, 1168. (1974)

88   F.S. Galasso.   The Structure, Properties and Preparation of Perovskite-Type Compounds.   International Series of Monographs in Solid State Physics.   **5**, (1969)

89   National. Bureau. Standards. Monogr. **25**. (1971)

90   V.M. Goldschmidt.   Str. Ner. Vidensk-Akad. Oslo. **1**, 1. (1926)

91   D.B. Currie, M.T. Weller. Acta. Cryst. **C47**, 696-8. (1991)

92   J. Roy. J. Am. Chem. Soc. **38**, 108. (1955)

93   A. Magneli, B. Blomberg. Acta. Chem. Scand. **5**, 372-8. (1951)

94   V.N. Panyusshkin, G. Pasquali, I.G. Drickamer. J. Chem. Phys. **51**, 3305-8. (1969)

95   K. Poeppelmeir. J. Sol. Stat. Chem. **44**, 89. (1982)

96   H.L. Yakel. Acta. Cryst. **8**, 394. (1955)

97   H.S. Horowitz, J.M. Longo, J.T. Lewandowski. Mat. Res. Bull. **16**, 489. (1981)

98   J.B. MacChesney, R.C. Sherwood, J.F. Potter. J. Chem. Phys. **43**, 1907-13. (1965)

99   D. Baltz, K. Pleith. Z. Electrochem. **59**, 545. (1955)

100   P. Poix. J. Sol. Stat. Chem. **31**, 95. (1980)

101   S.N. Ruddlesden, P. Popper. Acta. Cryst. **10**, 538. (1957)

102   S.N. Ruddlesden, P. Popper. Acta. Cryst. **11**, 54. (1958)

103   I.D. Brown. Chem. Soc. Revs. **7**, 359. (1975)

104   I.D. Brown, D. Aldermatt. Acta. Cryst. **B32**, 1957. (1976)

105   I.D. Brown. J. Sol. Stat. Chem. **82**, 122, (1989)

CHAPTER 2

Experimental Techniques

2.1 PREPARATION

2.1.1 Preparation of Materials in the Solid State

A wide range of preparative methods are available for the synthesis of high oxidation state transition metal oxides. The two main methods are reaction in solution with a strong oxidising agent such as chlorine (1) and high temperature sintering followed by oxygen annealing (2). Novel methods of synthesis such as recently developed electrochemical methods (3) are less common. During the course of this work only direct solid state reaction followed by oxygen annealing was employed.

The solid state reaction technique simply involves the combination of the powdered reactants, usually being the relevant component metal oxides. A carbonate or some other oxo-salt which decomposes to the oxide on heating is commonly used if the oxide is hygroscopic. The homogeneity of the sample and the particle size within that sample are major factors in the time scale of the experiment and the final purity of the product. Experiments in the solid state tend to be long since diffusion in and between solid particles is slow. Reaction times are also increased by large particle sizes which reduce interfacial contact.

Combination of the reactants is usually achieved by one of two methods. The simplest method requires homogeneous grinding of the powdered reactants in a pestle and mortar and sintering them at high temperature. Generally this method does not affect mixing on an atomic scale and results in long sintering times and large particle sizes. Reaction times can be reduced by maximising the sintering temperature to increase atom mobility, however care must be taken to avoid incongruent melting. Particle size can be reduced by frequent regrinding and interfacial contact increased by pressing the samples into pellets. The other commonly used method involves the coprecipitation of samples from solution using a precipitant. The problems of mixing on an atomic scale, and thus the need for high sintering temperatures, are largely overcome in this method, however, the precipitant must be carefully chosen so that one component is not preferentially precipitated from solution.

This work uses the former method of solid state preparation and individual reaction conditions using ambient conditions are described where appropriate. Samples requiring

strong oxidising conditions were oxygen annealed using the high pressure annealing apparatus (4) shown in Fig 2.1
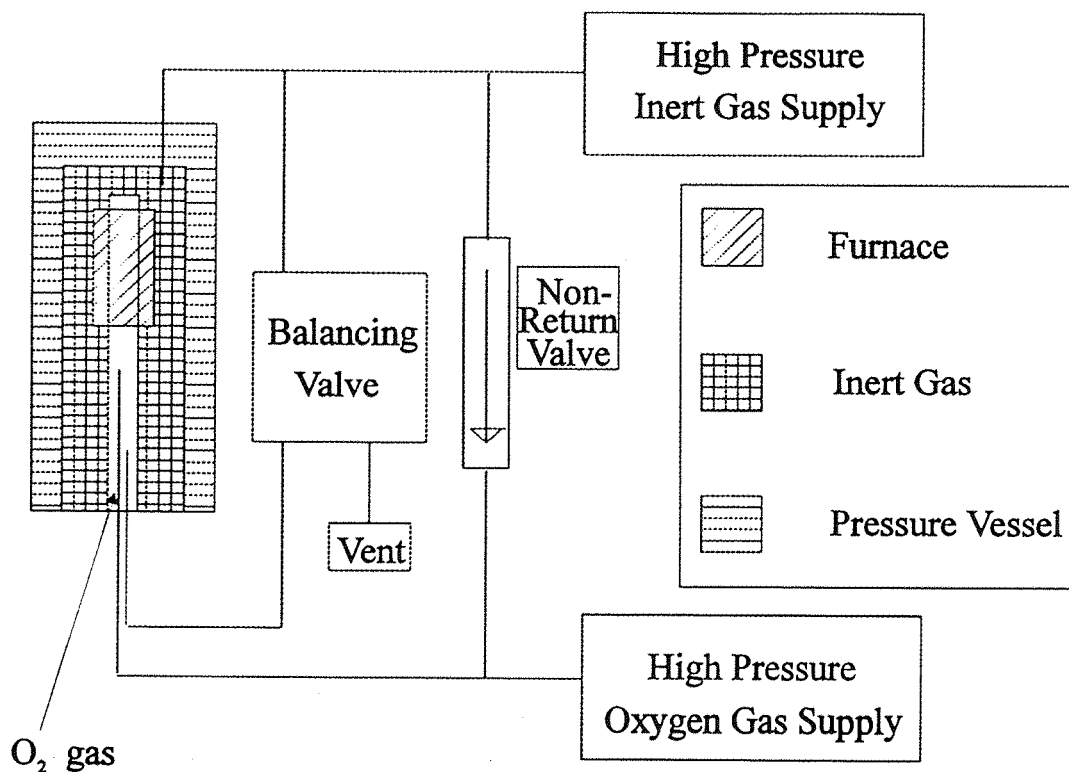
Figure 2.1 Diagram of the High Pressure Annealing Apparatus

The reaction mixture is kept within an alumina, or gold, crucible encased in a reaction tube containing hot pressurised oxygen. Fracture of the tube is prevented by containment in inert gas at an equivalent pressure. The reaction tube is mounted vertically with a small furnace around its upper end so that while the sample is at furnace temperature, the seal is kept at room temperature. Initially the whole system is filled with inert gas from a compressed gas supply. Oxygen is then fed into the sample chamber and a balancing valve is used to equilibrate between the oxygen and inert gas pressure. This valve ensures that the walls of the crucible never experience a differential pressure of more than a few atmospheres. Maximum operating temperature and pressure are 1200°C and 700 Atm of oxygen respectively and individual experimental conditions are described where appropriate.

2.2 ANALYTICAL TECHNIQUES

2.2.1 Powder X-ray Diffraction (PXD)

X-ray diffraction is one of the principal techniques available to the solid state chemist. PXD can be employed in a variety of applications including crystal structure determination, measurement of particle size, detection of crystal defects and disorder and determination of phase transitions. The main application of PXD in this work was phase identification of samples in powder form and determination of cell parameters. There are also some examples of x-ray data being used for preliminary Rietveld (5) analysis

2.2.1.1 Theory of X-ray Diffraction

A crystal may be divided into layers by sets of planes passing through lattice points. Each of the planes are described by h,k,l (the Miller Indices) which describe a full set of planes running through a crystal structure separated by a perpendicular distance called the d spacing described by d_{hkl}. The d-spacing, d_{hkl}, can be related to both the diffraction angle and wavelength in a diffraction experiment using Braggs law. In the simplest analogy, a crystal should display diffraction data from each lattice plane which gives rise to an observed 2θ value on the diffraction pattern.

However, since reflection conditions and systematic absences resulting from the symmetry of the system can cause interference effects, intensity is not always observed for all planes. In addition to absences arising from a non-primitive lattice type, a number of space symmetry elements can lead to systematic absences. These include glide planes and screw axes which apply to two dimensional and one dimensional sets of reflections respectively. These absences can be useful when attempting to designate a space group for a new material.

2.2.1.2 The Diffraction Experiment

Powder x-ray diffraction (PXD) has been used generally throughout the course of this work to assess sample purity. PXD data have been used to calculate refined unit cell

parameters for systems which were shown to be single phase. The powder x-ray diffraction data were collected on a Siemens θ-2θ D5000 diffractometer.

An x-ray tube fitted with primary monochromator provides copper $K_{\alpha 1}$ radiation which is collimated through an aperture diaphragm onto the sample. The sample is mounted in a recessed flat aluminium or plastic holder. This sample can them be rotated at velocities up to 120rpm to overcome the effect of preferred orientation. The diffracted radiation then passes through another diaphragm before noise is absorbed by a 1.2mm nickel filter. The x-rays are then detected by a standard scintillation counter. The sample rotates with a constant angular velocity such that the angle of incidence of the primary beam changes, whilst the detector rotates at double the angular velocity around the sample. This results in the diffraction angle being twice the glancing angle. Collection times for diffraction patterns gathered to ascertain sample purity were in the order of 20-40mins. Accurate lattice parameters were then determined by employing longer collection times. Diffraction patterns for Rietveld analysis were collected typically over a period of 15hrs. The data are transferred continuously to a microvax computer where a real time display of the data can be viewed. Once data collection has been completed, the diffraction data can be managed using the SIEMENS DIFFRAC 500 version 2.0 software package. This software package also allows access to the JCPDS Powder Diffraction Files enabling any diffraction pattern to be very easily checked for possible impurity phases. Periodically the diffractometer is recalibrated. A diagram of the diffractometer is shown in Fig 2.2.

Lattice parameters are calculated using the CELL program on the IBM 3090 mainframe computer at Southampton. This program minimises the expression

$$M = \sum_i \omega_i \, (\sin^2\theta_i^{obs} - \sin^2\theta_i^{calc})^2 \qquad [1]$$

using an iterative least squares, procedure where ω_i is a weighting factor proportional to $\tan\theta$

The diffractometer can operate in two different scanning modes. The general operating mode is a continuous scan which moves between points without pausing. A

39

second mode involves a stepped scan in which the scan is discontinued between points so
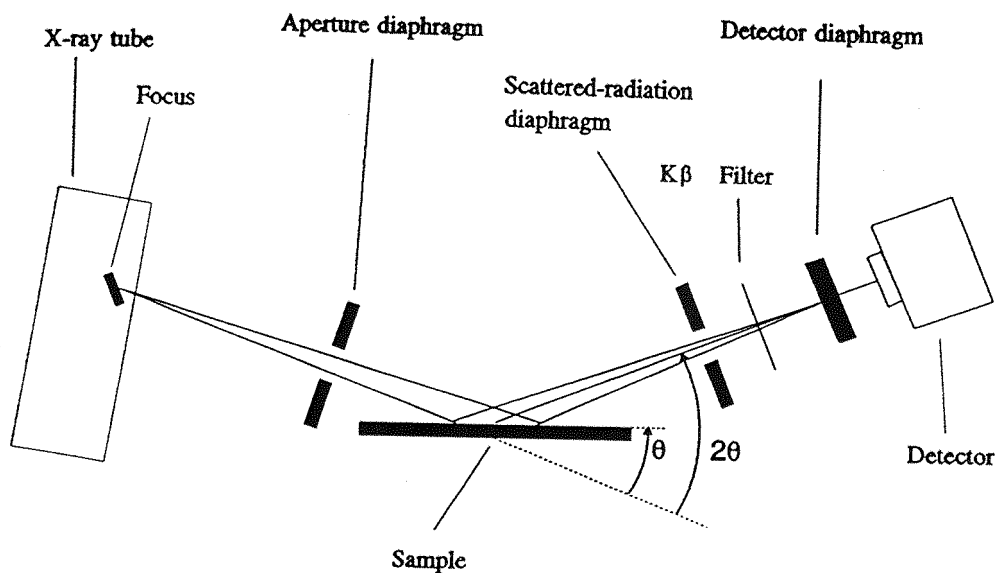
Figure 2.2 Schematic Diagram of the D5000 Diffractometer

that a broken line is produced and is preferred when dealing with very small cell distortions allowing deconvolution of closely spaced reflections which would be poorly resolved by the continuous scan method. The apertures are carefully chosen to obtain the right balance between removal of noise, associated with x-ray fluorescence and intensity.

2.2.2 Powder Neutron Diffraction (PND)

2.2.2.1 Introduction

Powder neutron diffraction (PND) is a very powerful technique for the study of complex oxide materials. PND can allow the accurate determination of light atoms in the presence of heavy ones and, since it is not affected by a form factor, has significant advantages over the analogous x-ray method.

The applicability of neutrons to the diffraction technique is a result of a number of properties, including a wavelength comparable to atomic separation and an intrinsic magnetic moment. The intrinsic spin of the neutron can interact with an ordered spin

arrangement and give rise to magnetic scattering, in addition to scattered intensity from the nuclear unit cell. This allows neutron diffraction to probe local magnetic order in matter, but since the effect is based on the interaction between the intrinsic moment of the neutron with the spin oriented electrons, it is affected, in a similar way to x-rays, by a form factor.

2.2.2.2 Instrumentation

During the course of this work a number of different instruments have been used to collect PND data. The fixed wavelength diffractometer D1A at the Institut Laue Langevin(ILL), Grenoble and three "time of flight" diffractometers at the spallation neutron source ISIS at the Rutherford Appleton Laboratory. The latter were the high resolution powder diffractometer, HRPD, the medium resolution instrument POLARIS and the Liquid and Amorphous diffractometer, LAD, which was used for some of the magnetic experiments.

D1A (Fig 2.3) is a high resolution instrument ($\Delta d/d = 2 \times 10^{-3}$ at $2\theta = 120°$) which was designed to enable structure refinement of compounds with unit cell volumes up to 1000Å^3. It has several special features including a large monochromator take off angle to provide good resolution at high angles, rapid selection of a wide choice of wavelength ($\lambda = 5.7 - 1.2$Å) and a 60° bank of ^{3}He counters which may be swept through $0 \leq 2\theta \leq 160°$ in steps of 0.05°. Counting statistics are improved by summing scans and typical scan times are 6-8hrs. Samples are mounted in cylindrical vanadium cans (from which no appreciable scattering takes place) and the wavelength chosen for the experiments was 1.909Å.

The three instruments at the Rutherford Appleton Laboratory use proton spallation on a uranium target to generate pulses of white neutrons which are detected after scattering from a sample over a small fixed 2θ range by time of flight techniques. θ is held constant and wavelength determined by measuring the time taken for the neutrons to travel the known distance to the detectors. The wavelength is then obtained using the De Broglie relation ($\lambda = h/mv$). Samples were mounted in cylindrical vanadium cans which could be sealed with indium wire to prevent sample decomposition if the samples were air sensitive.

HRPD (fig 2.4) was designed to handle cell volumes up to 2500Å^3 with 400 structural parameters. Resolution is quoted as $\Delta d/d = 4 \times 10^{-4}$ and the neutron pulses

have a wavelength of typically 0.5-0.8Å allowing collection to $d_{min} = 0.25$Å in backscattering. Data are mostly collected at high 2θ as the resolution has been shown to be of the form

$$R = \left[(\frac{\Delta t}{t}) + (\frac{\Delta l}{l}) + COT^2\theta\Delta\theta \right]^{\frac{1}{2}}$$

[2]

where t is the time of flight to the detector, 2θ is the scattering angle and $\Delta\theta$ the uncertainty in the measured angle θ and l and Δl are the path length and the uncertainty in the path length respectively.

Therefore, long path lengths and corresponding long times of flight give the best resolution; the path length in HRPD is 95m. The high d-spacing range provided by HRPD makes this a superb instrument for the determination of oxygen distribution and occupancy factors due to the great amount of high angle data. The best range of data for a reactor based instrument is approximately $d_{min} = \lambda/2 = 0.6$Å.

POLARIS (Fig 2.5) is a medium resolution instrument which has time focused ^{3}He detectors placed at $\pm$ 150 and at low angle. Originally, this instrument was designed to investigate polarised neutron spectroscopy, but, with the polarising filters removed can be used as a powder diffractometer for relatively simple structures. Both backscattering and low angle bank detectors were used in studies on magnetic behaviour used in conjunction with a cryostat ranging in temperature from room temperature to 4.2K.

LAD (Fig 2.6) is a total scattering instrument which has been optimised for the study of liquid and amorphous materials. It can also be used as a moderate resolution powder diffractometer. In contrast to POLARIS there are two different sorts of detectors on LAD. There are ^{3}He detectors at 5°, 10°, and 150° and scintillator banks at 20°, 35°, 58° and 90°. In the following experiments LAD was used as a powder diffractometer with medium flux to study magnetic ordering behaviour.

The vanadium sample containers used in all these experiments are run as a blank on each instrument and subtracted from each experimental diffraction pattern. Background samples are also run in conjunction with the cryostat for low temperature experiments and subtracted before analysis.
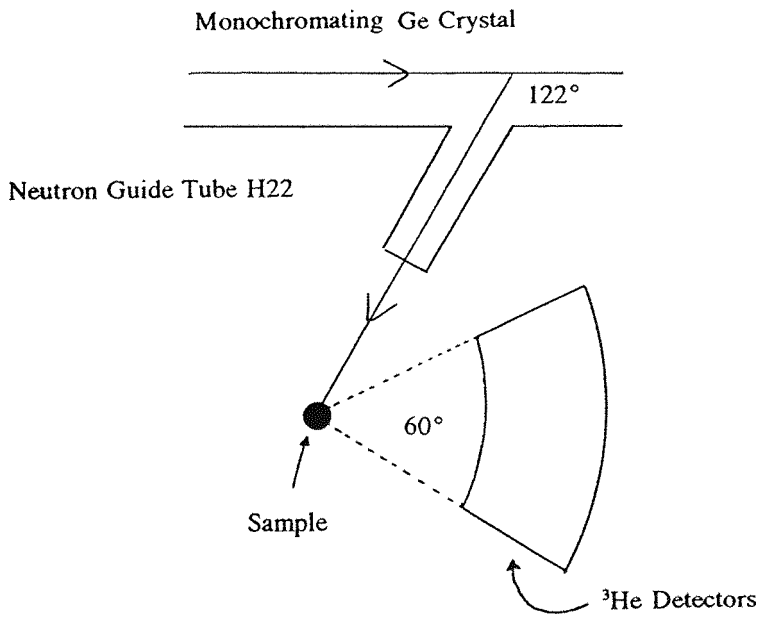
Figure 2.3 Schematic Diagram of the D1A Spectrometer, ILL
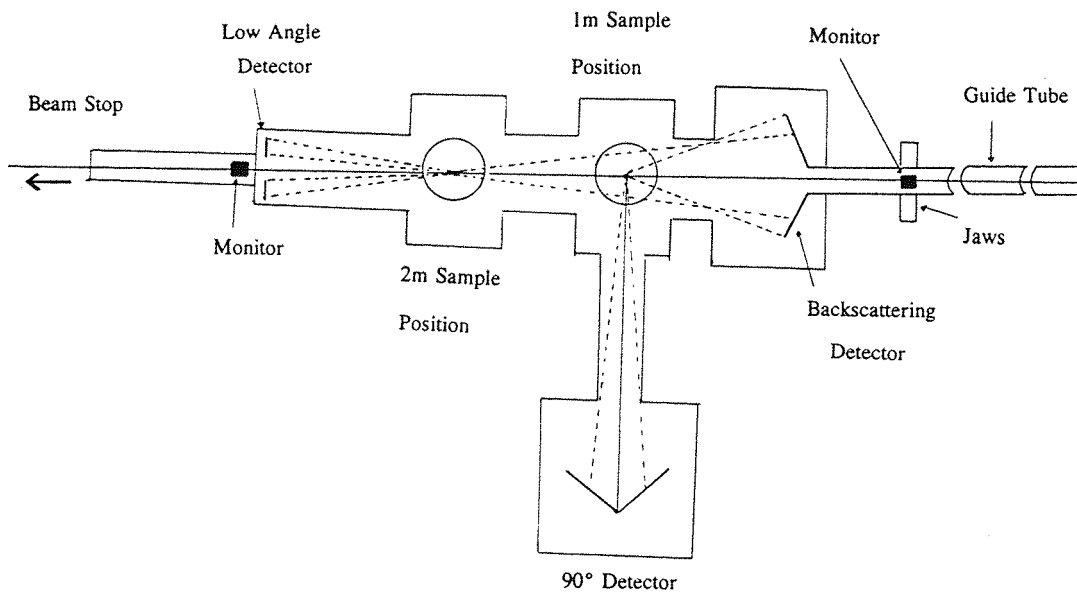
Figure 2.4 Schematic Diagram of the HRPD Spectrometer, RAL

43
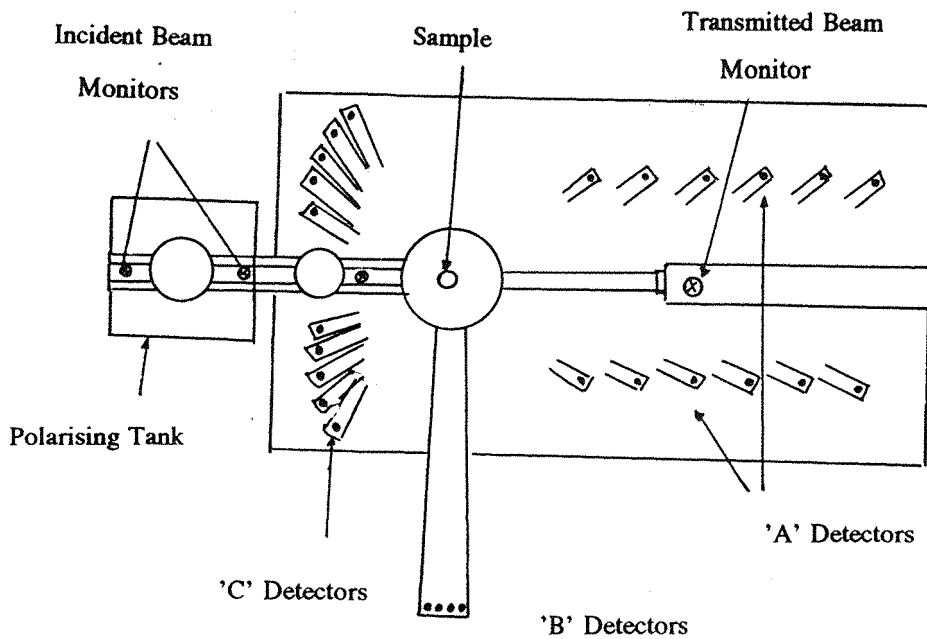
Figure 2.5 Schematic Diagram of the POLARIS Diffractometer, RAL
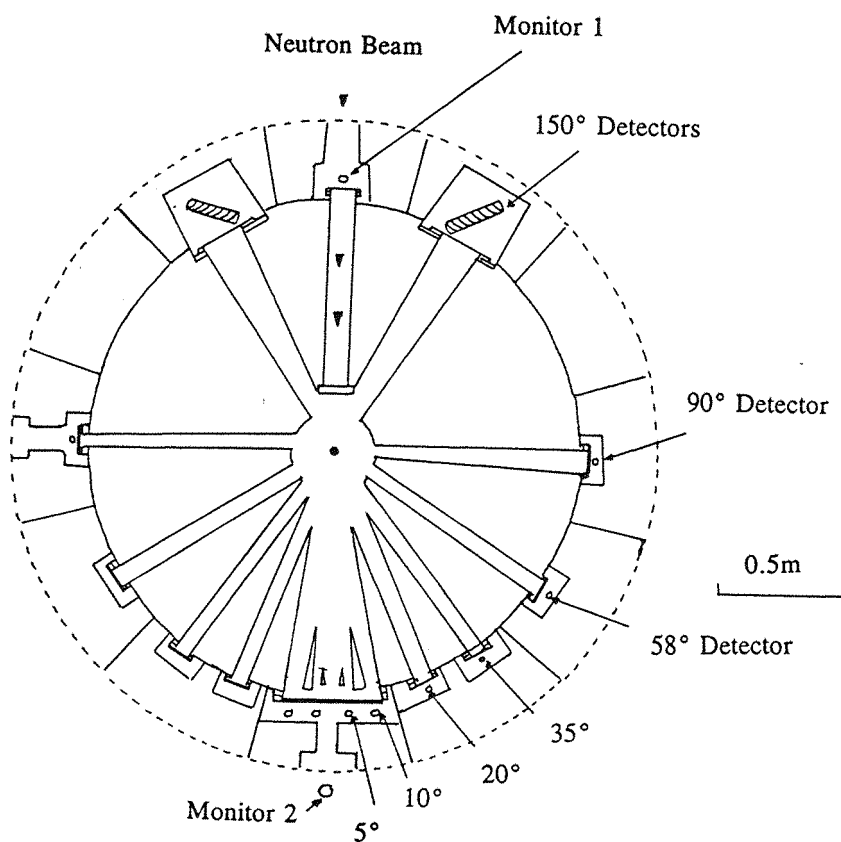
Figure 2.6 Diagram of the LAD Diffractometer, RAL

2.2.3 Data Handling - The Rietveld Method

The single crystal method of structure determination is not always applicable to solid state chemistry. The very nature of the high temperature experiment and frequent regrinding leads to a very small crystal size. Single crystal x-ray experiments typically require $0.2mm^3$ crystals and larger crystals of typically $1cm^3$ are required for neutron experiments which have significantly lower flux.

H. M. Rietveld (5) has devised a technique which allows structure determination using a method of profile refinement.

The Rietveld technique is based upon the comparison of a calculated profile and the observed profile from the diffraction experiment. The calculated profile is postulated from a trial structure using the relevant structural and instrumental parameters. Once a calculated profile has been obtained an iterative least squares procedure can be utilised to minimise the difference between the calculated and observed data by subtle modification of the parameters used to generate the profile. The final refined and structural and instrument parameters can be collected when the minimisation procedure has been completed.

Several different versions of the Rietveld method have been used to refine x-ray, single wavelength neutron and time of flight neutron diffraction data

2.2.3.1 Theoretical Considerations

It may be shown that for any regular array of stationary atoms, the structure factor F, is the sum of the contributions of the scattering amplitudes, b, and the phases, ϕ, of each atom [4], leading to the following expression.

$$F = \sum_{j=1}^{N} b_j \exp [\, i\, \phi_j\,] \qquad\qquad [3]$$

45

In a unit cell, the total phase shift of an atom, at a point (x_j, y_j, z_j) from the origin is the sum of the phase shifts in each direction when the phase shift is evaluated; the structure factor for the unit cell becomes

$$F_{hkl} = \sum_{j=1}^{N} b_j \exp [2\pi i (hx_j + ky_j + lz_j)] \qquad [4]$$

where h, k and l are the Miller Indices that define the plane from which the reflection takes place. For very small crystals, it may be shown that the intensity of the scattered beam is proportional to the square of the structure factor

$$I_{hkl} = k \, l^2 \, [F_{hkl}]^2 \qquad [5]$$

where k is a scaling constant and L the lorentz factor, a geometric function of the method of data collection and as a result of the particular instrument used. In real crystals, the scattered intensity is modified by imperfections in the lattice structure. Defects and substitutional disorder cause local structural irregularities, particularly in non-stoichiometric materials. In addition, thermal motion causes a reduction in scattered intensity as a result of time independent vibrations of the atoms about their mean positions ;the atoms in a plane are displaced randomly from their ideal in plane positions, disrupting the in-phase behaviour of their combined scattering. The correction to a structure factor reflected by a plane hkl is of the form [4]

$$T_{hkl} = \exp [- B_{hkl} \frac{\sin^2\theta}{\lambda^2}] \qquad [6]$$

so that for a unit cell, the structure factor becomes:-

$$F_{hkl} = \sum_{j=1}^{N} b_j \, n_j \exp [- B_j \frac{\sin^2\theta}{\lambda^2}] \exp [2\pi i (hx_j + ky_j + z_j)] \qquad [7]$$

46

where n_j is the occupation factor of the jth atom, equal to one in the structure free defects. However, this assumes that the thermal displacements are isotropic, a situation that is only rarely encountered on highly symmetric special sites of cubic space groups. A more general analysis [4,5] describes the anisotropy of the thermal motion in the form of an ellipsoid replacing [6] with

$$T_{hkl} = \exp[-\tfrac{1}{4}(B_{11} h^2 a^{*2} + B_{22} k^2 b^{*2} + B_{33} l^2 c^{*2}$$
$$2 B_{12} h k a^* b^* + 2 B_{23} k l b^* c^* + 2 B_{13} h l a^* c^*)]$$

[8]

A number of expressions can be used to simulate the thermal motion, but the form given above has been used throughout this work.

2.2.3.2 X-ray Diffraction Data

Rietveld analysis of x-ray diffraction data preceding June 1992 was achieved using the version of the Rietveld refinement program (MPROF) running on the CONVEX at Daresbury. This program is further described in section 2.2.3.3.

After June 1992 this was replaced by the DBWS - 9006PC (6) Rietveld program running locally on personal computers. This program is designed for single wavelength data using a variety of peak shape functions and a refinable background

The observed intensity y_i^{obs}, at each point $2\theta_i$, on the profile are compared to the calculated intensity y_i^{calc} and the parameter that defines the latter are refined by an iterative least squares procedure to subtly adjust y_i^{calc} such that M in the following expression is minimised.

$$M = \sum_{i=1}^{N} \omega_i (y_i^{obs} - c\, y_i^{calc})^2$$

[9]

where ω_i is a weighting factor denoted by $1/y_i$ and c is a scale factor. The calculated

47

intensity y_i^{calc} are determined by summing the contributions from neighbouring Bragg reflections (k) plus the background b_i

$$y_i^{calc} = \sum_k L_k |F_k|^2 \phi (2\theta_i - 2\theta_k) P_k + y_{bi}$$ [10]

where L_k contains Lorentz polarisation and multiplicity factors, F_k is the structure factor and P_k the preferred orientation factor as defined by

$$P_k = (G_2 + (1 - G_2) \exp(G_1\alpha_k^2))$$ [11]

where G_1 and G_2 are refinable parameters, α_k is the angle between the presumed cylindrical symmetry axis and the preferred orientation axis direction.
The background is refined from the expression

$$y_{bi} = \sum_{m=0}^{s} B_m \left[\left(\frac{2\theta_i}{BKPOS} \right)^{-1} \right]^m$$ [12]

where BKPOS is the background position specified in the input file.

Since a comparison of intensities is performed at every point, it is essential for construction of the calculated profile to accurately describe the shape of the Bragg reflections. Peak shape is generally dictated by the instrument; for the Siemens D5000 the peak shape is pseudo voigt and thus described by the equation

$$\eta L + (1 - \eta) G$$ [13]

where L and G are the Lorentzian and Gaussian contributions to the peak shape and η is the mixing parameter. The mixing parameter is defined by the equation

48

$$\eta \;=\; N_A \;+\; N_B \,(\, 2\,\theta\,) \qquad\qquad\qquad [14]$$

where the parameters N_A and N_B are refinable parameters allowing the background to be refined as a function of 2θ.

The contribution of a pseudo voigt peak of integrated intensity I_k to the observed profile y_i is given by

$$y_i \;=\; I_k \exp\left[\,-b_k(\, \eta\, L \;+\; (\,1 - \eta\,)\, G\, \right] \qquad\qquad [15]$$

where

$$b_k \;=\; \frac{4\,\ln 2}{H_k^2} \qquad\qquad\qquad\qquad [16]$$

and

$$I_k \;=\; t\, F_k^2\, j_k\, L_k \left(\frac{4\,\ln 2}{H_k^2\,\pi} \right)^{\!\!1/2} \qquad\qquad [17]$$

where F_k is the structure factor, t is the counter step width, j_k is the multiplicity of the reflection and L_k is the Lorentz factor.

The Gaussian and Lorentzian contributions to the peak shape, G and L respectively, are described by the equations

$$L \;=\; \frac{\sqrt{2}}{\pi\, H_k} \; \frac{1\,/\,[\,3\,(\,2\theta_i \;-\; 2\,\theta_k\,)^2\,]}{H_k^2} \qquad\qquad [18]$$

$2\theta_k$ is the calculated position for the Bragg peak corrected for the counter zeropoint and

$$G = \frac{(4 \ln 2)^{\frac{1}{2}}}{H_k \sqrt{\pi}} \exp\left(\frac{-4 \ln 2}{H_k^2} (2\theta_i - 2\theta_k)^2\right) \qquad [19]$$

H_k is the full width at half maximum (FWHM) of the peak.

The FWHM has been shown to be a function of the scattering angle $2\theta_k$ [10] and is described by

$$H_k = U \tan^2\theta_k + V \tan\theta_k + W \qquad [20]$$

U,V,W are dependant on the instrument being used but may also account for peak broadening effects resulting from particle size. As a result of the finite sizes of the beam and sample, at low $2\theta_k$ the peak shape shows marked asymmetry with the peak maximum shifting to slightly lower angle while the integrated intensity remains unaffected. The asymmetry is corrected by multiplication of the equation [17]) by

$$\frac{1 - S P (2\theta_i - 2\theta_k)^2}{\tan\theta_k} \qquad [21]$$

where P is the defined asymmetry parameter and S = 1, 0 or -1 when $2\theta_i - 2\theta_k$ is negative, zero or positive.

The refinable parameters for any least squares refinement are of two kinds. Firstly there are the structural parameters which describe the contents of the unit cell and include the overall isotropic temperature factor, positions, occupancies and temperature factors of each atom in the asymmetric unit. Secondly, there are the profile parameters which define the position, shape and FWHM of each peak. These are scale factor, cell parameters, U,V,W, zeropoint, asymmetry and preferred orientation correction. The agreement is measured in terms of reliability factors $R_{weighted\ profile}$, $R_{intensity}$ and $R_{expected}$. The last is calculated from the statistics of the refinement. The R-factors are given by :

50

$$R_{weighted\ profile} = 100 \left[\frac{\sum_i \omega_i [\ y_i^{obs} - y_i^{calc}\ ]^2}{\sum_i \omega_i [\ y_i^{obs}\ ]^2} \right]^{1/2}$$

[22]

$$R_{intensity} = 100 \left[\frac{\sum_k |\ I_k^{obs} - I_k^{calc}\ |}{\sum_k I_k^{obs}} \right]$$

[23]

$$R_{expected} = 100 \left[\frac{(N - P + C)}{\sum_i \omega_i [\ y_i^{obs}]^2} \right]$$

[24]

$$\chi^2 = \left[\frac{R_{weighted\ profile}}{R_{exp}} \right]^2$$

[25]

where N is the number of observations, P the number of parameters and C the number of constraints.

Data sets for x-ray Rietveld analysis were collected typically over the region 20 to 120 degrees with a step size of $0.02°$ for 15hrs.

2.2.3.3 Neutron Diffraction Data

The refinement of neutron diffraction data has significant advantages over the x-ray method. As previously described, the scattering length of a particular atom is related to the size of the nucleus and not the number of electrons it possesses. Neutron diffraction experiments are not affected by a form factor and, therefore, allow a much larger data set to be collected. Refinement is then possible over a much greater number of reflections. Preferred orientation effects are also much reduced in the neutron diffraction experiment.

Single wavelength neutron data were refined in a similar way to that described for

51

x-ray data in section 2.2.3.2 using the program MPROF (7). There are, however, two significant differences which are involved with determination of background and peak shape parameterisation.

Firstly, the background is not refined in the same manner but the intensity due to the background is estimated and subtracted from the observed profile. Secondly, the D1A instrument dictates an almost perfectly Gaussian peak shape for D1A data. The intensity equation previously described in [17] now becomes

$$y_i = I_k \exp [-b_k (2\theta_i - 2\theta_k)^2]$$ [26]

where

$$I_k = t\, S_k^2\, j_k\, L_k \left(\frac{4\, ln2}{H_k^2\, \pi} \right)^{1/2}$$ [27]

all other factors remain the same except the structure factor where $S_k^2 = F_k^2 + J_k^2$ where J_k^2 is the contribution due to the magnetic reflections. Magnetic reflections are affected by a form factor in a similar way to x-rays and are generally significantly weaker than the nuclear reflections meaning J_k^2 is only appreciable above 2.2Å.

The time of flight data from POLARIS or HRPD were refined using a similar Rietveld method running as part of the Cambridge Crystallographic Subroutine Library package on the VAX system at the Rutherford Appleton Laboratory (8). Time of flight data are readily converted to d spacings using the expression

$$t = \frac{2\, d m_n l \sin\theta}{h}$$ [28]

where m_n is the mass of a neutron, l is the total neutron flight path, 2θ the scattering angle and h is Plancks constant.

In using this method, however, a dependant absorption correction needs to be applied because of the range of incident neutron energies. Peak shape is more complex

52

than single wavelength data and peaks are fitted in terms of Gaussian, Lorentzian and exponential expressions. Background is fitted using a simple polynomial expression typically described by five terms.

2.2.4 Thermogravimetric Analysis TGA

Studies of thermal stability and absolute determination of oxygen content in oxide materials have been carried out using a Stanton Redcroft TG1000 series thermogravimetric analyser Figure 2.7 shows a schematic diagram.

A direct plot of weight versus temperature for any sample over the temperature range room temperature to 1000°C can be produced. The electronic microbalance has a quoted reproducibility of $\pm$ 0.5μg with a maximum load of 100mg. The sample is contained within a 5mm diameter, 2mm deep platinum crucible which can be heated in various static or flowing gas atmospheres.

Typically 20mg were used and, where applicable, with a 5% H_2/N_2 flow rate of 90ml/min. Experiments were repeated in duplicate to give concordant results.
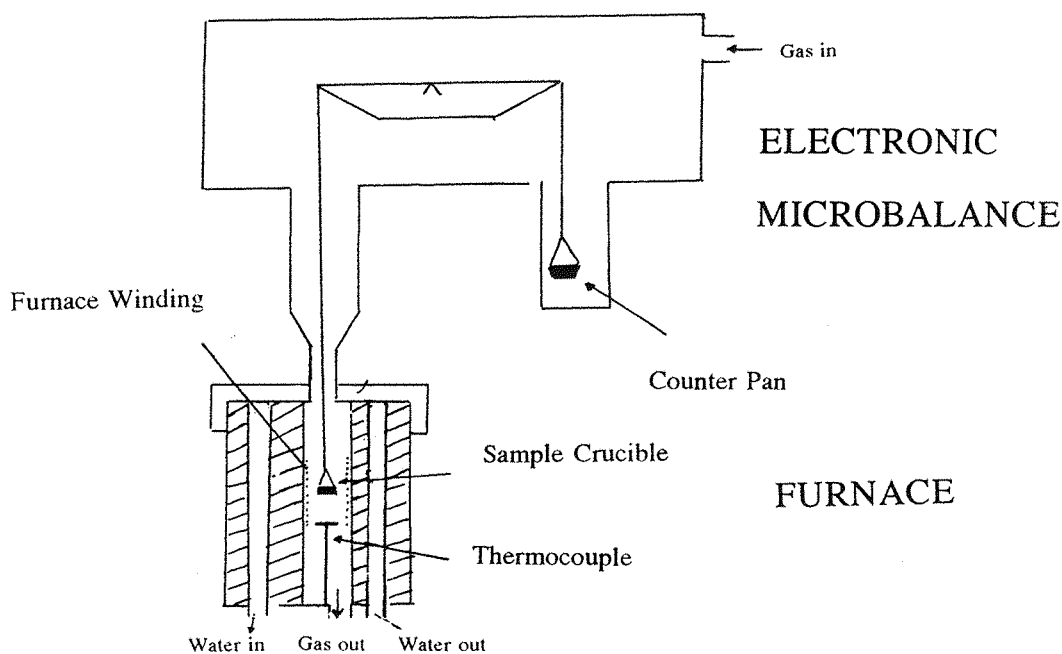
Figure 2.7 Schematic Diagram of the Thermogravimetric Analyser

2.2.5 Mössbauer Spectroscopy

The Mössbauer effect (9) was discovered by Rudolph Mössbauer in 1957-8 and involves the phenomenon of the emission or absorption of a γ-ray photon, without the loss of energy due to recoil of the nucleus, and without thermal broadening. The principle feature is the production of monochromatic electromagnetic radiation with a very narrowly defined energy spread which can be used to resolve minute energy differences. This allows detection of slight variations in the energy of interaction between the nucleus and the extra nuclear electrons.

2.2.5.1 Theory of the Mössbauer Effect

Consider an isolated atom in the gas phase with an excited state E_e, ground state E_g and the difference between the two levels E. If the nucleus (mass M) emits a photon (assuming that recoil and emission of the γ-ray photon occur in the same dimension and there is no motion in the other two directions) with initial velocity V_x in the chosen direction x, the total energy of the atom above the ground state while *at rest* would be given by

$$E \;+\; \tfrac{1}{2} M \, V_x^2 \tag{29}$$

After *emission* the γ-ray has an energy E_γ and the nucleus a new velocity ($V_x + v$) due to recoil. Using the conservation of momentum

$$E \;+\; \tfrac{1}{2} M \, V_x^2 \;=\; E_\gamma \;+\; \tfrac{1}{2} M \, (\, V_x + v \,)^2 \tag{30}$$

The energy difference between the energy of the nuclear transition (E) and the energy of the emitted γ-ray photon E_γ is given by E - E_γ

$$\delta E \;=\; E - E_\gamma \;=\; \tfrac{1}{2} M \, v^2 + M \, v \, V_x$$

$$\delta E \;=\; \tfrac{1}{2} M \, v^2 + M \, v \, V_x \tag{31}$$

54

where $\frac{1}{2}Mv^2$ is the recoil energy (E_R) and MvV_x is the Doppler effect energy (E_D).

Ideally, for an atom to absorb the gamma ray produced by the excited atom, the energy of the τ-ray would need to be equal to the separation between the two levels, E. However the energy available from the γ-ray for reexcitation is less than E due to the energy removed by recoil. Now considering the quantities E_R and E_D as a function of the γ-ray energy. Since V_x and v are both much smaller than the speed of light it is possible to use non-relativistic mechanics. The mean kinetic energy per translational degree of freedom of a free atom in a gas with random thermal motion is given by:

$$E_k = \frac{1}{2} M V_x^2 \approx \frac{1}{2} K T \qquad [32]$$

The mean broadening due to the Doppler effect can then be described by

$$E_D = M v (V_x^2)^{\frac{1}{2}} = M v \left[\frac{2 E_k}{M} \right]^{\frac{1}{2}} = 2 \sqrt{E_k E_R} \qquad [33]$$

The energy of recoil and the doppler effect energy can be expressed in terms of the γ-ray photon using the conservation of momentum

$$E_R = \left[\frac{E_\gamma^2}{2 M c^2} \right] \qquad\qquad E_D = E_\gamma \sqrt{\frac{2 E_k}{M c^2}} \qquad [34]$$

The Mössbauer experiment therefore utilises the solid matrix of a crystal lattice effectively (making M very large) in both source and absorber. This results in the recoil momentum being taken up by the crystal as a whole since the free atom recoil energy is insufficient to eject an atom from the lattice site thus precluding momentum transfer to linear motion of the nucleus or lattice vibrations. Since the mass of the lattice is large and the lattice vibrations are quantised, for a fraction of events the energy will be entirely transferred to the γ-ray photon (ie $E = E_\gamma$).

2.2.5.2 The Mössbauer Experiment

The principal technique of Mössbauer Spectroscopy (Fig 2.8) is tuning the γ-ray energy, using the Doppler effect and oscillating the source relative to the detector, to the energy difference between the excited and ground state in the absorber. The suitability of a particular isotope for Mössbauer spectroscopy depends on several factors. The radioactive source in the excited state must produce a γ-ray with energy 10-100KeV, the excited state must be short lived with a half life of 1-100ns, to avoid thermal broadening, and have a high probability of producing a γ-ray. The source must also have a long lived precursor which can be obtained in high activity and therefore used for a long period with minimum handling. The γ-ray energy must have a small spread and the ground state population in the source must be small. The solid matrix should also contain elements which do not give non-resonant scattering and have a high melting point. A high natural abundance of the chosen isotope is clearly helpful when detecting the isotope in the test material. Although Mössbauer spectroscopy is applicable to forty-two different elements the most abundant and widely used application is in the study of iron. Due to the low natural abundance of ^{57}Fe (c.a. 2%) samples for Mössbauer analysis are often synthesised using ^{57}Fe enriched material.

CYLINDRICAL SCATTERER
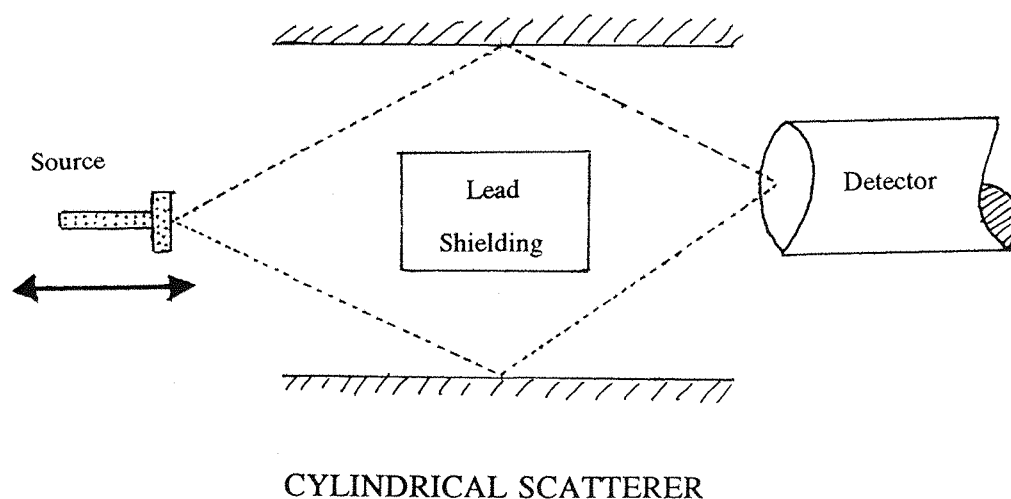
Figure 2.8 Schematic Diagram of the Mössbauer Experiment

If this energy difference between ground and excited state in the absorber is matched with the effective γ-ray energy at a certain Doppler velocity, absorbtion will be at a maximum and count rate at a minimum. At slightly higher or lower applied velocity the absorption will be weaker until it is effectively zero giving a well defined resonance.

The shift in velocity required to produce a resonance maximum is called the chemical shift and is quoted with reference to a particular source. For ^{57}Fe the reference material is normally α-iron.

The chemical shift is a displacement in the absorption due to the chemistry of the system. The major influence on the shift is the electrostatic interaction between the s-electron wavefunction and the nucleus. The magnitude of the chemical shift is therefore dependant on the number of s-electrons, the quantity of shielding which the p,d and f electrons produce, and the electronegativity of the surrounding ions.

The chemical shift is described by the equation

$$\delta E = K [\psi (0)]^2 R^2 \qquad [35]$$

where E is the energy of interaction, $\Psi(0)$ is the s electron density at the nucleus and R is the radius of the nucleus.

The size of the radius of the atom is dependant on whether the nucleus lies in the ground or excited state. The different wavefunctions of source and absorber must, therfore, be taken into account. The chemical shift equation [35] becomes

$$\textit{Chemical Shift} = K (R_e^2 - R_g^2) (\psi^a (0)^2 - \psi^s (0)^2) \qquad [36]$$

where R_e and R_g are considered to be independent of chemical environment. Approximating gives

$$\textit{Chemical Shift} \quad = \quad 2 \; K \; R^2 \left(\frac{\delta R}{R} \right) [\psi^a \; (0)^2 \; - \; c] \qquad\qquad [37]$$

where c is the source characteristic and δR the difference in radius between ground and excited states.

There are two other factors which affect the appearance of a Mössbauer spectrum. The first is quadrupole splitting which is associated with the symmetry of the nucleus. If the nuclear spin quantum number, I, is greater than or equal to one then the nucleus is no longer spherical, but elliptical, and a non-symmetric field is produced which gives rise to an electric field gradient (E.F.G.)
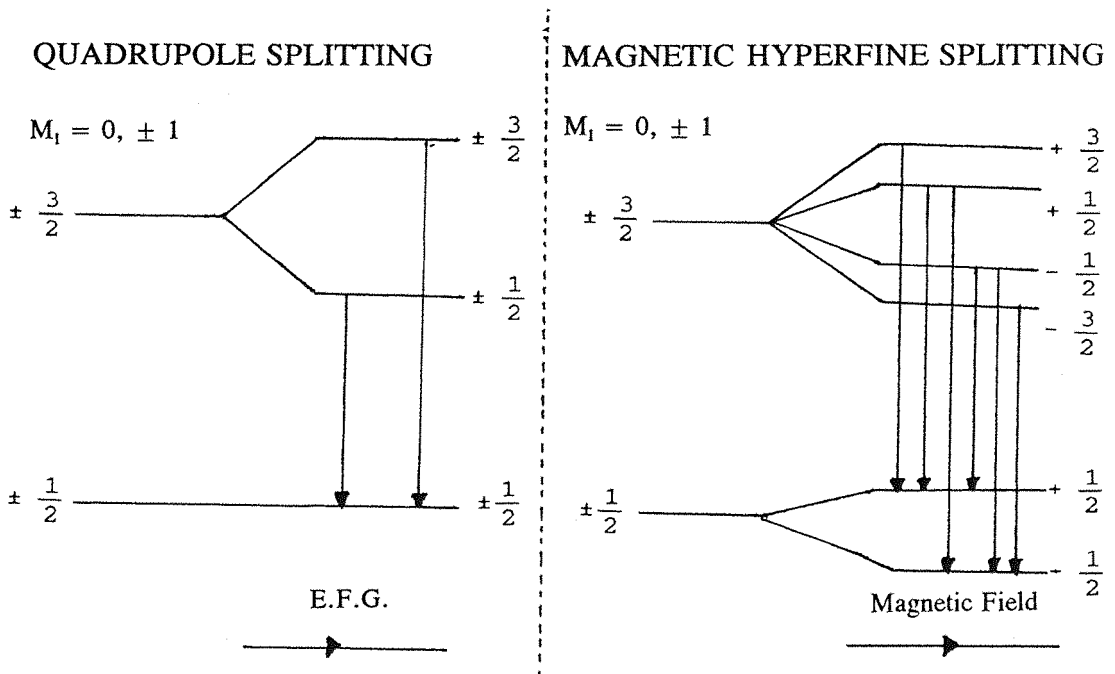
Figure 2.9 Diagrammatic Representation of Quadrupole and Hyperfine Splitting

Considering two axially symmetric electrons about a nucleus (eg in a p orbital)
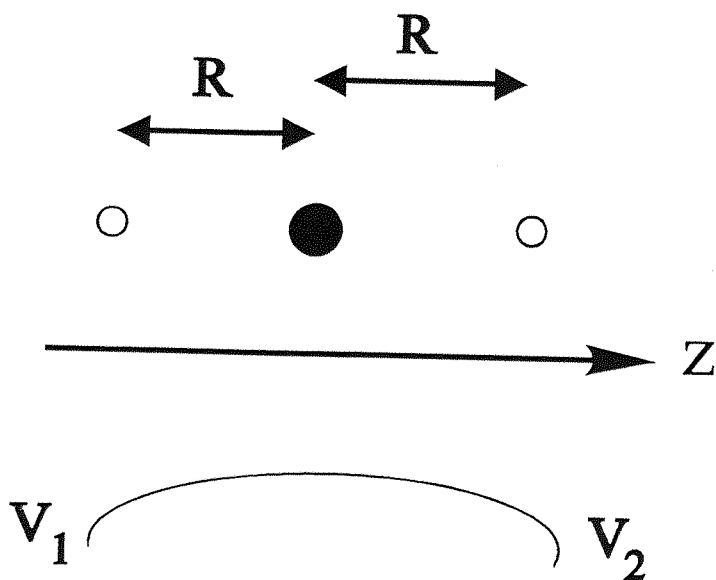
Potential at the nucleus $V_1 + V_2$ [38]

Electric Field $\delta V/dZ = 0$ [39]

Electric Field Gradient $\delta^2 V/dZ^2 = $ -ve (maximum at origin)   [40]

Numerically $V_1 = -e/Z$ $V_2 = -e/2R\text{-}Z$ [41]

       $\delta V/dZ = -e/Z^2 - -e/Z^2 = 0$ [42]

$$\delta^2 V/dZ^2 = -2e/Z^3 - 2e/(2R\text{-}Z)^3 = -4e/R^3 \qquad [43]$$

Therefore, the electric field gradient is finite at the nucleus. If all the orbitals were filled there would be zero EFG since the overall field would be symmetric. d and f electrons can also contribute to the electric field gradient but on a smaller scale and spherically symmetric distributions such as high spin d^5 give no EFG.

Magnetic ordering effects, external or internal, cause the nuclear spin quantum levels to split into their components. (Fig 2.9) The six transitions will be equally separated unless quadrupole splitting occurs simultaneously with intensity ratios typically 3:2:1:1:2:3. A diagram of the expected spectra for the different kinds of spectrum are shown in Fig 2.10 which shows typical Mössbauer spectra expected for a) symmetric field,

b) non-symmetric field (E.F.G.), c) magnetically ordered and d) magnetically hyperfine split with a non-symmetric field. Multiple sets of lines are viewed for more than one type of nucleus in a structure, e.g. different oxidation states or different coordinations.
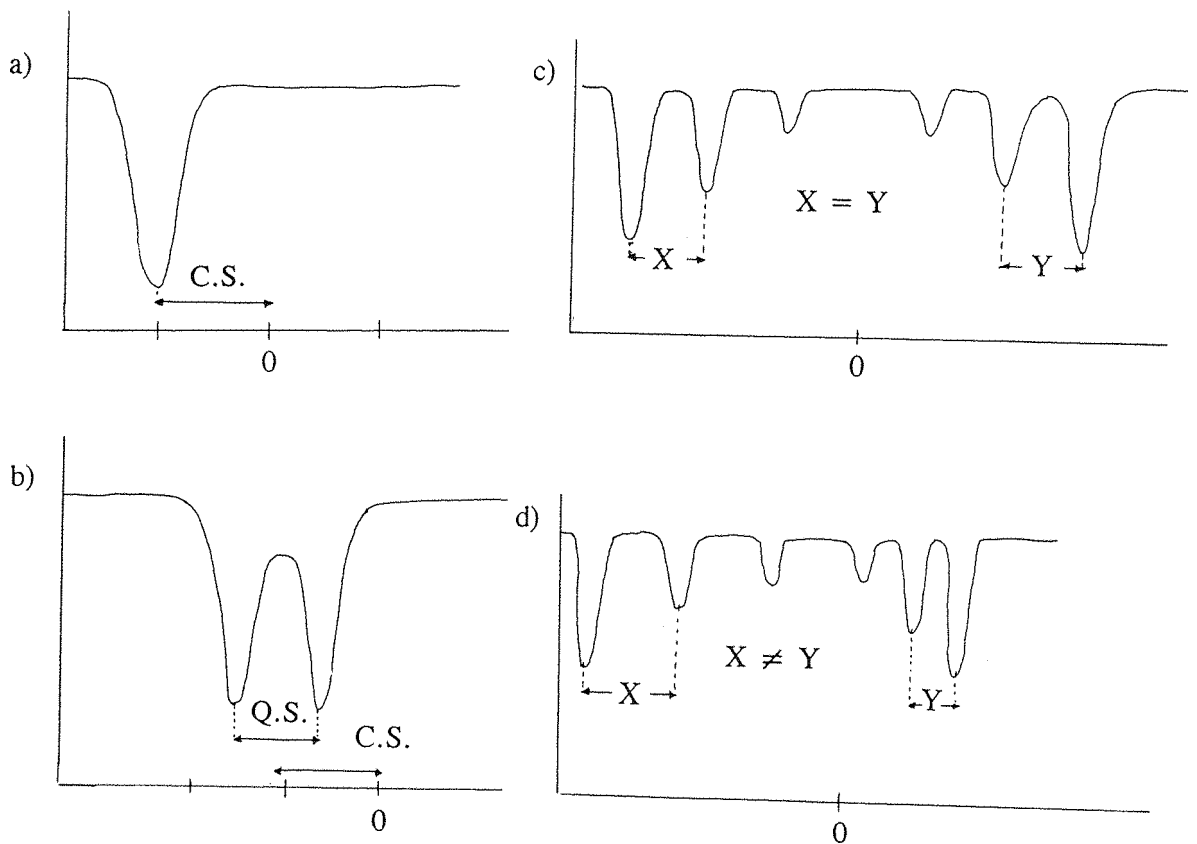
Figure 2.10 Examples of Mössbauer Spectra

2.2.6 Magnetic and Electrical Measurements

During the course of this work the magnetic ordering behaviour and electrical resistance of some samples were studied using vibrating sample magnetometry and a four-probe rig respectively. Described below is a brief summary of the function of these instruments.

2.2.6.1 Vibrating Sample Magnetometry

Experiments were performed on many of the samples to discover the antiferromagnetic ordering temperature and number of unpaired electrons in the sample. The vibrating

sample magnetometer, using Faraday's law, vibrates the sample perpendicularly in a magnetic field. The current produced, which is proportional to the number of unpaired electrons, is then measured as a function of the temperature.

μ_{eff} is then calculated using the spin only formula (first row transition metals only) of the following equation:

$$\chi_{eff} = \frac{N_A \, g^2 \, \mu_B^2 \, J \, (J + 1)}{3 \, K_B \, (T - \theta)} \qquad [44]$$

where N_A is Avagadros number, χ_{eff} the molar susceptibility, $g^2 J(J+1) = \mu_{eff}^2$, μ_B the Bohr magneton, K_B the Boltzmann constant, T, the temperature in Kelvin and θ the Neél temperature in Kelvin.

Then μ_{eff} can be calculated by plotting a graph of the reciprocal of the molar susceptibility against the temperature.

$$\mu_{eff} = \left[\frac{3}{3.75 \; x \; gradient} \right]^{\frac{1}{2}} \qquad [45]$$

2.2.8.2 Electrical Measurements

Resistivity measurements were made on a few samples using the four probe rig depicted in Fig 2.11. Four wires were attached to a sample pellet using silver paint. The four terminal resistance was determined using a 1- 10mA DC current source and the potential difference was measured using a 7075 Solartron digital voltameter (resolution 100 nV). Applying a current, I, through a bar of cross sectional area (w x h) and measuring the potential difference, V, across a length, L, of the sample allows determination of the resistivity ρ, by combining

$$\rho = R_s A/L \qquad [46]$$

with Ohms Law

$$V = R_s I \qquad [47]$$

61

giving

$$\rho = \frac{V\,A}{L\,I} \qquad\qquad [48]$$

The large internal resistance of the voltameter ensured minimal current being drawn into the measuring loop which is in parallel with R_s and so the contact resistances, $R_{CV}{}^+$ and $R_{CV}{}^-$ were assured to have no effect on the measurement of R_s
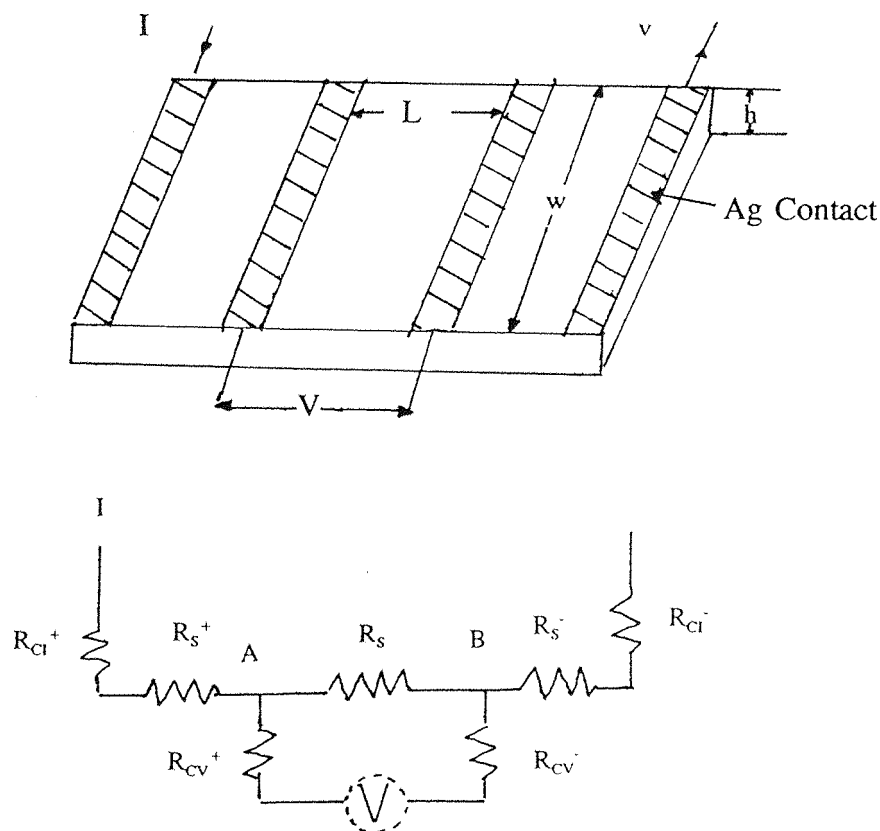
Figure 2.11 Diagrammatic Representation of the Four Probe Rig

The most difficult measurement was in the determination of L and the estimated error $\pm$ 0.5mm which gives rise to 10% error in the final resistivity measurement. The use of the four probe method eliminates the problems of the contact resistances, $R_{CI}{}^+$ and $R_{CI}{}^-$ as the potential difference is not measured across them. Experiments were performed in a continuous flow cryostat between 77 and 300K. The temperature was measured with calibrated silicon diode sensor maintained in close thermal contact with the sample. Due

to a non-linear response, the accuracy of the sensor diode varies with temperature such that there is an error of $\pm$ 0.1K between 4 and 24K, $\pm$ 0.2 between 24 and 100K and $\pm$ 0.5 for temperatures exceeding 100K.

Significant thermal EMFS were generated, especially when investigating semiconducting materials. This was taken into account in calculating resistivity and the rate of change of temperature of the sample was closely monitored. Thermal effects produce a temperature gradient ΔT across A-B creating a thermocouple voltage V_t which can be detected by a voltameter in addition to the potential difference caused by R_s. Obviously as $T \rightarrow 0$ then $V_T \rightarrow 0$, but when $V_T \neq 0$ the thermocouple voltage V_T is significant and the potential difference should be amended. The measurement of the potential difference, $V+V_t$, may be corrected by switching off I at intervals, measuring V_t and subtracting it from the total potential difference measured when the current is switched back on.

2.3 References

1   R.H. Wood. J. Am. Soc. **80**, 2038-41. (1958)

2   J.B. MacChesney, R.C. Sherwood, J.F. Potter. J. Chem. Phys. **43**, 1908-13.
     (1965)

3   A. Wattiaux, L. Fournes, A. Demourges, N. Bernaben, J.C. Grenier, M.
     Pouchard. Sol. Stat. Comm. **77**, 489-93. (1991)

4   D.B. Currie, B. Cleaver. High T. High P. **22**, 263-9. (1990)

5   H.M. Rietveld. Acta. Cryst. **22**, 151. (1967)

6   A. Sakthivel, R.A. Young. User Guide to DBWS - 9006PC. (1991)

7   A.D. Fitch, A.D. Murray. MProf Version X15.0, Manual for Multipattern
     Rietveld Refinement Program. (1989)

8   M.J. Johnson, W.I.F. David. Rutherford Appleton Laboratory Report No 81/112
     (1985)

9   T.C. Gibb. *Principles of Moessbauer Spectroscopy.* Chapman and Hall, London.
     (1976)

CHAPTER 3

The Preparation and Characterisation

of Sr_2FeO_4

3.1 Introduction

The strontium ferrate $SrFeO_3$ (1-3) has been prepared by a number of authors and crystallises with a perfect cubic perovskite structure, a = 3.840Å. However more complex materials containing strontium, iron(IV) and oxygen had been poorly characterised. By the introduction of SrO layers between the $SrFeO_3$ blocks, a new structure would be generated similar to that of K_2NiF_4. Tolerance factors developed by Goldschimdt (4) are often used to the predict the stability of a hypothetical structure (where $r_A + r_O = \sqrt{2}t(r_B + r_O)$ where r_A, r_B and r_O are the ionic radii and for the K_2NiF_4 structure $0.85 < t$, tolerance factor < 0.985). For Sr_2FeO_4 this gives a value for t of 0.96 which implies the structure should be stable (Figure 3.1).

K_2NiF_4 Tolerance Factor
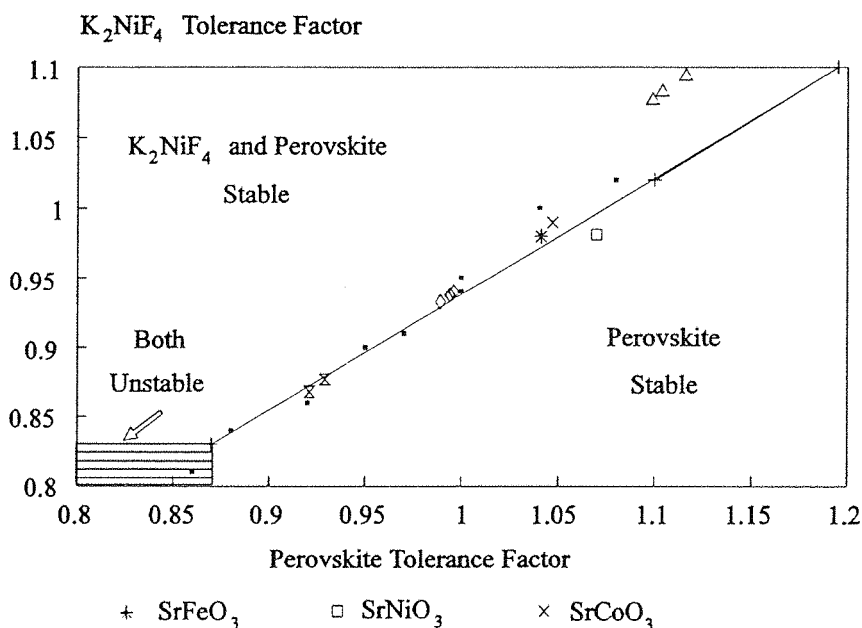
Figure 3.1 Stability Diagram of K_2NiF_4 and Perovskite.

Previous attempts at the preparation of Sr_2FeO_4 (5,6) reported in the literature were unsuccessful, generally with only partial oxidation of the iron forming $Sr_2FeO_{4-\delta}$ and little structural characterisation. Scholder *et al* (5) attempted the preparation of Sr_2FeO_4 using the thermal oxidation of some strontium/iron hydroxy-salts under atmospheric oxygen pressure, whereas MacChesney, using a similar method to that described herein but at a higher temperature, produced a sample of composition $Sr_2FeO_{3.7}$.

This section reports the preparation of Sr_2FeO_4 under high oxygen pressure and its

structural characterisation using powder x-ray and neutron diffraction. The low temperature structure and magnetic ordering behaviour were also studied using powder neutron diffraction. Mössbauer spectroscopy was used to investigate changes in magnetic behaviour and structure at different temperatures. Electrical and magnetic properties were studied using vibrating sample magnetometry and four probe resistivity.

3.2 Experimental

$SrCO_3$ and Fe_2O_3, in a 4:1 molar ratio were intimately ground and fired at $1100^\circ C$ for 24hrs. The product was then reground and heated for a further 24hrs at $1300^\circ C$. Examination of the sample by powder x-ray diffraction revealed the presence of $Sr_3Fe_2O_{7-\delta}$ and SrO. Further heat treatment, including annealing in 1atm of flowing oxygen, produced no change in sample composition beyond a small increase in the oxygen content. The final conversion to Sr_2FeO_4 was achieved through annealing at $750^\circ C$ under 200atm of flowing O_2 gas for 24hrs. Initial x-ray data collected on the Siemens diffractometer showed complete conversion to a K_2NiF_4 phase.

Primary Rietveld analysis was performed using powder x-ray diffraction data collected in the range $13.5 - 93.5^\circ$ over a period of 9hrs. Monochromatic $CuK_{\alpha 1}$ radiation was employed with a step size of 0.02°. The MPROF profile refinement program running on the convex at the Daresbury Laboratory was used for the refinement. Initial stages of the refinement used the typical coordinates of the K_2NiF_4 structure; for example, those given by Soubeyroux et al (1981) for $LaSrFeO_4$ (8). Final stages of the refinement included all atomic coordinates and isotropic temperature factors for all atoms. Attempted refinement of the two oxygen sites resulted in only small deviations from unity that were within the e.s.d.s; the occupancies were consequently fixed at that value.

Thermogravimetric analysis using platinum crucibles and flowing $5\%H_2/N_2$ gave an oxygen content of 4.00 ± 0.05; powder x-ray diffraction data of the t.g.a. product on a silicon wafer revealed unequivocally a mixture of $Sr_3Fe_2O_6$ and SrO.

3.3 Powder Neutron Diffraction

The structure refinements for Sr_2FeO_4 at 4K and 100K were carried out using the

backscattering data from POLARIS. Due to the relatively small unit cell volume (less than 200Å^3) structure refinement was possible using the POLARIS data. The model used for the refinement was that determined at room temperature for this compound using x-ray diffraction data (7) in the space group I4/mmm; no evidence was found for structural distortion below the Néel temperature though the moderate resolution for the POLARIS instrument would preclude the observation of a very small structural change. The refinement converged smoothly and final cycles of the refinement included all instrumental and positional parameters including anisotropic temperature factors.

An investigation of the magnetic ordering behaviour of Sr_2FeO_4 was carried out using the data collected in the high d-spacing range (A bank) of the POLARIS instrument. Below the Néel temperature, at 4.2K, the data were closely examined for additional reflections which could belong to a magnetic unit cell.

3.4 Mössbauer Spectroscopy

Mössbauer spectra of Sr_2FeO_4 were collected at room temperature and at intervals to 4.2K using a conventional transmission spectrometer with a double ramp waveform to give a flat background. Sources of up to 100mCi of ^{57}Co in Rh were used and the spectrometers calibrated using α-iron at room temperature. The powdered sample was weighed and ground with boron nitride to randomise the orientations of the microcrystals (9).

3.5 Susceptibility Measurements

Magnetic ordering behaviour was studied using vibrating sample magnetometry with and without an external field. Electronic behaviour was studied using the four probe method.

3.6 Results and Discussion

X-ray Structure Refinement

Final reliability factors achieved for the refinement of the x-ray diffraction data were R_I = 3.70, R_{wp} = 8.01 and R_{exp} = 5.86 and the profile fit is shown in Figure 3.2. Refined
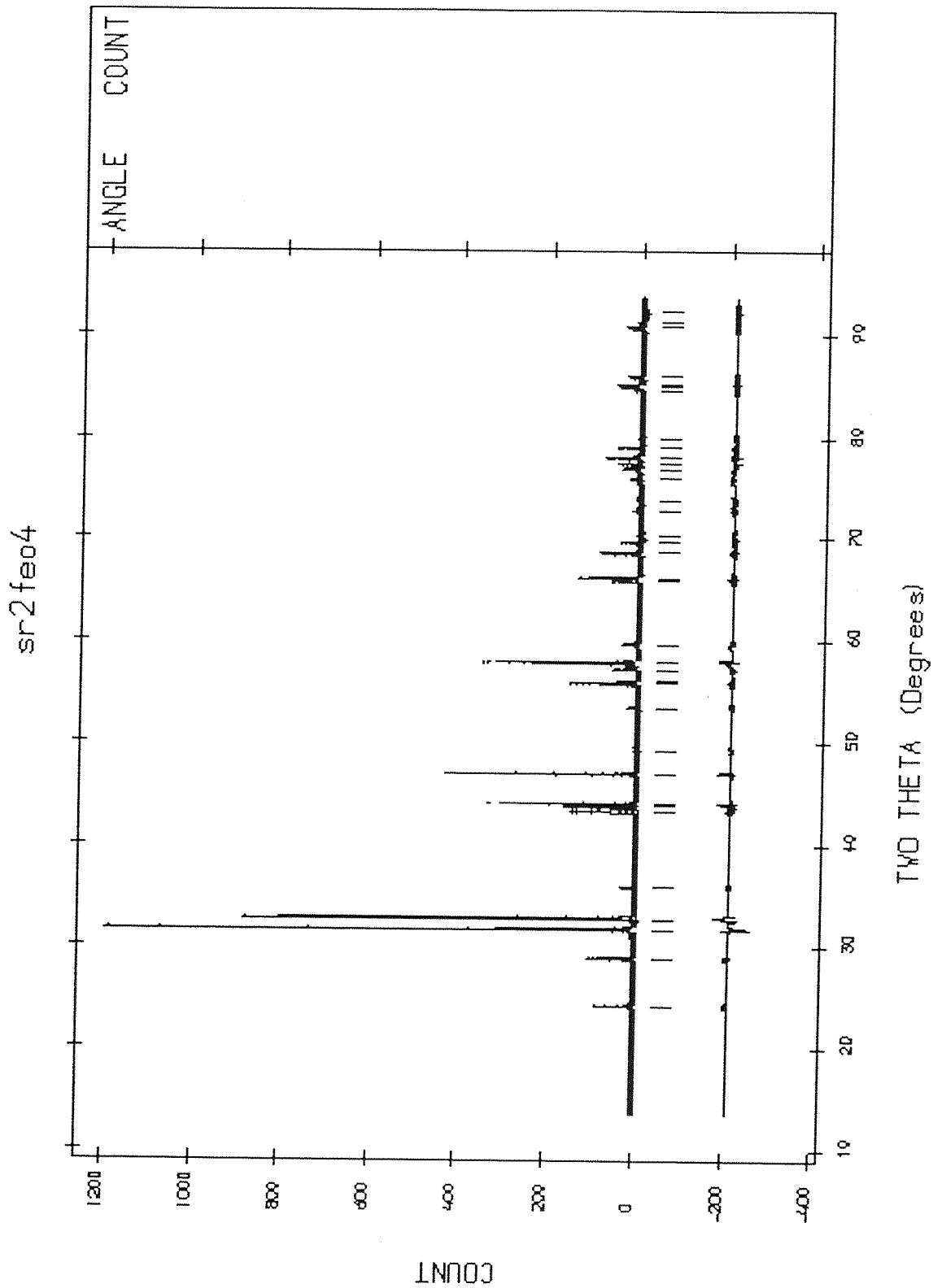
Figure 3.2 X-ray Diffraction Data Refinement Profile of Sr_2FeO_4

The dotted line is the observed data and the solid line the calculated pattern.

The lower solid line represents the difference; obs-calc.

atomic coordinates are summarised in Table 3.1 and derived interatomic distances in Table 3.2. The observed and calculated intensities are compared in Table 3.3. The refinement of x-ray diffraction data confirms that Sr_2FeO_4 crystallises with the K_2NiF_4 structure but is unusual in that the coordination of the iron is almost perfectly octahedral. This is similar behaviour to that seen for the cubic perovskite $SrFeO_3$, where no Jahn-Teller distortion has been observed. Bond valence calculations using the method devised by Brown (10) calculated a derived iron valence of 3.7 using the parameters for an Fe^{3+} ion.

Final refined coordinates for Sr_2FeO_4 (4K and 100K) are given in Table 3.4 and are in good agreement with those refined from powder x-ray data. Bond lengths and angles of interest are summarised in Table 3.5. The final fit to the 4.2K POLARIS data is shown in Figure 3.3. The final fit factors obtained to the 4K and 100K data sets were in both cases excellent with χ^2 values of 1.10 and 1.64 respectively. Bond lengths are in excellent agreement with those calculated from refinement of the x-ray data. The iron environment consisting of an almost regular octahedron with the apical Fe-O bond being only 0.93% longer than the four in-plane interactions. Variations in lattice parameters and derived bond lengths as a function of temperature were very small and comparable to the e.s.d.'s. This evidence leads to the conclusion that this material does not undergo a structural distortion below the Néel temperature.

The data collected in the POLARIS A bank 3-8Å from Sr_2FeO_4 is shown in Figure 3.4. The major peaks are readily identified as the crystallographic 002 and 101 reflections; the only additional feature is a very weak, broad peak at ≈ 5.9Å. The lack of magnetic reflections indicates that Sr_2FeO_4 orders antiferromagnetically only in two dimensions at 60K and the structure has not ordered in three dimensions even at 4K. Since there is only one peak which is possibly magnetic, little can be said about the two-dimensional magnetic structure.

A likely reason for the weak magnetic ordering in Sr_2FeO_4 is that the structure is two-dimensional with respect to the iron atoms. The nearest neighbour iron-iron interaction in the a b plane is much shorter than in the a c plane. The coupling between planes in pseudo two-dimensional structures such as Sr_2FeO_4 cannot proceed via a superexchange mechanism and is, therefore, considerably weaker than the in-plane interactions. Assessments of the various magnitudes of in-plane (J) and interplane (J') coupling constants in K_2NiF_4 type structures are of the order of 10^{-4} (11). This quantity

Table 3.1 Refined Atomic Coordinates

Atom	Site Symmetry	x	y	z	B_{eq}
Sr	4e	0	0	0.3570(1)	0.05(5)
Fe	2a	0	0	0	0.39(9)
O1	4c	0	½	0	0.58(24)
O2	4e	0	0	0.1573(8)	0.33(20)

Table 3.2 Derived Atomic Distances (Å)

Atom - Atom	Distances (Å)
Sr - O2	1 x 2.475(9)
Sr - O1	4 x 2.623(1)
Sr - O2	4 x 2.738(1)
Fe - O1	4 x 1.932(1)
Fe - O2	2 x 1.950(9)

Table 3.3 Comparison of Observed and Calculated Intensities

h k l	2θ	I_{calc}	I_{obs}	h k l	2θ	I_{calc}	I_{obs}
1 0 1	24.07	432	471	2 2 0	68.61	796	764
0 0 4	28.75	548	597	1 1 8	69.67	361	322
1 0 3	31.64	6840	6721	2 2 2	70.50	12	13
1 1 0	32.71	5145	5211	1 0 9	72.81	88	115
1 1 2	35.85	143	143	3 0 1	73.88	39	22
1 0 5	43.29	867	866	2 2 4	76.04	169	238
0 0 6	43.75	1063	1103	0 0 10	76.80	46	112
1 1 4	44.12	1981	1985	2 1 7	77.01	364	375
2 0 0	46.96	2854	2868	3 0 3	77.54	511	467
2 0 2	49.33	60	28	3 1 0	78.12	744	734
2 1 1	53.46	156	128	2 0 8	79.14	445	452
1 1 6	55.70	1062	1053	3 1 2	79.92	17	5
2 0 4	56.01	378	354	3 0 5	84.71	98	129
1 0 7	57.14	384	395	2 2 6	85.02	474	482
2 1 3	57.75	2448	2587	3 1 4	85.28	520	489
0 0 8	59.58	279	282	1 1 10	86.02	276	260
2 1 5	65.79	431	418	1 0 11	90.76	427	411
2 0 6	66.13	1035	1029	2 1 9	91.28	101	106
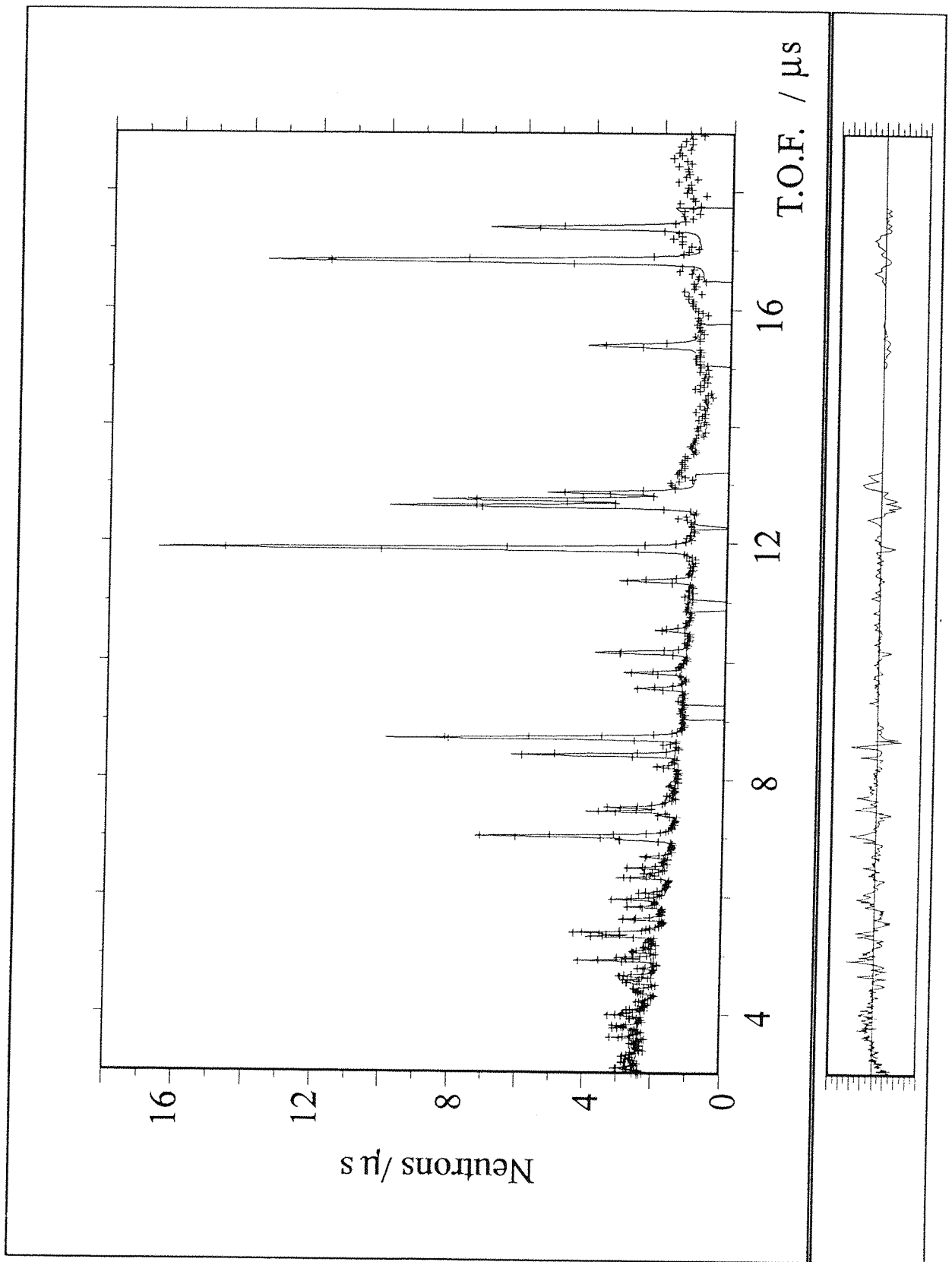
Figure 3.3 Refinement Profile of 4.2K POLARIS Data

The dotted line is the observed data and the solid line the calculated pattern. The lower solid line represents the difference; (obs - calc)/e.s.d

73

Table 3.4 Refined Atomic Parameters at 4.2 and 100K

Cell Parameters(Å)			100K $a = 3.8624(1)$ $c = 12.4000(10)$		4.2K $a = 3.8610(1)$ $c = 12.3993(2)$	
Atom	x	y	z	B_{11}, B_{22}, B_{33}	z	B_{11}, B_{22}, B_{33}
Sr	0	0	0.3570(1)	0.25(4), 0.25(4), 0.21(4)	0.3572(1)	0.17(2), 0.17(2), 0.27(3)
Fe	0	0	0	0.09(3), 0.09(3), 0.42(6)	0	0.05(2), 0.05(2), 0.43(4)
O1	0	½	0	0.39(6), 0.82(7), 0.45(6)	0	0.37(5), 0.79(5), 0.31(5)
O2	0	0	0.1567(2)	0.33(3), 0.33(3), 0.28(5)	0.1571(1)	0.30(3), 0.30(3) 0.23(4)
R_{wp}			4.59%		3.21%	
R_{exp}			4.38%		2.50%	
χ^2			1.10		1.64	

Table 3.5 Derived Bond Lengths at 4.2 and 100K (Å)

Atom1 - Atom 2	RT	100K	4.2K
Sr - O1	2.623(1) x 4	2.622(1) x 4	2.620(1) x 4
Sr - O2	2.475(9) x 1	2.484(3) x 1	2.481(2) x 1
Sr - O2	2.738(1) x 4	2.737(1) x 4	2.736(1) x 4
Fe - O1	1.932(1) x 4	1.931(1) x 4	1.931(1) x 4
Fe - O2	1.950(9) x 2	1.943(3) x 2	1.948(1) x 2
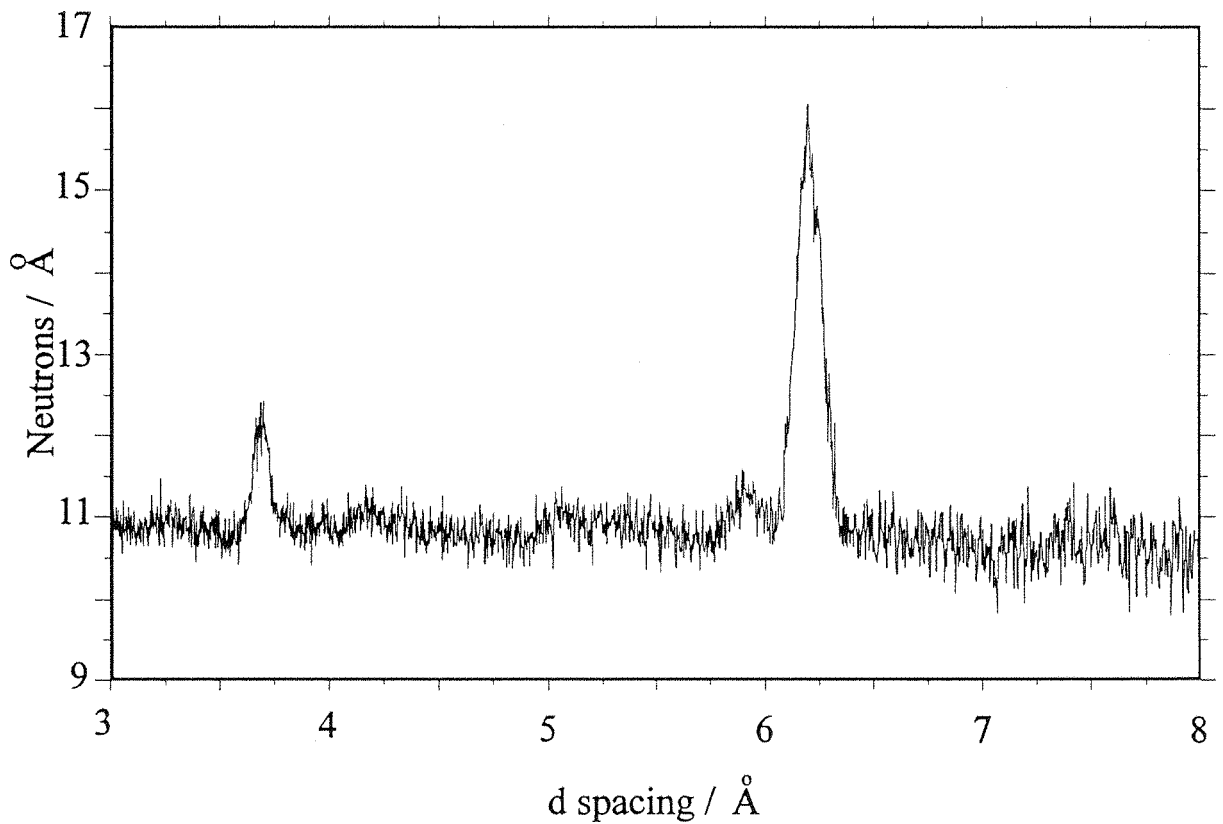
Figure 3.4 Sr_2FeO_4 data from POLARIS A bank.

is dependant on several factors including interplanar separation and dipolar coupling constants.

Mössbauer Spectroscopy

The spectra of Sr_2FeO_4 taken at 300K and 4.2K are shown in Figure 3.5 and 3.6 respectively. The parameters of the fits are listed in Table 3.6 with those of $SrFeO_3$ (2) for comparison. It is seen that the 300K spectrum is well fitted by a single component corresponding to a unique set of site conditions for the Fe ions. The isomer shift value $\delta = -0.01$mms^{-1} corresponds to iron in a high charge state which can be assigned as Fe^{4+} from consistency with the measured composition. The quadrupole splitting, q=0.44mms^{-1} indicates the presence of an electric field gradient at the nucleus. The direction of V_{zz}, the principal axis of this electric field gradient will lie along the axis of maximum symmetry, parallel to the crystal c axis. The elongation of the nearest neighbour octahedron along the direction of this axis gives rise to the electric field gradient.

At 4.2K the spectrum shows a complex magnetic structure. At least four components are required to give a reasonable fit to the experimental spectrum and further components give minor improvement to the fit. All four components used in the fit shown in Figure 3.6 had the same value of the isomer shift $\delta = -0.07$mms^{-1} corresponding to an Fe^{4+} charge state. The difference in isomer shift between the 300K and the 4.2K spectra is due to second order Doppler shift. The challenge in explaining the 4.2K spectrum is to understand how Fe^{4+} ions in a unique site can exhibit at least four different values of the hyperfine field B_{hf}.

The first step in the explanation lies in the different values of the quadrupole interaction listed in Table 3.6 for the different components. Such different values can arise at a unique site if in each component the hyperfine field makes a different angle with V_{zz}, the principal axis of the electric field gradient. As V_{zz} is always expected to lie parallel to the c axis, the suggestion is that different components represent different orientations of the hyperfine field (and the magnetic moment of the Fe^{4+} ions.) The second step in the explanation is the recognition that in an Fe^{4+} ion the hyperfine field can have anisotropic contributions.

76
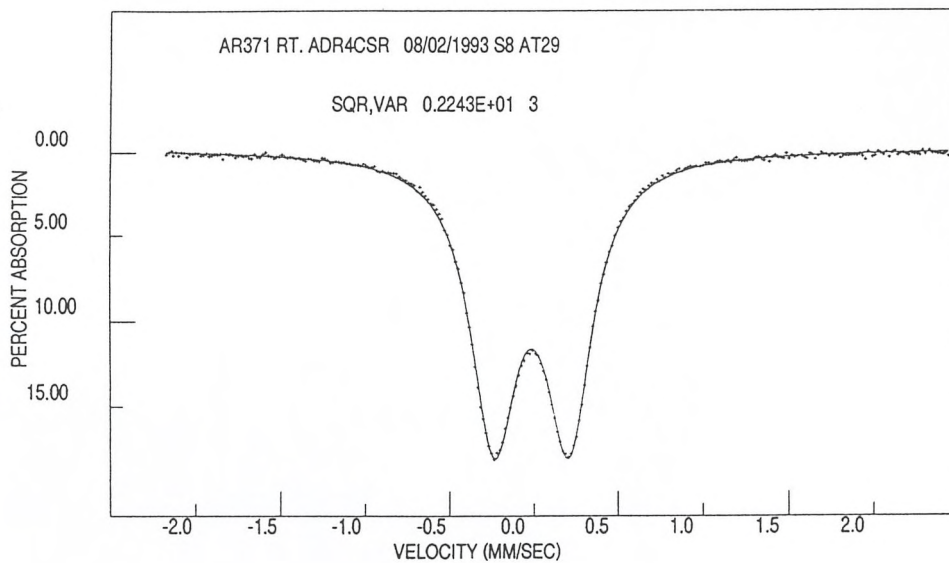
Figure 3.5 Mössbauer Spectrum of Sr_2FeO_4 at 300K
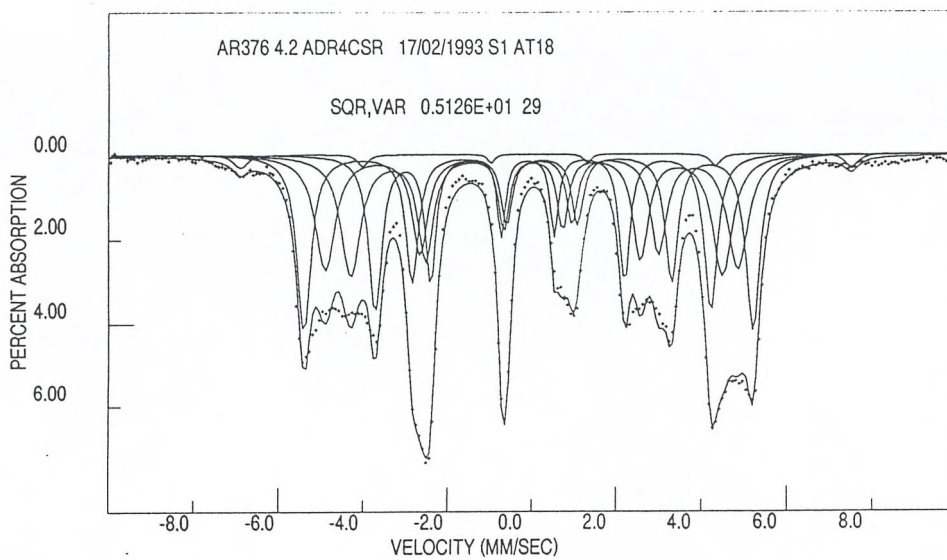
Figure 3.6 Mössbauer Spectrum of Sr_2FeO_4 at 4.2K

77

Table 3.6 Mössbauer Hyperfine Parameters

	$SrFeO_3^{(2)}$	Sr_2FeO_4
Symmetry	Cubic	Tetragonal
Cell Parameters (Å)	a = 3.850	a = 3.864 c = 12.340
$T_{Néel}$	134K	60K
μ_{eff}	5BM	5.6BM
RT Mössbauer Parameters	C.S. $0.07mms^{-1}$	C.S. $-0.01mms^{-1}$, Q.S. $0.44mms^{-1}$
4.2K Mössbauer Parameters	C.S. $0.17mms^{-1}$	1) 25% $0.07mms^{-1}$, Hi = 329kG, Q.S. $-0.33mms^{-1}$ 2) 25% $0.07mms^{-1}$, Hi = 303kG, Q.S. $-0.20mms^{-1}$ 3) 25% $0.07mms^{-1}$, Hi = 272kG, Q.S. $0.06mms^{-1}$ 4) 25% $0.07mms^{-1}$, Hi = 246kG, Q.S. $0.36mms^{-1}$

$$B_{hf} \quad = \quad B_{hf}(contact) \quad + \quad B_{hf}(dipolar) \quad + \quad B_{hf}(orbital)$$

In contrast to Fe^{3+}, where $B_{hf}(contact)$ dominates B_{hf}, significant contributions to the hyperfine field can arise from B_{hf} (dipolar) and B_{hf} (orbital) in Fe^{4+} ions. The dipolar contribution can be written as $B(3\cos^2\theta-1)/2$ where B is a constant and θ is the angle between B_{hf} and V_{zz}. This anisotropy is the same as that of the effective quadrupole interaction $q = q_0(3\cos^2\theta-1)/2$ thus the dipolar contribution to the hyperfine field can be represented as

$$B_{hf} \; (dipolar) \quad = \quad B_q$$

The orbital contribution to the hyperfine field can be written as $B_{hf}(orbital) = K<s>(g-2)$ where K is a constant and $<s>$ the mean value of the ionic spin. For ions in which the orbital angular momentum is quenched, $g = 2$, and the orbital contribution vanishes. For ions in which (g-2) is finite, but g is isotropic, the orbital contribution to the hyperfine field is isotropic and can be added to the isotropic contact term. Only if g is anisotropic will the orbital contribution to the hyperfine field be anisotropic. In the absence of knowledge of g values parallel and normal to the crystal c axis for the Fe^{4+} ion in Sr_2FeO_4 we assume that any orbital contribution is isotropic. In such a case the total hyperfine field can be written

$$B_{hf} \quad = \quad A \quad + \quad B_q$$

where A represents the isotropic contributions and B the magnitude of the dipolar contribution. Using the measured values of B_{hf} and q listed in Table 3.6 to fix best fit vales of A = 284kG and B = -117kG, the relation above gives predicted values of B_{hf} = 323kG, 308kG, 277kG and 242kG which are reasonable agreement with the experimental values of Table 3.6. Differences between these predicted values and those measured

experimentally may be due to an anisotropic orbital contribution.

Assuming that the value of q = -0.33mms^{-1} is the minimum possible value of quadrupole interaction, corresponding to B_{hf} normal to V_{zz}, the angles of the hyperfine fields to the V_{zz} axis for the other components are 69°, 51° and 34° respectively. Such an evaluation supposes that the maximum value of q = 0.66mms^{-1}. This modest increase on the value of q = 0.44mms^{-1} observed at 300K is not surprising for an Fe^{4+} ion. These results suggest the possibility that the magnetic state seen by Mössbauer spectroscopy has a spiral spin structure.

Susceptibility Data

Figure 3.7 represents the magnetic susceptibility data for Sr$_2$FeO$_4$ and Figure 3.8 the derived variation of $1/\chi$ with temperature. The Néel temperature of Sr$_2$FeO$_4$ is 60K and the derived magnetic moment 5.6BM. Fitting the data above 200K to a Curie-Weiss law, χ = C/(T-θ), gives a value of θ of 0. This suggests that the iron(IV) in this material is high spin d^4; the high value of μ_{eff} and θ = 0 may indicate some ferromagnetic interactions. However, comparison of data with, and without, an external field shows little difference indicating almost true antiferromagnetic ordering behaviour.

Four probe resistivity measurements showed Sr$_2$FeO$_4$ to be a semiconductor with a low room temperature resistance of a few ohms.

The properties of Sr$_2$FeO$_4$ can be compared with that of the other first row transition metal, Sr$_2$MO$_4$, materials where M = Ti, V, Cr, and Mn. All of these materials except Sr$_2$CrO$_4$ (12), which forms the ß-K$_2$SO$_4$ structure containing discrete CrO$_4$ and CrO$_6$ units, form the K$_2$NiF$_4$ structure. Selected aspects of the structural and behaviourial attributes of these materials are summarised in Table 3.7.

Initially both the a and c cell parameters fall as the series is crossed but at Sr$_2$FeO$_4$, the a parameter increases unexpectedly. The magnitude of the cell parameter, a, is controlled by the M - O1 - M distance. Since the positions of the atoms remain constant, within the unit cell, changes in a are solely related to the ionic size of M. The increase in the ionic radius for Fe^{4+} after Mn^{4+} (13) is presumably a result of the high spin d^4 configuration since the other members of the series can have only one such conformation (e.g. Mn^{4+} = d^3, t_{2g}^3, e_g^0). This information further supports the conclusion that Sr$_2$FeO$_4$
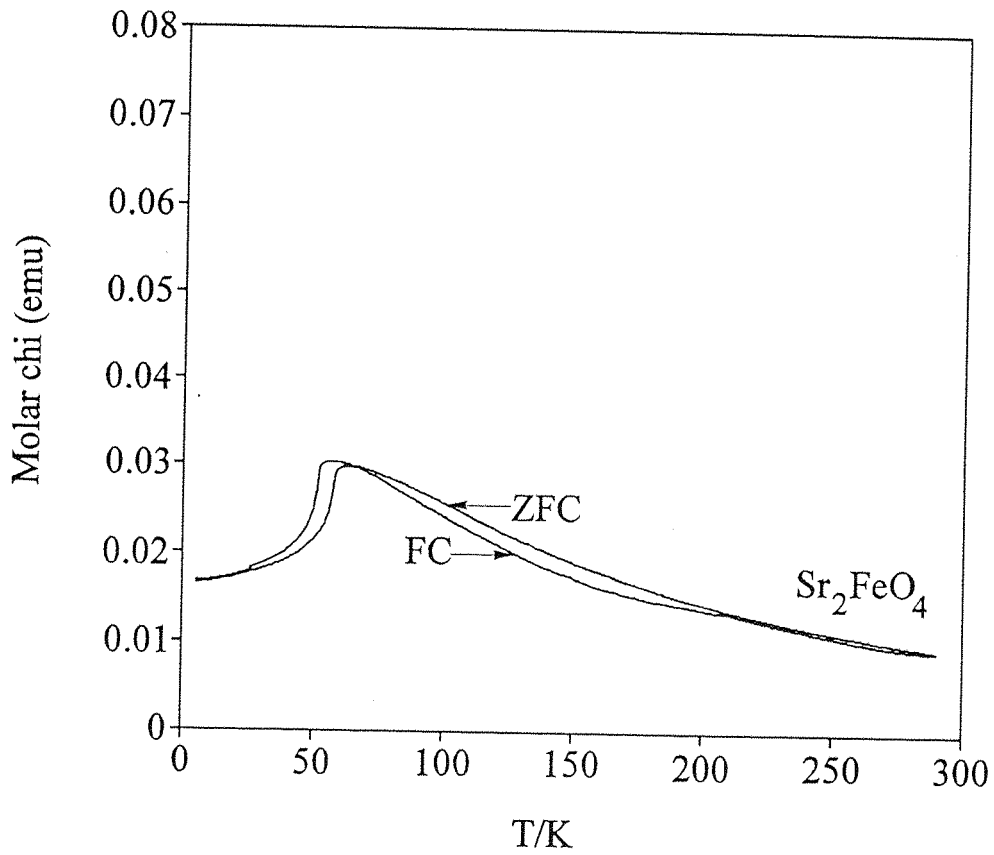
Figure 3.7 Susceptibility Data for Sr_2FeO_4
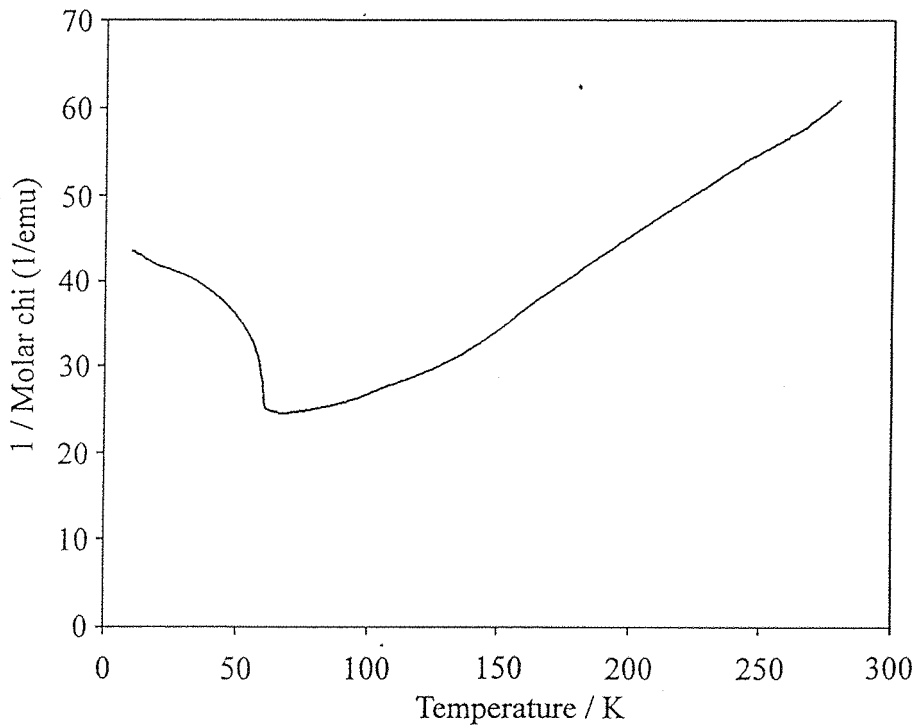
Figure 3.8 Variation of $1/\chi$ with Temperature.

81
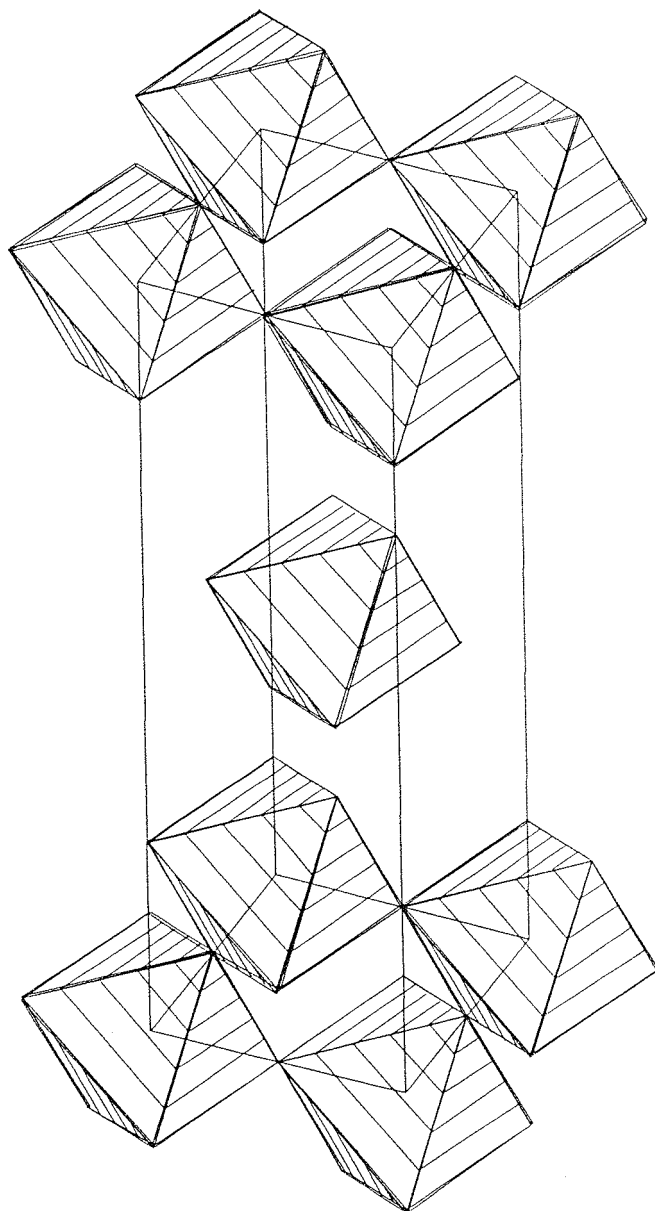
Figure 3.9 STRUPLO Plot (14) of the Structure of Sr_2FeO_4

Table 3.7 Comparison of First Row Transition Metal Sr_2MO_4 Compounds

	Sr_2TiO_4 (15)	Sr_2VO_4 (16)	Sr_2MnO_4 (17)	Sr_2FeO_4
Cell Parameters	a = 3.884Å c = 12.600Å	a = 3.834Å c = 12.587Å	a = 3.787Å c = 12.496Å	a = 3.862Å c = 12.397Å
Sr Position 0 0 z	z = 0.355	z = 0.344	z = 0.356	z = 0.357
O2 Position 0 0 z	z = 0.152	z = 0.158	z = 0.158	z = 0.157
Néel Temperature	-	10K	170K	60K
M - O Bond Distance	4 x 1.94 2 x 1.92	4 x 1.93 2 x 1.99	4 x 1.89 2 x 1.98	4 x 1.93 2 x 1.95
(13) M^{4+} Ionic Radius	0.61Å	0.58Å	0.53Å	0.59Å

is a high spin d^4 material.

Sr_2VO_4 (16) is an insulator with a Néel temperature of 10K. This compound was very difficult to prepare and the authors report a problem in obtaining reproducible results e.g. sometimes the Néel temperature varied up to 100K. A μ_{eff} of 0.6BM per vanadium was calculated and no magnetic reflections were seen in the powder neutron diffraction pattern. Despite the small magnetic moment of the vanadium ions, two-dimensional magnetic ordering behaviour similar to that seen in Sr_2FeO_4 was reported.

In contrast, Sr_2MnO_4 (17) is a semiconductor which exhibits both two- and three-dimensional ordering behaviour. Commonly, there are two types of three-dimensional magnetic ordering behaviour observed in layered K_2NiF_4 materials. They are depicted in Figure 3.10.
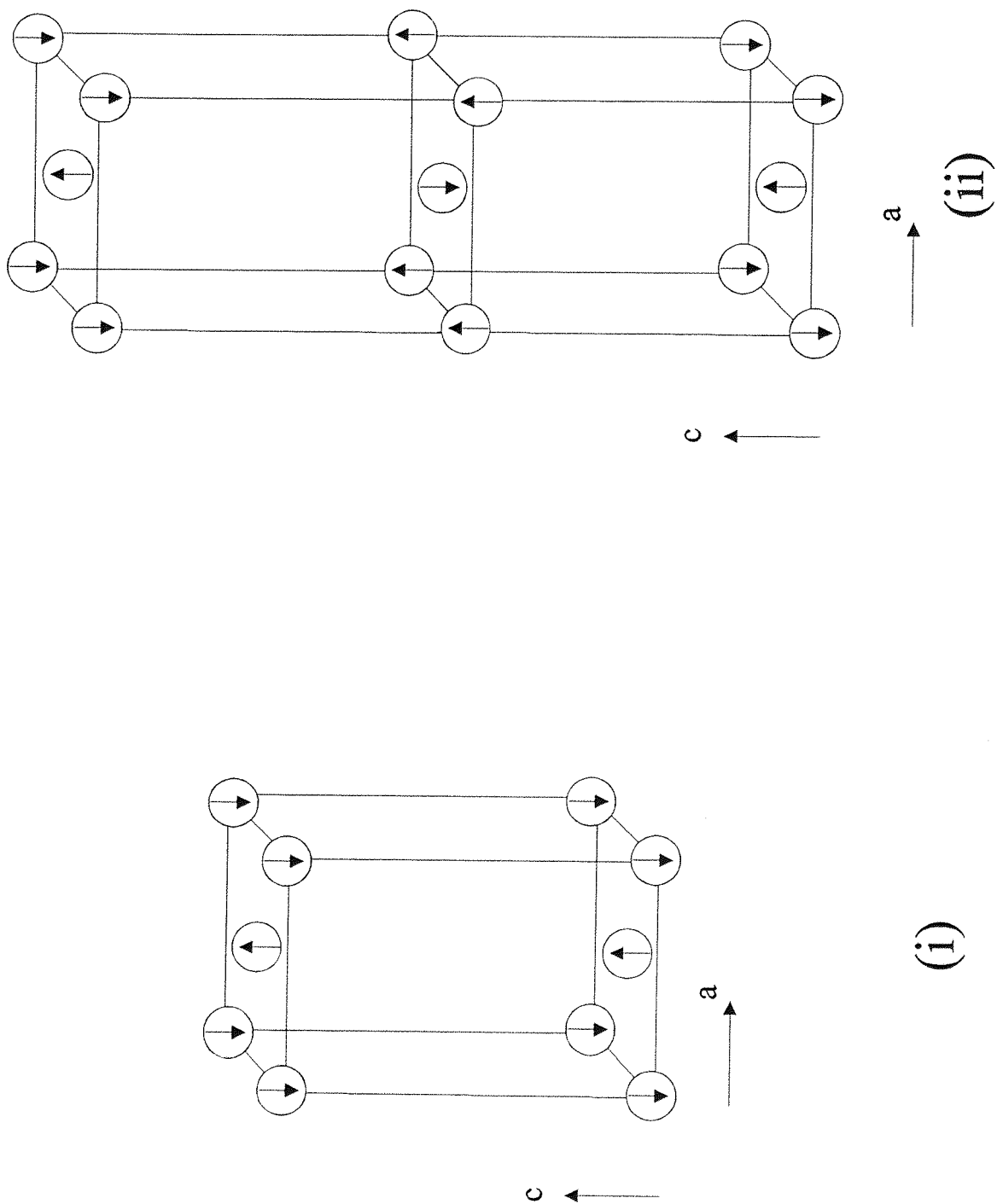
Figure 3.10 Antiferromagnetic Ordering of K_2NiF_4-type Materials

84

In the first type, as seen Fig 3.10i, the magnetic unit cell is related to the crystallographic unit cell by $\sqrt{2}a \times \sqrt{2}a \times c$ and this is exhibited by K_2NiF_4. Sr_2MnO_4 (17) and Ca_2MnO_4 (18), have a different magnetic structure where the ions are also antiferromagnetically ordered in c with a repeat distance now of 2c, as depicted in Figure 3.10ii.

Sr_2FeO_4 has a unique magnetically ordered spin lattice which is completely unrelated to these aforementioned magnetically ordered systems. No evidence for three-dimensional magnetic ordering has been obtained, although the low temperature Mössbauer spectrum may suggest a spiral spin structure. This is the case for $SrFeO_3$, but this material has a three-fold axis, whereas the symmetry axes for Sr_2FeO_4 are all 2n-fold where n is an integer. The single weak magnetic reflection observed in the low temperature neutron diffraction pattern does not allow assignment of a magnetic structure but the saw-toothed appearance is perhaps indicative of two-dimensional ordering behaviour. It should be noted that other materials with large magnetic moments, such as $Rb_3Mn_2F_7$ (19), also do not order magnetically in three-dimensions as a result of ferromagnetic interactions.

3.7 Conclusions

Fully oxygenated Sr_2FeO_4 has been prepared by high pressure methods. Sr_2FeO_4 crystallises with the K_2NiF_4 structure (Figure 3.9) with an unusually perfect octahedron for the iron coordination. As the temperature is lowered, there is no obvious change in the structure with atomic parameters and bond lengths differing to only a very small degree.

Magnetic measurements have shown Sr_2FeO_4 to be an antiferromagnetic semiconductor with a Néel temperature of 60K. However, only a single weak magnetic reflection was seen by neutron diffraction suggesting that the magnetic ordering behaviour was in two dimensions only. Assignment of a magnetic unit cell was not possible on the basis of a single reflection.

Mössbauer measurements have shown that Sr_2FeO_4 has a complex low temperature magnetic structure. Although the room temperature structure can be fitted by a single quadrupole split doublet, characteristic of a electronically asymmetric arrangement such as high spin d^4, the low temperature spectrum is much more complex based on at least

four and maybe more components. The variation of the inclination angle of the hyperfine field axis to the principal axis may suggest a spiral spin structure.

Magnetic measurements suggest that the iron(IV) is a high spin d^4 ion in this material. Antiferromagnetic ordering behaviour is exhibited with a Néel temperature of 60K although significant ferromagnetic interactions maybe be present giving a high value of μ_{eff} of 5.6BM.

3.8 References

1   A. Wattiaux, L. Fournes, A. Demourges, N. Bernaben, J.C. Grenier, M. Pouchard. Sol. Stat. Comm. **77**, 489-93. (1991).

2   J.B. MacChesney, R.C. Sherwood, J.F. Potter. J. Chem. Phys. **43**, 1907-13. (1965).

3   T. Takeda, Y. Yamagughi, J. Watanabe. J. Phys. Soc. Jpn. **35**, 967-9. (1972).

4   V.M. Goldschimdt. Str. Ner. Vidensk-Akad. Oslo. **1**, 1. (1926)

5   R. Scholder, H. Bunsen, Z. Weiss. Z. Anorg. Algem. Chem. **283**, 330-7. (1956).

6   P.K. Gallagher, J.B. MacChesney, D.N.E. Buchanan. J. Chem Phys. **45**, 2466-71. (1966)

7   J.L. Soubeyroux, L. Fournes, D. Fruchart, G. Le Flem. J. Sol. Stat. Chem. **31**, 313-20. (1978)

8   S.E. Dann, M.T. Weller, D.B. Currie. J. Sol. Stat. Chem. **92**, 237-40. (1991).

9   G.J. Long, T.E. Cranshaw, G. Longworth. Mössauer Effect Reference and Data Journal. **6**, 42-9. (1983)

10   I.D. Brown. Chem. Soc. Rev. **7**, 359. (1978)

11   L.J. de Jongh, A.R. Miedama. Advances in Physics. **23**, 1. (1974)

12   K.A. Wilhelmi. Chem. Comm. **20**, 157-65. (1966)

13   R.D. Shannon. Acta. Cryst. **A32**, 751-2. (1976)

14   R.X. Rischer. J. Appl. Cryst. **18**, 258. (1985)

15   K. Lukasewicz. Roczn. Chem. **23**, 239-42. (1959)

16   J.C. Bouloux, J.L. Soubeyroux, G. le Flem. P. Hagenmuller. J. Sol. Stat. Chem. **38**, 34-9. (1981)

17   J.C. Bouloux, J.L. Soubeyroux, G. le Flem. P. Hagenmuller. J. Sol. Stat. Chem. **85**, 321-5. (1990)

18   R.J. Birgeneau, H.J. Guggenheim, G. Shirane. Phys. Rev. Lett. **22**, 720. (1969)

19   R. Navarro, J.J. Smit, L.J. de Jongh, W.J. Crama, D.J.W. Ijdo. Physica. **83B**, 97. (1976)

CHAPTER 4

The Effect of Oxygen Stoichiometry in the System $Sr_3Fe_2O_{7-y}$ ($0 \leq y \leq 1$)

4.1 Introduction

The system $Sr_3Fe_2O_{7-y}$ was first investigated by MacChesney et al (1). No structural characterisation of the phases was performed in this study although cell parameters, based on the Ruddlesden-Popper phase $Sr_3Ti_2O_7$ (2), were derived. A structural study on this system was performed by Lucchini et al (3) on a compound with stoichiometry $Sr_3Fe_2O_{6.16}$. Lucchini (3) derived atomic coordinates and structural parameters for a unit cell with a c parameter double that of $Sr_3Ti_2O_7$ using x-ray data.

Magnetic effects observed in the system (1) were not definitively understood; $Sr_3Fe_2O_6$ is antiferromagnetically ordered at 298K; increasing the oxygen content, and therefore the Fe^{4+} concentration, results in a rapid decrease in the Néel temperature approaching 0K at $Sr_3Fe_2O_{6.5}$. As the oxygen content is further increased, the Néel temperature begins to rise to a value of 130K for $Sr_3Fe_2O_{6.91}$. This unusual magnetic behaviour was explained in terms of a weak Fe^{4+} - O^{2-} - Fe^{4+} ferromagnetic exchange interaction together with a strong Fe^{3+} - O^{2-} - Fe^{3+} interaction. No account was taken of the effect of changing oxygen stoichiometry or alterations in the iron positions on coupling between the iron centres.

Mössbauer measurements were indicative of a mixed valence phase although application of a Fe^{3+}/Fe^{4+} model to estimate oxygen stoichiometries gave poor agreement with analytically determined oxygen contents. Mössbauer parameters, assumed to belong to Fe^{4+} (δ = -0.01), were unusually low for typical tetravalent iron (4).

This study presents the determination of the structure of $Sr_3Fe_2O_{7-y}$ using powder diffraction techniques for four different values of y covering the full oxygen stoichiometry range. Accurate determination of atomic positions and temperature factors was performed using powder neutron diffraction data from HRPD and D1A. A low temperature study was performed using variable temperature neutron diffraction, on POLARIS, to investigate changes in structure and magnetic ordering behaviour. Oxygen content was determined by both thermogravimetric analysis and by the refinement of oxygen occupancies using neutron diffraction data. Magnetic and electrical behaviour was monitored using vibrating sample magnetometry and four probe resistivity. Mössbauer measurements were performed from room temperature down to 4.2K. The oxidation state of the iron ions were derived by comparison with other Mössbauer studies on iron(IV) materials. Oxygen

stoichiometries were calculated from the derived Mössbauer parameters and compared with the analytically determined values.

4.2 Experimental

A sample of $Sr_3Fe_2O_{7-y}$ was synthesised by direct reaction of $SrCO_3(99.5\%)$ and $Fe_2O_3(99.99\%)$ mixed thoroughly together in the correct molar proportions and heated at 1100°C in air for 16h and after regrinding, for a further 16h at 1300°C. Samples of this compound were then treated further to control the oxygen stoichiometry as shown in Table 4.1

Table 4.1 Annealing Treatment

Annealing Treatment	Oxygen Stoichiometry	Lattice Parameters	
		a/Å	c/Å
700°C/5%H$_2$/N$_2$ for 24 hrs Slow cooled 20°/min	6.00±0.05	3.892(1)	20.030(4)
Air Annealed at 482°C for 3 days Quenched	6.58±0.05	3.874(1)	20.171(6)
O$_2$ Annealed at 482°C for 3 days Slow cooled 20°/min	6.75±0.05	3.868(1)	20.164(4)
500atm O$_2$/ 500°C for 24hrs	7.00±0.05	3.853(1)	20.151(4)

Powder x-ray diffraction showed all products to be single phase. Oxygen contents were determined using thermogravimetric analysis under 5%H$_2$/N$_2$ in platinum crucibles to 750°C. These analytically determined stoichiometries are used to describe the compounds hereafter.

Compounds prepared at high temperature (c.a.1300°C) and quenched to room temperature were found to be extremely sensitive to atmospheric moisture. Decomposition could be observed in the powder x-ray diffraction pattern by the emergence of a peak at 2.19°, 2θ, corresponding to a c parameter approximately double that of $Sr_3Fe_2O_{7-y}$ phases and also by rapid efflorescence. No sign of a doubled unit cell, as used by Lucchini (3) in their x-ray data analysis, was found except in samples which had decomposed.

4.3 Powder Neutron Diffraction

Powder neutron diffraction data for structure refinement were collected using HRPD and D1A. Data from the parent material synthesised in air was collected on D1A at the (ILL) whilst data from the other three stoichiometries were obtained on HRPD at the Rutherford Appleton Laboratories (RAL). Data collection times ranged from 10-20hrs and final profiles were of excellent quality. Full profile refinements were carried out using the Rietveld technique (5). Data were collected in each case at room temperature for structure refinement. $Sr_3Fe_2O_6$ is below its Néel temperature at 298K and so some contribution to the scattered intensity from the magnetic structure may be expected. However the maximum d-spacing data used from HRPD for structure refinement was 2.2Å where magnetic scattering is weak and, in general, can be neglected.

The magnetic structures of these materials were studied using POLARIS for x = 0.0 and 1.0 and LAD for x = 0.42 and 0.25. For $Sr_3Fe_2O_7$ data were collected, below the Néel temperature of 110K, at 90K on POLARIS and at 6K on HRPD. The POLARIS data were collected solely for the purpose of scrutinising the high d-spacing data. High d-spacing data were collected on $Sr_3Fe_2O_6$ at 120K on POLARIS which is below the Néel temperature of 550K. LAD data were collected for the intermediate valence materials at several temperatures between room temperature and 4.2K. Differences in the lattice parameters at room temperature, below the Néel temperature and at near liquid helium temperature, are summarised in Table 4.2.

4.4 Mössbauer Spectroscopy

The Mössbauer spectra were obtained with a conventional transmission spectrometer using

91

a double ramp waveform to give a flat background. Absorbers were prepared of finely

Table 4.2 Changes in Lattice Parameters with Temperature (Å)

	$Sr_3Fe_2O_7$ T_N = 110K	$Sr_3Fe_2O_{6.75}$ T_N = 60K	$Sr_3Fe_2O_{6.58}$ T_N = 20K	$Sr_3Fe_2O_{6.00}$ T_N = 550K
300K	3.8526(1) 20.1490(1)	3.8642(1) 20.1569(1)	3.8704(1) 20.1763(3)	3.8940(1) 20.0396(1)
Below T_N	3.8523(1) 20.1651(1)	3.8599(2) 20.1430(2)	3.8614(2) 20.1420(3)	
He(l) Temp	3.8424(1) 20.1148(2)	3.8540(2) 20.1229(3)	3.8604(1) 20.1417(2)	

ground iron samples weighed to give optimum signal to noise (4) and mixed with boron nitride to randomise the orientations of the microcrystals. Sources of up to 100mCi of ^{57}Co in Rh were used and the spectrometers were calibrated using α-iron at 300K. Mössbauer spectra were recorded above and below the Néel temperature which required heating in the case of $Sr_3Fe_2O_6$. Permanent changes in the spectra caused by cooling and returning to room temperature were noted for the intermediate valence materials.

4.5 Magnetic and Electrical Measurements

The V.S.M. was used to measure the Néel temperature of the pure Fe^{4+} material and for the determination of the number of unpaired electrons. Magnetic ordering behaviour was studied by cooling with, and without, the magnetic field of 0.05T. Electronic behaviour was investigated using the four probe method.

4.6 Results and Discussion

Structure Refinements

Careful scrutiny of all the sets of data in the high d-spacing range showed no evidence of the doubled unit cell described by Lucchini (3), and all peaks could be indexed in the space group I4/mmm using the cells given in Table 4.1. In each case the structural parameters of $Sr_3Ti_2O_7$ were used as a starting model. Initial stages of the refinement included profile parameters such as scale factor, cell parameter, background and peak shape functions. Atomic positions were then refined. In the case of the materials with oxygen stoichiometry below seven refinement of oxygen site occupancies rapidly located the vacancies on the O3 site (2a;0,0,0) and showed that all other oxide ion sites were fully occupied. Full occupancy of the other sites was maintained throughout the rest of the refinement; in the analysis of the $Sr_3Fe_2O_6$ data the O3 site was removed from the refinement. Final stages of the refinement included isotropic temperature factors for $Sr_3Fe_2O_{6.58}$ and $Sr_3Fe_2O_{6.75}$ but anisotropic temperature proved refinable for $Sr_3Fe_2O_6$ and $Sr_3Fe_2O_7$. A typical final fit to the data from HRPD is shown in Figure 4.1. Tables 4.3a-d contain refined parameters for all four compounds, with their e.s.d.s given in parentheses, and final profile fit factors. For compounds where anisotropic temperature factors were refined $B_{equivalent}$ (6) values are given in the tables. Calculated bond distances are summarised in Table 4.4. In the mixed valence materials $Sr_3Fe_2O_{6.58}$ and $Sr_3Fe_2O_{6.75}$, the refined oxygen stoichiometries were in close agreement to the chemically analysed values of 6.64(3) and 6.74(2) respectively.

Figure 4.2 shows the variation of the lattice parameters in this system as a function of oxygen stoichiometry. The very accurate values from the neutron work were in excellent agreement with those from the powder x-ray results. The a parameter shows a linear decrease with diminishing y in $Sr_3Fe_2O_{7-y}$ as would be expected from the higher level of the smaller Fe^{4+} ion in these compounds. The a parameter is simply controlled by the Fe - O - Fe distance between the corner sharing octahedra. The c parameter behaviour is more complex. As the oxygen content rises above six a rapid increase in the c parameter occurs and a maximum is found with y $\approx$ 0.5, beyond this value the c lattice parameter contracts, though more slowly, as a function of the oxygen stoichiometry.
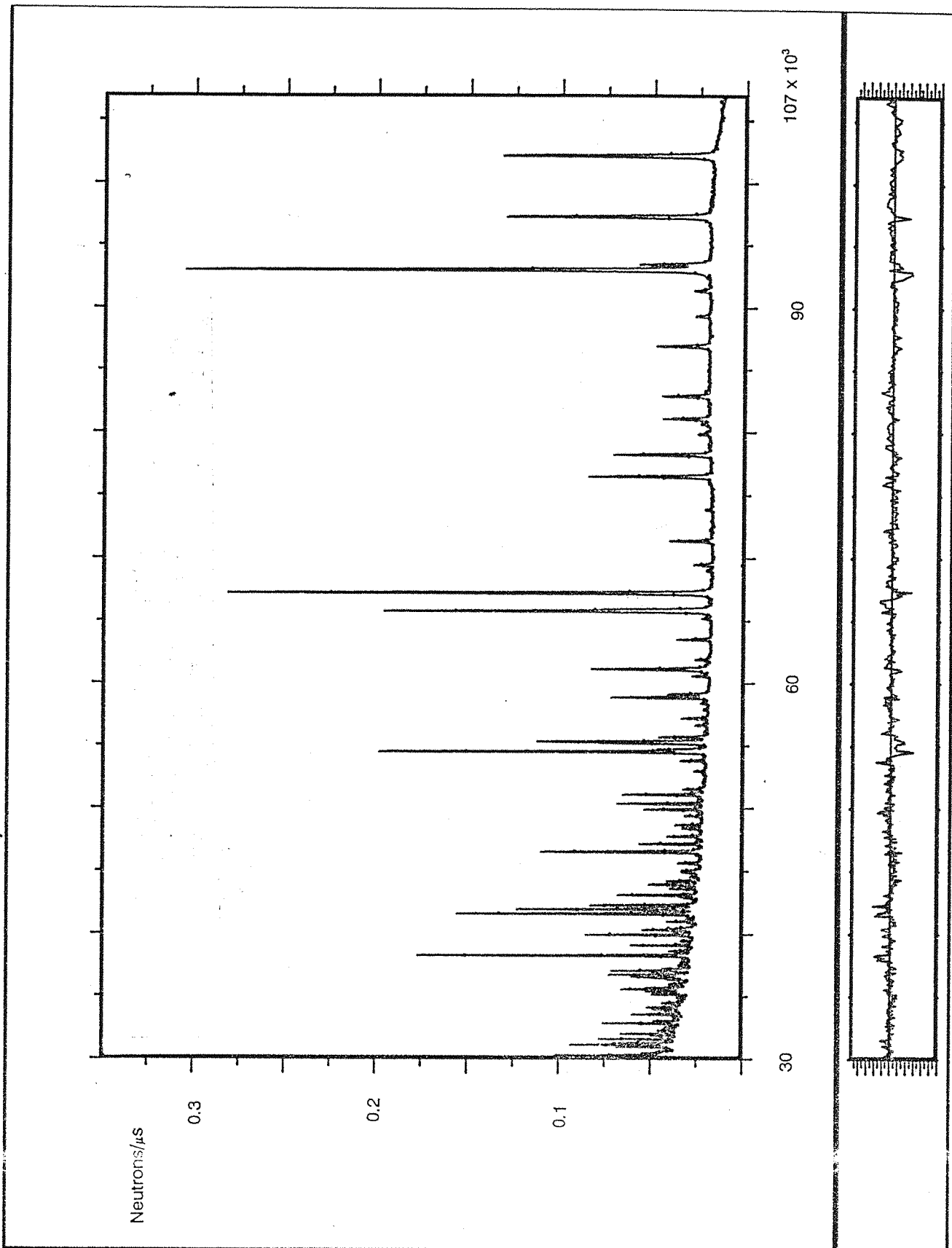
Figure 4.1 Profile fit to the HPRD data set for $Sr_3Fe_2O_7$.

Table 4.3a Refined Atomic Parameters for $Sr_3Fe_2O_{6.00}$

Atom	Site	x	y	z	B_{eq}	Occupancy
Sr(1)	2b	0	0	½	0.11(5)	1.00
Sr(2)	4e	0	0	0.3193(1)	0.27(3)	1.00
Fe	4e	0	0	0.1022(1)	0.01(2)	1.00
O(1)	8g	0	½	0.0843(1)	0.32(3)	1.00
O(2)	4e	0	0	0.1963(1)	0.44(4)	1.00
O(3)	-	-	-	-	-	-

a = 3.8940(1)   c = 20.0396(1)

R_{wp} = 6.99 R_{exp} = 6.15 χ^2 = 1.29

Table 4.3b Refined Atomic Parameters for $Sr_3Fe_2O_{6.58}$

Atom	Site	x	y	z	B_{eq}	Occupancy
Sr(1)	2b	0	0	½	0.81(5)	1.00
Sr(2)	4e	0	0	0.3176(1)	1.22(2)	1.00
Fe	4e	0	0	0.0972(1)	0.75(3)	1.00
O(1)	8g	0	½	0.0911(1)	1.24(4)	1.00
O(2)	4e	0	0	0.1950(1)	1.35(5)	1.00
O(3)	2a	0	0	0	0.98(4)	0.64(3)

a = 3.8704(1)   c = 20.1763(3)

R_{wp} = 8.48 R_{exp} = 4.51 χ^2 = 3.53

Table 4.3c Refined Atomic Parameters for $Sr_3Fe_2O_{6.75}$

Atom	Site	x	y	z	B_{eq}	Occupancy
Sr(1)	2b	0	0	½	0.41(2)	1.00
Sr(2)	4e	0	0	0.3175(1)	0.14(1)	1.00
Fe	4e	0	0	0.0984(1)	0.00(1)	1.00
O(1)	8g	0	½	0.0922(1)	0.51(1)	1.00
O(2)	4e	0	0	0.1942(1)	0.43(2)	1.00
O(3)	2a	0	0	0	0.15(6)	0.74(2)

$a = 3.8642(1)$ $c = 20.1569(1)$

$R_{wp} = 6.56$ $R_{exp} = 3.61$ $\chi^2 = 3.30$

Table 4.3d Refined Atomic Parameters for $Sr_3Fe_2O_{7.00}$

Atom	Site	x	y	z	B_{eq}	Occupancy
Sr(1)	2b	0	0	½	0.47(5)	1.00
Sr(2)	4e	0	0	0.3170(1)	0.31(4)	1.00
Fe	4e	0	0	0.0972(1)	0.22(3)	1.00
O(1)	8g	0	½	0.0945(1)	0.55(3)	1.00
O(2)	4e	0	0	0.1933(1)	0.63(5)	1.00
O(3)	2a	0	0	0	0.61(7)	1.00

$a = 3.8526(1)$ $c = 20.1490(1)$

$R_{wp} = 5.41$ $R_{exp} = 5.22$ $\chi^2 = 1.07$

Table 4.4 Important Bond Lengths for $Sr_3Fe_2O_{7-y}$ (Å)

	$Sr_3Fe_2O_{6.00}$	$Sr_3Fe_2O_{6.58}$	$Sr_3Fe_2O_{6.75}$	$Sr_3Fe_2O_7$
Sr(1)-O(1)	2.578(1) x 8	2.669(1) x 8	2.681(1) x 8	2.709(2) x 8
Sr(1)-O(3)	-	2.737(-) x 4[a]	2.732(-) x 4[a]	2.724(-) x 4
Sr(2)-O(1)	2.743(3) x 4	2.672(2) x 4	2.655(2) x 4	2.625(3) x 4
Sr(2)-O(2)	2.464(4) x 1	2.473(3) x 1	2.485(4) x 1	2.493(3) x 1
Sr(2)-O(2)	2.771(1) x 4	2.748(1) x 4	2.743(1) x 4	2.732(1) x 4
Fe-O(1)	1.980(1) x 4	1.942(1) x 4	1.936(1) x 4	1.927(1) x 4
Fe-O(2)	1.886(4) x 1	1.933(2) x 1	1.932(4) x 1	1.936(4) x 1
Fe-O(3)	-	2.002(2) x 1[a]	1.983(2) x 1[a]	1.958(2) x 1

[a]   Partially filled site.
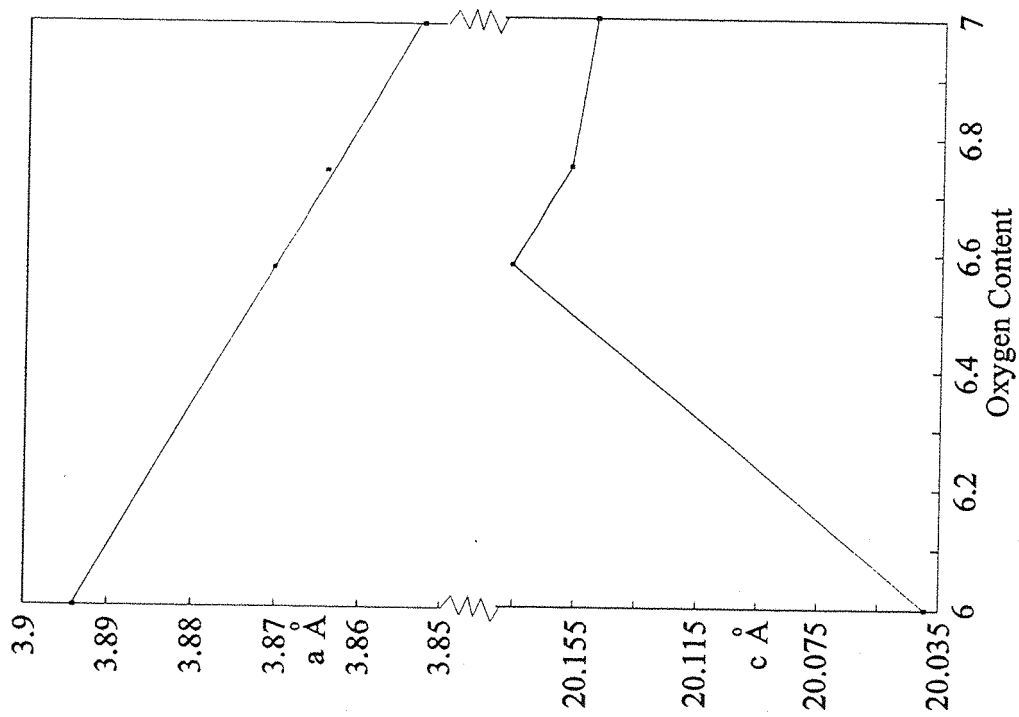
Figure 4.2 Change in Lattice Parameters with Oxygen Content (298K)
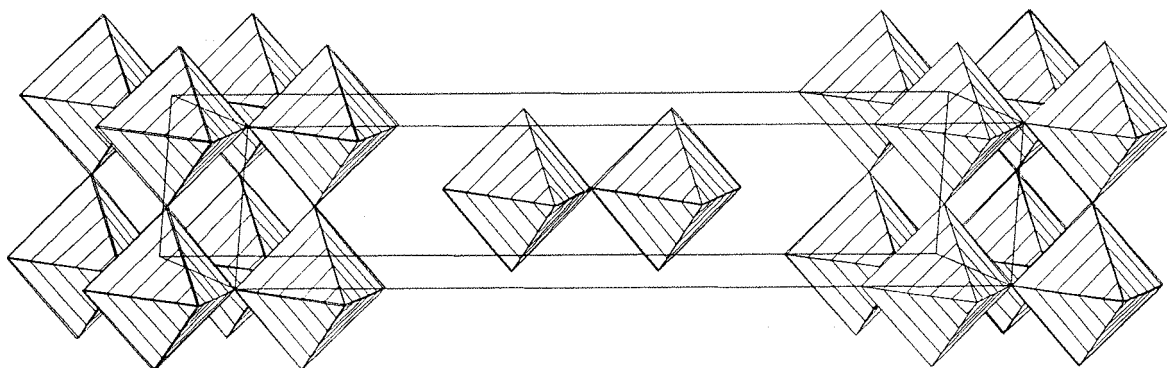
Figure 4.3 STRUPLO (7) plot of $Sr_3Fe_2O_7$

98

The variation of c with oxygen content is similar to that observed by MacChesney (8) although the values reported here are slightly higher. This behaviour can be explained in terms of the site occupied by the oxygen O3 (0,0,0). Figure 4.3 represents a STRUPLO (7) plot of $Sr_3Fe_2O_7$ showing the FeO_6 octahedra. In $Sr_3Fe_2O_6$ the oxygen linking the pairs of octahedra O3 in the c direction is absent. This gives rise in $Sr_3Fe_2O_6$ to a square pyramidal iron coordination geometry where the distance between the faces of the square pyramids is 3.38Å which is considerably less than twice a typical Fe^{3+} - O (1.95Å) or Fe^{4+} - O (1.90Å) distance. Addition of oxygen to the O3 site, between the two pyramids, therefore requires a considerable expansion along c, together with displacements of the relative iron and O3 positions, to form a more regular geometry around the metal atom.

The changes in the iron coordination geometry as the oxygen level increases is quite marked. In $Sr_3Fe_2O_6$ the trivalent iron atom has a square based pyramidal coordination which is rather rare for this ion in oxides, though is reasonably common for iron coordination complexes (9). The Fe - O distances for the four basal plane oxygens are typical for Fe^{3+} whilst the apical iron oxygen distance is very short. Bond valence calculations (10) on this site using the parameters for Fe^{3+} gave a reasonable calculated iron valence of 2.91. Introduction of oxygen on the O3 site obviously occurs randomly throughout the structure and, therefore, the refined coordinates in the mixed valence materials represent an average over the bulk. For iron this probably means an average of Fe^{3+} coordinated to five oxygens and Fe^{4+} coordinated to six oxygens is observed. This is reflected in a gradual increase in the iron to apical oxygen distance as the proportion of higher coordinate iron rises. On reaching $Sr_3Fe_2O_7$, the iron coordination geometry becomes an almost regular octahedron, with a slight axial distortion similar to that found in Sr_2FeO_4 (11).

The structural behaviour of this system as a function of oxygen content shows similar aspects to that seen in $La_2SrCu_2O_{6\pm y}$ system, but extends over a much larger stoichiometry range. In the $Sr_3Fe_2O_{7-y}$ system as the level of oxygen increases the coordination geometry of Sr(1) increases from 8 to 12; the average Sr(1) - O distances naturally increases. This shows that with strontium (or indeed the similar sized La^{3+}) on an inter - $(MO)_{3n}$ - layer site incorporation of oxygen between these planes with oxidation is facile. This is the likely reason why compounds which contain moderately large ions between Cu - O planes are not superconducting or show degraded superconducting

behaviour e.g. La_2SrCuO_6, $NdBa_2Cu_4O_8$ or $LaBa_2Cu_3O_7$.

Low Temperature Neutron Diffraction Study

The final fit factors obtained for the refinement of the $Sr_3Fe_2O_7$ data set at 6K were excellent giving a value of χ^2 of 1.10. This strongly supports the conclusion that this material does not undergo a structural distortion on cooling below the Néel Temperature of 110K. The refinement profile is shown in Figure 4.4. Bond lengths were in excellent agreement with those derived from the room temperature refinement and are compared in Table 4.5. A comparison of the refinement parameters at room temperature, 90K and 6K is summarised in Table 4.6. Variations in the atomic coordinates and cell parameters as a function of temperature were very small. At low temperature the refined temperature factors for the in-plane oxygen O1 $(0,\frac{1}{2},z)$ showed some anisotropy with B_{11} and B_{22} temperature factors of similar magnitude and B_{33} considerably larger.

Data collected at 90K from $Sr_3Fe_2O_7$ in the POLARIS A bank could be indexed totally on the crystallographic unit cell except for a weak feature at 4.6Å. This pattern (Figure 4.5) can be contrasted with that collected from $Sr_3Fe_2O_6$ during the same experimental period. High d-spacing data collected at 120K on POLARIS is shown in Figure 4.6. Magnetic reflections which were indexed as (101), (102), (103) and (104) on a magnetic supercell of dimensions $\sqrt{2}a$ x $\sqrt{2}a$ x c are indicated and are characteristic of three-dimensional magnetic ordering behaviour. Similar reflections are not present in the $Sr_3Fe_2O_7$, which suggests that this compound is not magnetically ordered in three-dimensions at 90K. The observed Néel temperature, therefore, must be indicative of another type of magnetic ordering behaviour. This is confirmed by the appearance of the saw-toothed reflection at 4.6Å which is characteristic of two-dimensional magnetic ordering behaviour. As previously noted for Sr_2FeO_4, coupling between planes in pseudo-two-dimensional structures such as $Sr_3Fe_2O_7$ cannot proceed via a superexchange mechanism and is, therefore, considerably weaker than the in-plane interactions (12). This quantity depends upon a number of factors such as the interplane separation and dipolar coupling constants. The antiferromagnetic coupling which is present in $Sr_3Fe_2O_6$ (Fe^{3+}) occurs despite an almost identical structure and, hence, separation between FeO_2 layers.
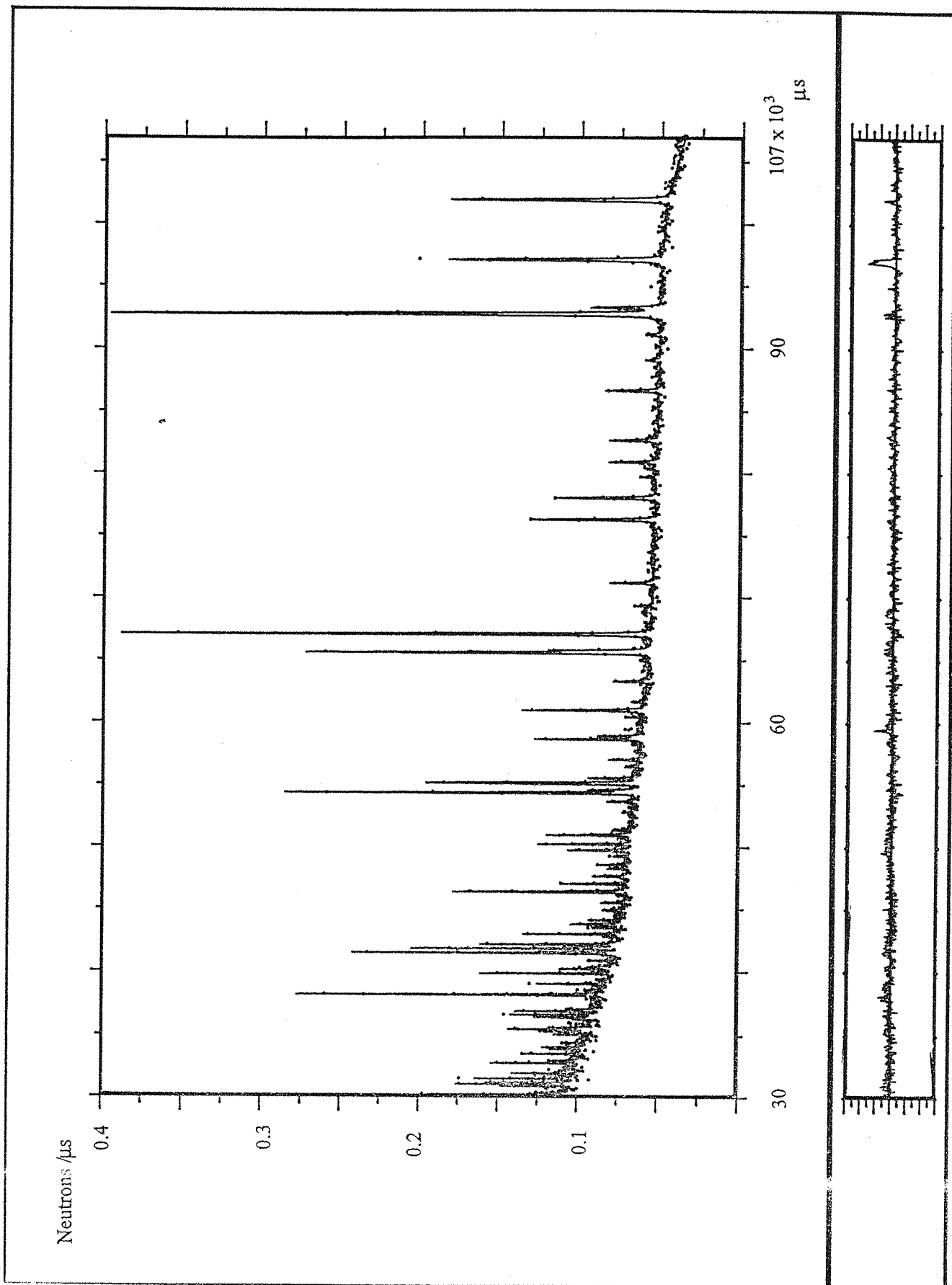
Figure 4.4 Refinement Profile of $Sr_3Fe_2O_7$ at 6K on HRPD

Table 4.5 Refined Atomic Parameters for $Sr_3Fe_2O_7$

Cell Parameters (Å)			300K (HRPD) $a = 3.8526(1)$ $c = 20.1490(1)$		90K (POLARIS) $3.8523(1)$ $20.1651(1)$		6K (HRPD) $a = 3.8424(1)$ $c = 20.1148(2)$	
Atom	x	y	z	B_{11}, B_{22}, B_{33}	z	B_{11}, B_{22}, B_{33}	z	B_{11}, B_{22}, B_{33}
Sr1	0	0	½	0.44(4),0.44(4),0.54(8)	½	0.21(3),0.21(3),0.39(5)	½	0.25(10),0.25(10),0.28(18),
Sr2	0	0	0.3170(1)	0.27(3),0.27(3),0.40(5)	0.3169(1)	0.13(2),0.13(2),0.19(3)	0.3169(1)	0.04(7),0.04(7),0.53(10),
Fe	0	0	0.0972(1)	0.04(2),0.04(2),0.42(3)	0.0972(1)	0.07(1),0.07(1),0.31(2)	0.0971(1)	0.02(4),0.02(4),0.44(7),
O1	0	½	0.0948(2)	0.43(3),0.39(3),0.82(4)	0.0947(1)	0.24(2),0.36(2),0.42(3)	0.0945(1)	0.31(7),0.40(8),0.61(9),
O2	0	0	0.1933(1)	0.57(4),0.57(4) 0.76(7)	0.1931(1)	0.32(2),0.32(2),0.22(3)	0.1935(2)	0.41(9),0.41(9),0.80(17),
O3	0	0	0	0.65(6),0.65(6),0.51(9)	0	0.43(4),0.43(4),0.80(8)	0	0.37(12),0.37(12),0.37(21),
R_{wp}			5.41%		2.00%		8.51%	
R_{exp}			5.22%		0.78%		8.09%	
χ^2			1.07		6.56		1.10	

Table 4.6 Derived Bond Lengths for $Sr_3Fe_2O_7$ (Å)

Atom1 - Atom2	RT	90K	4.2K
Sr1 - O1	2.709(2)	2.712(2)	2.709(3)
Sr1 - O3	2.724(4)	2.724(3)	2.717(3)
Sr2 - O1	2.625(3)	2.624(3)	2.617(5)
Sr2 - O2	2.493(3)	2.496(2)	2.481(5)
Sr2 - O2	2.732(1)	2.731(1)	2.725(1)
Fe - O1	1.927(1)	1.927(1)	1.922(1)
Fe - O2	1.936(4)	1.933(5)	1.940(5)
Fe - O3	1.958(2)	1.960(2)	1.952(3)

103
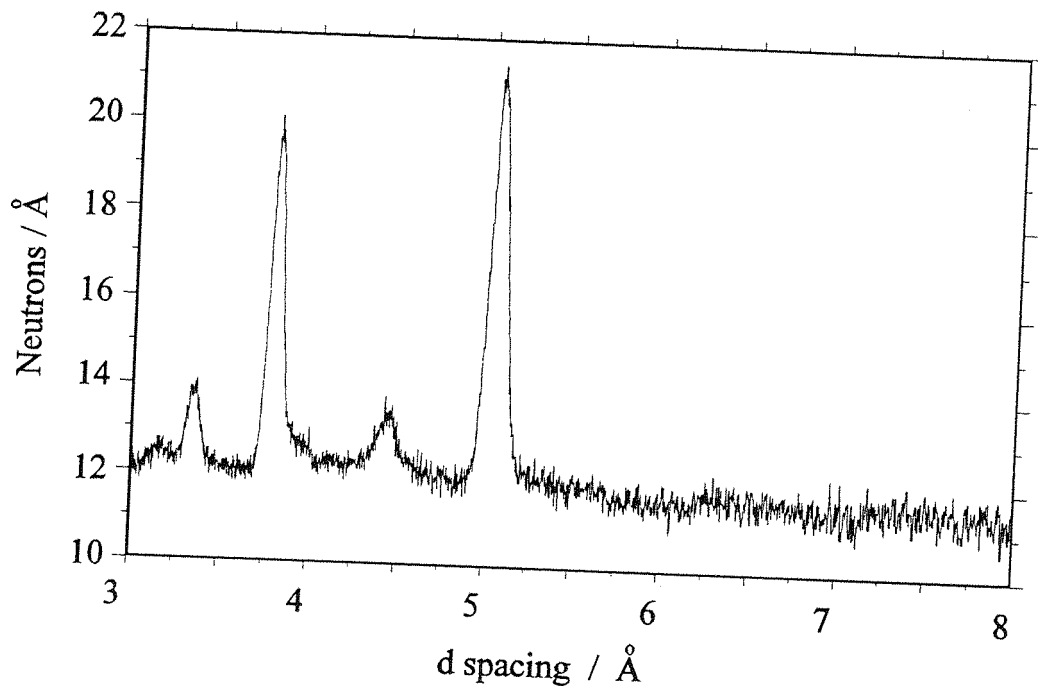
Figure 4.5 POLARIS A Bank Data for $Sr_3Fe_2O_7$
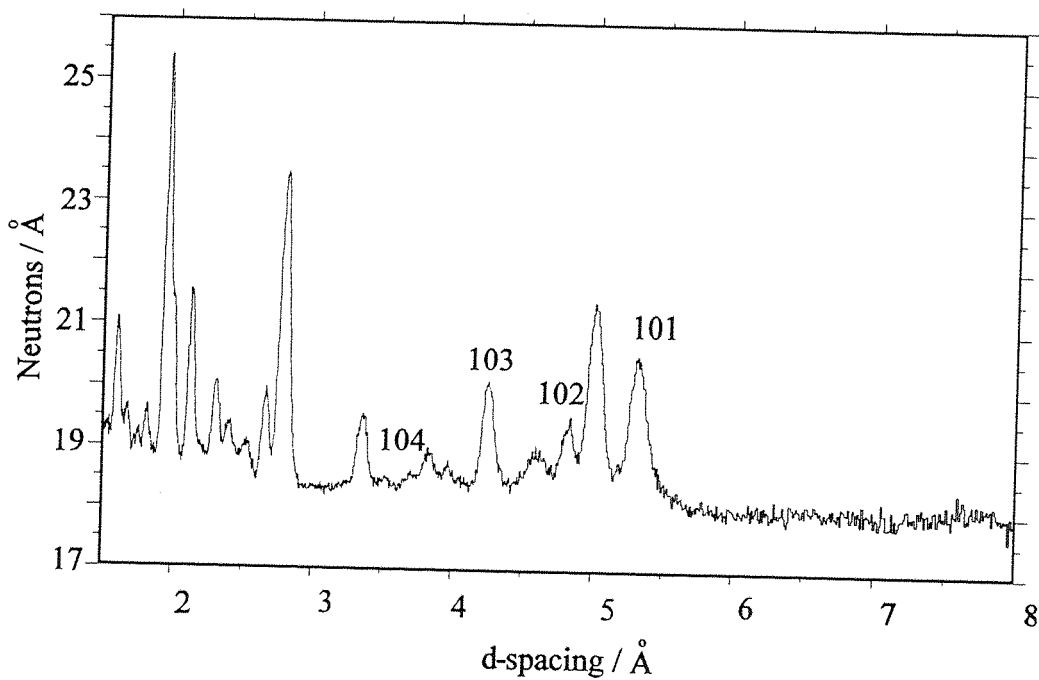
Figure 4.6 POLARIS A Bank Data for $Sr_3Fe_2O_6$

Mössbauer Measurements

Mössbauer spectra of $Sr_3Fe_2O_7$ taken at 300K and 4.2K are shown in Figures 4.7 and 4.8 respectively. The parameters of the fits are listed in Table 4.7 with those of $CaFeO_3$ (12) for comparison. It is seen that the 300K spectrum requires two components for a good fit. The fit shown corresponds to one of several hypotheses that give equally good representations of the spectrum. This particular hypothesis is chosen as the components can be identified as two distinct charge states whose parameters are consistent with assignments of Fe^{3+} and Fe^{5+} and where the equal intensities of these components agree with the chemically determined oxygen content. The averaged values of the isomer shift of these two components $\delta = 0.07$ is equal to that measured at 300K for $CaFeO_3$, a compound that shows Fe^{3+}/Fe^{5+} disproportionation at lower temperatures (12).

The spectrum at 4.2K can be well fitted with two magnetic sextet components of equal intensity whose parameters are consistent with the assignments of Fe^{3+} and Fe^{5+}. These parameters are almost identical with those observed at 4.2K for $CaFeO_3$ (12). It is thus shown that in $Sr_3Fe_2O_7$ charge disproportionation exists above the antiferromagnetic ordering temperature. For the samples with y = 0.42 and 0.25, Mössbauer spectra were collected using similar conditions. However, unlike $Sr_3Fe_2O_7$ and $Sr_3Fe_2O_6$, the spectra on cooling to 4.2K and heating back to 300K were not consistent. The permanent change observed in the Mössbauer spectra is thought to be due to decomposition of the samples in the timescale of the experiment. The Mössbauer spectra of $Sr_3Fe_2O_6$ at room temperature and above its Néel temperature of 550K are shown in Figure 4.9 and 4.10 respectively. The low temperature spectrum consists of a single antiferromagnetically split sextet whilst the high temperature spectrum is a quadrupole split doublet. The latter is consistant with the electronically asymmetric environment produced by a square pyramidal field.

Susceptibility Data

Figure 4.11 reproduces the susceptibility data from $Sr_3Fe_2O_7$ with, and without a magnetic field of 0.05T. The derived variation $1/\chi$ as a function of temperature is shown in Figure 4.12. The spectra show antiferromagnetic ordering behaviour with a Néel temperature of
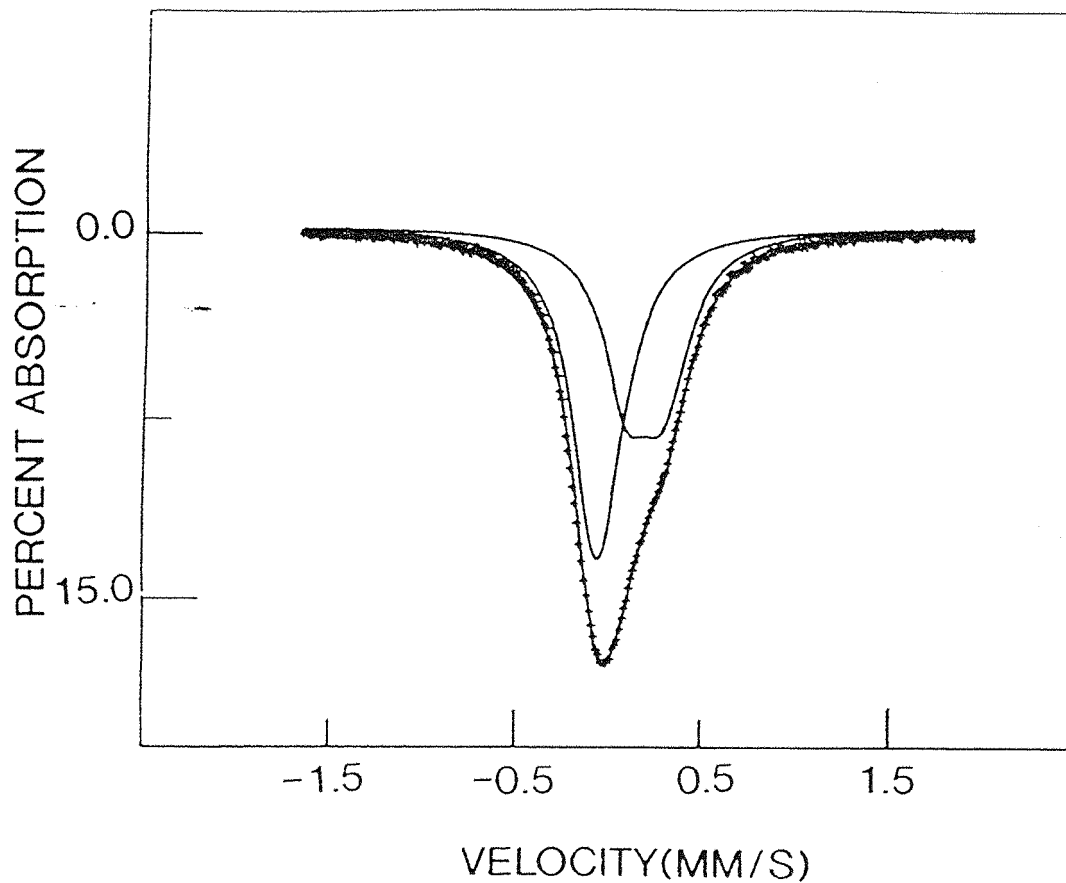
Figure 4.7 Mössbauer Spectrum of $Sr_3Fe_2O_7$ at 300K
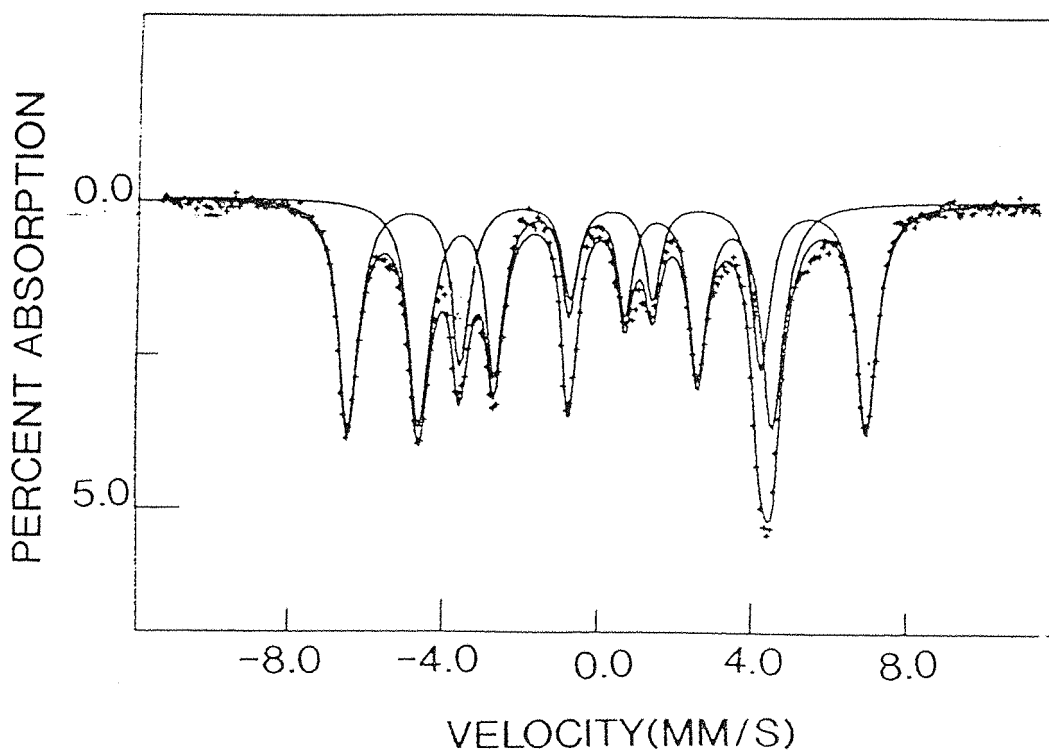
Figure 4.8 Mössbauer Spectrum of $Sr_3Fe_2O_7$ at 4.2K

106

Table 4.6 Mössbauer Parameters of $Sr_3Fe_2O_{7-y}$, $y = 0$.

	CaFeO$_3$[11]	Sr$_3$Fe$_2$O$_7$
Symmetry	Tetragonal	Tetragonal
Cell Parameters (Å)	a = 5.325 c = 7.579	a = 3.853 c = 20.149
T$_{N\acute{e}el}$	115K	110K
μ_{eff}	4.9BM	5.3BM
300K Mössbauer Parameters	C.S. 0.07mms^{-1}	1) 50% 0.20mms^{-1}, Q.S. =0.20mms^{-1} 2) 50% C.S. -0.06mms^{-1}
4.2K Mössbauer Parameters	1) 50% C.S. 0.34mms^{-1}, Hi 416kG 2) 50% C.S. 0.17mms^{-1}, Hi 279kG	1) 50% C.S. 0.32mms^{-1}, Hi = 417kG, Q.S.-0.07mms^{-1} 2) 50% C.S. -0.06mms^{-1}, Hi 283kG

107
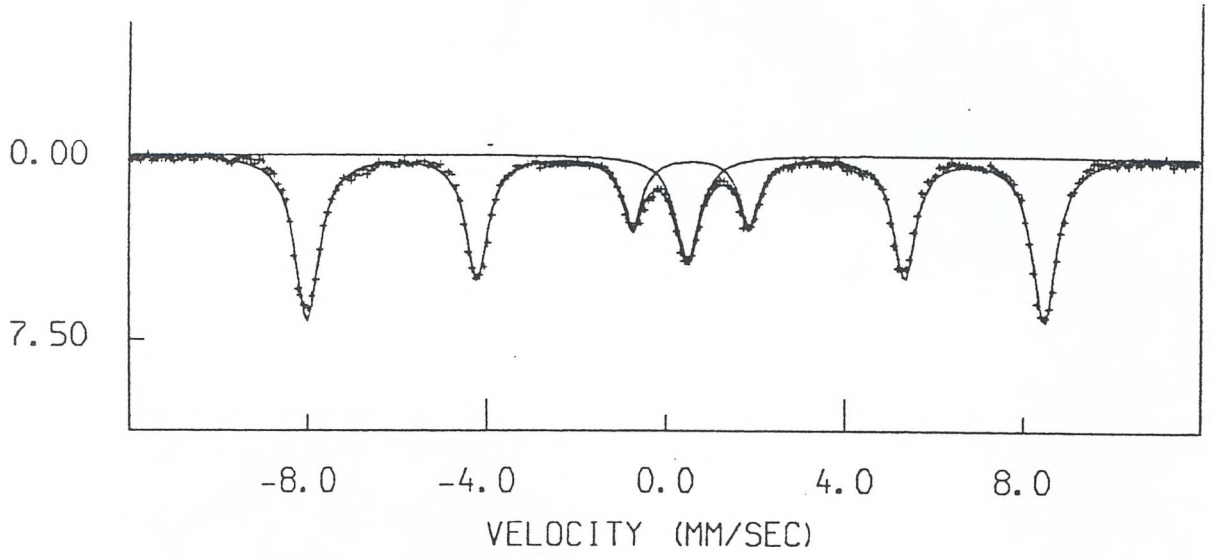
Figure 4.9 Mössbauer Data For $Sr_3Fe_2O_6$ at 300K
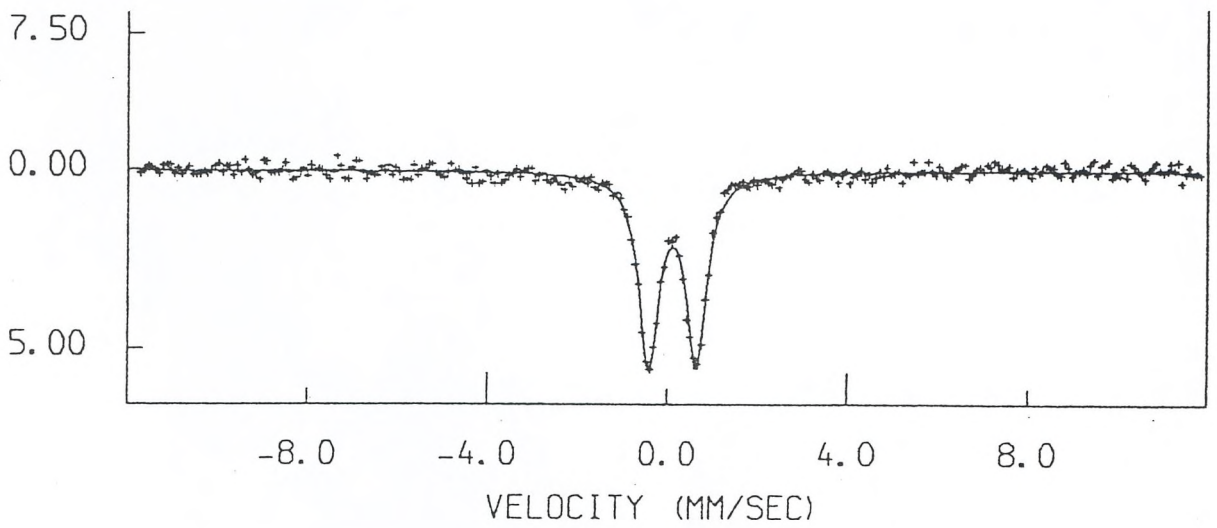
Figure 4.10 Mössbauer Spectrum of $Sr_3Fe_2O_6$ at 550K

108
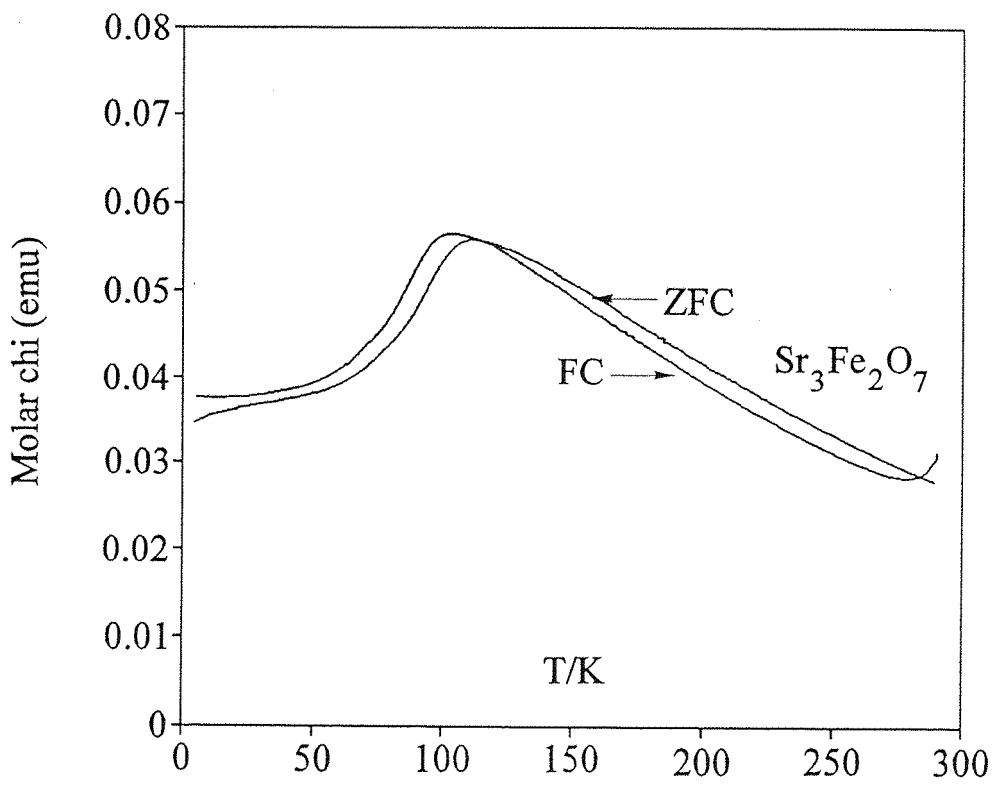
Figure 4.11 Magnetic Susceptibility of $Sr_3Fe_2O_7$
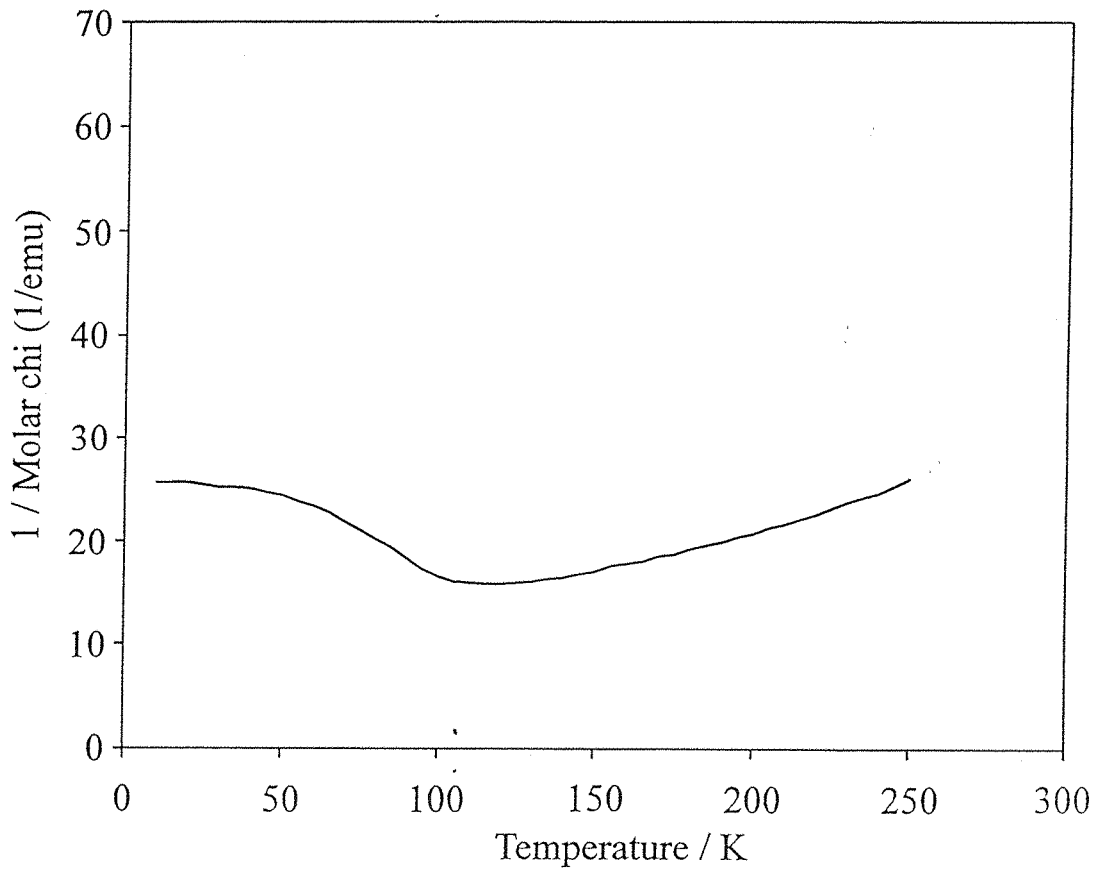
Figure 4.12 $1/\chi$ against Temperature for $Sr_3Fe_2O_7$

109

110K. The value obtained from $Sr_3Fe_2O_7$ is similar to that obtained by MacChesney (1) from the compound he described as $Sr_3Fe_2O_{6.9}$. This suggests the phase studied by MacChesney was probably not oxygen deficient. The derived magnetic moment was 5.3BM supporting the description of $Sr_3Fe_2O_7$ as a high spin d^4 material. The data above T_N can be fitted using a Curie Weiss law $\chi = C/T\text{-}\theta$ and fitting of the $1/\chi$ data above 200K gives a value of θ value of -15 suggesting a typical antiferromagnet. The high value of μ_{eff} and the differing behaviour with, and without an external field, may indicate possible ferromagnetic interactions in the FeO_2 planes.

4.7 Conclusions

The electronic and magnetic behaviour of iron(IV) is clearly very complex, the four ternary phases $SrFeO_3$, Sr_2FeO_4, $Sr_3Fe_2O_7$ and $CaFeO_3$ each showing different behaviour. The charge disproportionation reaction shown by both $CaFeO_3$ and $Sr_3Fe_2O_7$ in the Mössbauer spectra appears to have no structural repercussion in the case of $Sr_3Fe_2O_7$ with almost statistically perfect fits to the diffraction data with a single type of iron site. The ionic radii of Fe^{3+} and Fe^{5+} are markedly different although both ions, in the high spin state, would adopt perfect octahedral site geometry in contrast to Fe^{4+} which may, as a Jahn-Teller ion, be expected to show marked octahedral distortion. Powder x-ray diffraction measurements have, however, not shown any structural distortion in $CaFeO_3$ (13). In formally bismuth (IV) compounds e.g. $BaBiO_3$ (14) the coexistence of Bi^{3+} and Bi^{5+} manifests itself structurally as small differences in the coordination environments of two bismuth sites. Battle (15) has explained co-existence of Fe^{3+} and Fe^{5+} in $Sr_2LaFe_3O_{8.94}$ on crystallographically indistinguishable sites in terms of the coexistence of a spin density wave (SDW) and a charged density wave (CDW). These should manifest themselves in a structural distortion, but the absence of this for $Sr_2LaFe_3O_{8.94}$ was explained as a result of disorder in the strontium/lanthanum lattice. In $Sr_3Fe_2O_7$ no such metal disordering can occur. The apparent difference between the Mössbauer spectra and crystallographic results must lie in the timescale of the experiments. The Mössbauer timescale for ^{57}Fe is about $10^{-8}s$ and an electron pairing mechanism which forms Fe^{3+} and Fe^{5+} must occur slower than this in order to be resolved in the Mössbauer spectrum. Whilst the timescale for neutron diffraction is much shorter $10^{-18}s$ the experiment averages the scattering distribution over

the experimental period. Even a slow electron exchange mechanism producing Fe^{3+} and Fe^{5+} would show an averaged site single Fe^{4+} site. The only evidence to support this process might come from the refined anisotropic temperature factors. The values of B_{11}, B_{22} and B_{33} for the FeO_2 in plane oxygen O1 on $(0,\frac{1}{2},z)$ are respectively 0.31, 0.39 and 0.61Å^2. As this oxygen bridges two iron atoms the values of B_{11} and B_{33} would be expected to be markedly larger than B_{22} with the oxygen atom more freely vibrating perpendicular to the Fe-O-Fe direction. Indeed refined values from $Sr_3Fe_2O_6$ for this site were 0.27, 0.08 and 0.60 respectively. The comparably high value of B_{22} in $Sr_3Fe_2O_7$ would support the idea of some positional disordering of the oxygen along the Fe-O-Fe direction that would be associated with the two arrangements Fe^{3+}-O-Fe^{5+} and Fe^{5+}-O-Fe^{3+}. This view is further strengthened by a similar analysis of the anisotropic temperature factors of O3 and O2; these atoms lie along the z direction and vibrations would be expected to lead to higher values for B_{11} and B_{22} than for B_{33}. Again, however, all three anisotropic temperature factors are similar possibly indicating an attempt to model apical Fe-O distances around both Fe^{3+} and Fe^{5+}.

The magnetic ordering behaviour below the antiferromagnetic ordering temperature of $Sr_3Fe_2O_7$ is rather complex. Presumably the spins in the double layers are aligned antiparallel, as shown schematically in Figure 4.13, as found for the double layer fluorite $Rb_3Mn_2O_7$ (16). The coupling between the layers is obviously weak and no three-dimensional ordering is seen 20K below the Néel temperature. The transformation from a two-dimensional antiferromagnet to a three-dimensional one generally occurs at a lower temperature. For example, in layer structures of the K_2NiF_4 type e.g. two-dimensional ordering occurs at 200K for Ca_2MnO_4 whilst full 3D ordering in a perfect single crystal is not complete until 91.1K (17), between these temperatures no magnetic reflections are observed in the neutron diffraction profile. In other two-dimensional materials e.g. $Ba_2Cu_3O_4Cl_2$ (18) no magnetic reflections are observed in the diffraction pattern between 2K and the Néel temperature, 80K, again indicative of very weak coupling between layers.

Further neutron diffraction experiments would be necessary on $Sr_3Fe_2O_7$ at temperatures below 90K in an attempt to observe a transition to three-dimensional ordering. Dipolar couplings between the layers are stronger in $Sr_3Fe_2O_6$ leading to three dimensional ordering at room temperature, presumably as a consequence of the higher magnetic moment of Fe^{3+}.

111
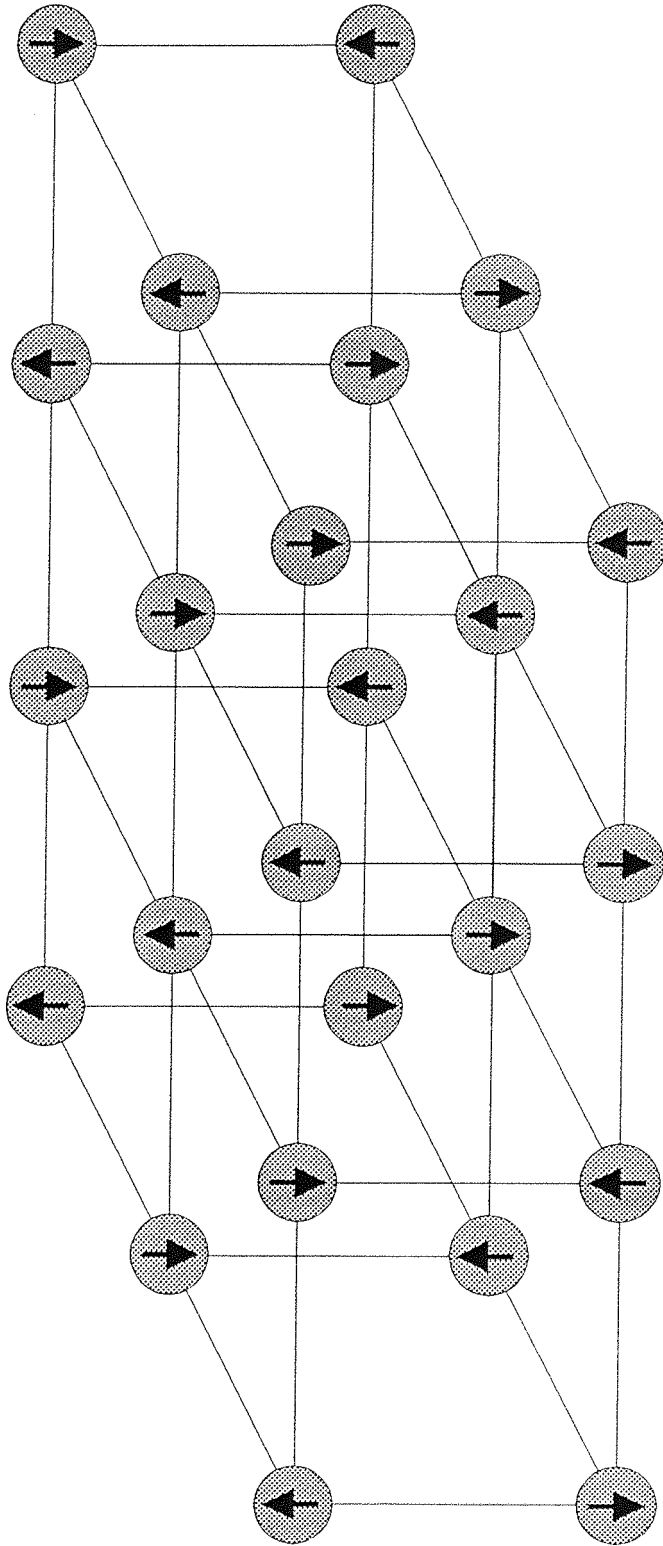
Figure 4.13 Ferromagnetic Ordering in Double Layers

112

4.9 References

1   P.K. Gallagher, J.B. MacChesney, D.N.E. Buchanan. J. Chem. Phys. **45**, 2466-71. (1966)

2   S.N. Ruddlesden, P. Popper. Acta. Cryst. **10**, 538. (1957)

3   E. Lucchini, D. Minichelli, G. Sloccari. Acta. Cryst. **B29**, 2356-7. (1973)

4   G.J. Long, T.E. Cranshaw, G. Longworth. Mössbauer Effect Reference and data Journal. **6**, 42-9. (1980)

5   H.M. Rietveld. Acta. Cryst. **22**, 151, (1967)

6   H.A. Levy. Acta. Cryst. **9**, 679, (1956)

7   R.X. Fischer. J. Appl. Cryst. **18**, 258. (1985)

8   P.K. Gallagher, J.B. MacChesney, D.N.E. Buchanan. Mat. Res. Bull. **1**, 113-22. (1966)

9   F.A. Cotton, G. Wilkenson. Advanced Inorganic Chemistry. **V**, 710. (1988)

10 I.D. Brown, D. Aldermatt. Acta. Cryst. **B41**, 244. (1985)

11 S.E. Dann, D.B. Currie, M.T. Weller. J. Sol. Stat. Chem. **92**, 237-40. (1991).

12 R. Navarro, J.J. Smit, L.J. de Jongh, W.J. Crama, D.J.W. Idjo. Physica. **83B**, 97, (1976)

13 Y. Takeda, Y. Yamaguchi, H. Takei, H. Watanabe. J. Sol. Stat. Chem. **42**, 101. (1977).

14 C. Bruder. Physica C. **693**, 153-5. (1988)

15 P.D. Battle, T.C. Gibb, P. Lightfoot. J. Sol. Stat. Chem. **84**, 271-9. (1990)

16 R. Navarro, J.J. Smit, L.J. de Jongh, W.J. Crama, D.J.W. Ijdo. Physica **83B**, 97. (1976)

17 R.J. Birgeneau, H.J. Guggenheim, G. Shirane. Phys. Rev. Let. **22**, 720. (1969)

18 M. Winklemann, H. Graf, A.W. Hewat. ILL Experimental Reports and Theory College Activities. **195**, 1991. (1992)

CHAPTER 5

Structure and Oxygen Stoichiometry

in the

System $Sr_3Co_2O_{7-z}$ $(0.94 \leq z \leq 1.22)$

5.1 Introduction

In chapter 1 consideration of the energetics of transition metal oxidation demonstrated that strongly oxidising conditions are required to produce stoichiometric cobalt(IV) materials. $SrCoO_3$ was first synthesised as a stoichiometric cubic phase in 1985 by reaction of CoO and $SrCO_3$ using an anvil device and a pressure of 65Kbar with $KClO_3$ as the oxygen source (1). This can be contrasted to $SrFeO_3$ (2) which requires a much lower pressure for synthesis $c.a.$ 800bar. Few other cobalt(IV) compounds are reported in the literature. Mixed valence compounds containing both cobalt(III) and cobalt(IV) are more common; these can be generated, formally from cobalt(IV) compounds, either by doping in trivalent cations e.g. $La_{1-x}Sr_xCoO_3$ (3) or by using low pressure routes to introduce oxygen vacancies e.g. $SrCoO_{2.7}$ (4). All these compounds have formulae and structure based on the perovskite $SrCoO_3$.

Whilst cobalt (IV) compounds are rare, more complex structures containing a tetravalent transition, metal ion, strontium and oxygen (5,6) have been shown to form for iron: for example those crystallising with the K_2NiF_4 (Sr_2FeO_4) (7) and the $Sr_3Ti_2O_7$ ($Sr_3Fe_2O_7$) (8) structures and have been discussed in the previous chapters. The oxidation state of the transition metal cation in these structures can be reduced below four; for example in the Ruddlesden-Popper phase $Sr_3Fe_2O_7$ (Figure 5.1) systematic removal of oxygen from the O3 (0,0,0) site, produces a novel square pyramidal coordination of the trivalent ion when the stoichiometry reaches six, although the symmetry is retained. Higher levels of deficiency can be introduced into the $A_3B_2O_{7-q}$ system. For example, Nguyen et al (9) showed that the compounds, $La_{2-x}Sr_{1+x}Cu_2O_{6\pm y}$ (Ln212), to have a structure derived from $Sr_3Ti_2O_7$ by powder x-ray diffraction studies . When y = 0, the copper atoms in the system have a square pyramidal coordination with four short basal Cu-O bonds and one long apical Cu-O distance with the O3 site vacant. Further oxygen deficiencies in the perovskite layers, ($y \leq 0$), result in two-dimensional CuO_2 planes with removal of oxygen from the O2 (0,0,z) site.

Nguyen extended this work by considering $Ln_{2-x}Sr_{1+x}Cu_2O_{6-y}$ (Ln636) where Ln = Sm, Gd, $0.7 \leq x \leq 0.9$ and Eu, $0.6 \leq x \leq 0.9$ (10) which resulted in semiconducting materials with a threefold superstructure along the b-axis, caused by both cation and oxygen ordering. The other notable attribute was that the oxygen stoichiometry was now
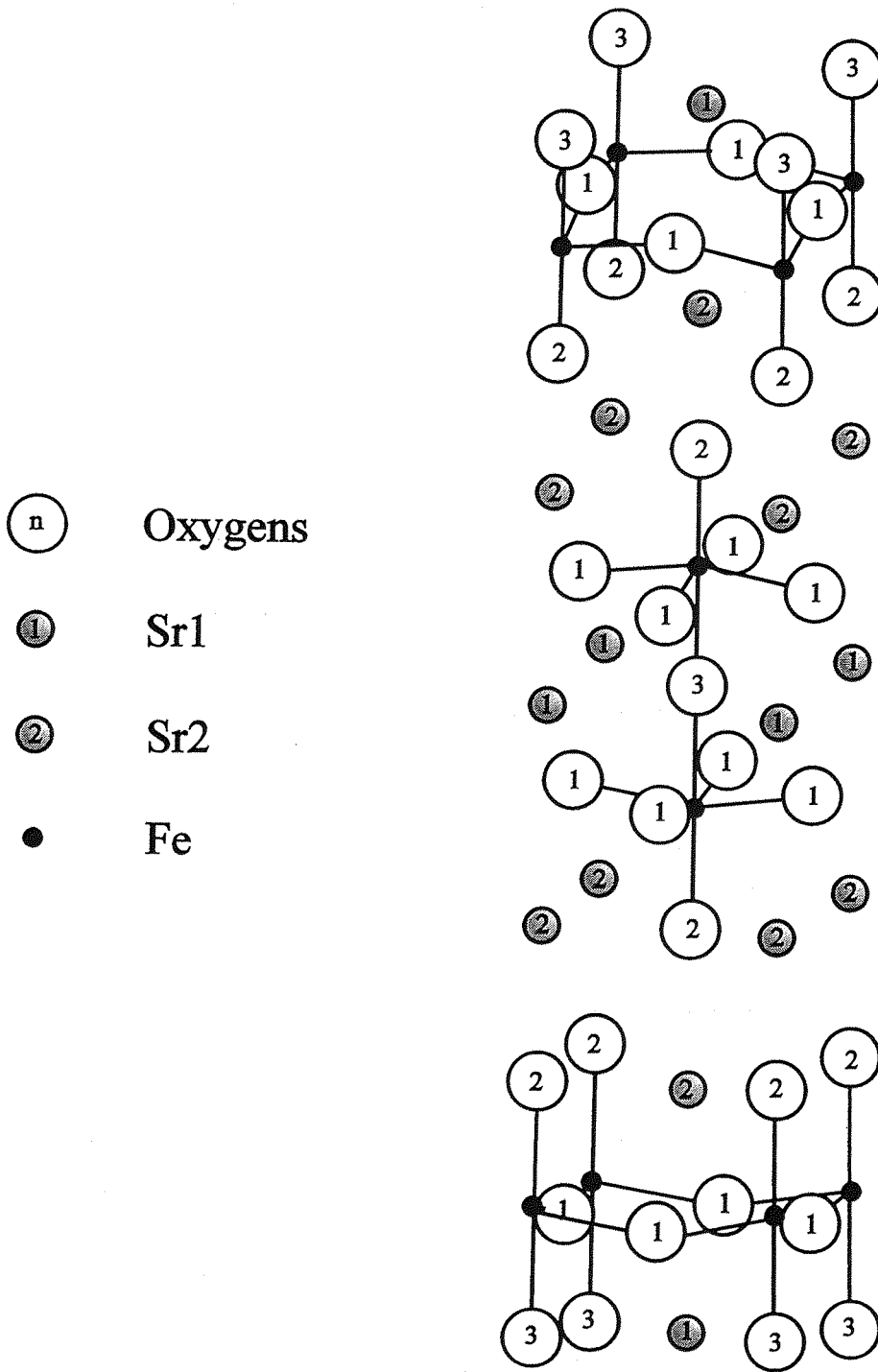
Figure 5.1 The Structure of $Sr_3Fe_2O_7$

116

much reduced below six i.e. $0.45 \leq y \leq 0.3$. A structural model (Figure 5.2) was proposed from x-ray data although considering the complexity of the structure and the limited amount of data available, a high level of uncertainty in the oxygen positions and occupancy factors resulted. A neutron diffraction study of these systems was not performed by Nguyen due to the high level of absorbtion of neutrons by all of these lanthanide nuclei. Grasmeder *et al* (11) prepared and then studied compounds in the system $Nd_{1.4}Sr_{1.6}Cu_2O_{6 \pm y}$ by powder x-ray and neutron diffraction. The structural model, proposed by Nguyen for the tripled structure, was confirmed for this compound although the ordering of cations and anionic vacancies was quite different with the lanthanide exclusively favouring the low coordination sites. An oxygen vacancy had previously been suggested by the x-ray diffraction study and was thought to give alternating $A_1Cu(2)O_3$ and $A_2Cu(1)O_2$ blocks. However, neutron refinement in the $Nd_{1.4}Sr_{1.6}Cu_2O_{6 \pm y}$ system showed the ordering to be more complex: absence of oxygen on the O3 ($\frac{1}{2}$,0,z) site produced discontinuities in the CuO_2 planes in the b-direction. Vertex-linked CuO_5 square pyramids, which form six-membered rings by corner sharing, constructed rectangular tunnels running parallel to the a-direction. These tunnels being partially empty due to oxygen absences on the O7 site. Occupation of the O7 site results in a Cu1 - O7 - Cu1 link which bridges the tunnel with a very short Cu1 - O7 contact distance.

This chapter reports an attempt to generate a Sr_2CoO_4 phase using stoichiometric starting materials and high oxygen pressure. A new phase $Sr_3Co_2O_{7-z}$ was generated in the system using ambient conditions of temperature and pressure. This previously unknown phase, $Sr_3Co_2O_{7-z}$ ($0.94 \leq z \leq 1.22$), was identified by comparison with other materials with structures based on the $Sr_3Ti_2O_7$ structure (8) and characterised using powder diffraction methods. Accurate structure determination was carried out using powder neutron diffraction on the high resolution powder diffractometer, HRPD at the Rutherford Appleton Laboratory. The oxygen content was determined by thermogravimetric analysis and the refinement of oxygen occupancies from powder neutron diffraction data.
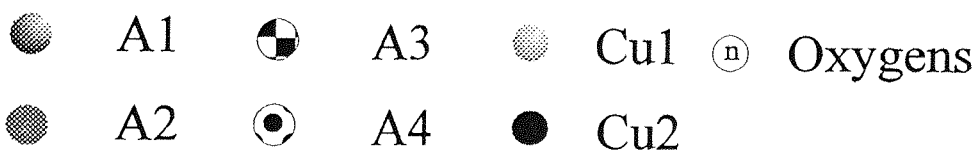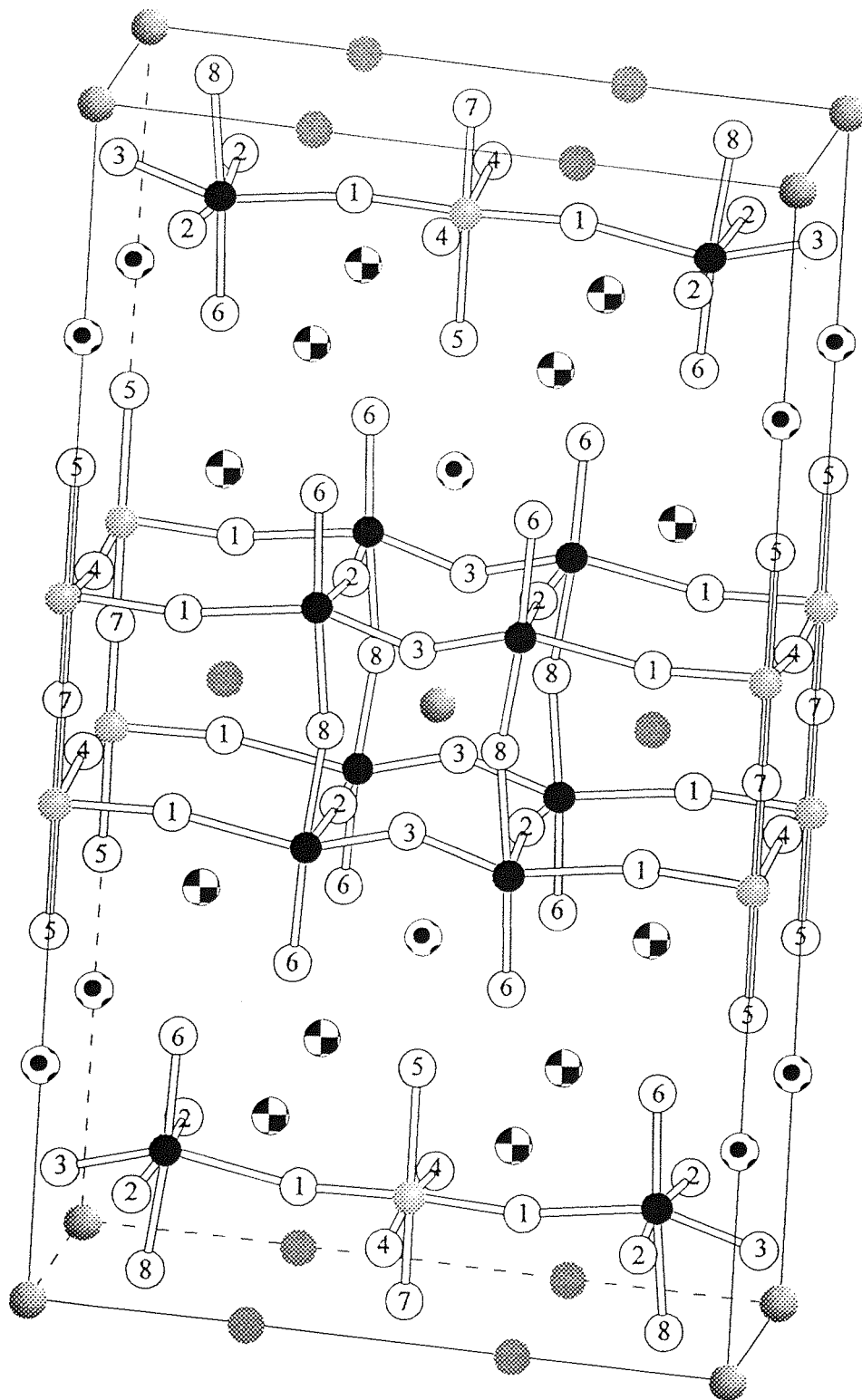
Figure 5.2 The Structure of the $Ln_{2-x}Sr_{1+x}Cu_2O_{6-y}$ (Ln = Sm, $0.7 \leq x \leq 0.9$)

5.2 Experimental

5.2.1 Attempted Preparation of Sr$_2$CoO$_4$

SrCO$_3$ and CoO in a 2:1 molar ratio were intimately ground and heated to 1000°C in air for 16hrs. After regrinding the mixture was returned to the box furnace and heated at 1200°C for a further 24hrs. On quenching to room temperature the material proved to be sensitive to atmospheric conditions and was thereafter transferred to a glove box whilst still hot. The sample was mounted in the x-ray sample holder in the glove box which was sealed using mylar film. An example of the x-ray pattern of an air quenched sample is shown in Figure 5.3.
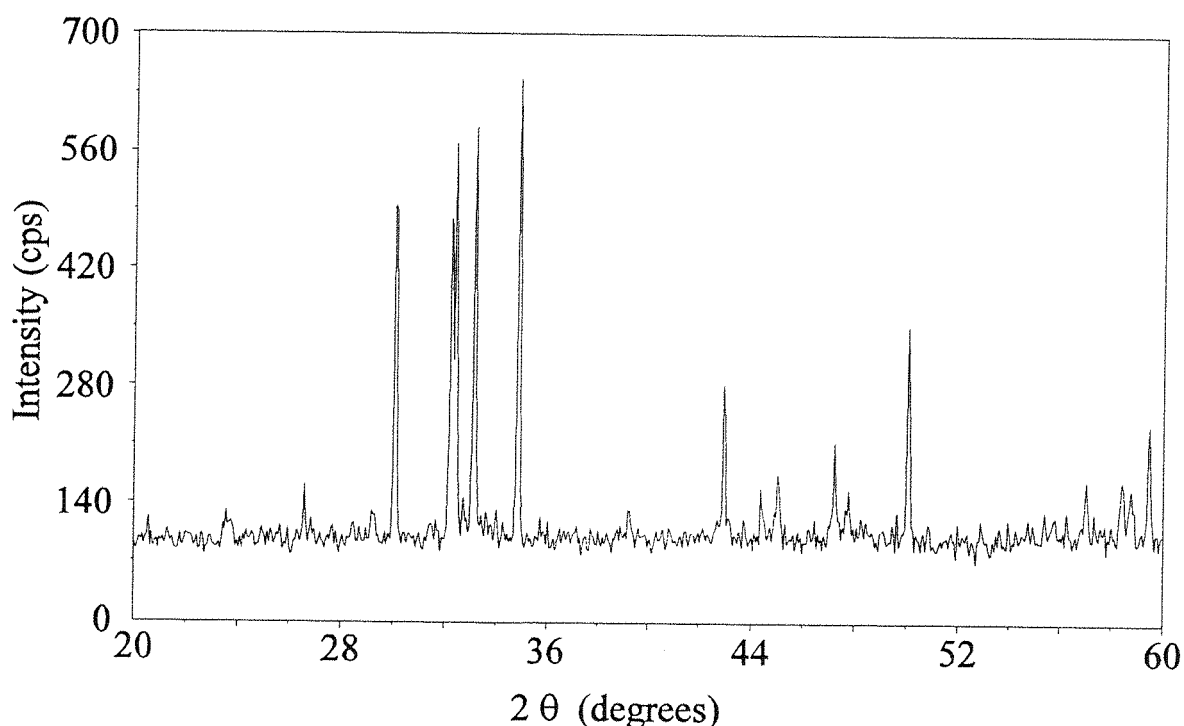
Figure 5.3 X-ray Diffraction Pattern of the Air Quenched Sample.

The diffraction pattern showed a mixture of SrO and a second, at this stage

119

unidentified, phase. This mixture was then heated at 800°C at 200atm of oxygen pressure for 24hrs. On cooling to room temperature the sample coloration had changed from brown to black. This material was identified as a mixture of hexagonal $SrCoO_{2.7}$ (4) and SrO. The diffraction pattern of this product is shown in Figure 5.4. Further attempts to generate Sr_2CoO_4 using the maximum temperatures and pressures possible for the high pressure annealing apparatus were also unsuccessful generating the hexagonal phase and either SrO or SrO_2. A diffraction pattern, characteristic of the K_2NiF_4 structure, was never obtained.

Close scrutiny of the air quenched sample revealed a mixture of an orthorhombic phase, with approximate cell parameters 3.8Å, 11.4Å and 20.3Å, and SrO. The emphasis now focused on generating the pure orthorhombic phase. Comparison with iron materials suggested that the new phase was similar to $Sr_3Fe_2O_7$ (6). A comparison of the two diffraction patterns is shown in Figure 5.5.
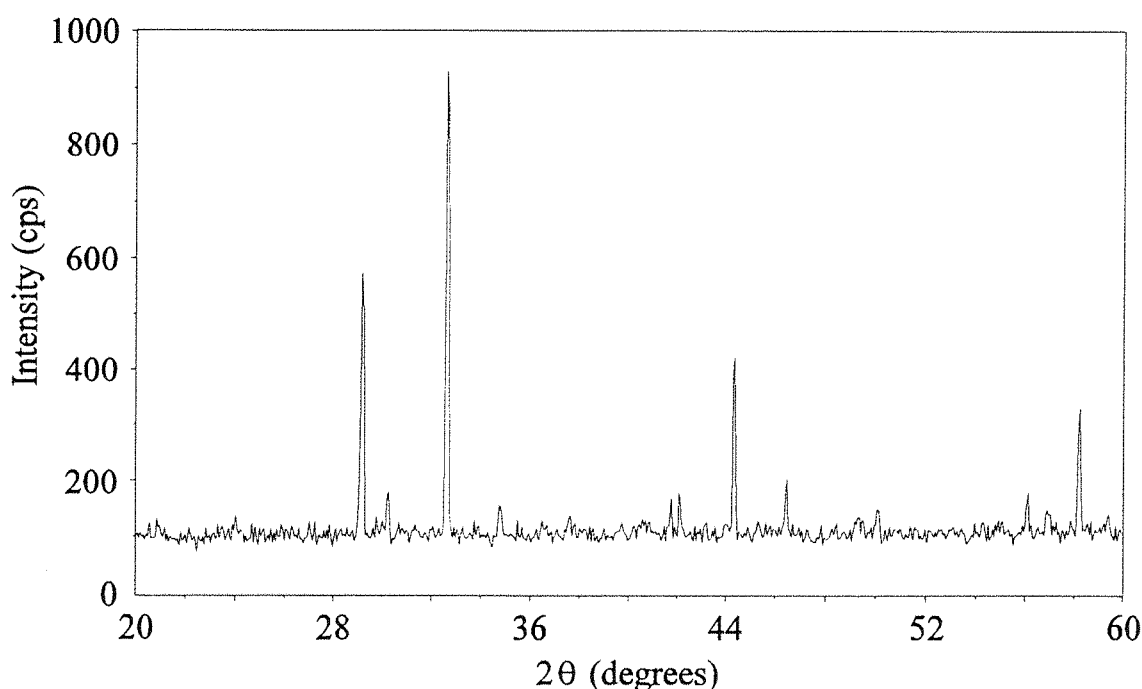
Figure 5.4 X-ray Diffraction Pattern of the High Pressure Annealed Sample

5.2.2 Preparation of $Sr_3Co_2O_{7-z}$

A sample of $Sr_3Co_2O_{7-z}$ was synthesised by direct solid state reaction of $SrCO_3$ (99.9%)

120
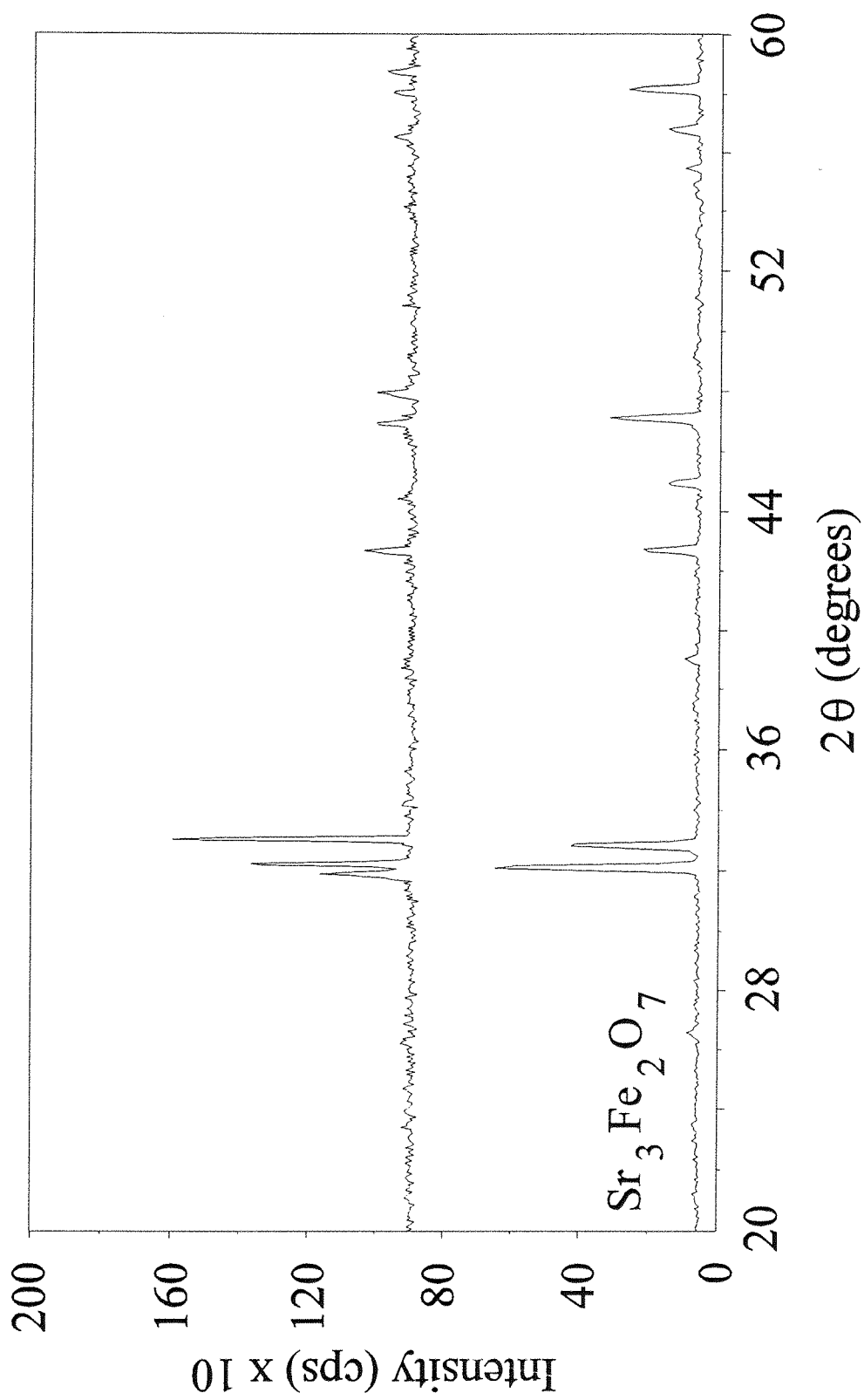
Figure 5.5 Comparison of $Sr_3Fe_2O_7$ with the Orthorhombic Phase

and CoO (99.99%), in a molar ratio, of 3:2 heated at 1000°C in a box furnace for 24hrs. After air quenching and regrinding, samples of this compound were then treated further to control the oxygen stoichiometry, as shown in Table 5.1.

Powder x-ray diffraction data were collected, on the products of the annealing experiments, and showed the samples to be single phase (Figure 5.6). Oxygen content was determined by thermogravimetric analysis under $5\%H_2/N_2$ in platinum crucibles heating to 1000°C. Powder x-ray diffraction analysis of the t.g.a. product showed a mixture of SrO and an amorphous phase, with metallic behaviour, which was assumed to be cobalt metal. The analytically determined oxygen content will be used hereafter to describe the samples.

Table 5.1 Annealing Conditions

Treatment	a/b (Å)	c(Å)	3a/b	7-z
Air/1200°C for 3 days Quenched	a = 3.864(1) b = 11.435(4)	20.233(9)	1.014	5.78(5)
O_2/1000°C for 3 days Slow cool/440°C Quenched	a = 3.838(1) b = 11.492(3)	20.099(10)	1.002	5.94(5)
O_2/1000°C for 3 days Slow cool/200°	a = 3.830(3) b = 3.830(3)	20.075(11)	1.000	6.06(5)

Annealing of samples at temperatures lower than 480°C caused deterioration of the sample crystallinity and formation of impurity phases.

Close scrutiny of the x-ray diffraction patterns of the samples, 7-z = 5.78, 5.94 and 6.06, revealed a change in structure as the oxygen content increased above six (Figure 5.6).

On this basis, it was decided to collect powder x-ray diffraction data over an extended period, for structure refinement on samples from the two structural regions.
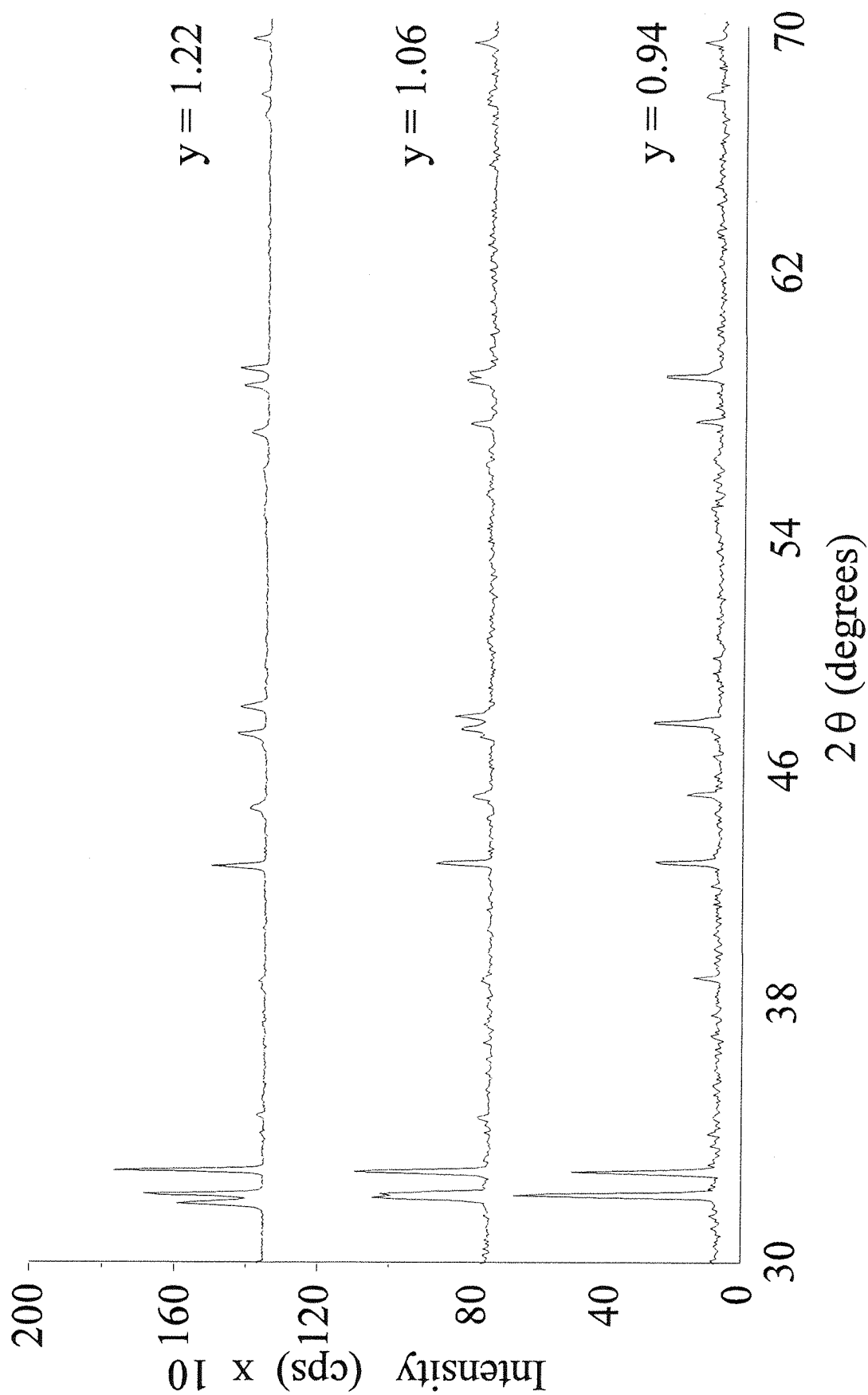
Figure 5.6 X-ray Patterns of the System $Sr_3Co_2O_{7-z}$

123

Powder x-ray diffraction data were collected on the samples 7-z = 5.78 and 6.06 sealed in aluminium sample holders under mylar. A stepsize of 0.02° in the 2θ range 30-120° was employed to collect data over a period of 15hrs. The final profiles were of good quality although the low angle reflections, in the range 10 - 30° were obscured by the absorption of the amorphous mylar film.

In the case of the tetragonal sample, $Sr_3Co_2O_{6.06}$, there were no additional reflections in the diffraction pattern to suggest orthorhombic symmetry, but there was evidence of line broadening in the h00 reflections.

Refinements were undertaken using the DBW-9006pc program running locally on personal computers using the Rietveld method (12)

5.3 Powder Neutron Diffraction

In order to fully investigate the orthorhombic structure, particularly the oxygen positions, powder neutron diffraction data were collected using the high resolution diffractometer HRPD on samples 7-z =5.78 and 5.94. Due to the low flux of HRPD, (which receives only one in five neutron pulses from the source), large samples $c.a$ 5g were synthesised. These sample were transferred hot to a glove box where they were separated into two specimens, one of which (0.5g) was analysed using powder x-ray diffraction and thermogravimetric analysis to ensure sample purity and measure the oxygen content, and the other, (4-5g), was transferred to a vanadium can and sealed with indium wire. The scattering length of cobalt is small (b = 0.25 x 10^{-12} Fm^2) and consequently long collection times (>12hrs) were used to obtain the high quality data appropriate for the structure refinement of this complex structure. A wide range, 0.6 - 2.2Å, of chemically useful data was collected and the data profile was of good quality.

5.4 Results and Discussion

X-ray Structure Refinement

The structure of the air quenched sample, $Sr_3Co_2O_{5.78}$, was refined in the space group Immm using the atomic coordinates of $Nd_{1.4}Sr_{1.6}Cu_2O_{5.79}$ (11) as a starting model.

124

Refinement of the heavy atom positions and instrumental parameters proceeded steadily in the space group Immm. However, the oxygen positions were very difficult to refine and would not give a steady refinement when varied simultaneously. Evidence for low angle reflections to confirm the assignment of a tripled structure in the b-direction was obscured by the amorphous scattering of the mylar film. However, indexing of all reflections was not possible without this assignment. Initially all eight oxygen sites were allowed to be fully occupied, corresponding to seven oxygens per formula unit. The oxygen occupancies refined rapidly although this was not possible without fixing isotropic temperature factors. This process suggested total vacancy on the O3 site with possible vacancies on sites O7 and O8.

Oxygen occupancies could also be refined, if the temperature factors were held constant, and indicated vacancies on the O3, O7 and O8 sites. Refined heavy atom positions are tabulated in Table 5.2. The refinement profile is shown in Figure 5.7.

The tetragonal sample, $Sr_3Co_2O_{6.06}$, was refined in the space group I4/mmm using the parameters of $Sr_3Fe_2O_6$ (6) as a starting model. All positional parameters and isotropic temperature factors could be refined simultaneously. The occupancies of all the oxygen atoms were varied. Both the O1 and O2 site showed only a small deviation from unity and were subsequently fixed. The O3 site, refined to a partial occupancy of 0.13, which was in good agreement with the analytically determined value of 6.06(5). Essentially this suggests most cobalt atoms in this structure are in five-fold coordination with 10% in six-fold coordination (O3 site filled). This material seems to have a similar structure to that of $Sr_3Fe_2O_6$ (6) containing square-pyramidal sheets of CoO_5 units. Refined parameters and calculated bond lengths are given in Tables 5.3 and 5.4 respectively.

Powder Neutron Diffraction

Examination of the patterns after data collection showed both phases, $Sr_3Co_2O_{5.78}$ and $Sr_3Co_2O_{5.94}$, to be orthorhombic and refinement proceeded in the space group Immm. The refined atomic positions from the x-ray refinement were used as the starting point for the neutron refinement. Refinement of the strontium and cobalt positions was achieved quickly although the latter had relatively large e.s.d's, probably associated with the small scattering length of cobalt. Oxygen positions and isotropic temperature factors refined
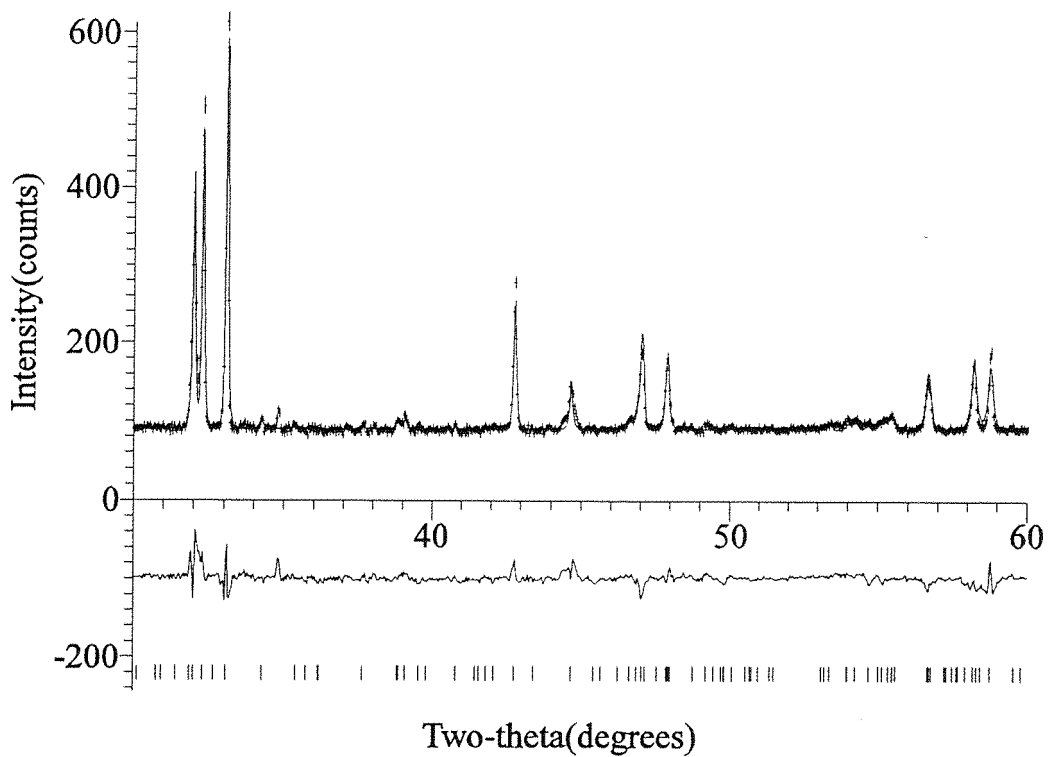
Figure 5.7 Refinement Profile for $Sr_3Co_2O_{5.78}$

Table 5.2 Heavy Atom Positions for $Sr_3Co_2O_{5.78}$

Atom	x	y	z
Sr1	0	0	0
Sr2	0	0.3418(22)	0
Sr3	0	0	0.1904(10)
Sr4	0	0.3346(26)	0.1768(11)
Co1	0	0	0.6088(15)
Co2	0	0.3246(32)	½

a = 3.8615(1)Å   b = 11.3894(3)Å   c = 20.2793(3)Å

126

Table 5.3 Refined Atomic Parameters for $Sr_3Co_2O_{6.06}$

Atom	x	y	z	B_{eq}	Occupancy
Sr1	0	0	½	0.67(3)	1.00
Sr2	0	0	0.3183(3)	0.43(6)	1.00
Co	0	0	0.0999(6)	0.66(5)	1.00
O1	0	½	0.0888(4)	0.13(8)	1.00
O2	0	0	0.1986(8)	0.75(8)	1.00
O3	0	0	0	5.39(8)	0.13(5)

$a = 3.8321(1)$Å $c = 20.0826(1)$Å

$R_{exp} = 2.86$ $R_{wp} = 6.04$ $R_p = 4.37$

Table 5.4 Derived Bond Distances for Oxygen Annealed $Sr_3Co_2O_{6.06}$ (Å)

Atom - Atom	Distance (Å)
Sr1 - O1	2.618(1) x 8
Sr1 - O3	2.710(1) x 4
Sr2 - O1	2.674(6) x 4
Sr2 - O2	2.404(17) x 1
Sr2 - O2	2.731(17) x 4
Co - O1	1.929(2) x 4
Co - O2	1.982(18) x 1
Co - O3	2.006(12) x 1*

*denotes partially occupied site.

127

easily although they could not be refined simultaneously with occupancy factors. Oxygen vacancies were implied by very high temperature factors on the O3, O7 and O8 sites. The first, O3, was eventually fixed at zero having refined the occupancy to almost zero and the temperature factors remaining high. The O7 and O8 occupancies refined to constant values where they were fixed, after several cycles of refining the temperature factor and occupancy separately. Final stages of the refinement included tying the temperature factors of like atoms on similar sites.

The refinement of peak parameters for the oxygen annealed sample, $Sr_3Co_2O_{5.94}$, was quite complex. Fitting of the reflections at short d-spacing was initially difficult due to the extensive number of closely-spaced reflections. Therefore, the peak shape was initially fitted by refining the high d-spacing data, where there are more unique reflections and then, in the latter stages of refinement, including the low d-spacing data.
The O7 and O8 sites occupancies refined to partial occupancy at 39% and 77% occupancy respectively. The refinement parameters are tabulated in Table 5.5. Calculated bond distances are tabulated in Table 5.6a and 5.6b for strontium and cobalt respectively. Important bond angles around the cobalt centre are given in Table 5.6c.

Refinement of the air quenched sample was more difficult due to broadening of the 001 reflections. This is likely to be a result of stacking faults in the long axis direction (13) which can be observed in many materials with one crystallographic axis much longer than the others. For example, the repeat in $A_3B_2O_7$ is K_2NiF_4 : perovskite : K_2NiF_4 : perovskite. A stacking fault may involve, K_2NiF_4 : perovskite : perovskite : K_2NiF_4 i.e. a portion of $A_4B_3O_{10}$ structure. For this reason, the oxygen annealed sample was initially refined and used as a basis for the refinement of the air quenched sample. The occupancy of the O7 and O8 sites refined to give 42% and 52% occupancy respectively. Final refined atomic parameters are summarised in Table 5.7 and calculated bond distances for strontium and cobalt 5.6a and 5.6b. Derived bond angles around the cobalt are given in Table 5.6c. The profile fit is shown in Figure 5.8 and a diagram of the structure in Figure 5.9.

Attempts to refine the samples in a smaller crystallographic cell, without tripling the unit cell in the b-direction, and in other space groups was unsuccessful with much poorer fit parameters and many of the high d-spacing reflections excluded from the profile refinement.

Table 5.5 Refined Atomic Parameters for $Sr_3Co_2O_{5.94}$

	x	y	z	B_{eq}	Site
Sr1	0	0	0	1.14(5)	1.00
Sr2	0	0.3365(8)	0	1.14(5)	1.00
Sr3	0	0	0.1819(5)	1.14(5)	1.00
Sr4	0	0.3299(5)	0.1806(2)	1.14(5)	1.00
Co1	0	0	0.5929(9)	0.39(7)	1.00
Co2	0	0.3249(5)	0.6007(5)	0.39(7)	1.00
O1	0	0.1672(6)	0.4081(3)	0.32(2)	1.00
O2	0	0.1644(7)	0.0912(4)	0.32(2)	1.00
O3	½	0	z	-	-
O4	½	0	0.4081(3)	0.32(2)	1.00
O5	0	0	0.6910(5)	0.32(2)	1.00
O6	0	0.3267(6)	0.6940(2)	0.32(2)	1.00
O7	0	0	½	0.32(2)	0.39(4)
O8	0	0.3389(10)	½	0.32(2)	0.77(2)

a = 3.8379(1)Å   b = 11.4898(5)Å   c = 20.0812(9)Å

R_{wp} = 8.71 R_{exp} = 4.97 χ^2 = 3.06

Oxygen content = 5.97(8)

Table 5.6a Calculated Strontium Bond Distances (Å)

	$Sr_3Co_2O_{5.94}$	$Sr_3Co_2O_{5.78}$
Sr1 - O2	2.631(8) x 4	2.708(5) x 4
Sr1 - 08	2.666(4) x 4*	2.730(8) x 4*
Sr2 - O1	2.663(4) x 4	2.615(1) x 4
Sr2 - O2	2.695(14) x 2	2.701(13) x 2
Sr2 - O4	2.633(8) x 2	2.592(8) x 2
Sr2 - O7	2.685(6) x 2*	2.717(6) x 2*
Sr2 - O8	2.783(11) x 2*	2.761(10) x 2*
Sr3 - O2	2.624(6) x 2	2.601(6) x 2
Sr3 - O5	2.552(14) x 1	2.497(7) x 1
Sr3 - O6	2.768(5) x 4	2.727(4) x 4
Sr4 - O1	2.618(5) x 2	2.726(3) x 2
Sr4 - O2	2.615(9) x 1	2.603(7) x 1
Sr4 - O4	2.664(7) x 1	2.713(8) x 1
Sr4 - O5	2.747(4) x 2	2.723(5) x 2
Sr4 - O6	2.652(6) x 2	2.729(6) x 2
Sr4 - O6	2.501(6) x 1	2.518(6) x 1

* denotes partially occupied site

Table 5.6b Calculated Cobalt Bond Distances (Å)

	$Sr_3Co_2O_{5.94}$	$Sr_3Co_2O_{5.78}$
Co1 - O1	1.911(7) x 2	1.917(6) x 2
Co1 - O4	1.919(1) x 2	1.947(2) x 2
Co1 - O5	1.970(21) x 1	1.958(19) x 1
Co1 - O7	1.866(18) x 1*	1.995(18) x 1*
Co2 - O1	1.831(9) x 1	1.954(15) x 1
Co2 - O2	1.932(1) x 2	1.934(1) x 2
Co2 - O6	1.874(11) x 1	1.924(11) x 1
Co2 - O8	2.029(10) x 1*	2.024(10) x 1*

* denotes partially occupied site.

131

Table 5.7 Calculated Bond Angles Around Cobalt (°)

Atom - Atom - Atom	$Sr_3Co_2O_{5.94}$	$Sr_3Co_2O_{5.78}$
O1 - Co1 - O1	178.8	165.2
O1 - Co1 - O4	90.0	89.0
O1 - Co1 - O5	90.6	97.4
O1 - Co1 - O7	89.4	82.6
O4 - Co1 - O5	91.6	98.1
O4 - Co1 - O7	88.4	81.9
O5 - Co1 - O7	180.0	180.0
O1 - Co2 - O2	93.0	88.9
O1 - Co2 - O6	96.4	96.4
O1 - Co2 - O8	89.0	84.2
O2 - Co2 - O6	95.7	92.6
O2 - Co2 - O8	84.0	87.4
O6 - Co2 - O8	174.6	179.5

Table 5.7 Refinement Parameters for $Sr_3Co_2O_{5.78}$

	x	y	z	B_{eq}	Site
Sr1	0	0	0	1.52(3)	1.00
Sr2	0	0.3330(8)	0	1.52(3)	1.00
Sr3	0	0	0.1818(3)	1.52(3)	1.00
Sr4	0	0.3339(6)	0.1819(2)	1.52(3)	1.00
Co1	0	0	0.5984(9)	1.12(6)	1.00
Co2	0	0.3356(12)	0.5998(5)	1.12(6)	1.00
O1	0	0.1663(5)	0.4130(1)	1.01(2)	1.00
O2	0	0.1669((5)	0.0947(2)	1.01(2)	1.00
O3	½	0	z	-	0
O4	½	0	0.4136(3)	1.01(2)	1.00
O5	0	0	0.6950(2)	1.01(2)	1.00
O6	0	0.3330(5)	0.6947(2)	1.02(2)	1.00
O7	0	0	½	1.02(2)	0.42(2)
O8	0	0.3314(10)	½	1.02(2)	0.52(1)

a = 3.8631(1)Å   b = 11.4319(1)Å   c = 20.2265(1)Å

R_{wp} = 8.87 R_{exp} = 2.74 χ^2 = 10.49

Oxygen content = 5.82(2)
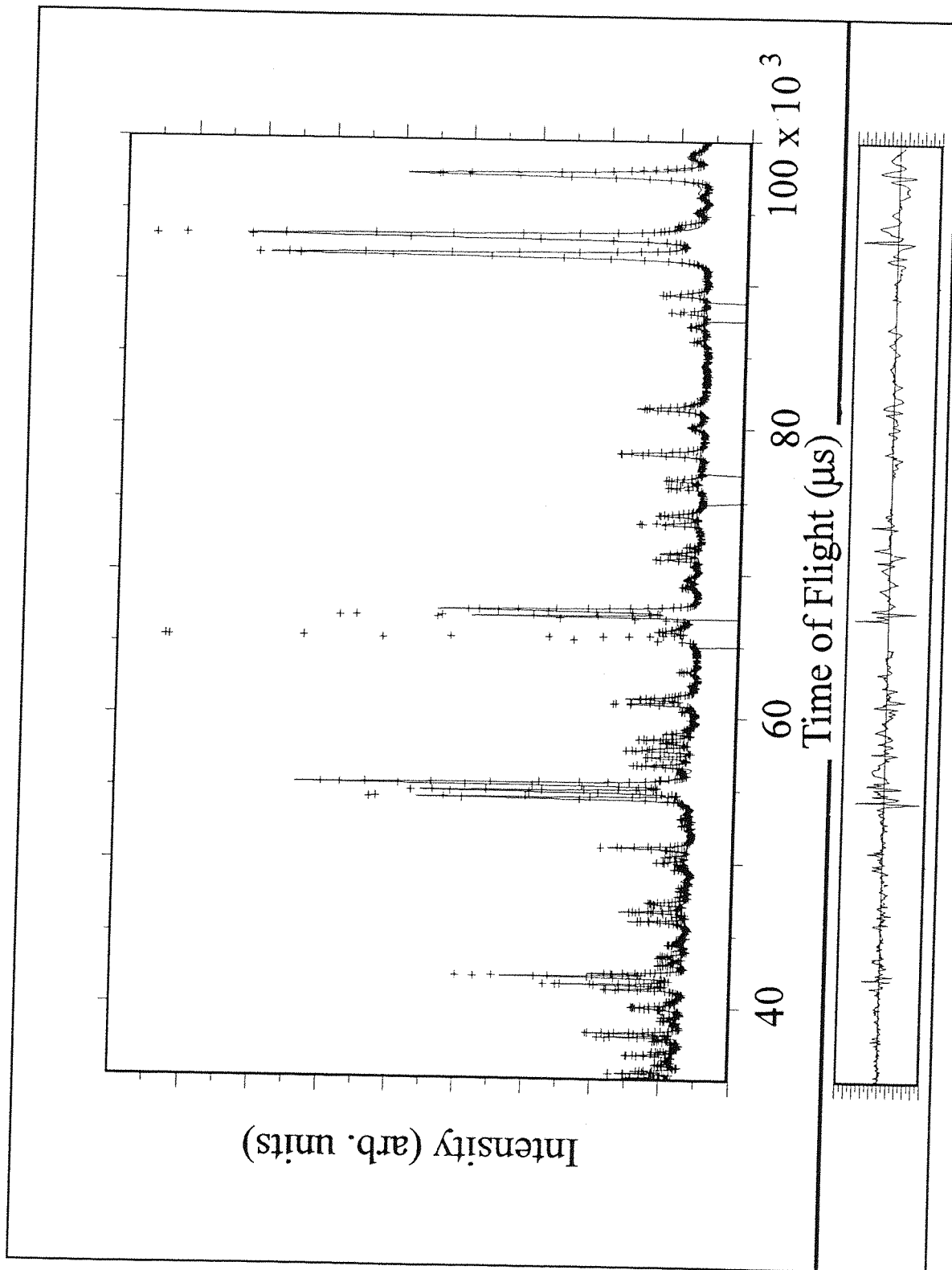
Figure 5.8 Refinement Profile of $Sr_3Co_2O_{5.78}$

134
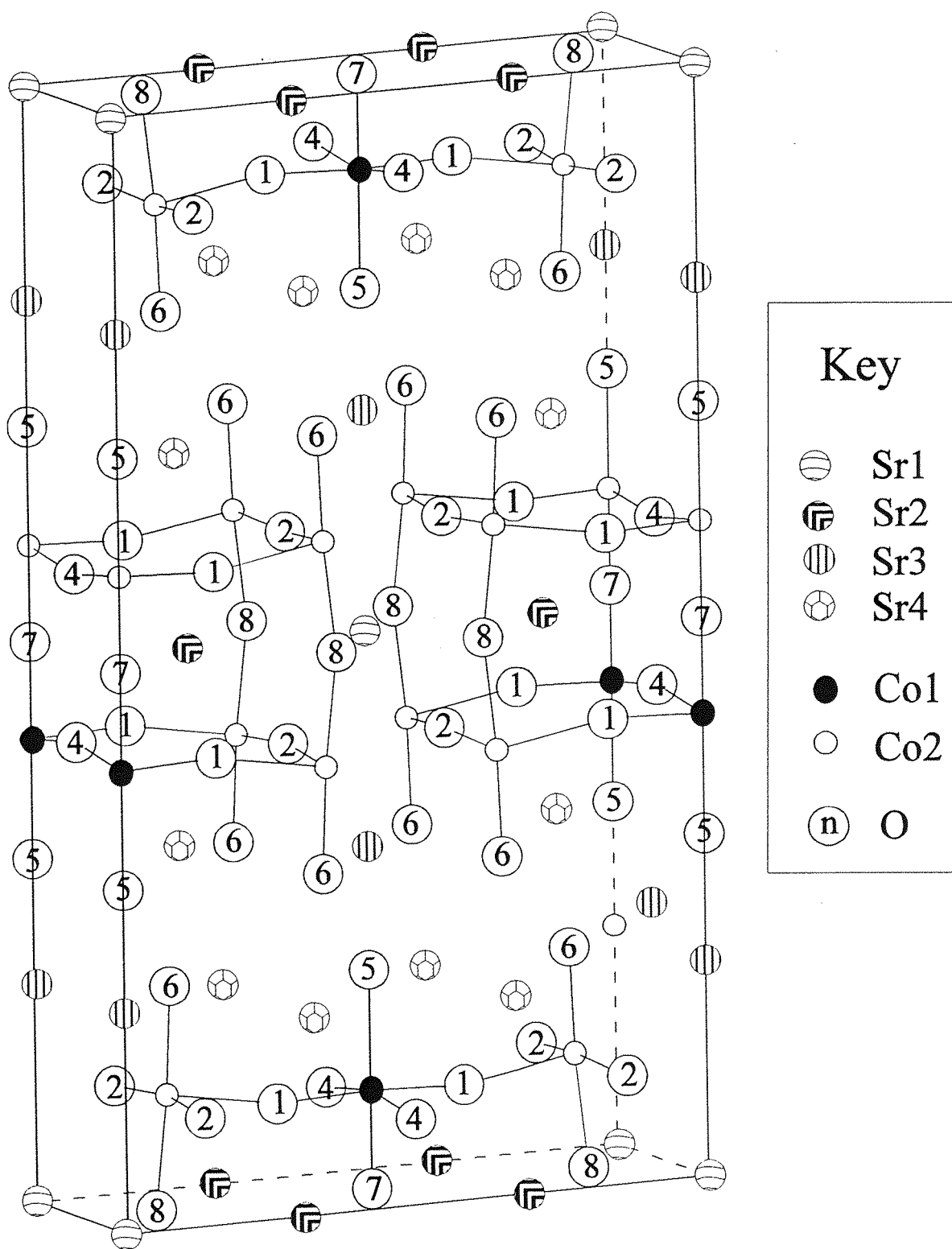
Figure 5.9 Diagram of the Refined Tripled Structure

135

The attempt to prepare a K_2NiF_4 structure containing strontium, cobalt and oxygen was unsuccessful. The calculations, used to predict the stability of the structure at the beginning of chapter 3 are based on ionic radii, and are purely empirical, taking no account of conditions required to achieve the structure. Considering the preparative conditions required to produce the perovskite structure (65Kbar, 1273K) using these elements, then it is probably not unreasonable to assume that the conditions required to produce the K_2NiF_4 structure with these elements is well beyond the capability of the apparatus (800bar). It is worth noting that exceptional pressures, such as 65Kbar, favour structures with high density, whereas high oxygen pressures favour the high oxidation states.

Refinement of the tetragonal $Sr_3Co_2O_{6.06}$ sample was successfully achieved in the space group I4/mmm using powder x-ray data. Comparison of this sample with the trivalent iron analogue $Sr_3Fe_2O_6$ shows some notable differences. The iron system has a completely vacant O3 site and the apical Fe - O2 distance is very short (1.886Å) with four Fe - O1 equatorial bonds of 1.980Å. In the cobalt sample there are four short equatorial bonds at 1.929Å with two long apical distances of Co - O1 (1.980Å) and Co - O2 (2.006Å). The comparatively long distances in the c-axis direction is a good indication that there is indeed oxygen on the O3 site: in the iron system there is a large expansion in the c-axis direction as soon as oxygen is placed on the O3 site and the Fe - O1, Fe - O2 distances become more similar. For example in $Sr_3Fe_2O_{6.58}$ the Fe - O2 distance becomes 1.933Å with four Fe - O1 bonds at 1.942Å. If the O3 site was totally vacant the Co - O2 distance would be expected to be considerably shorter. Bond valence calculations on the cobalt and strontium sites using the parameters for the divalent ions give 2.12 Sr1 and 2.11 for Sr2 and 2.62 for Co. This suggests the valence of the cobalt site is greater than two since the divalent ion would be extremely overbonded on this site. This implies that the cobalt ions are in the trivalent state; calculated bond valence parameters for ions in an $n+1$ oxidation state using the A^{n+} bond valence parameter generally give values of $n+0.6/7$. Both calculated valences for the strontium sites are in good agreement with the theoretical oxidation state of strontium of two. Refinement of the oxygen occupancy suggested a small amount of oxygen (occupancy = 0.13) on the O3

site which gave excellent agreement with the analytically determined oxygen stoichiometry of 6.06(5). However, it should be noted that the e.s.d on this occupancy is large, giving a value which lies within three e.s.d.'s of zero and may indicate a very low occupancy.

Refinement of the tripled structures using the refinement of x-ray data was not ideal due to the complexity of the structure; the paucity of the data. However, characterisation of the heavy atom sites was possible, but, in general, gave poor agreement with that of the neutron diffraction results. The x-ray refinement is unfavourably affected by both the form factor and also by x-ray fluorescence resulting from the use of copper radiation. Refinement of $Sr_3Co_2O_{7-z}$ samples using powder neutron diffraction from HRPD, however, gave much better results due to the high quality and quantity of data. The structure was successfully refined in the space group Immm and shows evidence of a complex oxygen ordering mechanism. Comparison of the typical Ruddlesden-Popper cell and the tripled cell coordinates derived from this unit cell are shown in Table 5.8. Cation positions in the tripled unit cell are displaced only very slightly from the positions created by stacking three tetragonal unit cells together. This suggests that the tripled structure is a result of oxygen ordering. This is in contrast with the tripled structure of Ln636 cuprates, where both cation and oxygen ordering are clearly evident. As previously noted in the Ln212 systems (14), the tripled structure only occurs when there is a large amount of strontium present. Strontium is unusual in that it can sustain a variety of coordination numbers, i.e. 6,7,8,9,10 and 12 fold are all known. In $Nd_{1.4}Sr_{1.6}Cu_2O_{5.79}$, the A1 and A3, low coordination, sites are filled by the neodymium with Sr on the 12-fold A2 site and a mixture of the two ions on the A4 site. The lowest coordination number in the tripled Ln212 structure is seven; strontium can exist in this coordination environment and, indeed, any other coordination environment present in 636. Bond valence (15) calculations on the strontium and cobalt sites are summarised in Table 5.9.

It can be seen that Sr is underbonded on the A1 and A3 sites which are the low coordinate 8- and 7-fold sites. A better situation is achieved on the A2 and A4 sites. The site valence for Sr1, Sr2 and Sr4 is more acceptable in the oxygen annealed sample, and this may be a result of oxygen ordering where the air quenched sample will be affected by disorder. However, bond valence parameters are calculated for each atom in many different structures and as a result will be most appropriate for the most common coordination numbers i.e. for strontium this is twelve. The low values obtained for the

137

Table 5.8 Positional Coordinates

Ruddlesden-Popper	Tripled Cell				5.94	5.78
Sr1 0 0 0	Sr1'	0	0	0		
	Sr2'	0	⅓+*	0	* = 0.0032	* = -0.0003
Sr2 0 0 z	Sr3'	0	0	z^1		
	Sr4'	0	⅓+*	z^2	* = -0.034	* = 0.0006
B 0 0 z^i	B1'	0	0	z^3		
	B2'	0	⅓+*	z^4	* = -0.084	* = 0.0024
O1 0 ½ z^{ii}	O1'	0	1/6+*	z^5	* = 0.0006	* = -0.0003
	O2'	0	1/6+*	½-z^6	* = -0.022	* = 0.0003
	O3'	½	0	z^7		
	O4'	½	0	z^8		
O2 0 0 z^{iii}	O5'	0	0	z^9		
	O6'	0	⅓+*	z^{10}	* = 0.0066	* = 0.0003
O3 0 0 ½	O7'	0	0	½		
	O8'	0	⅓+*	½	* = 0.0056	* = 0.0019

* indicates different increments

138

Table 5.9 Calculated Site Valences

Atom	$Sr_3Co_2O_{5.78}$	$Sr_3Co_2O_{5.94}$
Sr1	1.40	1.70
Sr2	2.40	2.08
Sr3	1.68	1.51
Sr4	2.35	2.20
Co1	2.65	3.00
Co2	2.38	2.65

seven and eight coordination sites must therefore be treated with caution. In both cases the calculated valence of the cobalt sites is significantly elevated above two suggesting the sites are very overbonded for a divalent cobalt ion. The high values for the cobalt valence implies these sites are accommodating a large proportion of cobalt(III). In both cases the six fold site (Co1) has a higher calculated valence than the five fold (Co2) site. In the oxygen annealed sample, where oxygen ordering has time to occur this situation is accentuated.

Another property of the tripled cuprate structures which is emphasised in this system is the behaviour towards oxygen. For example in the $Sm_{1.3}Sr_{1.7}Cu_2O_{6\pm y}$ (11) system very marginal oxygen uptake occurs on annealing and the lattice parameters remain the same within the limits of experimental error. The ability to pick up extra oxygen increases with lanthanides greater in size than strontium, but has not yet been possible above six in these cuprates. However, in the normal Ruddlesden-Popper phase, a oxygen level of six is readily obtained. The small degree of oxidation in the $Sm_{1.3}Sr_{1.7}Cu_2O_{6\pm y}$ causes a contraction of both a and b axes with the former being more prominent. This process is consistent with oxygen being placed on the O3 or O7 site. Different behaviour is noted in the cobalt system: the largest contraction is in c with a small decrease in a and increase in b. Considering the two samples prepared under different conditions it can be seen that although the occupancy of the O7 site remains constant within the limits of experimental

error there is a large change in the occupancy of the O8 site which, in conjunction with O7, has the largest affect on the c-axis. However, during this process the average Co2 - O8 - Co2 distance changes very little, where a shortening would be indicative of filling the O8 site. The other apical distance, Co2 - O6, shrinks by 0.05Å during the oxidation which is consistent with an increase in the valence of the Co2 ion. An explanation for this change in the coordination environment of the O2 ion lies in the other atoms coordinated to the O8 atoms. The part of the structure containing the Co2 - O8 distance is already under compression: further shortening of the bond is disfavoured due to the associated increase in the already overbonded Sr2 bond valence. This process increases the Sr2 - O8 distance and gives Sr2 a more acceptable coordination. At the same time the Co1 - O7 - Co1 distance decreases by 0.26Å indicating a contraction into the perovskite blocks. The strontium atoms in the NaCl type layers (Sr3, Sr4) experience a drop in the calculated bond valence. In both oxygen annealed and air quenched sample there is overwhelming evidence that the O3 site is vacant.

It should be taken into consideration that these refinements are highly affected by the initial model. The model includes partially vacant sites and the refinement produces an averaged structure over all the crystallites. The end result of this is an averaged structure which does not take into account the individual case. For example, the Co2 has an averaged coordination of five. Close examination of the effect of oxygen annealing on the site in more detail shows that the Co atom moves into the O1-O2-O1 plane on oxygen annealing. This may indicate, in the air quenched sample, an attempt to model a different situation. The partial occupancy of the O8 site is indicative of a site which is filled 50% of the time. When the site is empty the coordination approximates to tetrahedral which may be modelled by the Co2 atom moving above the plane (Figure 5.10). Calculation of the bond valence of this tetrahedral site gives 2.06 which suggests divalency. This value increases to 2.46 when the site is completely filled i.e. tending towards trivalency. In order to obtain a good representation of the structure a technique such as EXAFS, which studies the local coordination of atoms would need to be utilised.

Low temperature annealing of the sample has caused a phase change to the tetragonal system when the oxygen content rises above six as seen in the analogous copper system. However, at large levels of oxygen intercalation the structure falls apart
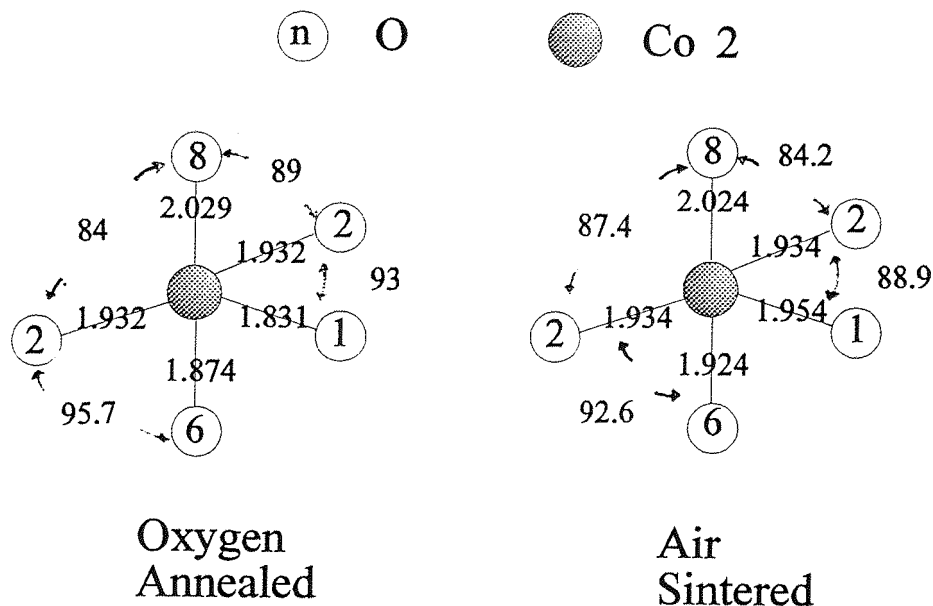
Figure 5.10 Coordination around the Co2 centre

completely to give a mixture of the hexagonal cobalt phase and SrO. This is probably the result of a too large contraction in the A1Co(1)O3-δ and A4Co(2)O3-δ blocks. On annealing all the bonding distances around the Sr3 atom increase leading to a drop in the bond valence of the site. Assuming this situation would continue to worsen on increasing the oxygen level then eventually the structure would no longer be stable and fall apart.

All these phases have shown sensitivity to atmospheric conditions. This is similar to the iron system, where the phases $Sr_3Fe_2O_{6.58}$ and $Sr_3Fe_2O_{6.75}$, are both extremely sensitive to atmospheric moisture. This phenomenon is clearly not just due to the instability of the tetravalent ion, since the pure iron(IV) sample has a much extended lifetime under the same conditions. Considering all the samples, the common characteristic of all the samples of both cobalt and iron showing poor resistance to atmospheric conditions is a long c-axis. The long c-axis is a feature of compounds with partial oxygen vacancy on the sites controlling the interplanar B - B distance. This suggests a tendency to pick up atoms from the atmosphere to fill the deficient coordination sphere which is most facile when the interplanar distance is large.

141

5.5 Conclusions.

Preparation of a sample containing only tetravalent cobalt, strontium and oxygen is not possible using oxygen pressure up to 700atm. This means that the Goldschimdt method of using tolerance factors to predict the stability of structures based on close-packed units is purely empirical, where the final tolerance factor is unrelated to the difficulty of synthesis. This is, generally, a treatment based on the requirement of a structure and takes no account of the thermodynamics of the system.

A new phase with the Ruddlesden-Popper, $Sr_3Ti_2O_7$, structure has been shown to exist for cobalt. The $Sr_3Co_2O_{7-z}$ system hosts a wide range of oxygen stoichiometry with $0.94 \leq z \leq 1.22$. At high values of z, the system crystallises orthorhombic in the space group Immm with a threefold tripling of the Ruddlesden-Popper phase along b. This property is also exhibited by the some semiconducting cuprate phases, $Ln_{2+x}Sr_{1+x}Cu_2O_{6-y}$, Ln = Gd, Sm and Eu where the tripling is a direct result of cationic ordering and the ordering of oxygen vacancies. In contrast, the cobalt system is tripled due to oxygen vacancy ordering only. The O3 site is completely vacant with partial occupancy on the O7 and O8 sites. This generates both octahedral and square-pyramidal cobalt sites. Increasing the oxygen content, lowering z, can be achieved by oxygen annealing at temperatures in excess of 1000°C and causes a phase change to tetragonal. The normal Ruddlesden-Popper phase is now restored and the cobalt sites are mostly square pyramidal (90%) with the remainder (10%) having octahedral coordination. Increasing the oxygen content further by oxygen annealing at temperatures below 500°C causes the crystallinity of the samples to deteriorate and the appearance of impurity phases.

Refinements to determine the crystal structure of these materials was achieved using the Rietveld method. This gives an averaged picture of the whole structure therefore to fully characterise the local structure, a technique such as EXAFS which studies the local coordination of ions, would be required.

5.6 References

1   I.S.Shaplygin, V.B. Lazerev. Russ. J. Inorg. Chem. (Eng. Trans.) **30**, 3214-6. (1985)

2   J.B.MacChesney, R.C.Sherwood, J.F.Potter. J. Chem. Phys. **43**, 1908-13. (1965)

3   A.N.Petrov, V.A.Chereparov, O.F.Konochuk, L. Ya. Govnlova. J. Sol. Stat. Chem. **87**, 69-76. (1990)

4   H.Takei, H. Oda, H. Watanabe. J. Materials. Sci. **13**, 519-22. (1978)

5   S.E.Dann, D.B.Currie, M.T.Weller. J. Sol. Stat. Chem. **92**, 237-41 (1991)

6   S.E.Dann, D.B.Currie, M.T.Weller. J. Sol. Stat. Chem. **97**, 179-185 (1992)

7   D.Baltz, K.Pleith. Z. Electrochem. **59**, 545-51. (1951)

8   S.N.Ruddlesden, P.Popper. Acta. Cryst. **4,** 503. (1951)

9   N.Nguyen, L.Er-Rakho, C.Michel, J.Choisnet, B.Raveau. Mat. Res. Bull **15**, 891. (1980)

10   N.Nguyen, C.Michel, J.Choisnet, B.Raveau. Mat. Res. Bull **17**, 567. (1982)

11   J.R. Grasmeder. Ph.D. Thesis. University of Southampton. (1989)

12   H.M. Rietveld. Acta. Cryst. **22**, 151. (1967)

13   J. Drennan, C.P. Tavares, B.C. H. Steele. Mat. Res. Bul. **17**, 62-6. (1982)

14   I.D. Brown, D. Aldermatt. Acta. Cryst. **B41**, 244. (1985)

15   J.R. Grasmeder. PhD. Thesis. University of Southampton. (1989)

CHAPTER 6

Preparation of $Sr_3M_{2-x}N_xO_{7-g}$ Phases

M, N = Fe, Co, and Ni

6.1 Introduction

Whilst the phase Sr_2MO_4 is stable for the early transition metals, decreasing the size of the M^{4+} ions on crossing the first row, destabilises the K_2NiF_4 structure. This can be seen from Figure 3.1, tetravalent Ni and Sr in the K_2NiF_4 structure with oxygen is disfavoured on grounds of the incompatible relative sizes of the ionic radii. No information exists in the literature for either Sr_2NiO_4 or $Sr_3Ni_2O_{7-w}$ type materials and attempts to make $A_{n+1}B_nO_{3n+1}$ type materials with strontium, nickel and oxygen have also been unsuccessful (1) and *vide infra*. Instability of such Ruddlesden-Popper (2) phases is not unexpected, as they contain portions of the K_2NiF_4 structure. However, given the stability of the $Sr_3Fe_2O_{7-y}$ and $Sr_3Co_2O_{7-z}$ systems, it was conjectured that nickel could be doped into the $Sr_3M_2O_{7-z}$ (M = Fe, Co) systems with the intention of obtaining more information about the phase formation of $A_3B_2O_{7-p}$ compounds.

In chapter 4, $Sr_3Fe_2O_7$ has been shown clearly to exhibit unusual charge disproportionation behaviour, Fe^{4+} ---> Fe^{3+} and Fe^{5+} (3). If this process could be slowed down or modified in some way, for example by exchanging some of the iron atoms for other ions, then this behaviour could be characterised in more detail. Substitution of iron atoms by elements of similar and variable valence, such as other transition metals, is a natural choice.

This section reports the preparation of mixed transition metal Fe, Co and Ni Ruddlesden-Popper type phases. Phase purity and crystallographic changes were first investigated using powder x-ray diffraction. Full structure determination was then performed using the high resolution neutron diffractometer, HRPD, at the Rutherford Appleton Laboratory. Oxygen content was measured by thermogravimetric analysis and refinement of oxygen occupancies using powder neutron diffraction data. The effect of doping on iron disproportionation behaviour was monitored by Mössbauer spectroscopy.

6.2 Experimental.

6.2.1 Preparation of $Sr_3Fe_{2-x}Ni_xO_{7-\alpha}$

NiO, Fe_2O_3 and $SrCO_3$ in the correct molar proportions, covering the range $0 \leq x \leq 1.2$,

were intimately ground and heated at 1100°C for 24hrs. After quenching and regrinding the samples were returned to the box furnace and heated for a further 24hrs at 1300°C.

X-ray diffraction analysis of the samples showed them to be single phase up to and including $x = 0.8$. Oxygen content was determined by thermogravimetric analysis in 5% H_2/N_2, which showed two weight losses; one at 540°C characteristic of Fe^{4+} reducing to Fe^{3+}, and a second at 650°C. At higher values of x, additional reflections, corresponding to NiO, appeared in the diffraction pattern.

Oxygen annealed samples were then prepared by heating the air quenched samples at 480°C for 24hrs and slow cooling to room temperature. Reduced samples were prepared by heating the air quenched samples in a tube furnace at 850°C in 5% hydrogen in nitrogen overnight and slow cooling to room temperature. Changes in lattice parameters with x are summarised in Tables 6.1, 6.2 and 6.3. The $x = 0$, $Sr_3Fe_2O_{7-x}$, samples are included for comparison.

Table 6.1 Lattice Parameters for $Sr_3Fe_{2-x}Ni_xO_{7-\alpha}$, Air Quenched Samples (Å)

x	a(Å)	c(Å)	Oxygen Content
0	3.874(1)	20.171(6)	6.58 ± 0.05
0.2	3.864(1)	20.149(10)	6.45 ± 0.05
0.4	3.855(1)	20.142(7)	6.38 ± 0.05
0.6	3.851(1)	20.138(6)	6.37 ± 0.05
0.8	3.842(1)	20.135(6)	6.35 ± 0.05

6.2.2 Preparation of $Sr_3Fe_{2-x}Co_xO_{7-\beta}$

CoO, $SrCO_3$ and Fe_2O_3 in the correct molar proportions, covering the range $0 \leq x \leq 0.4$ were intimately ground and heated at 1100°C in a box furnace. After air quenching and regrinding the samples were returned to the box furnace and heated for a further 24hrs at

146

Table 6.2 Lattice Parameters for $Sr_3Fe_{2-x}Ni_xO_{7-\alpha}$, Oxygen Annealed Samples (Å)

	a(Å)	c(Å)	Oxygen Content
0	3.868(1)	20.164(2)	6.75 ± 0.05
0.2	3.861(1)	20.142(7)	6.66 ± 0.05
0.4	3.853(1)	20.101(9)	6.71 ± 0.05
0.6	3.846(2)	20.076(11)	6.71 ± 0.05
0.8	3.839(2)	20.024(8)	6.72 ± 0.05

Table 6.3 Lattice Parameters for $Sr_3Fe_{2-x}Ni_xO_{7-\alpha}$, Reduced Samples (Å)

	a(Å)	c(Å)	Oxygen Content
0	3.890(1)	20.040(1)	6.00 ± 0.05
0.2	3.887(1)	20.104(4)	5.90 ± 0.05
0.4	3.875(1)	20.184(7)	5.80 ± 0.05
0.6	3.855(2)	20.314(6)	5.70 ± 0.05
0.8	3.835(2)	20.465(15)	5.60 ± 0.05

1200°C. On quenching to room temperature, these samples proved to be sensitive to atmospheric conditions and were thereafter transferred to a glove box whilst still hot. The samples were mounted in the x-ray sample holder in the glove box which was sealed using mylar film. Derivation of cell parameters for x = 0.2 gave a = 3.837(3)Å and c = 20.439(10)Å for the majority phase although there were additional reflections in the diffraction pattern. Many attempts were made to produce single phase samples in this system but they were unsuccessful, usually yielding a second phase of poor crystallinity.

6.2.3 Preparation of $Sr_3Co_{2-x}Ni_xO_{7-\phi}$

CoO, NiO and $SrCO_3$ in the correct molar proportions, covering the range $0 \leq x \leq 1.2$, were heated at 1200°C in a box furnace and air quenched. Progressive increases in the nickel content showed that the solution limit was 1.0; further increase in the nickel content resulted in additional reflections belonging to NiO appearing in the diffraction pattern. Oxygen content was measured by thermogravimetric analysis. X-ray diffraction analysis of the products after heating at 1200°C overnight showed a phase change from orthorhombic to tetragonal at $x = 0.4$. The changes in lattice parameters are summarised in Table 6.4. The lattice parameters of the pure cobalt compound is also included in Table 6.4 for comparison.

Attempts to increase the oxygen content by prolonged annealing in air and oxygen were unsuccessful, generally producing a mixture of phases of poor crystallinity which were very sensitive to atmospheric conditions.

Table 6.4 Lattice Parameters for $Sr_3Co_{2-x}Ni_xO_{7-\phi}$ (Å)

x	a(Å)	c(Å)	Oxygen Content
0	a = 3.863(1) b = 11.432(4)	20.227(10)	5.78 ± 0.05
0.2	a = 3.863(1) b = 11.442(3)	20.271(9)	5.71 ± 0.05
0.4	a = 3.839(1)	20.301(10)	5.68 ± 0.05
0.6	a = 3.835(1)	20.289(8)	5.66 ± 0.05
0.8	a = 3.832(1)	20.277(7)	5.62 ± 0.05
1.0	a = 3.828(1)	20.268(5)	5.60 ± 0.05

6.3 Powder Neutron Diffraction

6.3.1 $Sr_3Fe_{2-x}Ni_xO_{7-\alpha}$

Powder diffraction data were collected on both oxygen annealed and air sintered samples for x = 0.2, 0.4, 0.6 and 0.8 using the high resolution diffractometer, HRPD. Large samples were synthesised, $c.a.$ 5g, for the neutron experiments. Collection times varied from 4-6hrs giving excellent quality data; all atoms have large scattering lengths.

6.3.2 $Sr_3Co_{2-x}Ni_xO_{7-\Phi}$

Powder diffraction data were collected on samples x = 0.2, 0.6 and 1.0 using the high resolution diffractometer, HRPD. Large samples, $c.a.$ 5g, were synthesised for the neutron experiments. These samples were transferred hot to a glove box where they were separated into two specimens, one of which (0.5g) was analysed using powder x-ray diffraction and thermogravimetric analysis to ensure sample purity and measure the oxygen content, and the other, (4,-5g) was transferred to a vanadium can and sealed with indium wire. Long collection times were employed (>12hrs) to obtain high quality data for structure refinement and overcome the small scattering length of cobalt (b = 0.25 x 10⁻ $^{12}Fm^2$).

6.4 Mössbauer Spectroscopy.

Mössbauer spectra were collected on the $Sr_3Fe_{2-x}Ni_xO_{7-\alpha}$, air quenched, samples between room temperature and 4.2K. Absorbers were prepared of finely ground samples together with boron nitride to randomise the orientations of the microcrystals. The samples were weighed to give optimum signal to noise (4) Sources of up to 100mCi in Rh were used and the spectrometers calibrated using α iron at room temperature.

6.5 Results and Discussion

Structure Refinements

6.5.1 $Sr_3Fe_{2-x}Ni_xO_{7-\alpha}$

Full profile refinements were carried out in the space group I4/mmm using the starting models of $Sr_3Fe_2O_{6.58}$ and $Sr_3Fe_2O_{6.75}$ (3) respectively for the air sintered and oxygen annealed samples.

Initial stages of the refinement included profile parameters such as scale factor, cell parameters and peak shape functions. Atomic parameters were then refined. Refinement of oxygen occupancy located the vacancies on the O3 site (Figure 6.1) and indicated all other oxygen sites were filled with an occupancy factor barely varying from unity and always within the e.s.d. Full occupancy was therefore maintained on the O1 and O2 sites for the rest of the refinement. No additional peak was present in the diffraction pattern suggesting that the formation of solid solution was successful and the samples were above any magnetic ordering temperature. Final stages of the refinement included isotropic temperature factors. Table 6.5a-d and 6.6a-d contain refined parameters for all four compounds under air sintered and oxygen annealed conditions. Bond lengths are given in Table 6.7 and 6.8, compared with those of the pure iron sample prepared under similar conditions. An example of the profile fit is shown in Figure 6.2.

6.5.2 $Sr_3Co_{2-x}Ni_xO_{7-\Phi}$

Full profile refinements were carried out in the space groups Immm for x = 0.2, and I4/mmm for x = 0.6 and 1.0, using the starting models of $Sr_3Co_2O_{5.78}$ (5) and $Sr_3Fe_2O_6$ (3) respectively for the air sintered and oxygen annealed samples.

In the case of the orthorhombic sample, x = 0.2, simultaneous refinement of isotropic temperature factors and atomic positional parameters gave rise to unstable parameters which were varying outside their e.s.d. Having fixed the positional parameters refinement of temperature factors proceeded smoothly. High temperature factors indicated possible partial occupancy on the O3, O7 and O8 sites (as defined in Figure 6.3).

150
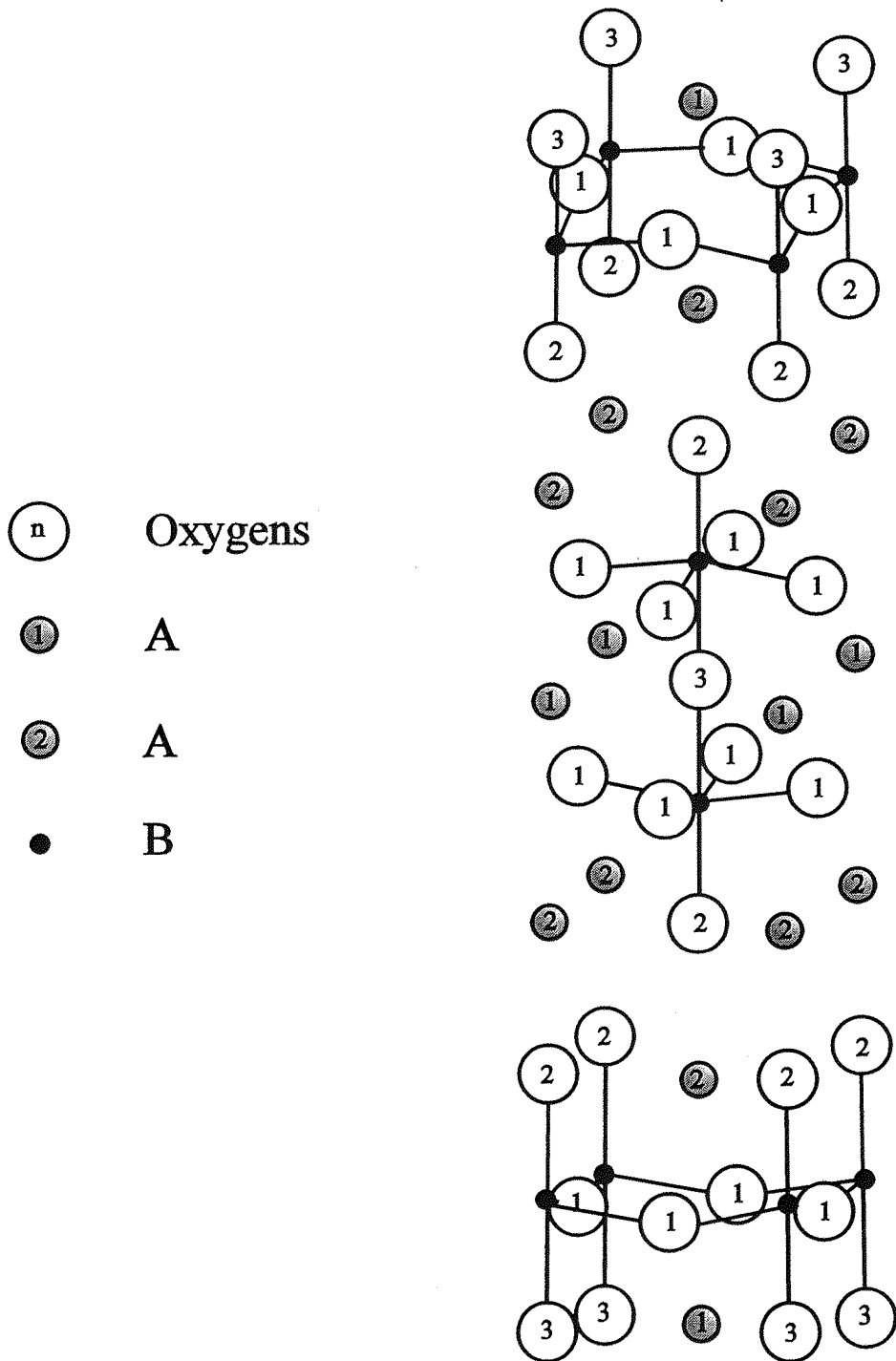
Figure 6.1 Diagram of the Structure of A_3B_2O7-q

151

Table 6.5a Refined Atomic Parameters for $Sr_3Fe_{1.8}Ni_{0.2}O_{6.45}$

Atom	Site	x	y	z	B_{eq}	Occupancy
Sr1	2b	0	0	½	0.81(5)	1.00
Sr2	4e	0	0	0.3180(1)	1.00(3)	1.00
Fe/Ni	4e	0	0	0.1004(1)	0.70(2)	0.9/0.1
O1	8g	0	½	0.0888(1)	1.02(2)	1.00
O2	4e	0	0	0.1956(1)	1.01(3)	1.00
O3	2a	0	0	0	0.98(17)	0.44(1)

$a = 3.8653(1)$Å, $c = 20.1560(1)$Å. $R_{wp} = 11.35$, $R_{exp} = 7.05$, $\chi^2 = 2.59$

Table 6.5b Refined Atomic Parameters for $Sr_3Fe_{1.6}Ni_{0.4}O_{6.38}$

Atom	Site	x	y	z	B_{eq}	Occupancy
Sr1	2b	0	0	½	1.06(4)	1.00
Sr2	4e	0	0	0.3184(1)	0.86(3)	1.00
Fe/Ni	4e	0	0	0.1004(1)	0.70(2)	0.8/0.2
O1	8g	0	½	0.0883(1)	1.09(3)	1.00
O2	4e	0	0	0.1956(1)	1.04(3)	1.00
O3	2a	0	0	0	1.14(2)	0.36(2)

$a = 3.8586(1)$Å, $c = 20.1541(1)$Å. $R_{wp} = 11.63$, $R_{exp} = 5.51$, $\chi^2 = 4.45$

Table 6.5c Refined Atomic Parameters for $Sr_3Fe_{1.4}Ni_{0.6}O_{6.37}$

Atom	Site	x	y	z	B_{eq}	Occupancy
Sr1	2b	0	0	½	1.05(5)	1.00
Sr2	4e	0	0	0.3186(1)	0.97(4)	1.00
Fe/Ni	4e	0	0	0.1004(1)	0.75(3)	0.7/0.3
O1	8g	0	½	0.0876(1)	1.20(3)	1.00
O2	4e	0	0	0.1956(1)	1.04(3)	1.00
O3	2a	0	0	0	1.14(25)	0.35(9)

$a = 3.8505(1)Å$, $c = 20.1490(1)Å$. $R_{wp} = 12.67$, $R_{exp} = 8.85$, $\chi^2 = 2.05$

Table 6.5d Refined Atomic Parameters for $Sr_3Fe_{1.2}Ni_{0.8}O_{6.35}$

Atom	Site	x	y	z	B_{eq}	Occupancy
Sr1	2b	0	0	½	0.97(4)	1.00
Sr2	4e	0	0	0.3186(1)	0.68(3)	1.00
Fe/Ni	4e	0	0	0.1004(1)	0.59(3)	0.6/0.4
O1	8g	0	½	0.0877(1)	0.59(2)	1.00
O2	4e	0	0	0.1958(1)	1.07(4)	1.00
O3	2a	0	0	0	0.92(24)	0.40(9)

$a = 3.8430(1)Å$, $c = 20.1440(1)Å$. $R_{wp} = 15.56$, $R_{exp} = 5.31$, $\chi^2 = 8.59$

Table 6.6a Refined Atomic Parameters for $Sr_3Fe_{1.8}Ni_{0.2}O_{6.66}$

Atom	Site	x	y	z	B_{eq}	Occupancy
Sr1	2b	0	0	½	0.88(3)	1.00
Sr2	4e	0	0	0.3173(1)	0.73(2)	1.00
Fe/Ni	4e	0	0	0.0983(1)	0.51(2)	0.9/0.1
O1	8g	0	½	0.0925(1)	0.87(2)	1.00
O2	4e	0	0	0.1940(1)	0.90(2)	1.00
O3	2a	0	0	0	0.92(9)	0.75(1)

$a = 3.8575(1)Å, \quad c = 20.1089(1)Å. \quad R_{wp} = 10.65, \ R_{exp} = 6.92, \ \chi^2 = 2.37$

Table 6.6b Refined Atomic Parameters for $Sr_3Fe_{1.6}Ni_{0.4}O_{6.71}$

Atom	Site	x	y	z	B_{eq}	Occupancy
Sr1	2b	0	0	½	0.56(4)	1.00
Sr2	4e	0	0	0.3177(1)	0.51(4)	1.00
Fe/Ni	4e	0	0	0.0983(1)	0.32(2)	0.8/0.2
O1	8g	0	½	0.0920(1)	0.66(3)	1.00
O2	4e	0	0	0.1940(1)	0.63(4)	1.00
O3	2a	0	0	0	0.23(6)	0.66(2)

$a = 3.8523(1)Å, \quad c = 20.0900(1)Å. \quad R_{wp} = 11.94, \ R_{exp} = 8.91, \ \chi^2 = 1.80$

Table 6.6c Refined Atomic Parameters for $Sr_3Fe_{1.4}Ni_{0.6}O_{6.71}$

Atom	Site	x	y	z	B_{eq}	Occupancy
Sr1	2b	0	0	½	0.55(2)	1.00
Sr2	4e	0	0	0.3175(1)	0.35(2)	1.00
Fe/Ni	4e	0	0	0.0982(1)	0.17(1)	0.7/0.3
O1	8g	0	½	0.0924(1)	0.53(2)	1.00
O2	4e	0	0	0.1936(1)	0.55(2)	1.00
O3	2a	0	0	0	0.54(8)	0.70(9)

$a = 3.8466(1)$Å, $c = 20.0565(1)$Å. $R_{wp} = 8.39$, $R_{exp} = 4.23$ $\chi^2 = 3.89$

Table 6.6d Refined Atomic Parameters for $Sr_3Fe_{1.2}Ni_{0.8}O_{6.72}$

Atom	Site	x	y	z	B_{eq}	Occupancy
Sr1	2b	0	0	½	0.79(3)	1.00
Sr2	4e	0	0	0.3175(1)	0.49(2)	1.00
Fe/Ni	4e	0	0	0.0982(1)	0.35(2)	0.6/0.4
O1	8g	0	½	0.0924(1)	0.65(2)	1.00
O2	4e	0	0	0.1939(1)	0.71(2)	1.00
O3	2a	0	0	0	0.88(1)	0.71(1)

$a = 3.8431(1)$Å, $c = 20.0315(1)$Å. $R_{wp} = 8.76$, $R_{exp} = 4.45$, $\chi^2 = 3.88$

Table 6.7 Derived Bond Lengths for Oxygen Annealed $Sr_3Fe_{2-x}Ni_xO_{7-\alpha}$ (Å)

	$Sr_3Fe_2O_{6.75}$	$Sr_3Fe_{1.8}Ni_{0.2}O_{6.66}$	$Sr_3Fe_{1.6}Ni_{0.4}O_{6.71}$	$Sr_3Fe_{1.4}Ni_{0.6}O_{6.71}$	$Sr_3Fe_{1.2}Ni_{0.8}O_{6.72}$
Sr1 - O1	2.681(1) x 8	2.680(1) x 8	2.670(1) x 8	2.670(1) x 8	2.667(1) x 8
Sr1 - O3	2.732(1) x 4*	2.728(1) x 4*	2.724(1) x 4*	2.720(1) x 4*	2.718(1) x 4*
Sr2 - O1	2.655(2) x 4	2.648(2) x 4	2.646(2) x 4	2.639(2) x 4	2.634(2) x 4
Sr2 - O2	2.485(4) x 1	2.479(3) x 1	2.486(3) x 1	2.485(3) x 1	2.476(3) x 1
Sr2 - O2	2.743(1) x 4	2.737(1) x 4	2.734(1) x 4	2.730(1) x 4	2.727(1) x 4
Fe(Ni) - O1	1.936(1) x 4	1.932(1) x 4	1.930(1) x 4	1.927(1) x 4	1.925(1) x 4
Fe(Ni) - O2	1.932(4) x 1	1.924(3) x 1	1.920(3) x 1	1.913(3) x 1	1.915(3) x 1
Fe(Ni) - O3	1.983(2) x 1*	1.977(2) x 1*	1.975(2) x 1*	1.970(2) x 1*	1.969(2) x 1*

* denotes partially filled site.
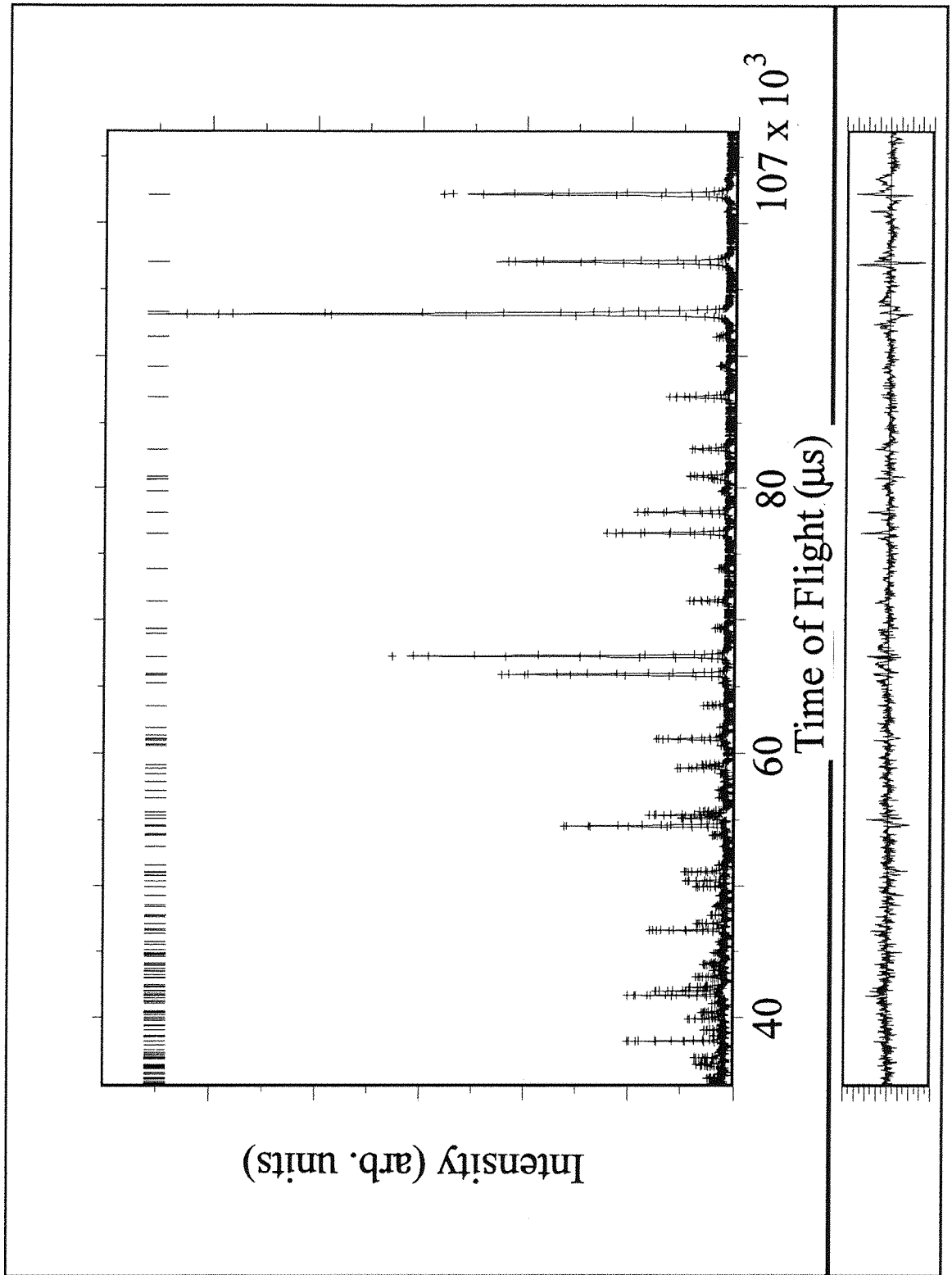
Figure 6.2 Profile Fit for the x = 0.4 Oxygen Annealed Sample.

157

Table 6.8 Derived Bond Lengths for Air Sintered $Sr_3Fe_{2-x}Ni_xO_{7-\alpha}$ (Å)

	$Sr_3Fe_2O_{6.58}$	0.2	0.4	0.6	0.8
Sr1 - O1	2.669(1) x 8	2.634(1) x 8	2.625(1) x 8	2.612(1) x 8	2.610(1) x 8
Sr1 - O3	2.737(1) x 4*	2.733(1) x 4*	2.728(1) x 4*	2.723(1) x 4*	2.717(1) x 4
Sr2 - O1	2.672(2) x 4	2.694(2) x 4	2.695(2) x 4	2.698(2) x 4	2.694(1) x 4
Sr2 - O2	2.485(4) x 1	2.467(3) x 1	2.475(3) x 1	2.476(3) x 1	2.474(3) x 1
Sr2 - O2	2.748(1) x 4	2.747(1) x 4	2.743(1) x 4	2.738(1) x 4	2.733(1) x 4
Fe(Ni) - O1	1.942(1) x 4	1.947(1) x 4	1.945(1) x 4	1.942(1) x 4	1.939(1) x 4
Fe(Ni) - O2	1.933(2) x 1	1.918(3) x 1	1.919(3) x 1	1.920(3) x 1	1.922(3) x 1
Fe(Ni) - O3	2.002(2) x 1*	2.024(2) x 1*	2.024(2) x 1*	2.023(2) x 1*	2.023(2) x 1*

* denotes partially filled site.

158
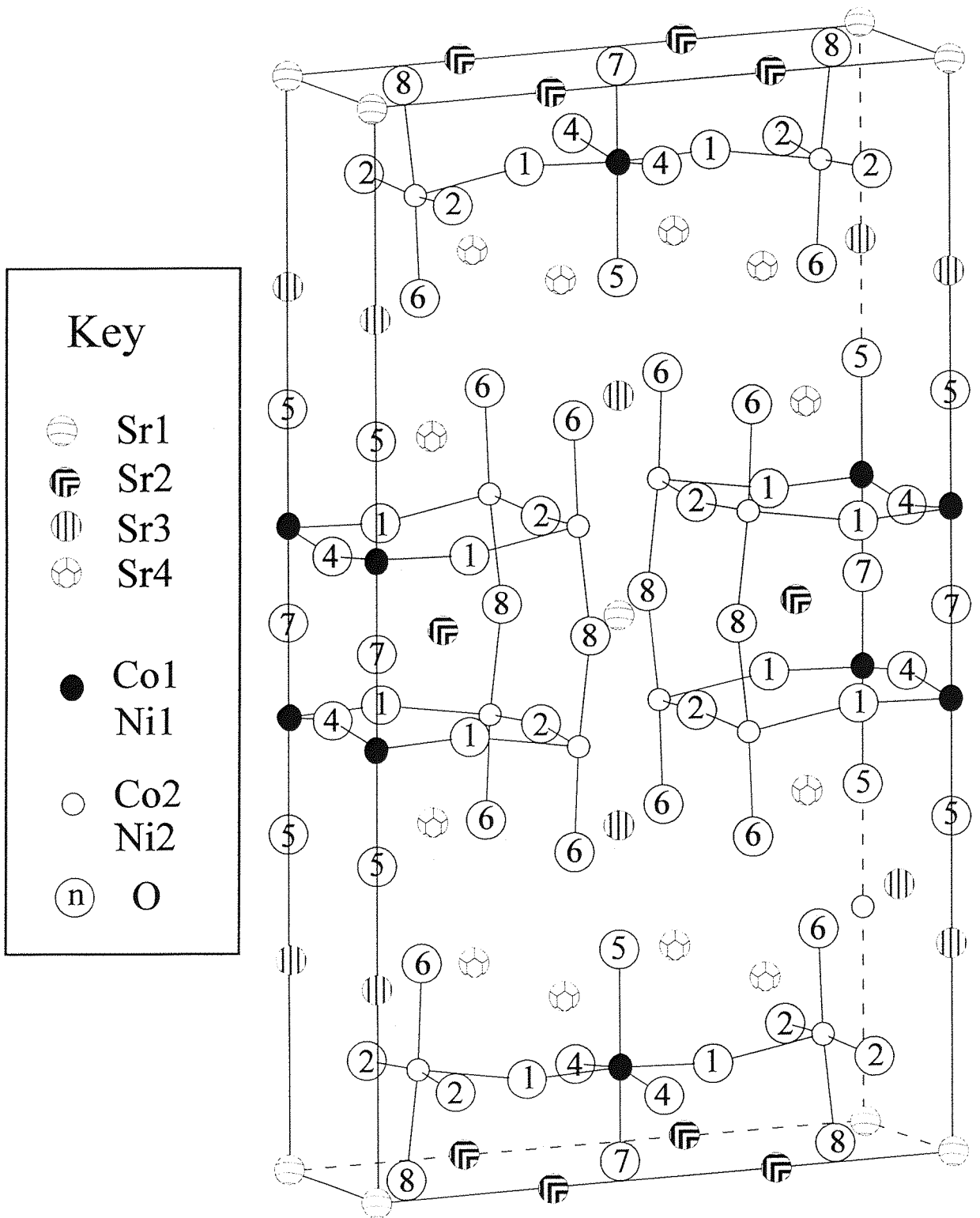
Figure 6.3 Diagram of the Tripled Orthorhombic Structure

159

Refinement of oxygen occupancy on these sites led to complete exclusion of the O3 site from the refinement and partial occupancy on the O7 and O8 sites. In fact, attempts to place oxygen on the O3 site, with subsequent refinement resulted in unstable temperature factor, z-coordinate and occupancy which oscillated about zero. Simultaneous refinement of temperature factors and occupancies was not possible and several cycles of fixing one and varying the other were performed to give steady values.

Final refined parameters are shown in Table 6.11. Calculated strontium and cobalt bond lengths are give in Tables 6.12a and 6.12b respectively. Bond angles around the transition metal centres are given in Table 6.12c.

Refinement of x = 0.6 and 1.0 proceeded smoothly in the space group I4/mmm. Atomic parameters could be refined simultaneously with oxygen occupancies and temperature factors. Refinement of oxygen occupancies suggested partial vacancies on O1 and O3 sites with full occupancy on the O2 site. The latter was subsequently fixed and partial occupancy refined on the O1 and O3 site. Final stages of the refinement included simultaneous refinement of all isotropic temperature factors and occupancies. Final refined parameters are shown in Table 6.9a and 6.9b and calculated bond distance in Table 6.10. Figures 6.4 and 6.5 show an example of the profile fit for the tetragonal and orthorhombic region respectively.

Mössbauer Spectroscopy.

The Mössbauer parameters for the nickel doped $Sr_3Fe_2O_{7-x}$ system at room temperature and 4.2K are given in Table 6.13 and 6.14. Examples of the spectra at room temperature and at 4.2K are given in Figures 6.6 and 6.7. In comparison to the spectrum from the iron system (Figures 4.7 and 4.8) these are much more complex. Generally these spectra can only be fitted successfully by using three different iron signals with different shifts. Two of these are very similar to that of the pure iron system and the third has intermediate parameters. The last is assumed to be iron(IV). The approximate iron oxidation state calculated from the relative proportions of the iron signals in the Mössbauer spectrum are given in Tables 6.13 and 6.14 with the nickel valence calculated from the oxygen stoichiometry. This implies the nickel oxidation state in all these materials is greater than two although when dealing with such low values of x the errors are likely to be large.

Table 6.9a Refined Atomic Parameters for $Sr_3Co_{1.4}Ni_{0.6}O_{5.66}$

Atom	Site	x	y	z	B_{eq}	Occupancy
Sr1	2b	0	0	½	1.71(3)	1.00
Sr2	4e	0	0	0.3175(1)	1.03(2)	1.00
Fe/Ni	4e	0	0	0.0988(1)	0.80(1)	0.7/0.3
O1	8g	0	½	0.0891(1)	1.14(3)	0.82(1)
O2	4e	0	0	0.1953(1)	1.06(2)	1.00
O3	2a	0	0	0	0.26(12)	0.37(1)

a = 3.8352(1)Å,   c = 20.2894(1)Å. R_{wp} = 6.48, R_{exp} = 4.11 χ^2 = 2.49

Table 6.9b Refined Atomic Parameters for $Sr_3CoNiO_{5.60}$

Atom	Site	x	y	z	B_{eq}	Occupancy
Sr1	2b	0	0	½	1.88(4)	1.00
Sr2	4e	0	0	0.3176(1)	1.12(3)	1.00
Fe/Ni	4e	0	0	0.0986(1)	0.91(3)	0.5/0.5
O1	8g	0	½	0.0894(1)	1.28(5)	0.81(1)
O2	4e	0	0	0.1949(1)	1.13(3)	1.00
O3	2a	0	0	0	1.16(16)	0.38(1)

a = 3.8281(1)Å,   c = 20.2684(1)Å. R_{wp} = 9.02, R_{exp} = 4.16 χ^2 = 4.70

161

Table 6.10 Calculated bond lengths for $Sr_3Co_{2-x}Ni_xO_{7-\delta}$ x = 0.6 and 1.0 (Å).

Atom - Atom	$Sr_3Co_{1.4}Ni_{0.6}O_{5.66}$	$Sr_3CoNiO_{5.60}$
Sr1 - O1	2.774(2) x 8*	2.767(2) x 8*
Sr1 - O3	2.712(1) x 4*	2.707(1) x 4*
Sr2- O1	2.562(2) x 4*	2.559(2) x 4*
Sr2 - O2	2.479(3) x 1	2.487(3) x 1
Sr2 - O2	2.724(1) x 4	2.719(1) x 4
Co/Ni - O1	1.928(1) x 4*	1.923(1) x 4*
Co/Ni - O2	1.958(3) x 1	1.952(3) x 1
Co/Ni - O3	2.005(2) x 1*	1.999(2) x 1*

* denotes partially filled site.

Table 6.11 Refined Parameters for Orthorhombic $Sr_3Co_{2-x}Ni_xO_{7-\delta}$ (Å).

	x	y	z	B_{eq}	Site
Sr1	0	0	0	1.98(28)	1.00
Sr2	0	0.3327(10)	0	2.06(14))	1.00
Sr3	0	0	0.1818(5)	2.29(20)	1.00
Sr4	0	0.3310(6)	0.1828(2)	1.62(9)	1.00
Co1	0	0	0.5974(8)	1.76(27)	1.00
Ni1	0	0	0.5974(8)	1.76(27)	1.00
Co2	0	0.3336(10)	0.5985(4)	0.90(13)	1.00
Ni2	0	0.3336(10)	0.5985(4)	0.90(13)	
O1	0	0.1657(5)	0.4109(2)	0.46(5)	1.00
O2	0	0.1650(7)	0.0915(3)	2.60(2)	1.00
O3	½	0	z	-	0
O4	½	0	0.4125(7)	2.78(2)	1.00
O5	0	0	0.6950(5)	1.65(18)	1.00
O6	0	0.3318(7)	0.6955(2)	1.66(9)	1.00
O7	0	0	½	1.44(5)	0.36(2)
O8	0	0.3408(14)	½	1.09(3)	0.39(1)

a = 3.8628(1)Å   b = 11.4420(1)Å   c = 20.2706(1)Å

R_{wp} = 9.77 R_{exp} = 3.19 χ^2 = 9.36

Oxygen content = 5.71(3)

Table 6.12a Calculated Strontium Bond Lengths for $Sr_3Co_{1.8}Ni_{0.2}O_{7-\Phi}$ (Å).

	$Sr_3Co_{1.8}Ni_{0.2}O_{5.71}$
Sr1 - O2	2.647(7) x 4
Sr1 - O8	2.654(11) x 4*
Sr2 - O1	2.645(14) x 4
Sr2 - O2	2.670(16) x 2
Sr2 - O4	2.609(17) x 2
Sr2 - O6	2.771(11) x 2
Sr2 - O7	2.719(1) x 2*
Sr3 - O2	2.630(10) x 2
Sr3 - O5	2.497(17) x 1
Sr3 - O6	2.740(6) x 4
Sr4 - O1	2.707(4) x 2
Sr4 - O2	2.652(9) x 1
Sr4 - O4	2.732(12) x 1
Sr4 - O5	2.744(5) x 2
Sr4 - O6	2.696(7) x 2
Sr4 - O6	2.468(7) x 1

* denotes partially filled site

164

Table 6.12b Calculated Cobalt Bond Lengths for $Sr_3Co_{1.8}Ni_{0.2}O_{7-\phi}$ (Å).

	$Sr_3Co_{1.8}Ni_{0.2}O_{5.71}$
Co1 - O1	1.903(6) x 2
Co1 - O4	1.941(2) x 2
Co1 - O5	1.978(21) x 1
Co1 - O8	1.974(16) x 1*
Co2 - O1	1.931(12) x 1
Co2 - O2	1.934(14) x 2
Co2 - O6	1.965(9) x 1
Co2 - O7	1.998(8) x 1*

Table 6.12c Derived Bond Angles for the Transition Metal Centre (°).

Atom - Co1 - Atom	Angle (°)	Atom - Co2 - Atom	Angle(°)
O1 - Co1 - O1	170.4	O1 - Co2 - O1	89.9
O1 - Co1 - O4	89.5	O1 - Co2 - O6	94.9
O1 - Co1 - O5	94.8	O1 - Co2 - O8	86.5
O1 - Co1 - O7	85.1	O2 - Co2 - O5	94.2
O4 - Co1 - O5	95.7	O2 - Co2 - O8	85.7
O4 - Co1 - O7	180.0	O6 - Co2 - O8	178.6
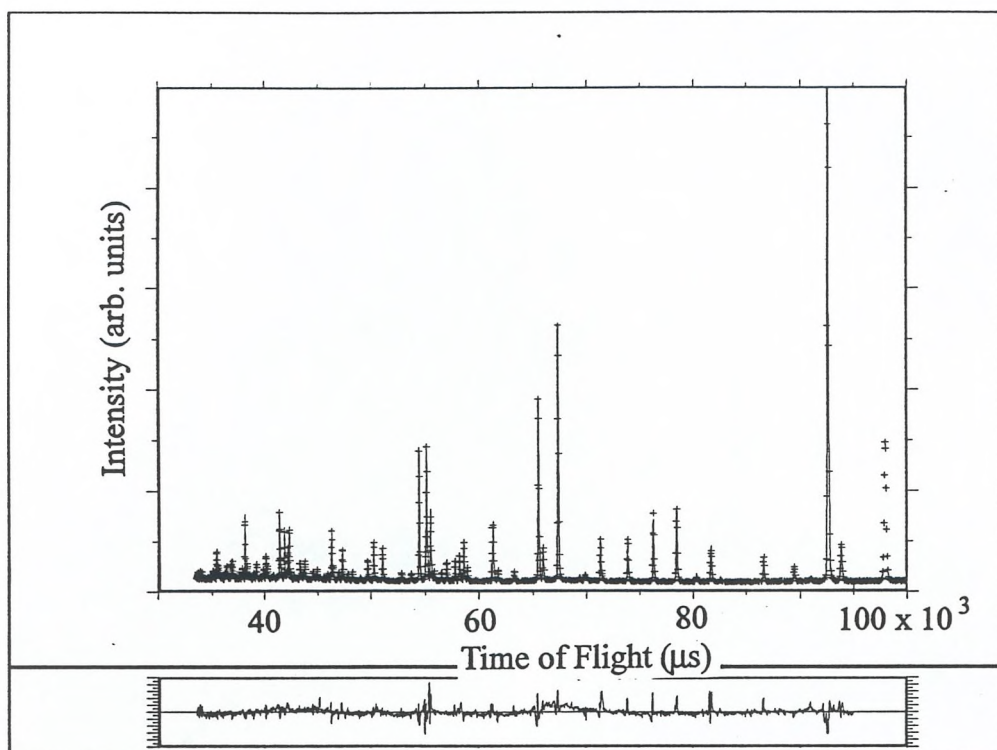
Figure 6.4 Refinement Profile for $Sr_3CoNiO_{5.60}$
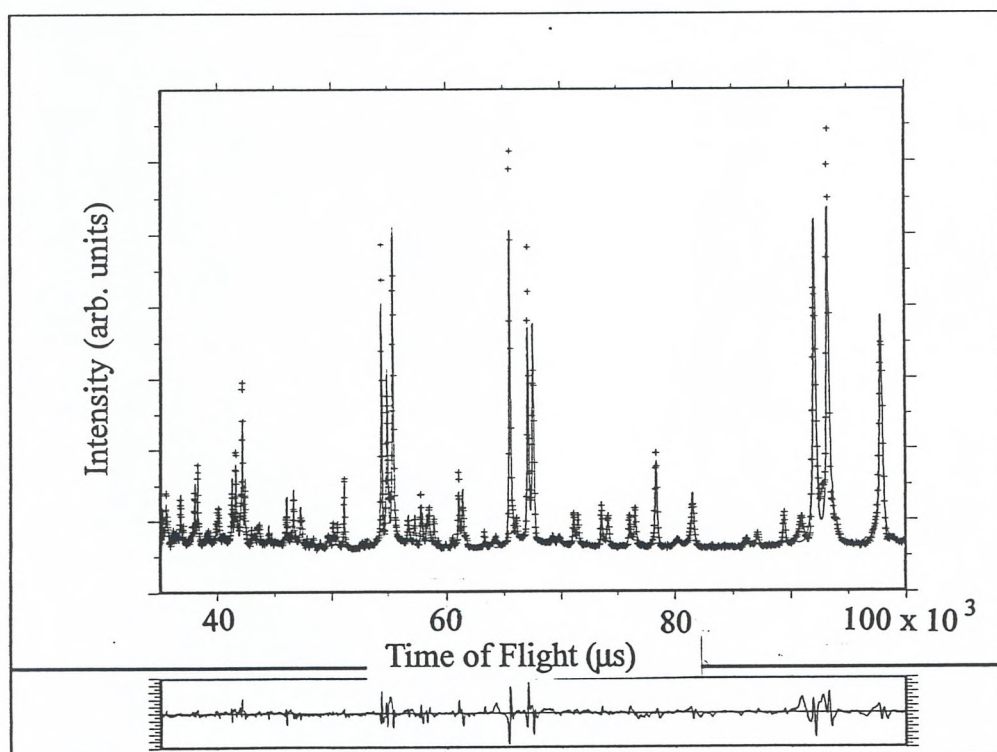
Figure 6.5 Refinement Profile for $Sr_3Co_{1.8}Ni_{0.2}O_{5.71}$

166
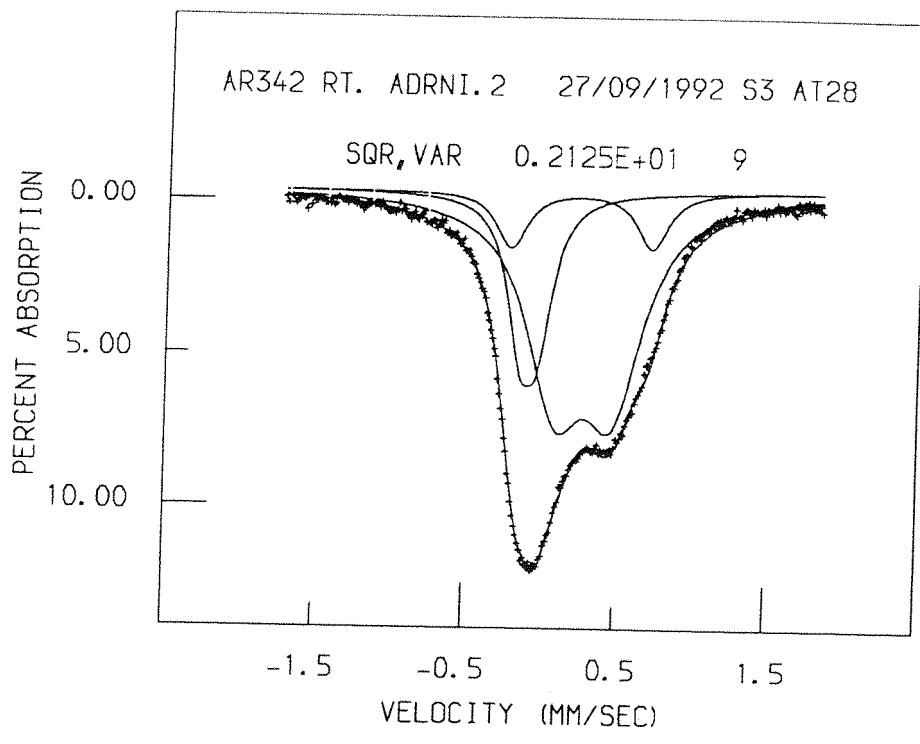
Figure 6.6 Mössbauer Spectrum for $Sr_3Fe_{1.8}Ni_{0.2}O_{6.45}$ at 300K
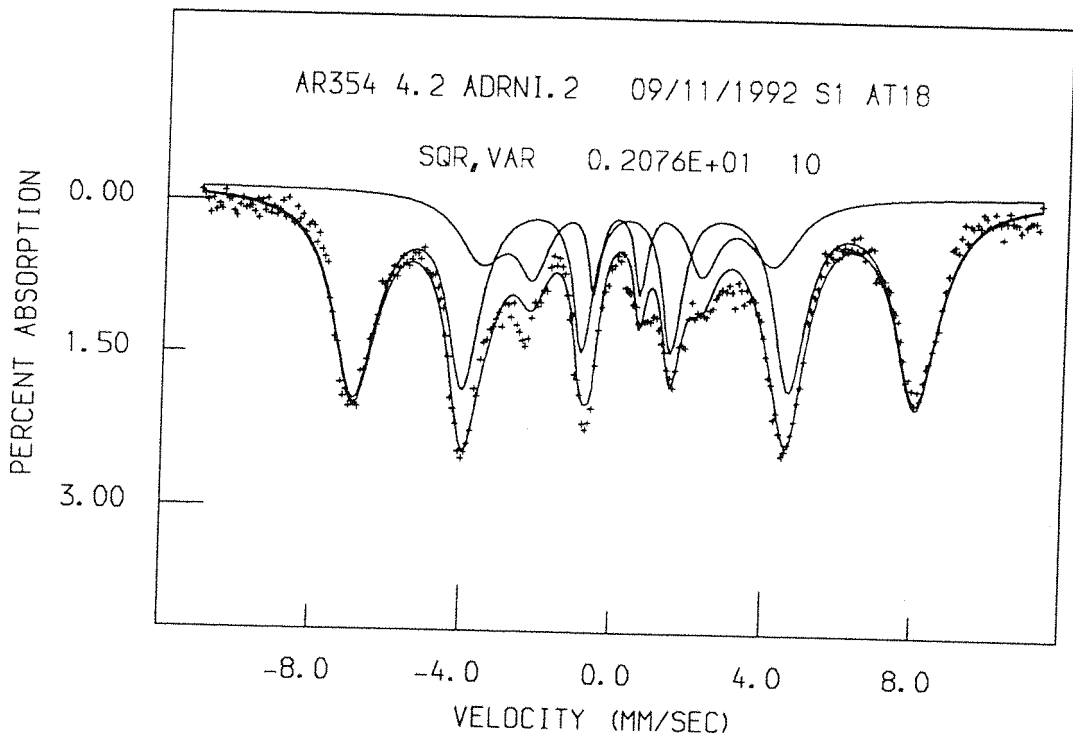
Figure 6.7 Mössbauer Spectrum for $Sr_3Fe_{1.8}Ni_{0.2}O_{6.45}$ at 4.2K

Table 6.13 Mössbauer Parameters at 300K for the Air Quenched Samples.

x	Chemical Shift	Quad Splitting	% Int	Iron Valence	Calc Fe Valence	Calc Ni Valence
0.2	$-0.09mms^{-1}$	$0.13mms^{-1}$	21	Fe^{5+}		
	$0.24mms^{-1}$	$0.94mms^{-1}$	11	$"Fe^{4+}"$	3.53	2.73
	$0.29mms^{-1}$	$0.38mms^{-1}$	68	Fe^{3+}		
0.4	$-0.08mms^{-1}$	$0.16mms^{-1}$	22	Fe^{5+}		
	$0.15mms^{-1}$	$0.42mms^{-1}$	22	$"Fe^{4+}"$	3.66	2.31
	$0.32mms^{-1}$	$0.44mms^{-1}$	56	Fe^{3+}		
0.6	$-0.06mms^{-1}$	$0.16mms^{-1}$	24	Fe^{5+}		
	$0.16mms^{-1}$	$0.25mms^{-1}$	32	$"Fe^{4+}"$	3.80	2.25
	$0.33mms^{-1}$	$0.39mms^{-1}$	44	Fe^{3+}		

Table 6.14 Mössbauer Parameters at 4.2K for the Air Quenched Samples

x	Chemical Shift	Quad Splitting	Hyp. Field.	% Int	Iron Valence	Calc Fe Valence	Calc Ni Valence
0.2	$0.14mms^{-1}$	$0.27mms^{-1}$	239kG	27	Fe^{5+}		
	$0.42mms^{-1}$	$0.26mms^{-1}$	462kG	73	Fe^{3+}	3.54	2.64
0.4	$0.12mms^{-1}$	$0.21mms^{-1}$	254kG	22	Fe^{5+}		
	$0.38mms^{-1}$	$0.22mms^{-1}$	396kG	22	$"Fe^{4+}"$	3.66	2.31
	$0.40mms^{-1}$	$0.56mms^{-1}$	454kG	56	Fe^{3+}		
0.6	$0.06mms^{-1}$	$-0.08mms^{-1}$	290kG	24	Fe^{5+}		
	$0.38mms^{-1}$	$0.14mms^{-1}$	418kG	34	$"Fe^{4+}"$	3.82	2.25
	$0.40mms^{-1}$	$-0.02mms^{-1}$	457kG	42	Fe^{3+}		

$"Fe^{4+}"$ indicates possibility of averaged state.

The average iron valence is shown to increase with x. The charge states for the x = 0.2 sample are reasonably well defined, for higher values of x, the nominally Fe^{4+}, becomes less well defined and the clarity worsens as x increases. Therefore, at x = 0.8 the assignment of the 4.2K spectra is almost impossible with any certainty. This parameter for "iron(IV)" maybe in fact due to an averaged iron(III)/iron(V) signal where the electron hopping is too fast for Mössbauer spectroscopy to discern.

Discussion

Figure 6.8 shows the variation in the cell parameters with varying nickel content for air sintered (+), oxygen annealed (•) and reduced (*) samples of the $Sr_3Fe_{2-x}Ni_xO_{7-\alpha}$ series. The a-parameter is simply controlled by the O1 - M - O1 distance and a drop in the magnitude of this distance will be a result of the larger Fe^{3+} (0.645Å (4)) being replaced by a smaller ion e.g. Ni^{3+} (0.56Å (4)) if the O1 site remains fully occupied. In all cases the a parameter reduces linearly with increasing nickel content. For the air sintered samples and oxygen annealed samples the oxygen content stays approximately constant over the range of x with the O1 site remaining fully occupied. In the case of the reduced sample, the Fe^{3+} ion is, presumably, now substituted by the larger Ni^{2+} (0.690Å (4)) ion and if the oxygen content was constant across the range of x the lattice parameter, a, would be expected to rise. However, the oxygen content has now dropped below six and an additional oxygen site will now be partially vacant (i.e assuming the O3 site becomes entirely vacant when α = 1.0 as in the pure iron system (1)). Since the size of the a parameter continues to fall then the vacancy is likely to be on the O1 site which affects the size of the a parameter. This is further confirmed by the c parameter graph which falls for the oxygen annealed and air sintered samples with x but rises in the case of the reduced sample. Here the larger size of the Ni^{2+} cation effects an increase in the c parameter and therefore the oxygen vacancies are unlikely to involve c. The length of the c parameter is affected by oxygen vacancies on the O2 and O3 sites which lie above and below the O1 - M - O1 plane. The latter, as seen from the $Sr_3Fe_2O_6$, is completely vacant when the stoichiometry reaches O_6. Assuming these samples are similar to the pure iron samples then the O2 site is likely to be filled. This is probably only the case when oxygen ordering has time to occur and the experimental result would probably be different for an
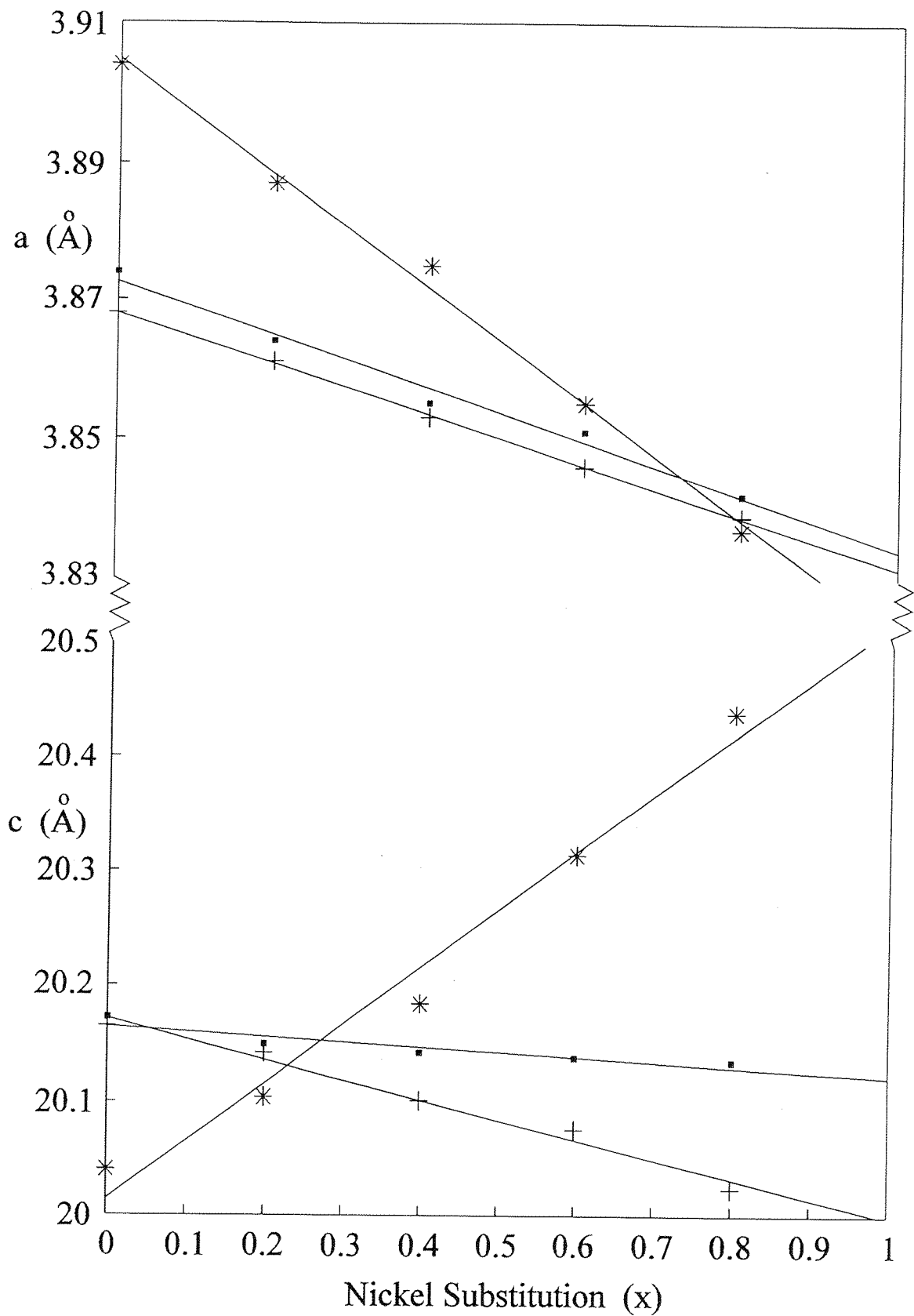
Figure 6.8 Change in Lattice Parameters with Nickel Content in $Sr_3Fe_{2-x}Ni_xO_{7-\alpha}$

171

air quenched sample. A better understanding of this behaviour could be achieved by preparing some more materials with the lower oxygen content.

The reduced samples, suggest oxygen vacancies on the O1 site. This result applies to the bulk sample and not the individual transition metal ion environments. Therefore, local changes in transition metal coordination or local ordering of the transition metal ions would not be resolved. In order to study the system more fully, a separate technique would be needed, which studies isolated ion configuration, such as EXAFS.

Bond valence calculations (6) have been performed on the metal sites and are summarised in Table 6.15a and 6.15b. For the transition metals this was achieved using the parameters for Fe^{3+} and Ni^{2+} since no parameters are available for the more oxidised ions. This shows there is little change in the calculated bond valence of either metal site with changing x. The calculations show a divalent nickel cation would be overbonded in this environment and supports the hypothesis that the oxidation state of the doped nickel ions is greater than two. The bond lengths around the transition metal centre in the oxygen annealed samples all decrease as the nickel level rises. This trend also supports the hypothesis that the iron atoms are being replaced with ions of a smaller ionic size; where trivalent nickel is smaller than trivalent iron. The absence of a similar trend in the air quenched samples is presumably a result of disorder in the system.

Mössbauer analysis also suggests that the nickel valence is greater than two. Calculations of overall iron valence, from the derived proportions of Fe^{3+}, Fe^{4+} and Fe^{5+}, also increases with x. Indeed, if the iron oxidation state is calculated from the determined oxygen content by t.g.a. (assuming the nickel to be essentially trivalent) then at x = 0.8 for the oxygen annealed sample Fe $= 4.2(2)^+$. This would give a good indication why solid solution limit is 0.8 i.e. further oxidation of the nickel would mean oxidation of iron to the pentavalent state which would be energetically unfavoured at low pressures.

In the $Sr_3Co_{2-x}Ni_xO_{7-\delta}$ series a phase change occurs around x = 0.4. Figure 6.9 shows the variation in the cell parameter as a function of x. In all cases the parameters are shrinking as the level of nickel increases. This behaviour could be predicted since cobalt(III) atoms in the structure are now being replaced by smaller (nickel(III)) or more oxidised (cobalt(IV)) ions.

The refined parameters of the tetragonal region gave steady results and showed the oxygen vacancies to be on the O1 and O3 sites. These samples however were, air

Table 6.15a Calculated Bond Valence of Metal Atom Sites for the Air Sintered Samples

Atom	$Sr_3Fe_{2-x}Ni_xO_{7-\alpha}$; x =				
	0.0	0.2	0.4	0.6	0.8
Sr1	2.24	2.32	2.31	2.38	2.38
Sr2	2.00	1.97	1.96	1.96	1.99
Fe	3.37	3.23	3.25	3.26	3.30
Ni	-	2.46	2.44	2.46	2.48

Table 6.15b Calculated Bond Valence of Metal Atom Sites for the Oxygen Annealed Samples

Atom	$Sr_3Fe_{2-x}Ni_xO_{7-\alpha}$; x =				
	0.0	0.2	0.4	0.6	0.8
Sr1	2.31	2.26	2.34	2.34	2.38
Sr2	2.05	2.09	2.09	2.12	2.14
Fe	3.51	3.56	3.54	3.60	3.61
Ni	-	2.68	2.65	2.71	2.72

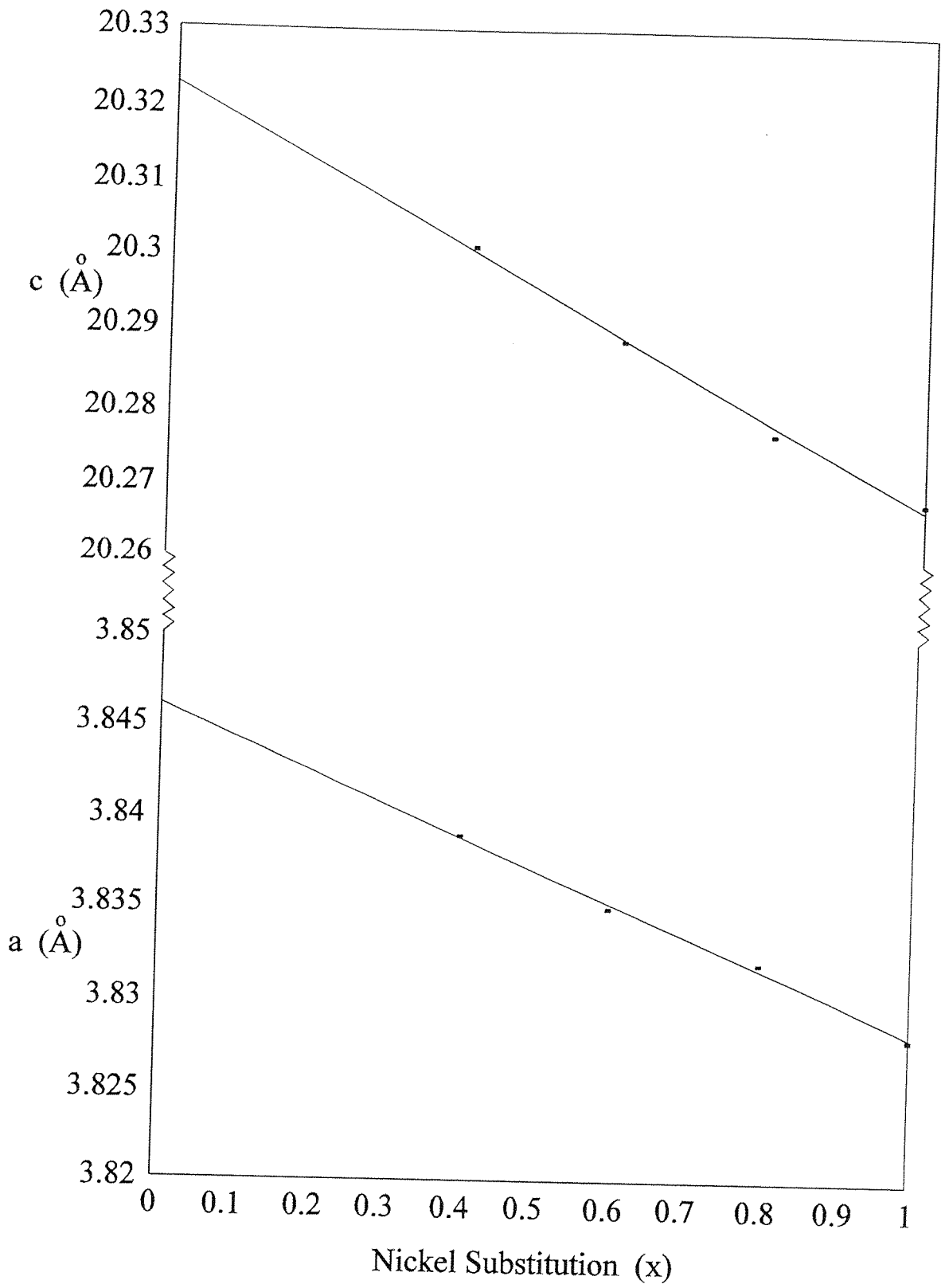**Figure 6.9** Change in Lattice Parameters with Nickel Content in $Sr_3Co_{2-x}Ni_xO_{7-\Phi}$

174

quenched, and oxygen ordering would not have had the opportunity to occur. The level of oxygen occupancy on the two partially occupied sites therefore, may be, different under preparative conditions which promote oxygen ordering e.g. slow cooling. This result does support the previous hypothesis that the second site to accommodate oxygen vacancies is the O1 sites.

As previously noted in the pure cobalt system the structural refinement represents an average over the sample. However, local ordering effects around the cobalt centres are now accompanied by possible ordering of the transition metal cations in both orthorhombic and tetragonal systems. This maybe the reason for the relatively poor profile fit obtained in the orthorhombic, x = 0.2, sample.

Bond valence calculations for the tetragonal and orthorhombic samples are summarised in Table 6.16a and 6.16b respectively using the parameters for cobalt(II) and nickel(II). In both cases the Sr1 site is extremely underbonded although in both cases these are low coordinate sites. This maybe the reason why the limit to the cobalt substitution is 1.0 where the Sr site becomes so underbonded that the structure is no longer stable and disassociates to more stable products.

Table 6.16a Calculated Bond Valence Parameters for the Tetragonal Region

Atom	$Sr_3Co_{1.4}Ni_{0.6}O_{5.66}$	$Sr_3CoNiO_{5.60}$
Sr1	1.40	1.43
Sr2	2.15	2.14
Co	2.38	2.39
Ni	2.15	2.16

In the tetragonal system the bond valence of the transition metal site shows a good approximation to a divalent nickel atom. However, the cobalt atoms are very overbonded. Using the experimentally determined oxygen content to derive a cobalt oxidation state (with nickel divalent) gives $Co^{3.40}$. This suggests that both trivalent and tetravalent cobalt atoms are present in the structure. In the x = 0.2 sample the six-fold site is overbonded

175

for the divalent atom. The degree of overbonding is much reduced in the five-fold site. Again there is evidence for the cobalt(IV) ion.

Unfortunately there is no definite proof of the individual oxidation states of the ions in these compounds although they could be predicted from the individual ionisation potentials. In order to confirm the assignments a spectroscopic method such as Auger spectroscopy could be employed although this technique does depend on comparison with known compounds and there are few pure materials with this level of oxidation.

Table 6.16b Calculated Bond Valence Parameters for the Orthorhombic Sample

Atom	Valence	Atom	Valence
Sr1	1.30	Co1	2.79
Sr2	2.44	Co2	2.20
Sr3	1.61	Ni1	2.51
Sr4	2.20	Ni2	1.99

6.6 Conclusions

Some mixed transition metal Ruddlesden-Popper phases, with the formula $Sr_3M_{2-x}N_xO_{7-g}$ $M,N = Fe$, Co and Ni, have been synthesised using solid state methods.

When $M = Fe$ and $N = Ni$, the system crystallises in the tetragonal space group I4/mmm. The oxygen stoichiometry of the structure can be altered by annealing in a variety of gases (air, $5\%H_2/N_2$ and O_2), and the structure remains tetragonal. When $g < 1$, the oxygen vacancies are exclusively confined to the O3 site which links the octahedra. As g rises above 1.0 additional vacancies are introduced on the equatorial O1 site. Mössbauer analysis suggests the iron oxidation state increases with rising x. This implies that Ni is in the trivalent state and iron as Fe^{3+}, Fe^{4+} and Fe^{5+}.

When $M = Fe$ and $N = Co$, a stable Ruddlesden-Popper phase is not formed. This may be related to a very long c parameter, and hence large interplanar distance

between the transition metal octahedra, allowing atmospheric water to occupy the voids in the structure.

When M = Co and N = Ni, a series of Ruddlesden-Popper phases are formed. At low values of x the system has orthorhombic symmetry and crystallises in the space group Immm. As x rises above 0.4 there is a phase change to tetragonal and crystallises in the space group I4/mmm. Oxygen vacancies, in the orthorhombic samples, lead to a threefold tripling along the b-axis. In the tetragonal samples the oxygen vacancies lie on the O3 site, linking the transition metal octahedra and on the equatorial O1 site.

Refinements to determine the crystal structure of these materials was achieved using the Rietveld method. This gives an averaged picture of the whole structure, therefore individual transition metal ion coordination would need to be investigated further by a technique such as EXAFS.

6.7 References

1   M. James, J.P. Attfield. J. Sol. Stat. Chem. **105**, 287-93. (1993)

2   S.N. Ruddlesden, P. Popper. Acta. Cryst. **10**, 538. (1957)

3   S.E. Dann, D.B. Currie, M.T. Weller. J. Sol. Stat. Chem. **97**, 179. (1992)

4   G.J. Long, T.E. Cranshaw, G. Longworth. Mossbauer Effect and Reference Journal. **6**, 42-9. (1983)

5   This work, Chapter 5. 133.

6   R.D. Shannon. Acta. Cryst. **A32**, 751. (1976)

7   I.D. Brown. Acta. Cryst. **B32**, 1957. (1976).

CHAPTER 7

The Effect of Oxygen Stoichiometry
on Phase Relations and Structure
in the System $La_{1-x}Sr_xFeO_{3-\delta}$

7.1 Introduction

The perovskite series $La_{1-x}Sr_xFeO_{3-\delta}$ was first studied by Waugh (1) who observed complex phase changes from orthorhombic at low x through rhombohedral to cubic as the stoichiometry approached $SrFeO_3$ ($\delta=0$). Since the distortions were very small no further structural information was obtained by Waugh although the complex magnetic properties of these materials were soon after investigated by Kelly (2). Preliminary Mössbauer measurements were undertaken by Shimony et al (3); at high values of x characteristic iron(IV) lines were observed with an isomer shift with respect to ^{57}Co in stainless steel of 0.1 to 0.2 mms^{-1}. Lower values of x, however, gave broad and varying linewidths which were attributed to an intermediate Fe^{3+}/Fe^{4+} valence state.

A later study by Takano et al (4,5) on $La_{1-x}Sr_xFeO_{3-\delta}$ using Mössbauer spectroscopy proposed a non-integral oxidation state of iron in these materials following disproportionation of the type:-

$$2Fe^{4+} \rightleftharpoons Fe^{4-\lambda} + Fe^{4+\lambda} \qquad (0 \le \lambda \le 1) \qquad [1]$$
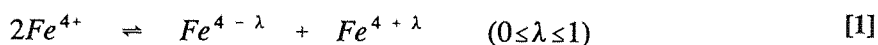
Lattice constants were defined for x = 0.4, 0.5, 0.7, 0.8 and 0.9 ($0 \le \delta \le 0.05$), but no further structural determination was attempted.

The most recent study to be performed on a compound in the $La_{1-x}Sr_xFeO_{3-\delta}$ system was by Battle et al (6). This series of compounds $LaSr_2Fe_3O_{9-y}$ ($0 \le y \le 1$), equivalent to x = 0.66, y = 3δ, using the Takano notation, was investigated using a variety of annealing techniques and characterised by powder x-ray and neutron diffraction. Mössbauer measurements showed the same disproportionation reaction as that seen in $CaFeO_3$ (7). However, the expected reduction in symmetry due to this ordering was not observed by either diffraction technique below the transition temperature. Takano had already suggested an explanation for this in his previous work on $CaFeO_3$, when he proposed the disproportionation reaction was a short range ordering effect.

An example of the magnetic structure for each crystallographic region of the fully oxidised, $\delta=0$, samples has been studied previously. Battle et al (8) studied the structure of the rhombohedral phase, x = 0.66, by neutron diffraction and indexed the magnetic reflections in a space group of lower symmetry than the crystal lattice, although the space

180

group was still trigonal. $LaFeO_3$ (9), x = 0, has a G type antiferromagnetically ordered spin lattice and $SrFeO_3$ (x = 1.0) has a magnetic structure based on an α helix (10). The magnetic structure of other compositions in the series has not been reported. The Neel temperature of the compounds drop dramatically as the value of x increases i.e. $LaFeO_3$ = 760K, $SrFeO_3$ = 134K.

This study describes the preparation of a range of samples in the $La_{1-x}Sr_xFeO_{3-\delta}$ series $(0 \leq x \leq 1)$, $(0 \leq \delta \leq 0.5)$ using a variety of annealing techniques and their characterisation by powder x-ray diffraction. The major part of this work involves high resolution structural studies on the highly oxidised materials using HRPD at the Rutherford Appleton Laboratory. Low temperature neutron diffraction measurements were performed on POLARIS to glean information on magnetic ordering behaviour with the structural changes observed. Oxygen content was measured by thermogravimetric analysis.

7.2 Experimental

Samples in the series $La_{1-x}Sr_xFeO_{3-\delta}$ $(0 \leq x \leq 1)$ were prepared by direct solid state reaction of $SrCO_3$ (99.9%), Fe_2O_3 (99.995%) and La_2O_3 (99.99%) mixed in the correct molar proportions in a pestle and mortar and initially fired at 1100°C in air. After regrinding, the samples were reheated at 1300°C for another 24hrs and compounds were then treated further to control the oxygen stoichiometry as defined in Table 7.1.

X-ray powder diffraction data were collected on all samples to assess sample purity. A stepped scan using a step size of 0.002° and long collection times were employed in an attempt to resolve the small structural distortions observed. Oxygen content was measured by thermogravimetric analysis using platinum crucibles under an atmosphere of $5\% H_2/N_2$ operating at 800°C.

7.3 Powder Neutron Diffraction

Powder neutron diffraction data were obtained on HRPD at the Rutherford Appleton Laboratory on the high pressure oxygen annealed samples for all values of x. Data collection times varied from 3-4hrs. Full profile refinements were carried out using a time

Table 7.1 Annealing Treatment

	Annealing Gas	Treatment
A	Air	Quenched from 1300°C
B	$1\%O_2/N_2$	Annealed 480°C overnight Slow cooled to RT
C	O_2	Annealed 480°C overnight Slow cooled to RT
D	$5\%H_2/N_2$	Annealed 480°C overnight Slow cooled to RT
E	Ar	Annealed 480°C overnight Slow cooled to RT
F	High Pressure O_2	Annealed at 900°C / 350atm flowing O_2 / slow cooled

of flight version of the Rietveld method (11). Although the samples x $=0.0$ to 0.3 were below their Neel temperatures at 298K, the maximum d-spacing used for the refinement was 1.7Å below which magnetic reflections are extremely weak and could be ignored. Refinements were carried out in the space group Pbnm, x $= 0.0$-0.2, $\overline{R3}c$ for x $= 0.4$-0.7 and Pm3m for x $= 0.8$-1.0, using the starting models of $GdFeO_3$ (12), $LaCuO_3$ (13), and $SrFeO_3$ (14) for the three structures respectively. Refinement included all atomic positions, cell parameters, scale factors, background and peak shapes. Oxygen stoichiometry was permitted to vary for all samples initially, but was finally fixed for samples x $= 0.0$ to 0.7 as the stoichiometry varied only marginally from three and was always within the E.S.D. Final stages of the refinements included anisotropic temperature

factors.

Magnetic neutron diffraction data were collected on the high pressure annealed samples x = 0.1, 0.5 and 0.8 using POLARIS. Diffraction data were collected for a period of 2hrs above and below the Neel temperature. At the time of collection there was no program for refining the magnetic data reflections and the intensities were therefore calculated using the PEAK program running on the Rutherford Vax.

7.4 Mössbauer Spectroscopy

Mössbauer data were collected on the high pressure oxygen annealed samples between 4.2K and room temperature using a conventional transmission spectrometer using a double ramp waveform to give a flat background. Absorbers were prepared of finely ground samples, which were weighed to give optimum signal to noise (15), mixed with boron nitride to randomise the orientations of the microcrystals.

7.5 Results and Discussion

Annealing Experiments

The annealing experiments revealed complex phase relations in the $La_{1-x}Sr_xFeO_{3-\delta}$ system. As first observed by Waugh (1) the system is composed of three regions of different symmetry at low values of δ. However, as demonstrated by Battle (6) in the $Sr_2LaFe_3O_{9-y}$ system, the purity and symmetry of this system shows extreme sensitivity to oxygen stoichiometry and sample preparation especially at high values of x. A summary of the annealing experiments including refined lattice parameters, oxygen content determined by thermogravimetric analysis and space group are included in Table 7.2.

Similar behaviour is also apparent in the $SrFeO_{3-\beta}$ system where the value of ß is very sensitive to both sample preparation and annealing conditions. The $SrFeO_{3-\beta}$ system has been studied extensively by many authors (16-18) and many different phases have been recognised in the system; MacChesney *et al* reported the presence of both a cubic (ß = 0) and tetragonal (ß = 0.14) phase. At higher values of ß several orthorhombic phases

183

Table 7.2 Results of Annealing Experiments (Å)

x_{Gas}	0.0	0.1	0.2	0.3	0.4	0.5	0.6	0.7	0.8	0.9
A	Pbnm 5.5553(8) 5.5663(8) 7.8545(13) $\delta = 0$	Pbnm 5.556(3) 5.539(3) 7.856(5) $\delta = 0$	Pbnm 5.550(2) 5.508(2) 7.844(5) $\delta = 0$	Mixture	$R\bar{3}c$ 5.5271(6) 13.4209(18) $\delta = 0$	$R\bar{3}c$ 5.519(3) 13.421(8) $\delta = 0$	Mixture	Mixture	Mixture	Mixture
B		Pbnm 5.558(3) 5.538(3) 7.850(5) $\delta = 0$	Pbnm 5.551(4) 5.508(4) 7.844(4) $\delta = 0$	Mixture	$R\bar{3}c$ 5.5286(4) 13.4202(9) $\delta = 0$	Mixture	Mixture	Mixture	3.881(2) 3.861(2) $\delta = 0.12$	3.8785(9) 3.8581(10) $\delta = 0.16$
C		Pbnm 5.566(2) 5.540(2) 7.858(2) $\delta = 0$	Pbnm 5.549(2) 5.514(2) 7.841(3) $\delta = 0$	Mixture	$R\bar{3}c$ 5.5283(4) 13.4206(8) $\delta = 0$	$R\bar{3}c$ 5.516(2) 13.417(4) $\delta = 0$	Mixture	Mixture	Mixture	3.8688(2) 3.8566(8) $\delta = 0.12$
D	Pbnm 5.5752(8) 5.5640(8) 7.8563(12) $\delta = 0.0$	Pbnm 5.564(3) 5.553(2) 7.852(4) $\delta = 0.05$	Pbnm 5.557(3) 5.540(3) 7.846(7) $\delta = 0.10$	Pm3m 3.9175(2) $\delta = 0.15$	Pm3m 3.9151(4) $\delta = 0.20$	Mixture	Mixture	Mixture	Mixture	Mixture
E		Pbnm 5.556(6) 5.540(2_) 7.855(3) $\delta = 0$	Pbnm 5.552(6) 5.520(2) 7.841(2) $\delta = 0$	Mixture	$R\bar{3}c$ 5.5304(6) 13.4272(13) $\delta = 0.08$	Mixture	Mixture	3.8948(6) 3.8613(6) $\delta = 0.12$	3.8836(6) 3.8542(6) $\delta = 0.16$	Mixture
F		Pbnm 5.556(2) 5.535(2) 7.848(3) $\delta = 0$	Pbnm 5.550(2) 5.512(3) 7.844(4) $\delta = 0$	Mixture	$R\bar{3}c$ 5.5269(2) 13.4209(6) $\delta = 0$	$R\bar{3}c$ 5.5093(8) 13.4121(18) $\delta = 0$	$R\bar{3}c$ 5.4945(1) 13.4108(14) $\delta = 0$	$R\bar{3}c$ 5.4767(6) 13.4049(5) $\delta = 0$	Pm3m 3.8610(13) $\delta = 0.03$	Pm3m 3.8556(3) $\delta = 0.04$

have been reported; when ß = 0.25 Greaves *et al* (19) reported a phase in which every other oxygen site was vacant in the 110 direction and this is related to the pure brownmillerite phase, $Sr_2Fe_2O_5$ (20) where all these sites are vacant.

Recent studies have further investigated the low symmetry phases and a variety of conclusions reached depending on sample preparation method. Takeda *et al* (21) produced a whole range of complex phases from a preparation technique involving quenching from high temperature. Lower temperature experiments performed by Yamauchi *et al* (22) produced more ordered samples of higher symmetry. Location of phase boundaries thus varied according to preparative conditions.

Described below is the effect of different annealing conditions on the $La_{1-x}Sr_xFeO_{3-\delta}$ system.

x = 0.0 to 0.2

At these low values of strontium substitution full oxygen stoichiometry is maintained within the limits of experimental error except during the reduction experiment. The symmetry of the samples remained Pbnm throughout the experiments although the orthorhombic distortion decreased slightly on reduction (D). In the high pressure oxygen annealed samples the orthorhombic distortion increases from x = 0.0 to 0.2 and this is reflected in the changing bond distances around the iron metal centre, *vide infra*.

x = 0.3

Initial examination of the x = 0.3 sample by x-ray diffraction showed it to be multiphase for all annealing experiments except the reduction (D). Close scrutiny of the XRD patterns showed a mixture of both rhombohedral and orthorhombic phases. Reduction of the 0.3 phase in hydrogen gave a phase which showed sharp reflections and no peak splitting or additional reflections to suggest a non cubic unit cell and was hence indexed on a primitive cubic unit cell with a cell parameter of 3.9175(4)Å.

185

The rhombohedral region shows a much wider range of oxygen non-stoichiometry and consequently more complex phase relations. The high pressure annealed samples exhibited the clearest distortions which were clearly visible for samples x = 0.4 to 0.6 by x-ray diffraction. The x = 0.7 sample at first appeared to be cubic although reflections were clearly broadened at high angle. The neutron diffraction experiments showed the sample to be rhombohedral with a very small $a\sqrt{6}/c$ distortion of 1.0008. The other annealing experiments gave differing results depending on the value of x.

For x = 0.4 the system remained rhombohedral through the entire range of annealing experiments except the reduction where a phase change to pseudo cubic occurred. δ remained very small when oxygen was present but increased to 0.08 in the argon annealing experiment with a corresponding increase in both cell parameters. The reduction produced a similar phase to the reduced x = 0.3 sample which was indexed as primitive cubic with a cell parameter of 3.9151(4)Å.

In the x = 0.5 sample only high pressure oxygen annealing and 100% oxygen of 1 atmosphere (C) produced a pure rhombohedral phase. The other experiments, excluding the reduction, produced a mixture of orthorhombic and rhombohedral phases. The reduction experiment produced a mixture of an orthorhombic $(AB)_3Fe_3O_8$ phase, as first observed by Grenier et al (23) and also observed by Battle (24), and the cubic phase.

A similar mixture of phases is observed when x = 0.6 except the multiphase region extends to the tube furnace annealed (C) sample. The only pure rhombohedral phase was produced by the high pressure experiment.

For x = 0.7 a pure rhombohedral phase was only produced by the high pressure experiment. The other three annealing techniques employing oxygen produced a mixture of orthorhombic and tetragonal phases as observed for $SrFeO_{3-\beta}$ (β = 0.27). However, argon annealing produced a pure tetragonal phase similar to that observed by many authors in $SrFeO_{2.78-2.86}$. The main phase from the reduction experiment (D) was $Sr_2LaFe_3O_8$ with a small amount of the reduced phase.

The last region produced the most complex systems of all due to the wide range of oxygen non-stoichiometry. At x = 0.8 a cubic phase was produced by the high pressure experiment with both oxygen annealed (C) and the as sintered sample (A) being a mixture of tetragonal and cubic phases. Both the oxygen in nitrogen (B) and the argon annealed (E) products were pure tetragonal phases. The hydrogen reduction (D) gave a complex mixture of $Sr_2LaFe_3O_8$ and $Sr_2Fe_2O_5$.

For x = 0.9 very similar properties are observed to those described above except the oxygen annealed sample was also tetragonal. Both the reduction (D) and the argon (E) experiment gave a mixture of $Sr_2LaFe_3O_8$ and $Sr_2Fe_2O_5$. A summary of the phase behaviour is shown in Figure 7.1. The data for the x = 1.0 series was taken from the results described by Yamauchi (22).

Neutron Diffraction Experiments

The neutron diffraction refinements of the orthorhombic samples proceeded steadily in the space group Pbnm. In the case of x = 0.0 and x = 0.1 some additional, magnetic, reflections just below 1.7Å had to be removed from the refinement. The final sample (x = 0.2) in this group was the most difficult to refine and close examination of the diffraction data showed misfitting on the low time of flight tail of some of the reflections. This is probably due to the fact that this sample lies on the border of the phase transition from orthorhombic to rhombohedral and that the likely cause of the misfitting is the presence of a small amount of the rhombohedral phase. Despite the impurity, for which due to overlap exclusion of peaks was not possible, both atomic positions and cell parameters were steady and remained within the E.S.D.'s. Final refinement parameters and important bond lengths and angles are listed in Table 7.3.

A multiphase refinement program was not available at the time of data collection and so the refinement of the HRPD data for the x = 0.3 sample was not possible. The rhombohedral phases refined rapidly in the space group $R\overline{3}c$ although the peak shape parameters were very difficult to fit in the case of x = 0.6 and 0.7 due to the small rhombohedral distortions giving rise to very small peak splittings. Final refinement
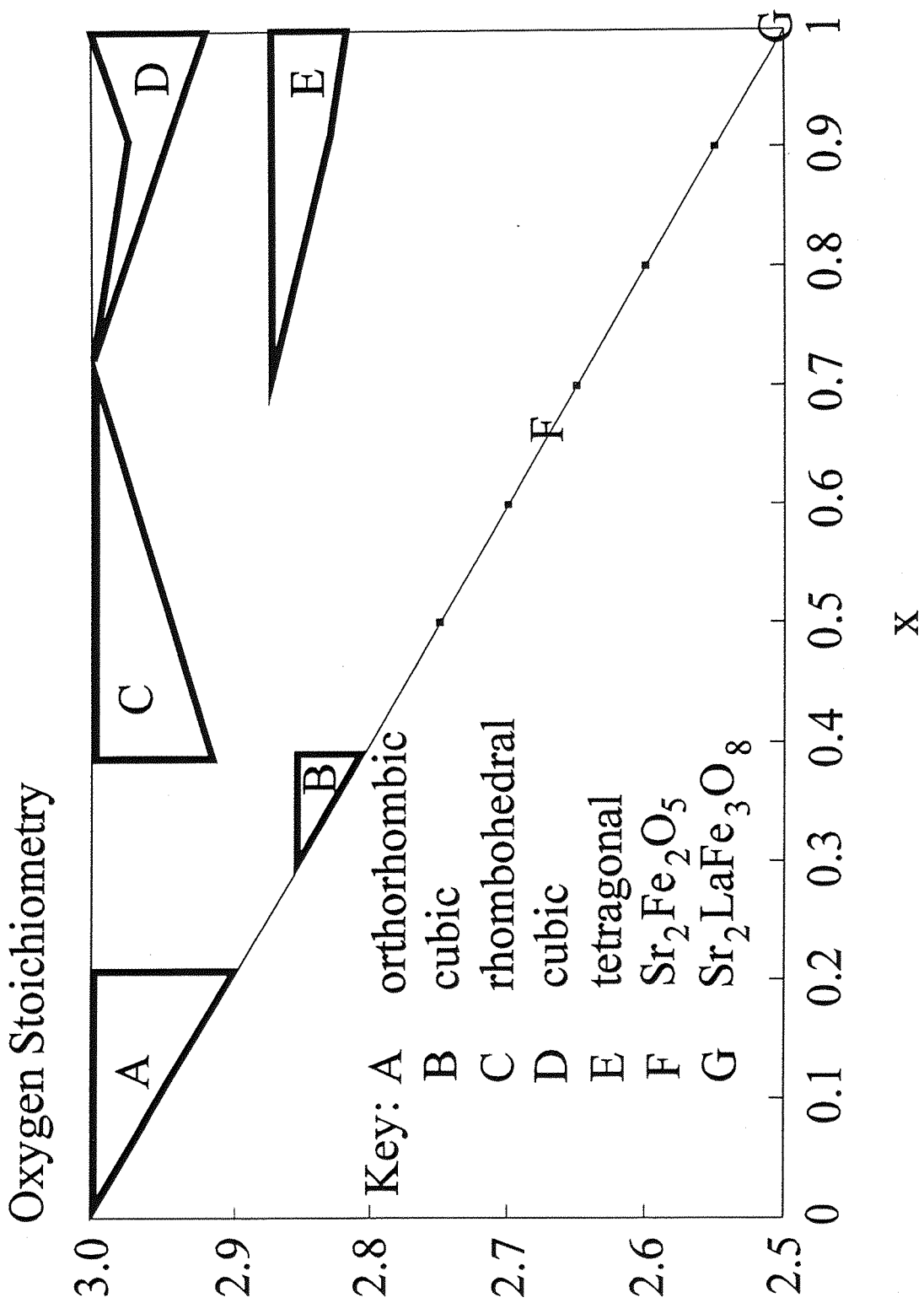
Figure 7.1 Phase Diagram Depicting Change in Structure with Oxygen Stoichiometry

188

Table 7.3 Refined Atomic Parameters for the Orthorhombic Region x = 0.0 - 0.2

x	Lattice Parameters (Å)	Atomic Parameters						Bond distances (Å)				Refinement Parameters
		Atom	x/a	y/b	z/c	B_{eq}	Occ	LA - O		FE - O		
0	a = 5.55702(2)	LA	0.9923(4)	0.0292(1)	0.25	0.52(1)	1.0	O1+ 3.059(2) x 1		O1* 2.008(1) x 2		$R_p = 2.33$
	b = 5.56521(1)	FE	0	0	0	0.73(1)	1.0	O1* 2.581(2) x 1		O2* 2.002(1) x 2		$R_{wp} = 3.37$
	c = 7.85426(2)	O1	0.0748(4)	0.4855(3)	0.25	0.37(2)	1.0	O1° 3.152(3) x 1		O2+ 2.010(1) x 2		$R_{exp} = 1.62$
		O2	0.7191(2)	0.2817(2)	0.0394(1)	0.35(1)	1.0	O1* 2.421(3) x 1				$\chi^2 = 4.33$
								O2* 2.648(2) x 2				
								O2° 2.805(1) x 2				
								O2^ 3.277(1) x 2				
								O2^I 2.450(2) x 2				
0.1	a = 5.55561(2)	LA	0.9940(11)	0.0200(5)	0.25	0.45(5)	0.9	O1+ 2.934(6) x 1		O1* 2.004(1) x 2		$R_p = 5.76$
	b = 5.53540(2)	SR	0.9940(11)	0.0200(5)	0.25	0.45(5)	0.1	O1* 2.668(6) x 1		O2* 2.026(3) x 2		$R_{wp} = 9.23$
	c = 7.85609(6)	FE	0	0	0	0.15(4)	1.0	O1° 3.144(9) x 1		O2+ 1.961(3) x 2		$R_{exp} = 2.64$
		O1	0.0714(12)	0.4958(10)	0.25	0.57(9)	1.0	O1* 2.419(9) x 1				$\chi^2 = 12.24$
		O2	0.7194(6)	0.2724(5)	0.0373(4)	0.32(6)	1.0	O2* 2.659(5) x 2				
								O2° 2.825(4) x 2				
								O2^ 3.202(5) x 2				
								O2^I 2.465(5) x 2				
0.2	a = 5.55002(12)	LA	0.9964(20)	0.0121(9)	0.25	0.30(6)	0.8	O1+ 2.725(13) x 1		O1* 1.994(1) x 2		$R_p = 13.92$
	b = 5.51209(9)	SR	0.9964(20)	0.0121(9)	0.25	0.30(6)	0.2	O1* 2.840(13) x 1		O2* 2.030(5) x 2		$R_{wp} = 18.6$
	c = 7.84394(17)	FE	0	0	0	0.19(8)	1.0	O1° 3.118(13) x 1		O2+ 1.930(5) x 2		$R_{exp} = 5.59$
		O1	0.0653(13)	0.5016(21)	0.25	0.36(6)	1.0	O1* 2.433(13) x 1				$\chi^2 = 11.89$
		O2	0.7261(7)	0.2612(10)	0.0356(5)	0.26(8)	1.0	O2* 2.639(08) x 2				
								O2° 2.865(08) x 2				
								O2^ 3.109(07) x 2				
								O2^I 2.502(07) x 2				

189

parameters and important bond lengths are listed in Table 7.4

The two cubic samples were refined in the space group Pm3m. Although 0.8 proceeded smoothly the 0.9 sample showed significant peak broadening and was more difficult to refine. However, no additional reflections were observed to suggest a lower symmetry. Close scrutiny of the neutron diffraction pattern shows a high angle tail which could be attributed to a $SrFeO_3$ impurity. Final refinement parameters and important bond lengths are listed in Table 7.5. An example of the profile fit to the data is shown in Figure 7.2

Figures 7.3 and 7.4 show the variation in lattice parameter with varying strontium content and a plot of the change in volume with strontium substitution for the high pressure oxygen annealed samples. A comparison of the two shows that although the overall volume is changing linearly with x the local environment of the ions and, hence, individual lattice parameters change significantly. Figure 7.3 shows that the variation in lattice parameter falls into three distinct regions corresponding to the different crystal systems. Although the change in lattice parameters within these systems is approximately linear, there is a discontinuity at the phase boundaries. The most obvious of these is in the region between 0.2 and 0.4 and perhaps this gives and indication as to why the 0.3 sample is multiphase and the 0.2 sample also shows signs of rhombohedral impurity.

A three region graph is also observed in Figure 7.5 and Figure 7.6 which show the variation in bond length around La/Sr and Fe with strontium substitution for the high pressure oxygen annealed samples. The non-continuity is most obvious between orthorhombic and rhombohedral, but it is also present between rhombohedral and cubic. If the La/Sr - O distances are extrapolated by a curve to a point where they coincide i.e. all twelve A cation to oxygen distances are equal as for a cubic system using the rhombohedral region of Figure 7.5, a phase change to cubic at x = 0.8 is implied by linear extrapolation but the rhombohedral distortion graph, Figure 7.7, suggests a slightly lower value between 0.72 and 0.73 i.e. a$\sqrt{6}$/c ration would equal one for a cubic phase. This would imply a relaxation of the local structure around the La when the structure becomes rhombohedral. The most likely explanation of the observed structural changes is the effect of the changing iron oxidation state as the series is transversed. Clearly there is both a change in ionic size and the oxygen ordering as iron moves from the tripositive to the tetrapositive state. The replacement of lanthanum by strontium is likely to have

Table 7.4 Refined Atomic Parameters for the Rhombohedral Region $x = 0.4 - 0.7$

x	Lattice Parameters (Å)	Atomic Parameters						Bond Distances (Å)		Refinement Parameters
		Atom	x/a	y/b	z/c	B_{eq}	Occ	LA - OX	FE - OX	
0.4	a=5.52728(1) c=13.42116(4)	LA	0	0	0.25	0.31(3)	0.6	OX* 2.997(2) x 3 OX^I 2.530(1) x 3 OX$^+$ 2.758(1) x 6	OX* 1.963(1) x 6	R_p = 7.34 R_{wp} = 8.86 R_{exp} = 3.41 χ^2 = 10.16
		SR	0	0	0.25	0.31(3)	0.4			
		FE	0	0	0	0.12(4)	1.0			
		OX	0.4577(2)	0	0.25	0.68(3)	1.0			
0.5	a=5.51107(1) c=13.41578(2)	LA	0	0	0.25	0.28(3)	0.5	OX* 2.947(1) x 3 OX^I 2.564(1) x 3 OX$^+$ 2.751(1) x 6	OX* 1.954(1) x 6	R_p = 5.39 R_{wp} = 6.87 R_{exp} = 2.89 χ^2 = 5.66
		SR	0	0	0.25	0.28(3)	0.5			
		FE	0	0	0	0.25(2)	1.0			
		OX	0.4651(1)	0	0.25	0.63(2)	1.0			
0.6	a=5.49367(1) c=13.41057(4)	LA	0	0	0.25	1.26(4)	0.4	OX* 2.894(2) x 3 OX^I 2.600(1) x 3 OX$^+$ 2.745(1) x 6	OX* 1.946(1) x 6	R_p = 8.13 R_{wp} = 10.75 R_{exp} = 3.17 χ^2 = 10.73
		SR	0	0	0.25	1.26(4)	0.6			
		FE	0	0	0	1.08(1)	1.0			
		OX	0.4733(2)	0	0.25	1.47(4)	1.0			
0.7	a=5.47623(1) c=13.40551(4)	LA	0	0	0.25	1.74(8)	0.3	OX* 2.811(2) x 3 OX^I 2.665(2) x 3 OX$^+$ 2.738(1) x 6	OX* 1.937(1) x 6	R_p = 6.45 R_{wp} = 9.30 R_{exp} = 3.07 χ^2 = 9.21
		SR	0	0	0.25	1.74(8)	0.7			
		FE	0	0	0	1.54(2)	1.0			
		OX	0.4867(3)	0	0.25	1.89(7)	1.0			

Table 7.5 Refined Atomic Parameters for the Cubic Region x = 0.8 - 0.9

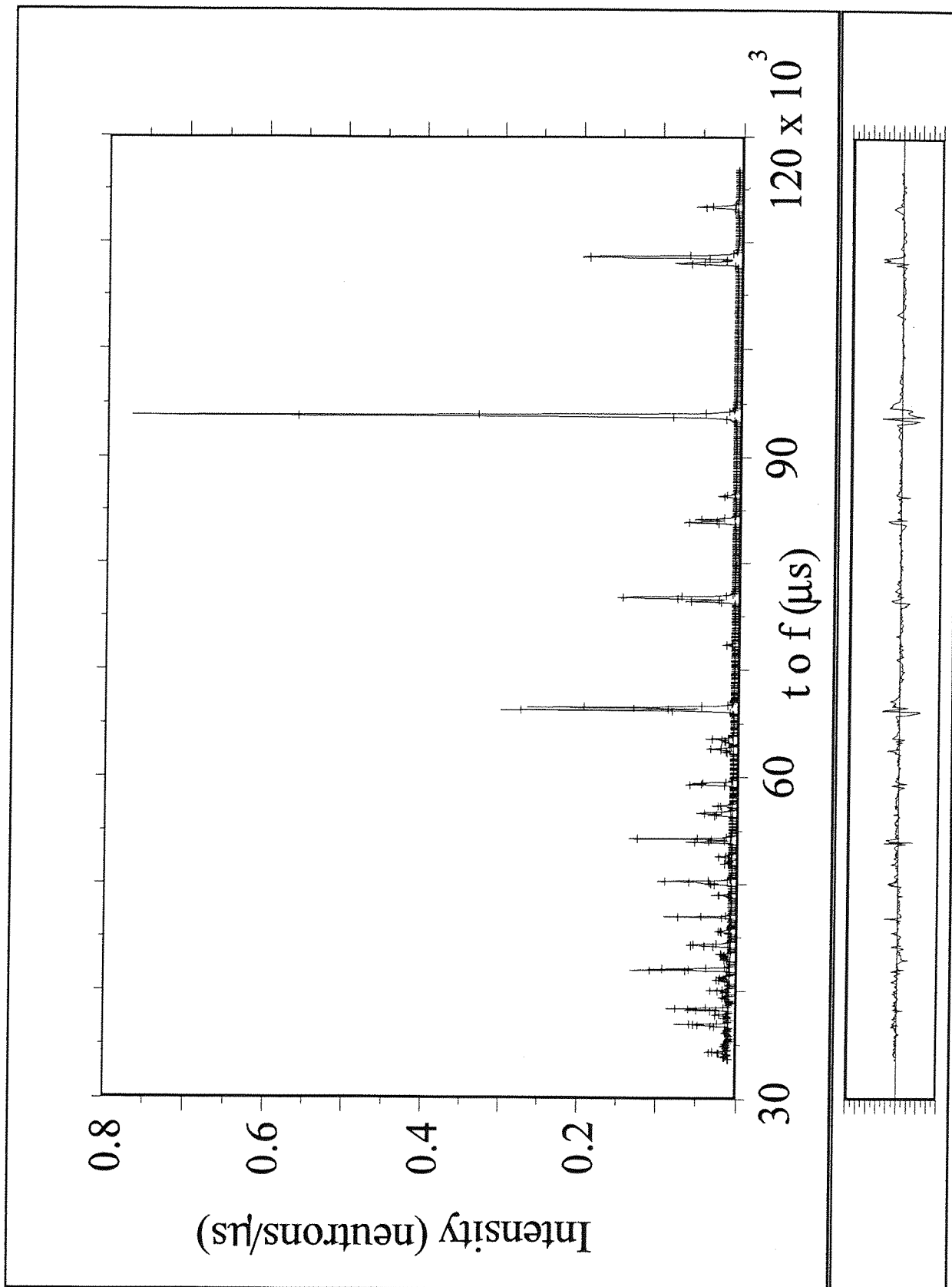| x	Lattice Parameters (Å)	Atomic Parameters						Bond Distances (Å)		Refinement Parameters
		Atom	x/a	y/b	z/c	B_{eq}	Occ	LA - O	FE - O	
0.8	3.86434(1)	LA	0	0	0	0.36(1)	0.2	O' 2.733(1) x 12	O' 1.932(1) x 6	R_p = 8.41
		SR	0	0	0	0.36(1)	0.8			R_{wp} = 9.64
		FE	0.5	0.5	0.5	0.10(1)	1.0			R_{exp} = 4.91
		O	0	0.5	0.5	0.67(1)	1.00(1)			χ^2 = 3.86
0.9	3.85609(1)	LA	0	0	0	0.27(4)	0.1	O' 2.727(1) x 12	O' 1.928(1) x 6	R_p = 13.92
		SR	0	0	0	0.27(4)	0.9			R_{wp} = 18.61
		FE	0.5	0.5	0.5	0.01(4)	1.0			R_{exp} = 5.59
		O	0	0.5	0.5	0.47(4)	0.99(3)			χ^2 = 10.99

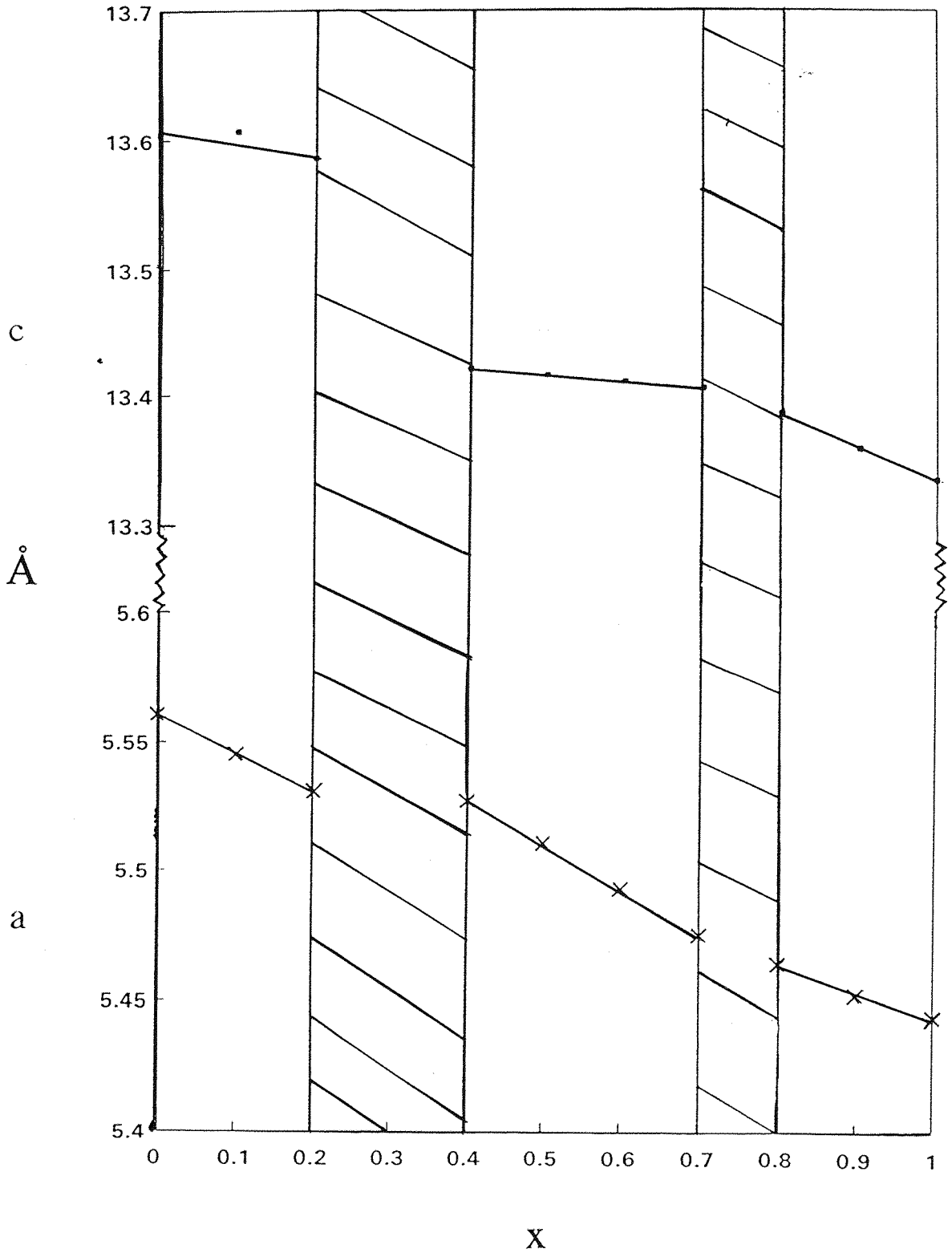**Figure 7.2** Refinement Profile of the HRPD data of x = 0.5

193

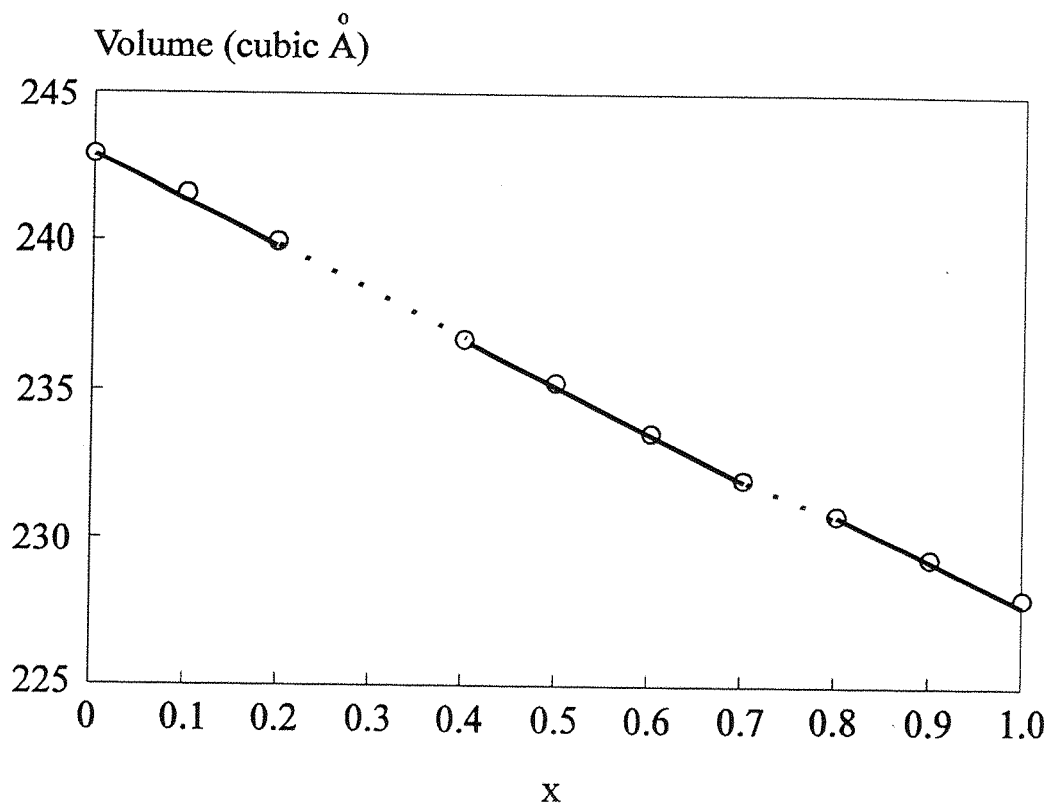**Figure 7.3** Variation of Lattice Parameters with Strontium Content

194

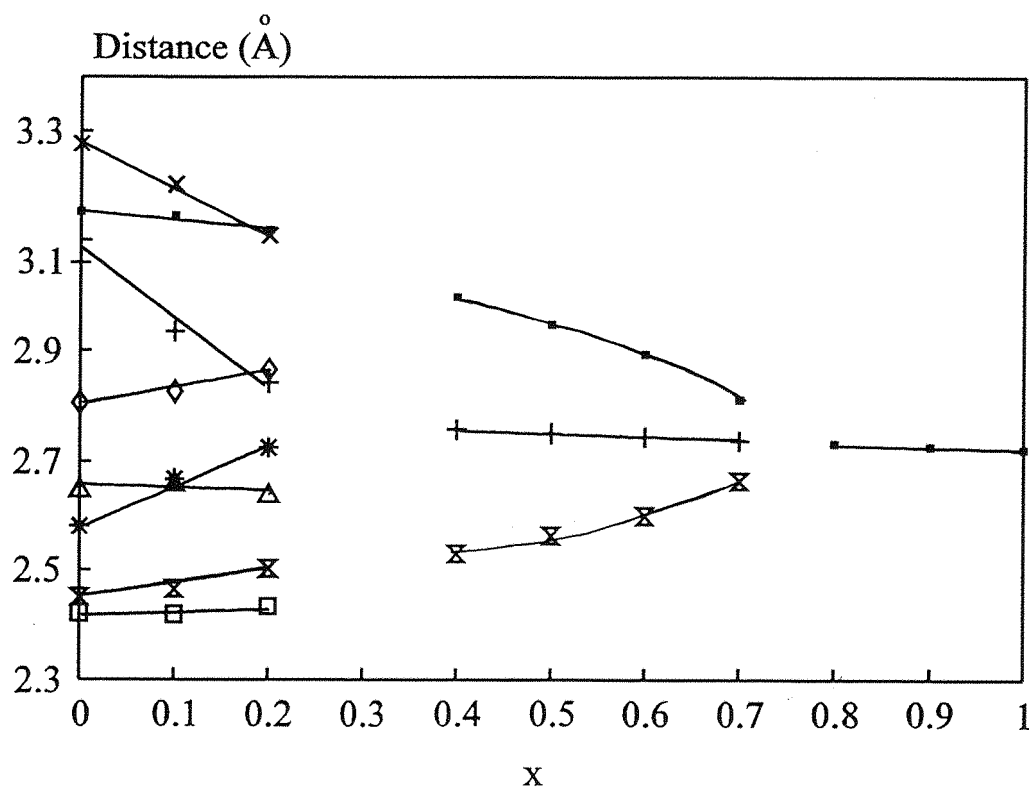**Figure 7.4** Variation of Cell Volume with Strontium Content, x.

Figure 7.5 Variation of Sr/La - O Bond Lengths with Strontium Content, x.
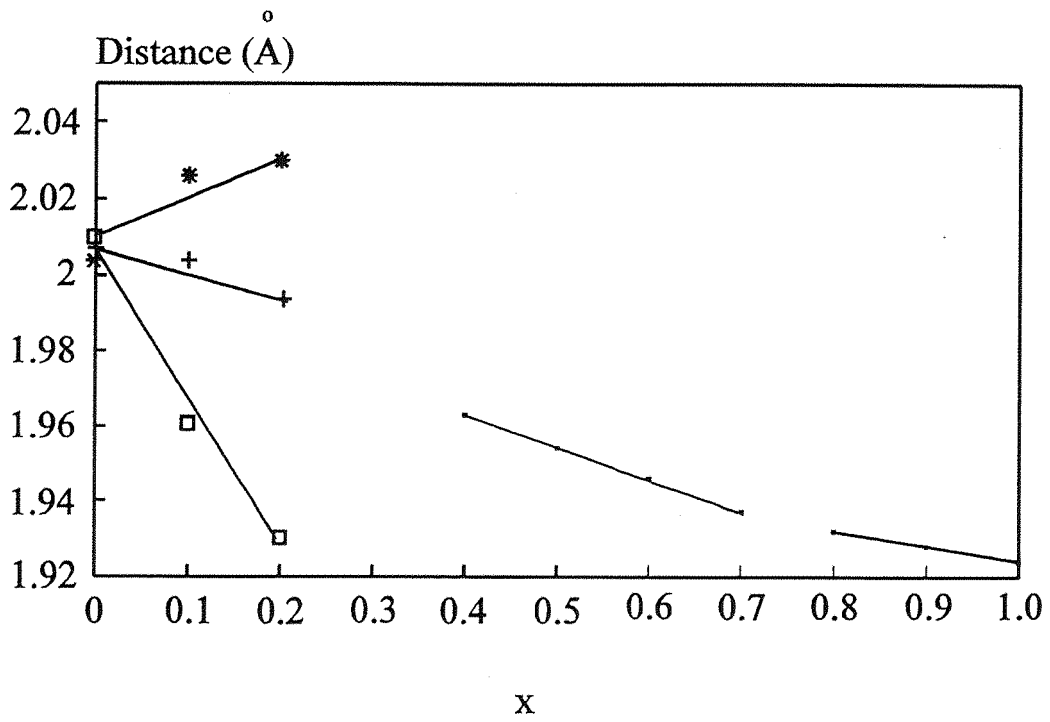
195

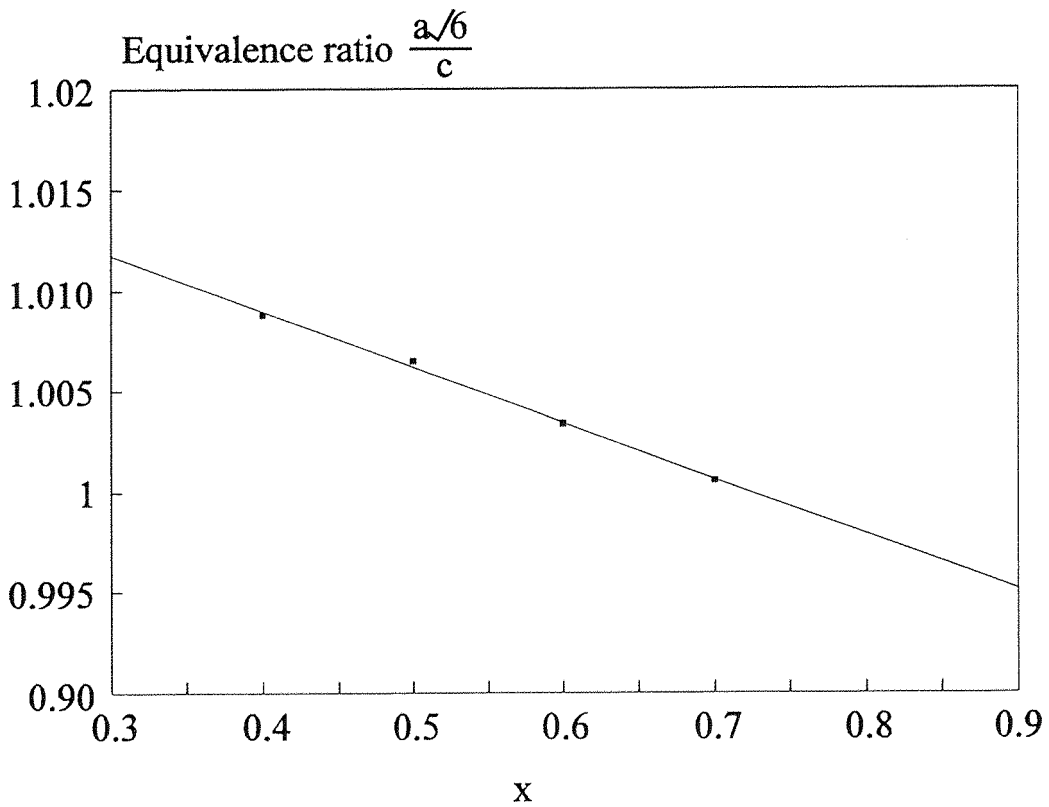**Figure 7.6** Variation of Fe - O Bond Lengths with Strontium Content, x.

Figure 7.7 Change in Rhombohedral Distortion with Strontium Content, x.

196

very limited structural impact since they are of similar size and prefer similar coordination geometries. Considering the first phase change between x = 0.2 and x = 0.4 the iron site changes from being very distorted to an almost regular octahedron with equal bond lengths and only slightly distorted bond angles from the idealised 90°, O - Fe - O, of 89.3° and 90.7°. The former situation is a highly unusual environment for both iron oxidation states.

Bond valences calculations on the iron site based on the bond lengths generated from the Rietveld analyses are summarised in Table 7.6.

Table 7.6 Comparison of Observed Fe^{n+} with Calculated Bond Valence

x	Oxidation State	Calculated Bond Valence
0.0	3.00	3.064
0.1	3.10	3.154
0.2	3.20	3.270
0.4	3.40	3.447
0.5	3.50	3.533
0.6	3.60	3.610
0.7	3.70	3.699
0.8	3.74	3.749
0.9	3.82	3.789

At high values of x the tabulated values show very good agreement. However, at low values of x in the orthorhombic region, the site valency gradually deviates to a greater extent from the theoretical value as x increases from 0.0 to 0.2. This behaviour suggests that the iron atom is being progressively more overbonded. Once the phase change has occurred to rhombohedral symmetry, the good agreement between site valency and

expected iron oxidation state determined by TGA is restored. This suggests that the first phase change is probably related to the preferred geometry of the iron as the average oxidation state increases. The second phase change from rhombohedral to cubic is more difficult to explain since the difference in the two coordination geometries is minimal. However, considering the A cation there is a significant difference in the geometry of the twelve fold site. In the cubic case all twelve bond distances are the same whereas the rhombohedral system has a distorted site. This distortion gradually decreases in the rhombohedral region until there is a changeover to cubic symmetry. This changeover is also reflected in a large drop in the temperature factors suggesting conversion from a 'rattling' iron in an overly large cavity to a more acceptable coordination.

Low Temperature Neutron Diffraction Experiments

The low temperature neutron diffraction study of the x = 0.1, 0.5 and 0.8 high pressure annealed samples showed three crystallographically and magnetically distinct regions. In all cases the nuclear reflections could be totally indexed on the room temperature structure suggesting no reduction in symmetry below the Néel temperature. However, the resolution of POLARIS would preclude the observation of a small structural change. The 0.1 sample was run at 100K, significantly below its Néel temperature of 580K and showed additional magnetic reflections which were coincident with the nuclear reflections which were similar to those observed fo $LaFeO_3$ at room temperature. This leads to the conclusion that there is no observable structural change associated with the disproportionation reaction seen in the Mössbauer. For the 0.5 sample the data was collected at 4.2K which is below, both the Néel temperature of 240K, and the temperature for disproportionation. Examination of the nuclear reflections at low temperature did not suggest a reduction in symmetry as a consequence of the disproportionation reaction. The low temperature behaviour and magnetic reflections are similar to those observed for $Sr_2LaFe_3O_{8.94}$, however both POLARIS and D1A have relatively poor resolution and tiny structural changes would probably not be resolved using these diffractometers. The x = 0.8 sample was run at 160K and exhibits very strong magnetic reflections which correspond to tripled a parameter. This is very similar to the $SrFeO_3$ magnetic structure which is based on an α-spin helix.

Mössbauer Spectroscopy

Experimentally determined Mössbauer parameters for the high pressure annealed samples at 4.2K and room temperature are summarised in Tables 7.7 and 7.8. The calculated oxygen content determined from the relative proportions of the integrated iron signals are included. An example of the Mössbauer spectra for all three crystallographically distinct regions, for high pressure annealed samples, at 4.2K and room temperature are shown in Figures 7.8 and 7.9.

The Mössbauer measurements on the high pressure oxygen annealed samples show a clear difference between the rhombohedral/orthorhombic and cubic regions. The rhombohedral region, which has been previously studied using Mössbauer spectroscopy by Takano[4,5] and more recently by Battle[6] on the sample $Sr_2LaFe_3O_{8.94}$, shows parameters which are most applicable to Fe^{3+} and Fe^{5+} valence states. At room temperature the rhombohedral spectrum can be interpreted as a mixed valence iron(III) and iron(IV) state which undergoes charge disproportionation at low temperature to give three hyperfine split sextets which are relatively sharp. The sharpness of the signal is indicative of an ordered spin arrangement and magnetic reflections are indeed observed at low temperature using the POLARIS neutron diffractometer at the Rutherford Appleton Laboratory. The Mössbauer parameters observed for the rhombohedral and cubic regions are similar to those observed for Takano[4,5] although in our case the best fit to the data was achieved using three iron signals instead of two which was used by Takano for most of his assignments. Averaged Mössbauer parameters in all cases are in very good agreement with those observed by Takano.

The disproportionation behaviour, producing Fe^{3+} and Fe^{5+}, clearly extends to the orthorhombic region although these samples are magnetically ordered at room temperature. Comparison of the 4.2K spectra with that of the rhombohedral region show obvious similarities. In contrast to this, the spectrum from the cubic region is very different with Mössbauer parameters characteristic of iron(III) and iron(IV) both at room temperature and 4.2K. This is similar to the behaviour noted for the slightly oxygen deficient cubic region of $SrFeO_{3-\delta}$, $\delta < 0.05$ (22)

Quadrupole splitting, where there is Fe^{3+}/Fe^{5+} disproportionation is in all cases

Table 7.7 Mössbauer Hyperfine Parameters at 300K

Mössbauer parameters at 298K

x	Fe^{3+} IS mms⁻¹	Fe^{3+} B_{hf} kG	Fe^{3+} QS mms⁻¹	Fe^{3+} Int %	Fe^{4+} IS mms⁻¹	Fe^{4+} B_{hf} kG	Fe^{4+} QS mms⁻¹	Fe^{4+} Int %	Fe^{5+} IS mms⁻¹	Fe^{5+} B_{hf} kG	Fe^{5+} QS mms⁻¹	Fe^{5+} Int %	Calc Oxygen Content
0.0	0.37	523	-0.08	100									3.00
0.1	0.38 0.33 0.32	537 417 411	-0.06 -0.06 0.03	57 23 11					-0.06	236	0.12	9	3.00
0.2	0.37 0.37	512 421	-0.06 -0.14	36 52					-0.07	227	-0.02	12	3.02
0.3	0.36 0.32 0.22	556 556 528	-0.04 -0.04 0.22	5 46.5 39.5					-0.19	268	-0.02	9	2.94
0.4	0.29		0.12	59	0.10			41					3.00
0.5	0.27		0.10	50	0.09			50					3.00
0.6	0.25		0.08	40	0.10			60					3.00
0.7	0.23		0.06	30	0.09			70					3.00
0.8	0.19		-	28	0.08			72					2.96
0.9	0.18		0.493	13	0.09			87					2.99
1.0					0.07			100					3.00

Table 7.8 Mössbauer Hyperfine Parameters at 4.2K

Mössbauer parameters at 4.2K

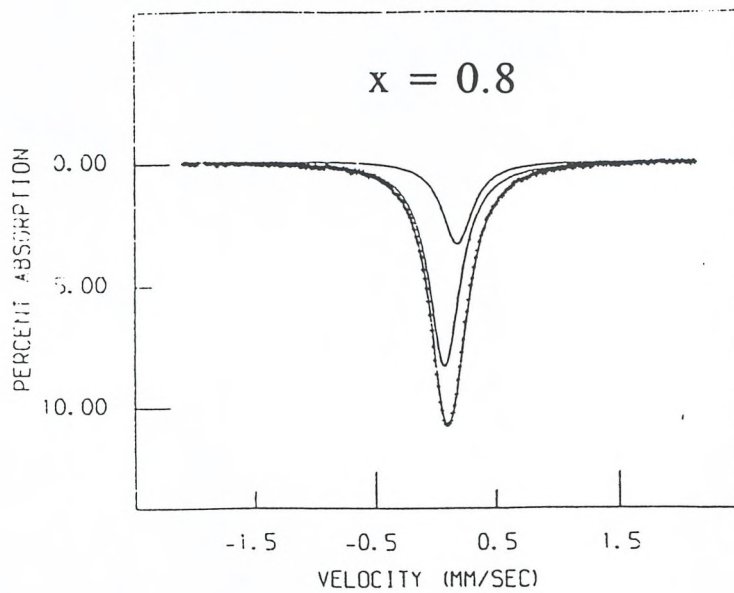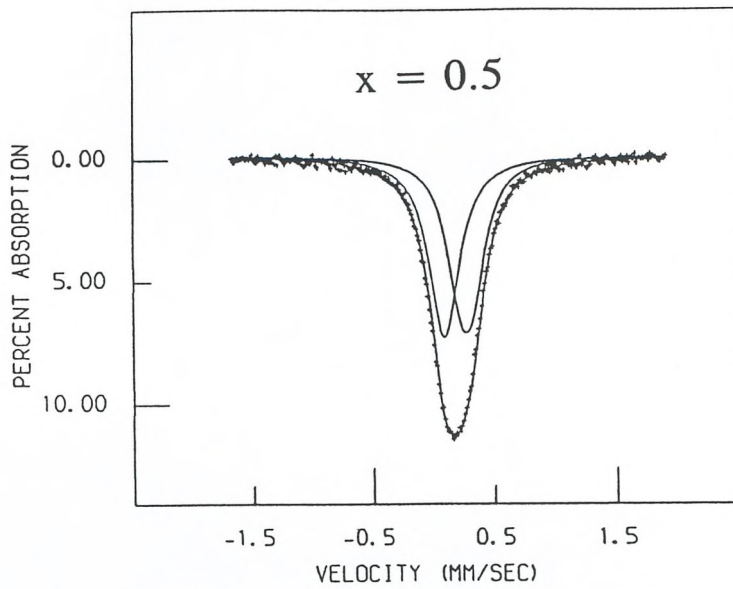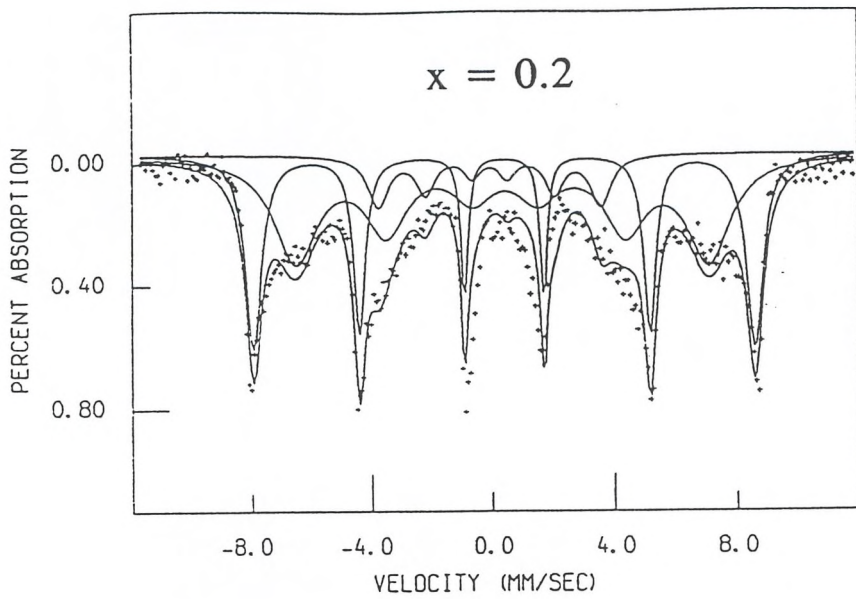| x	Fe^{3+}				Fe^{4+}				Fe^{5+}				Calc Oxygen Content
	IS mms^{-1}	B$_{hf}$ kG	QS mms^{-1}	Int %	IS mms^{-1}	B$_{hf}$ kG	QS mms^{-1}	Int %	IS mms^{-1}	B$_{hf}$ kG	QS mms^{-1}	Int %	
0.0	0.47	562	-	100									3.00
0.1	0.46 0.42	560 539	-0.09 -0.06	57 34					0.06	264	-0.02	9	3.04
0.2	0.47 0.43	560 537	-0.09 -0.05	35 54					-0.05	264	0	11	3.01
0.3	0.48 0.43	555 528	-0.04 -0.06	16 68					-0.04	267	-0.02	16	3.01
0.4	0.41 0.41	534 506	-0.04 -0.09	33 46					-0.04	271	-0.04	21	3.01
0.5	0.44 0.40	521 492	-0.05 -0.06	22 51					-0.02	272	-0.05	27	3.02
0.6	0.38 0.37	487 466	-0.02 -0.05	26 44					-0.03	262	0	30	3.00
0.7	0.37 0.35	466 452	-0.03 -0.03	24 41					-0.01	266	-0.04	35	3.00
0.8	0.37 0.30	451 396	-0.07 -0.02	23 14	0.18	337	-	49	-0.06	279	-0.09	14	2.96
0.9	0.39	447	0.06	12	0.17	333	-	88					2.99
1.0					0.07	326		100					3.00

201

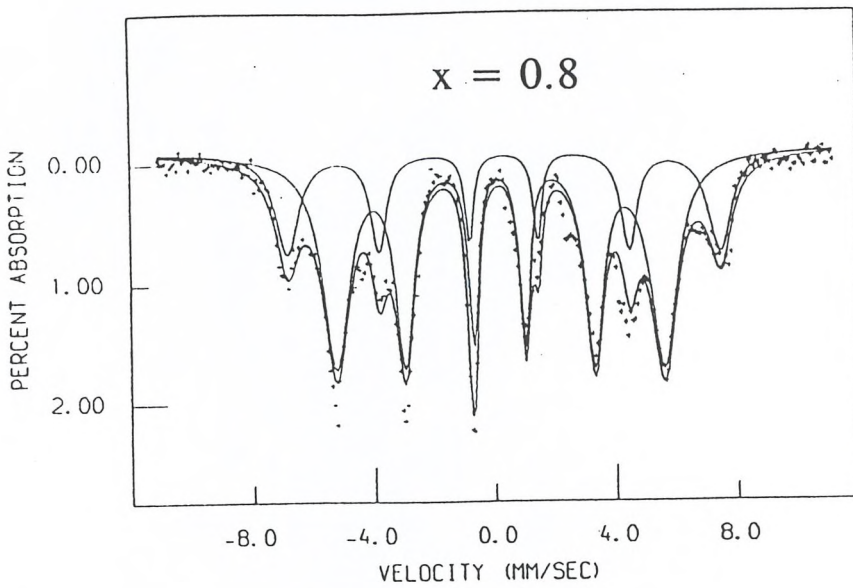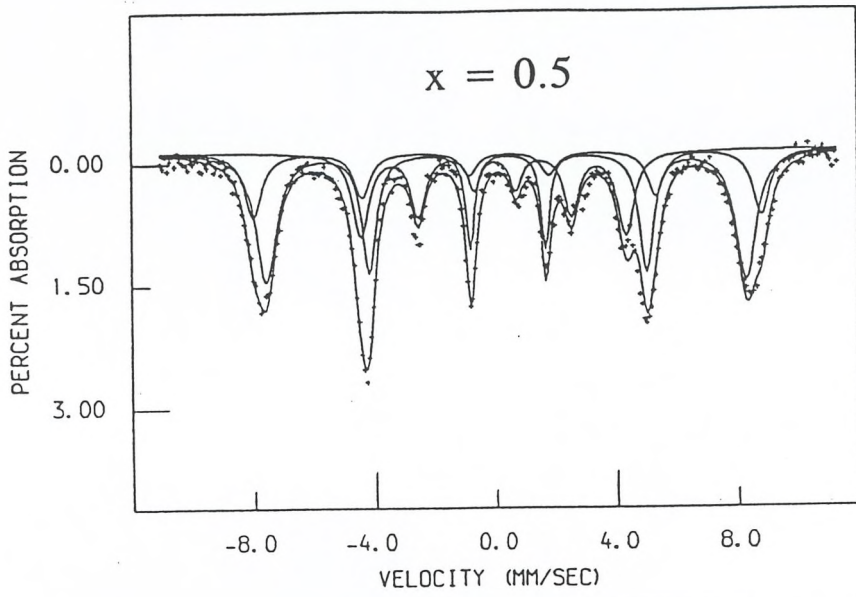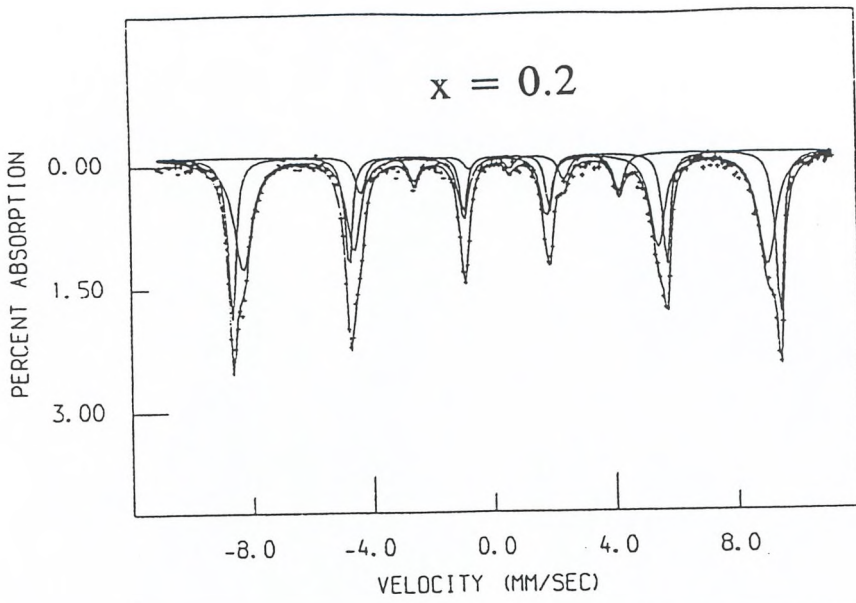**Figure 7.8** Mössbauer Spectra at 298K

202

Figure 7.9 Mössbauer Spectra at 4.2K

203

very small or negligible suggesting the crystallographic site is distorted from octahedral o a very small extent. This observation is in good agreement with the neutron diffraction data which show only a slightly distorted site with bond lengths typically in the range 1.93 - 2.03Å for the orthorhombic region and bond angles only slightly removed from 90° in both rhombohedral and orthorhombic regions.

7.6 Conclusions

The system $La_{1-x}Sr_xFeO_{3-\delta}$ is very complex and is highly sensitive to preparative conditions. The symmetry of the phases produced depends not only on the value of x but also the level of oxidation. Generally the phases produced have an analagous phase in the system $SrFeO_{3-\delta}$.

High pressure annealed samples were shown by neutron diffraction to fall into three distinct regions, each having different nuclear and magnetic structures. Determination of cell parameters and atomic coordinates was only possible on the high resolution instrument which allowed data of excellent quality to be collected. This allowed high quality refinements to be achieved even though the cell distortions were small. Minor quantities of impurity were revealed to be present at the phase boundaries.

The results from the neutron diffraction refinements were in close agreement with those first derived by x-ray diffraction. Oxygen content determined by TGA, neutron diffraction and those calculated from the relative proportions of iron^{n+} where n = 3^+, 4^+ and 5^+ determined by Mössbauer analysis were also in very good agreement ($\pm$ 0.02)

Mössbauer spectroscopy has also shown different behaviour for all three crystallgraphic regions of the high pressure oxygen annealed samples. The orthorhombic and rhombohedral systems both show charge disproportionation of the iron(IV) ions similar to that observed in $CaFeO_3$ (4). Above the Neel temperature the rhombohedral samples give an averaged Mössbauer signal. The third, cubic, region shows no disproportionation and remains a mixture iron(III)/iron(IV) system throughout the examined temperature range.

Further work is planned in the system to investigate the low temperature behaviour on a higher resolution neutron diffractometer to allow magnetic structure determination.

7.7 References

1   J.S. Waugh. M.I.T. Laboratory for Insulation Research. Technical Report No. 152 (1960)

2   W.F. Kelly. M.S. Thesis. M.I.T. (1961)

3   U. Shimony, J.M. Knudsen. Phys. Rev. **144**, 361-6. (1966)

4   M. Takano, N. Nakanishi, Y. Takeda, S. Naka, T. Takada. Mat. Res. Bull. **12**, 923-8. (1977)

5   M. Takano, J. Kawachi, N. Nakanishi, Y. Takeda. J. Sol. Stat. Chem. **39**, 75-84. (1981)

6   P.D. Battle, T.C. Gibb, S. Nixon. J. Sol. Stat. Chem. **79**, 75-85. (1989).

7   T. Takeda, Y. Yamaguchi, H. Watanabe. J. Phys. Soc. Jap. **33**, 967-9. (1972).

8   P.D. Battle, T.C. Gibb, P. Lightfoot. J. Sol. Stat. Chem. **84**, 271-9. (1990)

9   T. Peterlin-Neumaier, E. Steichele. J. Magnetism and Magnetic Materials. **59**, 351-6. (1986).

10   H. Oda, Y. Yamaguchi, H. Takei, H. Watanabe. J. Sol. Stat. Chem. **42**, 101. (1977).

11   M. J. Johnson, W.I.F. David. Rutherford Appleton Report No. 81/112. (1985).

12   S. Geller, A.E. Wood. Acta. Cryst. **9**, 563. (1969)

13   D.B. Currie, M.T. Weller. Acta. Cryst. **C47**, 696-8. (1991).

14   H.L. Yakel. Acta. Cryst. **8**, 394. (1955)

15   G.J. Long, T.E. Cranshaw, G. Longworth. Mössbauer Effect and Reference and Data Journal. **6**, 42-9. (1983).

16   J.B. MacChesney, R.C. Sherwood, J.F. Potter. J. Chem. Phys. **43**, 1908-13. (1965).

17   V.N. Panyustikin, G. Pasquali, G. Driakamer. J. Chem. Phys. **51**, 3305-8. (1965).

18   T. Takeda, Y. Yamaguchi, H. Watanabe. J. Phys. Soc. Jap. **33**, 967-9 (1972).

19   B.C. Tofield, C. Greaves, B.E.F. Fender. Mat. Res. Bull. **10**, 737-46. (1975)

20   M. Harder, H.K. Muller-Buschbaum. Z. Anorg. Allgem. Chem. **404**, 169-75. (1980).

21   Y. Takeda, K. Kanno, T. Takada, Y. Yamamoto, M. Takano, N. Nakayama, Y.

Bando. J. Sol. Stat. Chem. **63**, 237-49. (1986).

22 M. Mizusaki, M. Okayasu, S. Yamauchi, K. Fueki. J. Sol. Stat. Chem. **99**, 166-172. (1992)

23 J.C. Grenier, J. Daimet, H. Pouchard, P. Haggenmuller. Mat. Res. Bull. **11**, 1219-26. (1976).

24 P.D. Battle, T.C. Gibb, P. Lightfoot. J. Sol. Stat. Chem. **84**, 237-44. (1990).

25 I.D. Brown, D. Aldermatt. Acta. Cryst. **B41**, 244. (1983).

CHAPTER 8

Preparation and Characterisation of the System $LaFe_{1-x}Cu_xO_{3-\delta}$

8.1 Introduction

Iron doping experiments for copper in the high temperature superconducting cuprates have been of interest in the last few years. However, the location and oxidation state of the dopant atoms has been of debate (1, 2). Major problems are associated with the very low quantities of dopant (typically $\leq$ 5 molar percent). Techniques which are routinely utilised to identify iron oxidation state such as Mössbauer spectroscopy are often ineffective at these low levels.

Comparison of iron and copper in perovskite based structures shows the two are responsible for different types of anion vacancies. This is largely due to the different sort of coordination environment preferred by the two ions. In the case of iron, the octahedral or tetrahedral environment is preferred, whereas copper has a tendency towards square pyramidal or square planar geometries depending on the oxidation state of the cation.

Raveau *et al* (3) studied doping of copper into perovskite structures containing iron(IV). In the $SrFe_{1-x}Cu_xO_{2.5-x/2+\delta}$ system the doping of copper for iron had very little effect on the structure increasing the cubic cell parameter by only 0.4%. Using chemical analysis and Mössbauer spectroscopy the individual oxidation states of the ions: copper was both trivalent and divalent, all tetravalent atoms were iron. Addition of copper to a level of 20% caused a large increase in the conductivity resulting from an increase in the density of states at the conduction level based on the 3d atomic orbitals of copper. Similar behaviour was noted in the $La_{0.5}Ba_{0.5}Fe_{1-x}Cu_xO_{2.75-x/2+\delta}$ (4) system where high levels of both iron(IV) and copper(III) are reported.

$LaFeO_3$ has an orthorhombically distorted cubic perovskite cell and is made under atmospheric pressure at 1300°C in air (5). Crystallising in the space group Pbnm, it has iron in a distorted octahedral environment. In contrast, the copper analogue is rhombohedral and is formed by reaction of the constituent oxides with $KClO_3$ as an external source of oxygen at 50Kbar and 1500°C (6). Space group symmetry is $R\bar{3}c$ and the transition metal again has a distorted octahedral configuration. A solid solution between the two materials would be interesting on the grounds of the effect of changing transition metal on the structure, the electrical conductivity and the oxidation states of the ions.

This chapter reports the preparation of some compounds with the formula $LaFe_{1-}$

$_xCu_xO_{3-\delta}$, $0 \leq x \leq 0.5$, prepared using ambient conditions of temperature and pressure. Structural characterisation is performed by powder x-ray and neutron diffraction. The oxygen content of the materials are determined by thermogravimetric analysis and the iron oxidation state by Mössbauer spectroscopy. The copper oxidation state is then calculated by difference.

8.2 Experimental

Homogeneous samples of Fe_2O_3, CuO and La_2O_3 in the correct molar proportions were heated at $1000°C$ in a box furnace overnight ($0 < x < 0.6$). After quenching x-ray diffraction analysis of the products showed them to be a mixture of $LaFeO_3$, La_2CuO_4 and CuO (Figure 8.1). Oxygen annealing at $1150°C$ in oxygen and slow cooling to room temperature, showed complete conversion to an orthorhombic phase with a structure similar to that of $LaFeO_3$ (Figure 8.2). The colour of the phases changed from being red/brown in the case of $LaFeO_3$, to black on the addition of copper. Increasing the value of x showed that the solution limit was x = 0.3. Further increases in the level of copper substitution, resulting in irremovable quantities of La_2CuO_4 in the diffraction pattern. A summary of the change in lattice parameters is shown in Table 8.1

Table 8.1 Lattice Parameters of $LaFe_{1-x}Cu_xO_{3-\delta}$ (Å)

x	a(Å)	b(Å)	c(Å)
0.0	5.557(1)	5.565(1)	7.854(1)
0.1	5.555(1)	5.562(1)	7.851(2)
0.2	5.550(1)	5.555(1)	7.849(2)
0.3	5.545(1)	5.550(2)	7.845(2)

Thermogravimetric analysis was performed in platinum crucibles heating to $750°C$ in 5% H_2/N_2 and gave an oxygen content invariant from three (assuming iron and copper were reduced to Fe^{3+} and Cu^{2+} respectively). X-ray diffraction analysis of the t.g.a. product
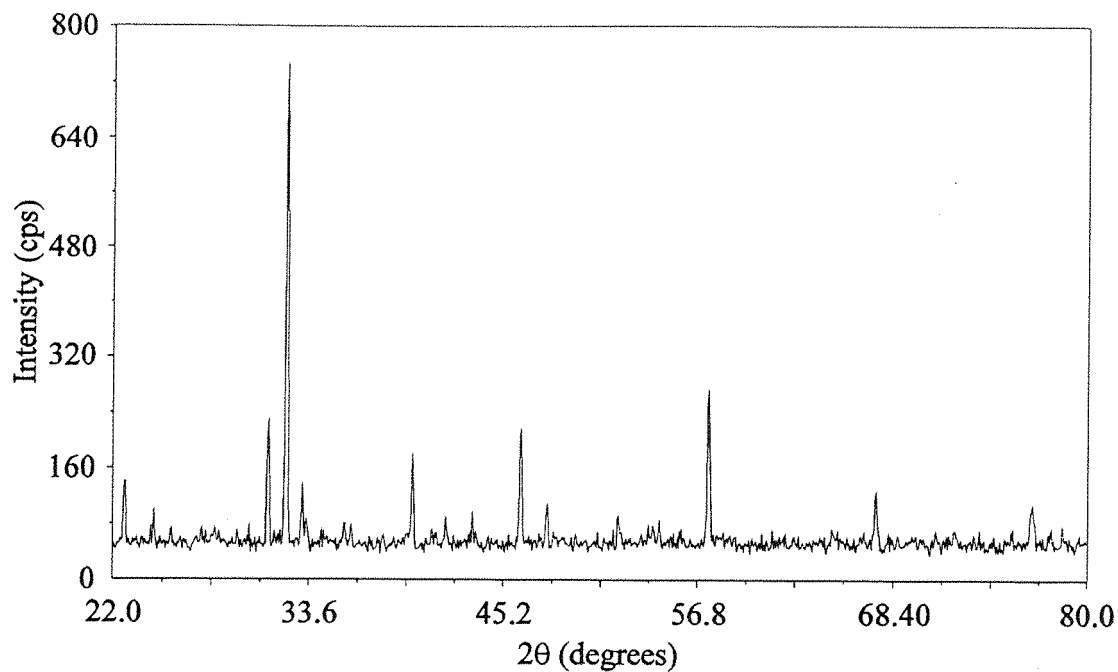
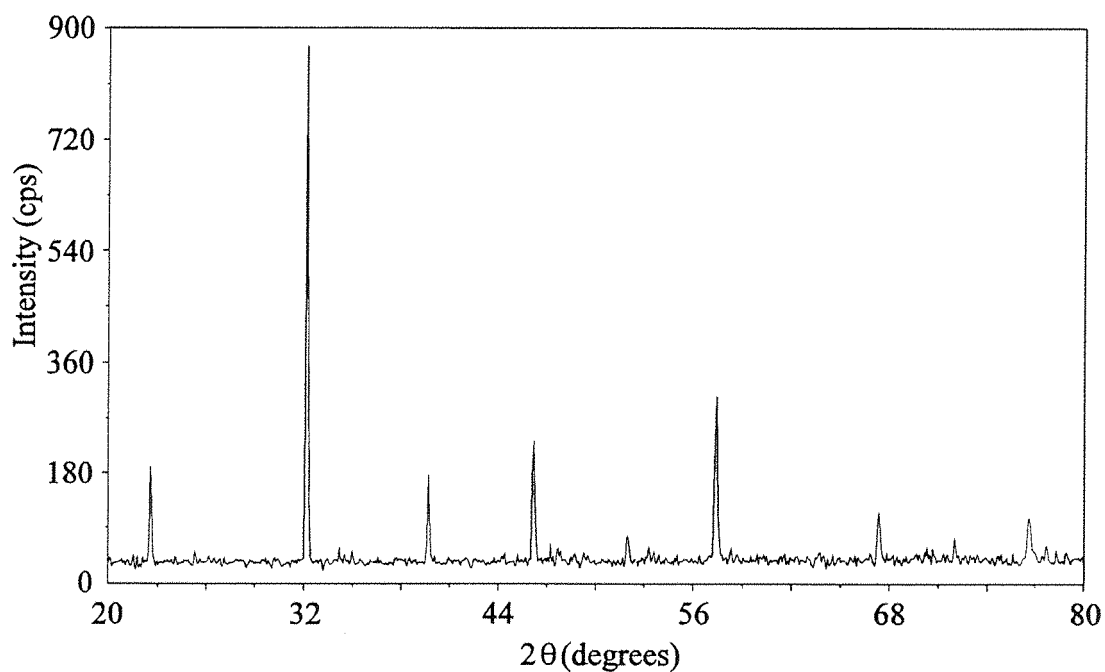**Figure 8.1** X-ray diffraction pattern of x = 0.2 air quenched

Figure 8.2 X-ray Pattern of sample x = 0.2 after Oxygen Annealing

210

gave an orthorhombic unit cell similar to the parent material but with a shift to lower 2θ.

8.3 Powder Neutron Diffraction

Powder neutron diffraction data for refinement were collected on the oxygen annealed sample x = 0.1 at the HRPD diffractometer at the Rutherford Appleton Laboratory. The substantial scattering lengths of the ions allowed collection of data of suitable quality for refinement in 4hrs.

High d-spacing neutron diffraction data for analysis of magnetic reflections were collected at 300K on the POLARIS diffractometer at the Rutherford Appleton Laboratory.

8.4 Mössbauer Spectroscopy

The Mössbauer data were obtained with a conventional transmission spectrometer using a double ramp waveform to give a flat background.   Finely ground samples were combined with boron nitride to randomise the orientations of the microcrystals and weighed to give optimum signal to noise (7).

8.5 Results and Discussion

Powder X-ray Diffraction

Initial x-ray data were collected on the Siemens D5000 diffractometer and showed complete conversion to a phase with an orthorhombic unit cell. Accurate positions of narrowly separated groups of reflections were pin-pointed using a continuous scan in the range 20 -80° using a step size of 0.02°. Deconvolution of groups of reflections was then achieved using a stepped scan, typically using a step size of 0.004°, counting for 10-15mins over each range of 2-3°. These reflections were then indexed by comparison with the JCPDS pattern of $LaFeO_3$ and cell parameters calculated using the CELL program.

The behaviour of the cell parameters with increasing copper substitution is shown in Figure 8.3. There is a reduction in all the cell parameters as the copper content, x, increases.   As the oxygen content, as determined by t.g.a, remains constant, this

behaviour is indicative of the trivalent iron (0.645Å) being replaced by a smaller ion. Clearly this substitution of a smaller ion can occur in two ways; either iron(III) is oxidised to iron(IV) and copper enters the structure as copper(II) or copper(III) is simply replacing iron(III) which is smaller in size (0.54Å). Alternatively, a mixture of the above processes could be occuring
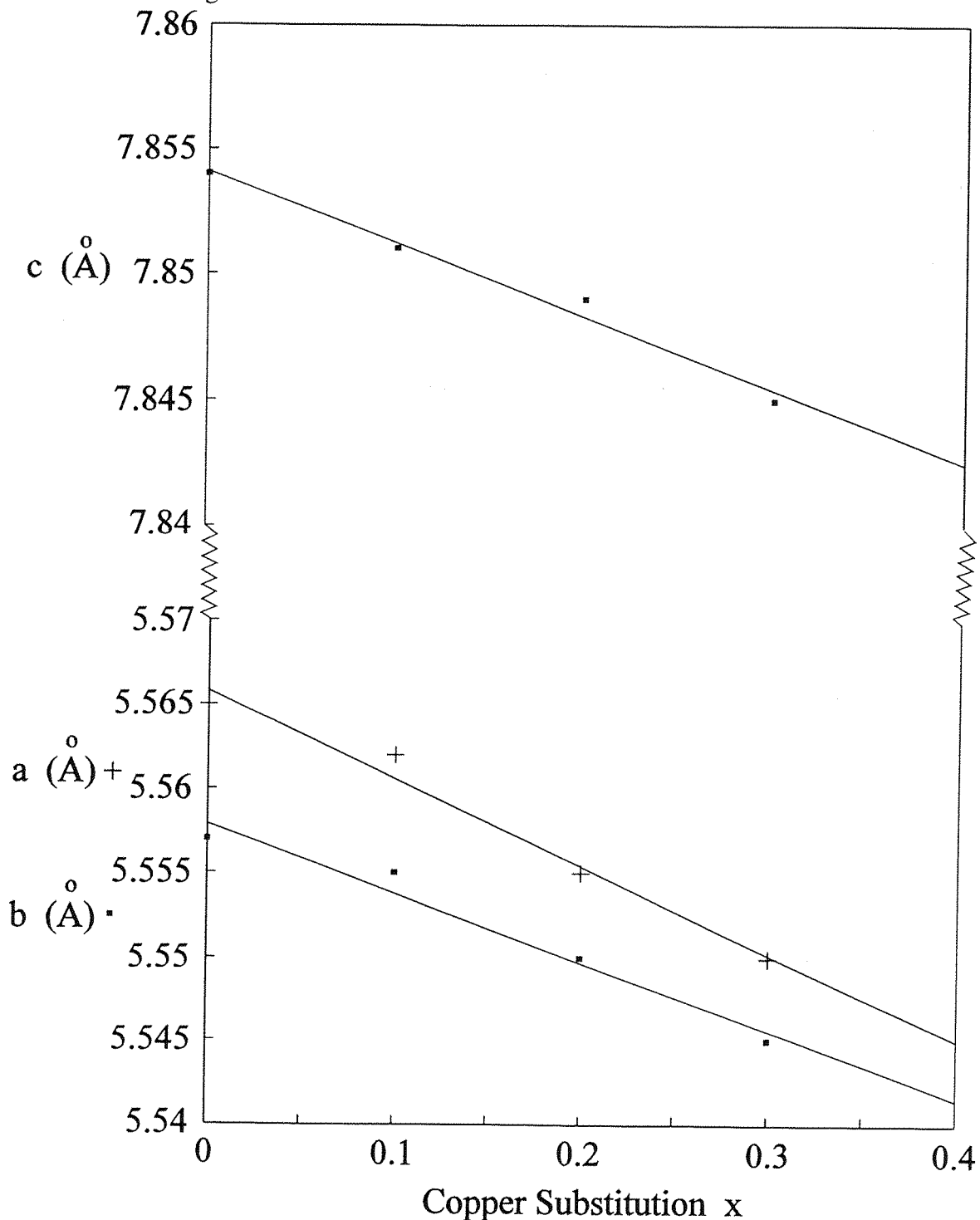

Figure 8.3 Change in the Lattice Parameters with Copper Substitution

212

Structure Refinement

Profile refinement of the $LaFe_{0.9}Cu_{0.1}O_3$ sample was performed in the space group Pbnm using the starting model of $LaFeO_3$ (5). Additional magnetic reflections were found in the refinement profile which could not be refined at the time of data collection. These reflections were, therefore, placed in excluded regions. Careful scrutiny of the diffraction pattern showed no further additional reflections and the refinement proceeded smoothly in the space group Pbnm. Initial stages of the refinement included lattice parameters and instrumental parameters such as background, peak shape functions and scale factor. Atomic positions were then refined. Refinement of temperature factors showed all oxygens to have similar values. Refinement of oxygen occupancies showed only very tiny deviations from unity which were always within the e.s.d. and so the values were fixed at full occupancy. Final stages of the refinement included anisotropic temperature factors. A summary of the refined parameters is given in Table 8.2 and the refinement profile is shown in Figure 8.4. Calculated bond distances and angles compared with the pure iron material is given in Tables 8.3a and b.

The latter two tables show there is very little change in bonding coordination around the transition metal centre on addition of copper. Copper(II) is a d^9 ion and many copper(II) materials show signs of Jahn-Teller distortion. For example, in La_2CuO_4 (8) the copper atoms has four short in-plane interactions (1.9Å) and two long apical bonds of (2.2Å). This distortion of the metal ion coordination is usually manifested as a deformation of the parent structure: $KCuF_3$ (9) has a tetragonally distorted structure based on the perovskite (10) structure and La_2CuO_4 has a orthorhombically distorted version of the K_2NiF_4 structure. In contrast, structures containing either Fe^{4+} or Cu^{3+} do not display this kind of distortion. For example, $SrFeO_3$ (11) forms a perfect perovskite cube with a = 3.850Å although the tetravalent iron is high spin d^4 and would be expected to show Jahn-Teller distortion. Trivalent copper is a d^8 ion and as a natural consequence has a tendency to be square planar. However, the six-fold octahedral coordination is also known e.g. $LaCuO_3$ (5) and is not highly distorted. This may indicate that the copper atoms are substituting in the trivalent state predominantly since there is no great change in the transition metal ion coordination on copper substitution.

213

Table 8.2 Refined Atomic Parameters

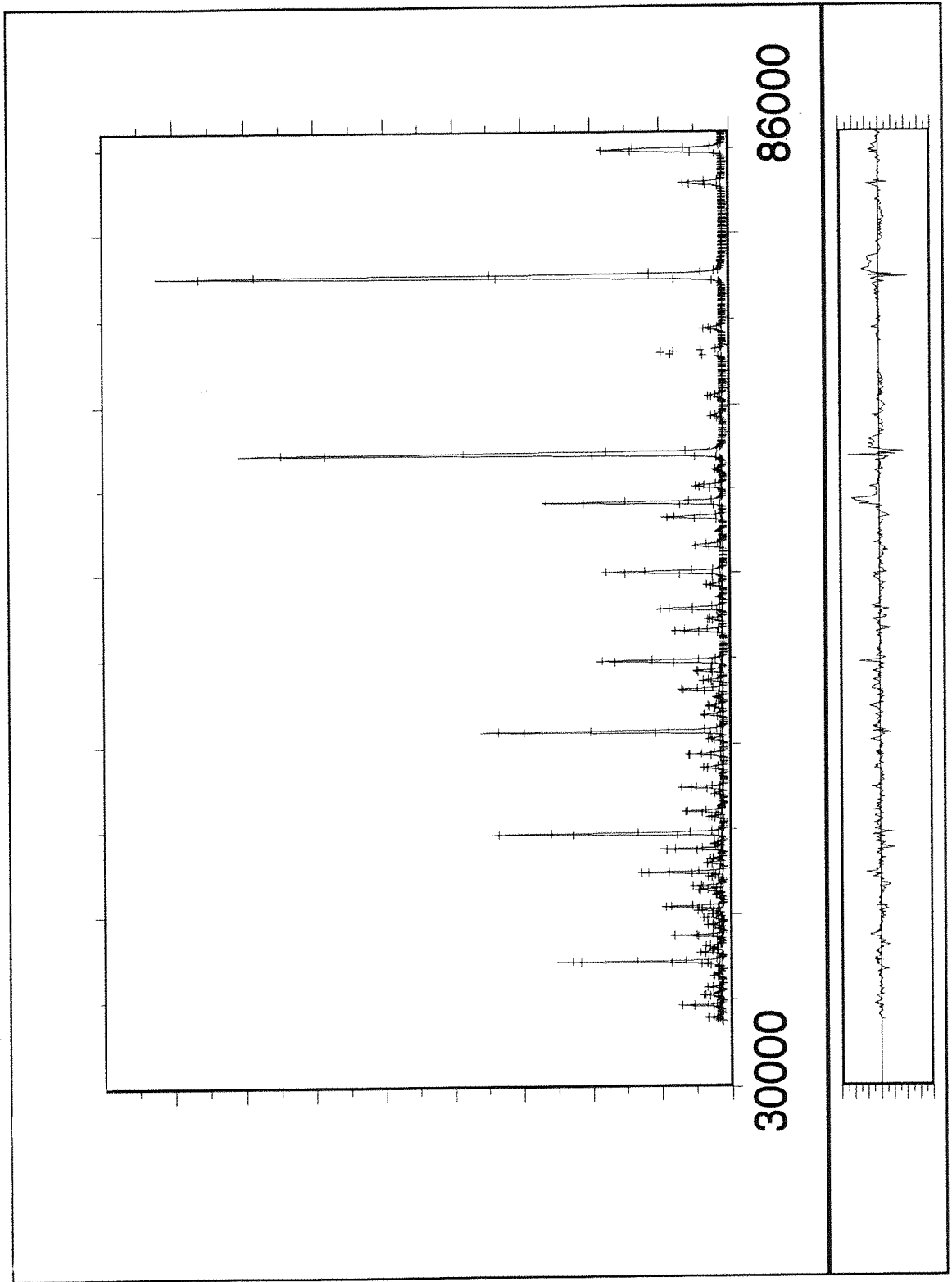| LaFeO$_3$				LaFe$_{0.9}$Cu$_{0.1}$O$_3$			
a = 5.55702(2)Å				a = 5.55693(4)Å			
b = 5.56521(1)Å				b = 5.56080(4)Å			
c = 7.85426(2)Å				c = 7.85295(5)Å			
Atomic Parameters				**Atomic Parameters**			
Atom	x	y	z	Atom	x	y	z
La	0.0923(4)	0.0292(1)	0.25	La	0.0923(1)	0.0284(4)	0.25
Fe	0	½	0	Fe	0	½	0
O1	0.0748(4)	0.4855(3)	0.25	O1	0.0758(10)	0.4863(8)	0.25
O2	0.7191(2)	0.2817(2)	0.0394(1)	O2	0.7186(6)	0.2800(6)	0.0388(4)
Anisotropic Temperature Factors				**Anisotropic Temperature Factors**			
Atom	$B_{11},B_{22},B_{33},B_{23},B_{13},B_{12}$			Atom	$B_{11},B_{22},B_{33},B_{23},B_{13},B_{12}$		
La	0.53(4),1.12(3),0.73(4),-,-,0.03(3)			La	0.53(1),0.88(10),0.56(10),-,-,0.17(9)		
Fe	0.84(4),0.95(3),0.39(3),0.00(1),0.09(4),0.05(5)			Fe	0.63(13),0.60(11),0.26(10),0.03(5),-0.07(1),0.24(10)		
O1	0.56(6),1.03(6),0.49(5),-,-,-0.06(4)			O1	0.24(18),1.15(18),0.14(9),-,-,-0.18(9)		
O2	0.63(4),1.01(3),0.70(4),-0.05(4),-0.05(4),0.05(4)			O2	0.84(13),0.50(11),0.74(10),-0.01(10),-0.01(10),0.05(5)		

Figure 8.4 Refinement Profile of $LaFe_{0.9}Cu_{0.1}O_3$

215

Table 8.3a Derived Bond Lengths (Å)

Atom - Atom	LaFeO$_3$	LaFe$_{0.9}$Cu$_{0.1}$O$_3$
La - O1	2.581 x 1	2.592 x 1
La - O1	3.059 x 1	3.041 x 1
La - O1	3.158 x 1	3.179 x 1
La - O1	2.421 x 1	2.397 x 1
La - O2	2.648 x 2	2.655 x 2
La - O2	2.805 x 2	2.804 x 2
La - O2	3.277 x 2	3.260 x 2
La - O2	2.450 x 2	2.458 x 2
Fe/Cu - O1	2.008 x 2	2.009 x 2
Fe/Cu - O2	2.002 x 2	2.001 x 2
Fe/Cu - O2	2.010 x 2	2.008 x 2

Table 8.3b Bond Angles Around the Transition Metal Centre (°)

Atom - Atom - Atom	LaFeO$_3$	LaFe$_{0.9}$Cu$_{0.1}$O$_3$
O1 - Fe/Cu - O1	180.0	180.0
O1 - Fe/Cu - O2	89.4	89.1
O1 - Fe/Cu - O2	89.8	89.7
O2 - Fe/Cu - O2	91.4	91.3
O2 - Fe/Cu - O2	88.6	88.7
O2 - Fe/Cu - O2	180.0	180.0

216

Although the refined structure represents an average over all the individual transition metal centres i.e. copper and iron, there is no evidence to suggest that addition of copper produces a large change in the coordination environment.

Low Temperature Neutron Diffraction

The low temperature neutron diffraction pattern of the $LaFe_{0.9}Cu_{0.1}O_3$ from the POLARIS A bank is shown in Figure 8.5 with the additional magnetic reflections indicated (*). Comparison with $LaFeO_3$ (12) reveals a very similar pattern although the magnetic reflections are somewhat weaker. This suggests that the copper-doped samples have a similar magnetic structure although magnetic interactions have become weaker. This is clearly what is expected since high spin Fe^{3+} ions are being replaced with atoms with a smaller magnetic moment.
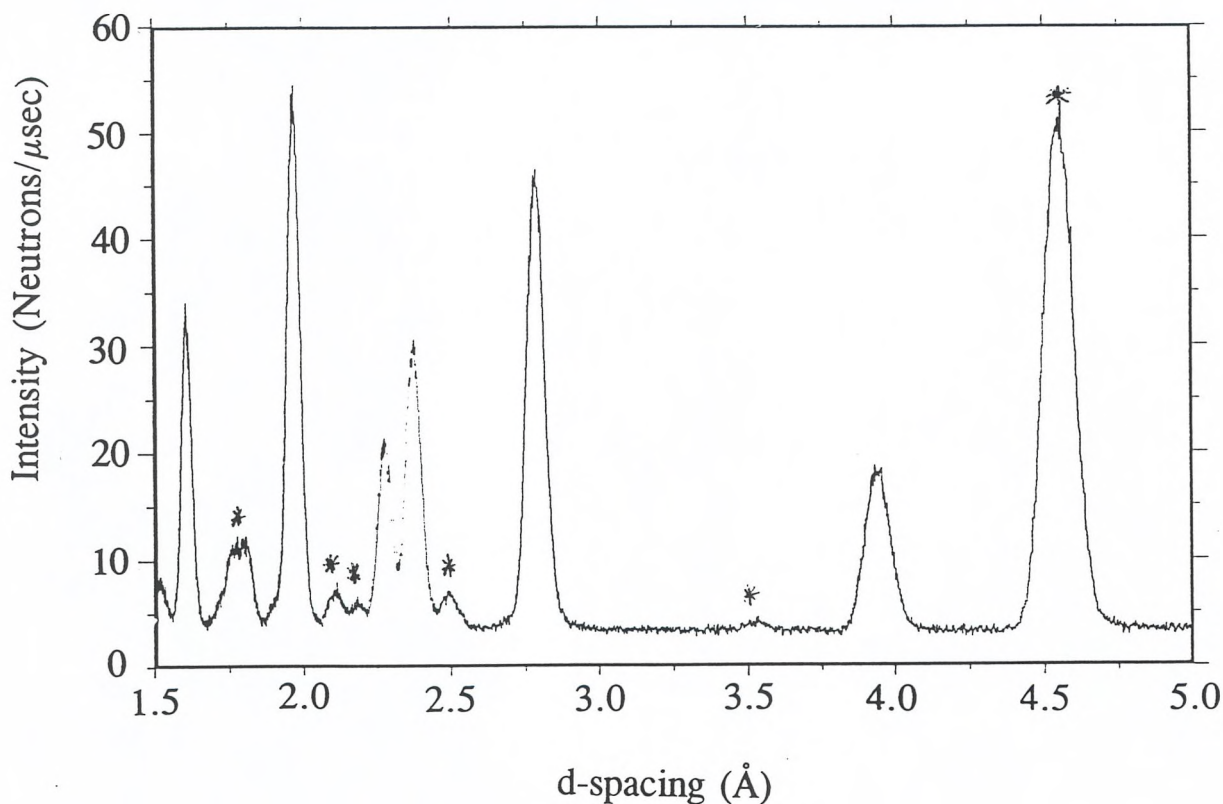

Figure 8.5 Low Temperature Neutron Diffraction Pattern

Mössbauer Spectroscopy

All the Mössbauer spectra in the series consists of a single resonance centred around $0.3 mms^{-1}$ shifting to lower isomer shift slightly as the level of copper increases. This can be attributed to a high spin trivalent iron atom in an octahedral environment where the bonding becomes less ionic on addition of copper. This essentially confirms that the copper is substituting as the tripositive cation since there is no evidence of an Fe(IV) signal in the Mössbauer spectrum. An example of the Mössbauer spectra at room temperature for $x = 0.2$ is shown in Figure 8.6.
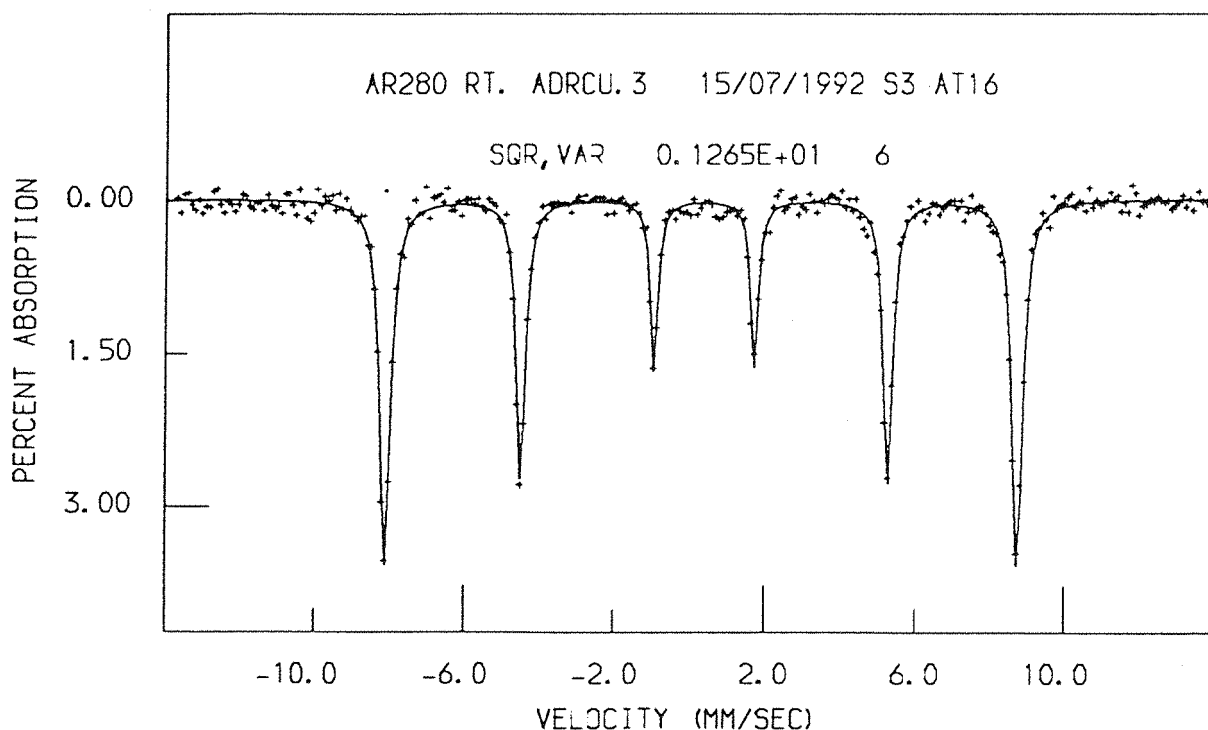

Figure 8.6 Room Temperature Mössbauer Spectrum for $LaFe_{0.8}Cu_{0.2}O_3$

8.6 Conclusions

A solid solution can be formed in the system La-Fe-Cu-O. At low levels of dopant, synthesised at ambient pressure, this appears to have no great effect on the bonding coordination of the transition metal centre. Magnetic interactions weaken on the addition of copper and the bonding becomes less ionic. All indications point to the copper being in the trivalent state.

8.7 References

1   I.Brosch, B. Rrosh. Phys. Rev. B. **43**, 364-7, (1991)

2   I.Felner, I.Nowik, U.Yaron, E.R.Bauminger, D.Hechel. Physica C. **185-9**, 1117-8. (1991)

3   L.Er-Rakho, C.Michel, F.Studer, B.Raveau. J. Phys. Shem. Solids. **49**, 1101-6. (1988)

4   L.Er-Rakho, C.Michel, J.Provost, B.Raveau. J. Sol. Stat. Chem. **37**, 151-6 (1981)

5   M.Marezio, P.D.Dernier. Mat. Res. Bull. **6**, 23-30. (1971)

6   D.B.Currie, M.T.Weller. Acta. Cryst. **C47**, 696-8. (1991)

7   G.J. Long, T.E. Cranshaw, G. Longworth. Mössbauer Effect and Reference Journal. **6**, 42-9. (1983)

8   M.J. Longo, P.M. Raccah. J. Sol. Stat. Chem. **6**, 526. (1973)

9   Natl. Bur. Stand. (U.S.) Monograph. **25**, 25-8. (1968)

10   F.S. Galasso. The Structure, Preparation and Properties of Perovskite Type Compounds. International Series of Monographs in Solid State Physics. **5**, (1968)

11   J.B. MacChesney, R.C. Sherwood and J.F. Potter. J. Chem. Phys. **43**, 1907-13. (1965)

12   T. Peterlin-Neumaier, E. Steichele. J. Magnetism and Magnetic Materials. **59**, 351-6 (1986).

CHAPTER 9

Conclusions

9.1 Conclusions

Tolerance factors have been used in this work to predict theoretically stable structures, based on close-packed arrays of ions. This procedure, clearly provides an indication of the stability of the final structure, in terms of the ionic radii, but cannot predict the synthetic conditions required. Clearly, this is purely a mathematical (empirical) argument, and does not consider the full thermodynamics of the system. The best application, is then, perhaps, as a method of predicting phases which will be unstable. For example, this procedure predicted that strontium, nickel and oxygen would not form the K_2NiF_4 structure, where the two cations are incompatible in terms of ionic size. Experimentally this has proved to be true, both by ourselves (1), and other workers (2). A second point, highlighted by Sr_2CrO_4, is the relationship between the formulation of the material and the actual structure. Sr_2CrO_4 (3) would be theoretically stable in the K_2NiF_4 structure with a tolerance factor of 0.94, but instead forms the ß-K_2SO_4 structure under ambient conditions (4), only adopting the K_2NiF_4 structure at high pressure (5). Therefore, even though tolerance factor arguments predict the K_2NiF_4 structure to be stable for chromium, strontium and oxygen, the full energetics of the system including formation of the M^{4+} ion, ultimately dictate the actual structure formed.

The use of tolerance factors in this work successfully predicted the stability of the phase Sr_2FeO_4. However, this procedure predicted that Sr_2CoO_4 could also be formed, although synthesis under similar conditions was unsuccessful. The very minimal difference in tolerance factors between these two materials gives no easy, conceptual, reason to the obvious difference in synthetic conditions.

Figure 9.1 summarises the M^{4+} ions which have been shown to adopt the K_2NiF_4 structure with Sr and O. As the first row of the transition metal series is transversed the M^{4+} ion becomes progressively more difficult to form as the ionisation potentials increase. Therefore, the Co and Ni analogues would be expected to require even stronger oxidising conditions than the Fe compound. The high oxidation states of the transition metals increase in stability relative to the $3d^n$ elements such that $5d^n > 4d^n > 3d^n$ ($n \leq 10$). When $n \leq 10$, the higher oxidation states also become more stable in relation to the low valence states. This means the Rh^{4+} and Ir^{4+} analogues of the K_2NiF_4 structure are known where the Co^{4+} analogue is not. For the d^5, d^6 and d^7 ions, only transition metals from

Ti[6]	V[7]	*Cr[5]	Mn[8]	Fe[9]	Co	Ni	Cu	Zn		
Zr[10]	Nb	Mo	Tc	Ru[11]	Rh[12]	Pd	Ag	Cd	In	Sn[13]
Hf[14]	Ta	W	Re	Os	Ir[15]	Pt	Au	Hg	Tl	Pb[16]

Figure 9.1 Ions forming the K_2NiF_4 Structure

Bold symbols represent M^{4+} cations for which the K_2NiF_4 structure forms, normal typescript describes phases which are unknown. Superscripts are reference numbers

* refers to the high pressure form, prepared at 65Kbar.

the first row have been show to form the K_2NiF_4 structure. This trend is a result of the increased stability of the d^{n+} ions, where n refers to the number of ground state d electrons, which tend to form in preference to the lower oxidation states. For example, reducing conditions were required to produce Sr_2VO_4, which contains the unusual V^{4+} ion. For both Nb and Ta the stable oxidation state is 5^+ and stringent reducing conditions are required for the lower oxidation states.

Figures 9.2 and 9.3 depict the change in lattice parameters with ion for the metals which form the K_2NiF_4 structure in the first row of the transition metal series. In Figure 9.2, there is a steady fall in the cell parameter, a, until Mn and then a sudden rise at Fe. This is further evidence to support the hypothesis that the iron is a high spin d^4 ion; the a parameter is simply controlled by the Fe - O - Fe distance, up to and including manganese the electrons are being placed in the low energy t_{2g} orbitals, a fourth electron, as in Fe^{4+}, must be either placed in the high energy e_g orbital, or be spin paired in the t_{2g} orbital. The former case, should produce a significant lengthening of the M - O bond and, therefore, cause the lattice parameter, a, to rise. The c-parameter, conversely, continues to shorten with Fe. This is not anomalous behaviour, however, since the c-parameter is not controlled uniquely by the Fe-O distance.

Figure 9.4 shows the known compounds which form the $Sr_3M_2O_7$ structure. It should be noted that the use of tolerance factors in the Ruddlesden-Popper series of oxides suggests that the range of tolerance factors decreases, as n increases (22). This would suggest that $Sr_{n+1}M_nO_{3n+1}$,where M is a transition metal and n = 2, 3, etc, would be increasingly more difficult to form as the value of n increases. However, there are few M^{4+} ions for which the n = 1 phase exists and the n = 2 phase does not. For the first row of the transition metal series; when n = 1, transition metals, up to and including M = Fe, can be incorporated into the K_2NiF_4 structure. This stability range is replicated in the n = 2 series with fully oxidised M^{4+} ions. However, results from this work, show that the n = 2 phase, $Sr_3Co_2O_{7-z}$, can be synthesised using ambient conditions where similar attempts in the n = 1 system failed. The most feasible reason for this anomaly is in the initial calculation. The tolerance factors used are those for tetravalent B cations in a fully stoichiometric oxygen lattice. In the $Sr_3Co_2O_{7-z}$ structure, the quantity z never falls below 0.94 (23), which implies a large number of oxygen vacancies in the structure. Therefore, the tetravalent ion is in very low concentration in this structure, with most
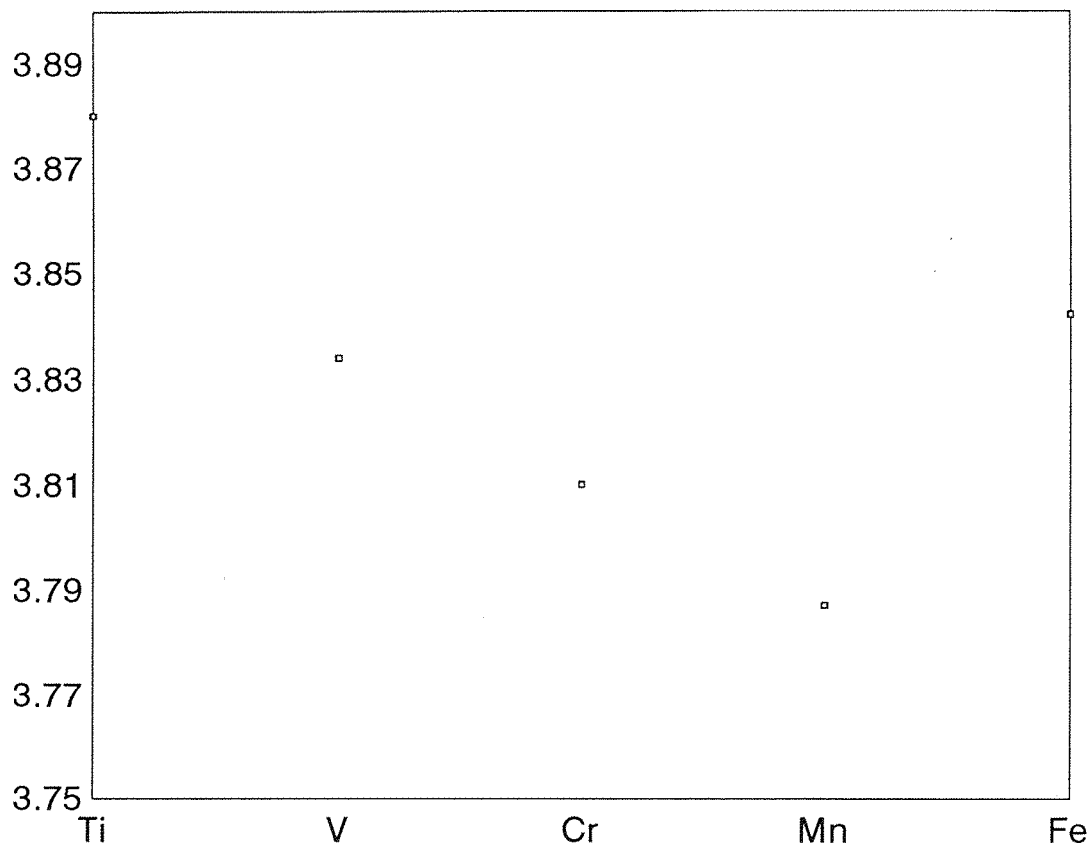
224

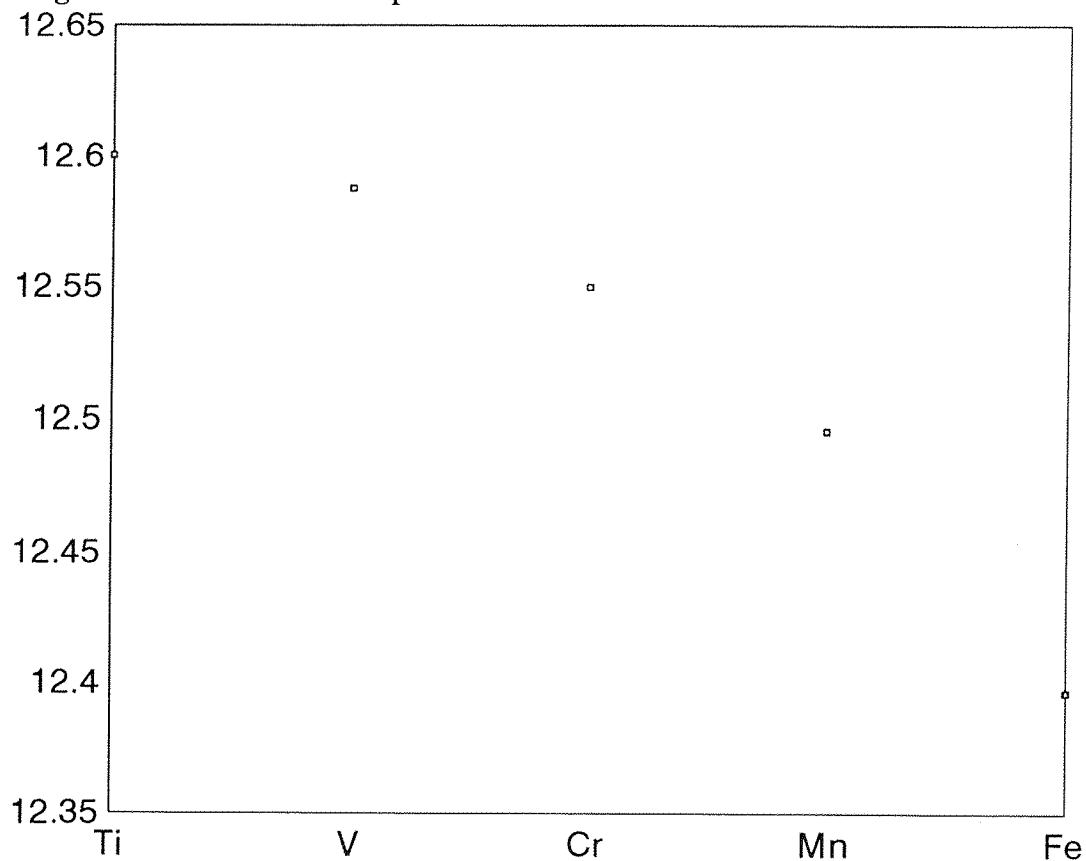**Figure 9.2** Variation in a-parameter with Transition Metal Ion.

Figure 9.3 Variation of c-parameter with Transition Metal Ion.

Ti[17]	V	**Cr**[5]	**Mn**[18]	**Fe**[19]	**Co**[20]	Ni	Cu	Zn		
Zr[10]	Nb	Mo	Tc	**Ru**[11]	**Rh**[12]	Pd	Ag	Cd	In	**Sn**[21]
Hf[14]	Ta	W	Re	Os	**Ir**[15]	Pt	Au	Hg	Tl	**Pb**[16]

Figure 9.4 Ions forming the $Sr_3M_2O_7$ structure.

Bold symbols represent M^{4+} cations for which the $Sr_3M_2O_7$ structure forms, normal typescript describes phases which are unknov Superscripts are reference numbers

226

cobalt ions being trivalent. This level of oxygen vacancy is much more unlikely in the Sr_2MO_4 structure where the lowest level of vacancy reported is that of $Ca_2FeO_{3.5}$, (24) whereas a level of oxygen as low as 5.7 (23,25) is not uncommon in the $n = 2$ phase. Comparatively, this means that a maximum of 12.5% of the total oxygen content can be lost from the Sr_2MO_4 which is much less than 18.5% of the total which can be lost from the $Sr_3M_2O_7$ lattice. A likely reason for the difference in ability of the structure to support non-stoichiometry is the coordination of the A cations. In the Sr_2MO_{4-y} structure the strontium has nine-fold coordination (Figure 9.5). Relatively little oxygen can be lost without the Sr becoming undercoordinated. In the $Sr_3M_2O_7$ system, there are two strontium sites, one twelve-coordinate and one nine-coordinate (Figure 9.6). Results from this work in the $Sr_3Fe_2O_{7-x}$ system ($0 \leq x \leq 1$) have shown that oxygen is initially exclusively lost from a site forming the twelve-coordination. This preference is maintained until all of the oxygen is lost from this site. By solely eliminating ions from the high coordination sphere, a significant proportion of oxygen can be eliminated before the coordination of the A cation becomes unacceptable.

This argument can be extended to the cobaltate phase, in which the $Sr_3M_2O_7$ structure is tripled in the B direction. This phase has been shown to become unstable at high levels of oxygen, where the Co(IV) ion is too small to satisfy the coordination requirements of the structure. As the level of Co(IV) rises the structure becomes significantly destabilised and no phase has been shown to exist where $z > 0.94$. However, as the oxygen content is lowered, the A cations become undercoordinated i.e with unusual geometries such as seven-fold coordination, and the structure again becomes unstable. This leads to a very small range of oxygen stability in the $Sr_3Co_2O_7$ phase.

This trend would suggest that the higher values of n would be able to support even higher levels of oxygen deficiency. However, the $Sr_4M_3O_{10}$ structure is relatively unknown for divalent A. Even the parent titanium structure, $Sr_4Ti_3O_{10}$ (17), has not been prepared as a pure phase and the theoretical Ruddlesden-Popper phase $Sr_5Ti_4O_{13}$ (17) has not been reported. This lower stability is continued across the first row of the transition series; by $Sr_4Mn_3O_{10}$, which can also only be produced as a mixed phase (26), the phase is very unstable and larger ions tend to be incorporated for the M cation to stabilise the structure e.g Pt ions from the reaction vessel. The stability of the higher n increases when the A cation is trivalent e.g. $La_4Ni_3O_{10}$ can be prepared using atmospheric conditions

Figure 9.5 The Sr_2MO_4 Structure
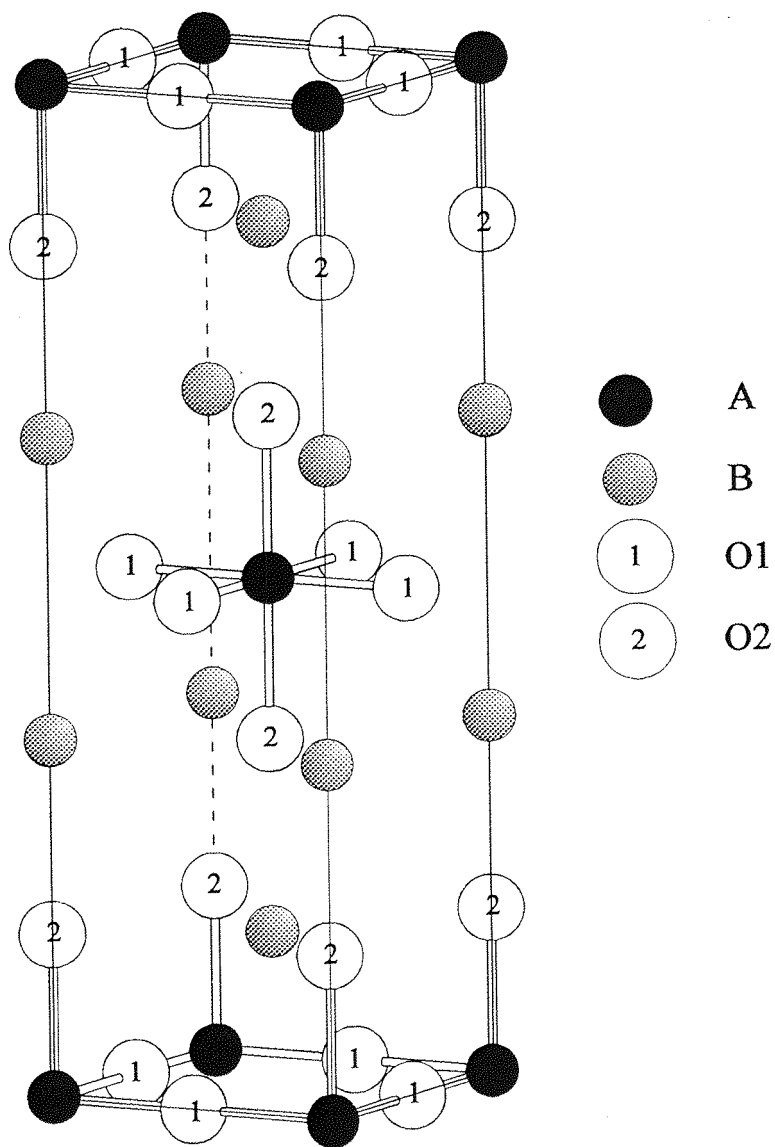
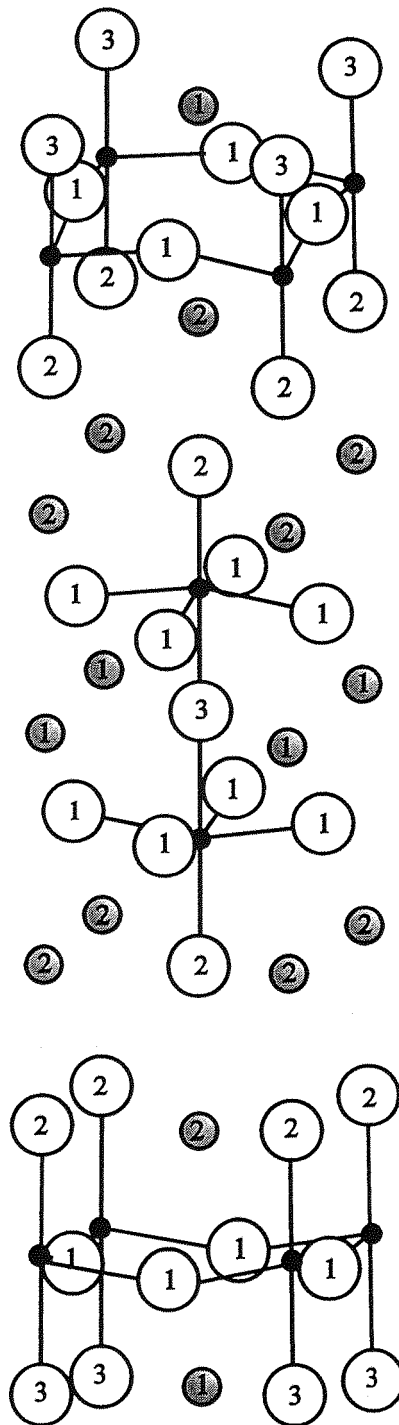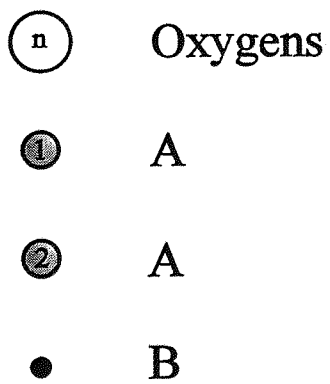**Figure 9.6** The $Sr_3M_2O_7$ Structure.

229

although long sintering times are required to produce the ordered phase (27). Reduction experiments have shown that this phase can lose up to two oxygens and support the thermodynamically unstable Ni(I) (28). This phase, therefore, demonstrates that at higher values of n in the Ruddlesden-Popper phases, an even greater level of oxygen stoichiometry can be supported (20%). These phases are unfortunately difficult to prepare, where the purity of the final structure depends on ordering of the K_2NiF_4 and perovskite blocks. As n increases, the structure is more susceptible to stacking faults in the correct sequence of building blocks, hence making pure Ruddlesden-Popper phases with n > 2 rare.

A large portion of this thesis was spent studying mixed transition metal oxides. Oxidation states of the transition metal ions were determined using TGA and Mössbauer experiments, for samples containing iron. This process revealed some interesting properties of these systems. As predicted in Chapter 1 the oxidations states of the transition metal ions were largely governed by the relative magnitudes of the ionisation potentials of the ions. For example, iron would be expected to be oxidised to Fe(IV) before copper is oxidised to copper(IV). This phenomenon has also been noted by other workers in their studies of mixed transition metal oxides (29,30). The cobalt-nickel systems are much more difficult to characterise, since it is difficult to determine the oxidation state of the individual transition metal ions. However, it could be conjectured that, these materials would behave in the same way as the iron systems. More information could be gleaned from experiments which consider the local coordination of the ions, such as EXAFS, where determination of bond lengths and angles may allow the oxidation states of the individual ions to be discerned. This could be achieved using Bond Valence calculations (31) which have been successfully applied in this work.

Some iron(IV) compounds in this work have been shown to exhibit disproportionation behaviour into Fe^{3+} and Fe^{5+}. This effect has been shown to exist previously by other authors using Mössbauer spectroscopy (32,33), although evidence for long range order has not been found using techniques such electron diffraction, neutron diffraction or x-ray diffraction. The sampling times of both the diffraction technique and Mössbauer spectroscopy is long in comparison to the time taken for the electron jump. However, in the case of the Mössbauer experiment, which considers only the iron nucleii, there is always a 50:50 mixture of Fe^{3+} and Fe^{5+}. In contrast, the diffraction experiments,

all average the structure over the timescale of the experiment. Therefore, for distinct iron sites to be observed, discrete iron(III)/iron(IV) sites would have to be maintained throughout the experiment. If the electron hopping mechanism resulted in the iron site changing from iron(III) to iron(IV) or vice-versa continually during the experimental period only an average would be observed.

Further experiments would be required to determine the causes of charge disproportionation in compounds of iron(IV). For example, it is still unclear why $SrFeO_3$ and Sr_2FeO_4 do not show signs of disproportionation behaviour but $CaFeO_3$ and $Sr_3Fe_2O_7$ disproportionate at temperatures close to room temperature. Other techniques, such as XANES, which can be used to determine oxidaion states may be applicable, although this would acquire model compounds containing Fe^{5+}, which are rare.

9.2 References

1   This work, Chapter 6.

2   M. James, J.P. Attfield. J. Sol. Stat. Chem. **105**, 287-93. (1993)

3   K.A. Wilhemi. Ark. Kemi. **26**, 149-156. (1966)

4   M.T. Robinson. J. Phys. Chem. **62**, 925-8. (1958)

5   J. Kafalas. J. Longo. J. Sol. Stat. Chem. **4**, 55. (1972)

6   S.N. Ruddlesden. P.Popper. Acta. Cryst. **10**, 538-9. (1957)

7   J.C. Bouloux, J.L. Soubeyroux, G. le Flem, P. Hagenmuller. J. Sol. Stat. Chem. **85**, 321-5. (1990)

8   J.C. Bouloux, J.L. Soubeyroux, G. le Flem, P. Hagenmuller. J. Sol. Stat. Chem. **38**, 34-9. (1981)

9   S.E. Dann, D.B. Currie, M.T. Weller. J. Sol. Stat. Chem. **92**, 237-40. (1991)

10   T. Foex. High. T. High. P. **1**, 409. (1969)

11   H.K. Muller-Buschbaum, J. Wilkens. Z. Anorg. Allgem. Chem. **591**, 161-6. (1990)

12   R. Weiss. R. Faivre. C.R. Acad. Sci. **248**, 106. (1959)

13   J. Gooden. Penn. State. Uni. University Park. Pennsylvania. JCPDS Grant in Aid Report. (1972).

14   G. Gerasimyuk. Inorg. Mat. **21**, 1019. (1985).

15   J.J. Randall, R.J. Ward. J. Chem. Soc. **79**, 266. (1957)

16   M. Keester, P.J. White. J. Sol. Stat. Chem. **2**, 68. (1970)

17   K. Lucaszewicz. Angew. Chem. **70**, 320. (1958)

18   N. Mizutani, A. Kitazawa, N. Onkuma, M. Kato. Kogyo Kogaku Zasshi. **43**, (1970)

19   S.E. Dann, D.B. Currie, M.T. Weller. J. Sol. Stat. Chem. **97**, 179-185 (1992)

20   This work, Chapter 6

21   P. Appendino, G. Rambarta. Ann. Chim. **60**, 407. (1970)

22   P. Poix. J. Sol. Stat. Chem. **31**, 95. (1980)

23   This work, Chapter 5.

24   K. Vidyasagar. Inorg. Chem. **23**, 1206. (1984)

25   N. Nguyen, J. Choisnet, B. Raveau. Mat. Res. Bull. **17**, 567. (1982)

26   J. Fabry, J. Hybler. Z. Jirak, K. Jurek, K. Maly, M. Nevriva, V. Petricek. J. Sol. Stat. Chem. <u>73</u>, 520-3. (1988)

27   C. Brisi, M. Vallino, F. Abbattista. J. Less. Comm. Metals. <u>79</u>, 215-9. (1981)

28   P.H. Lacorre. J. Sol. Stat. Chem. <u>97</u>, 495-500. (1992)

29   L. Er-Rakho, C. Michel, J. Provost, B. Raveau. J. Sol. Stat. Chem. <u>37</u>, 151-6.(1981)

30   L. Er-Rakho, C. Michel, F. Studer, B. Raveau. J. Phys. Chem. Solids. <u>49</u>, 1101-6. (1988).

31   I.D. Brown. Chem. Soc. Rev. <u>7</u>, 359. (1978)

32   M. Takano, J. Kawachi, n. Nakanishi, Y. Takeda. J. Sol. Stat. Chem. <u>39</u>. 75-84. (1981)

33   P.D. Battle, T.C. Gibb, P. Lightfoot. J. Sol. Stat. Chem. <u>84</u>, 271-9. (1990)